

School of Electrical Engineering, Computing and
Mathematical Sciences

Curtin Institute of Radio Astronomy

Constraining black hole natal kicks with high-precision
radio astrometry

Pikky Atri

This thesis is presented for the Degree of
Doctor of Philosophy
of
Curtin University

July 2020

To the best of my knowledge and belief this thesis contains no material previously published by any other person except where due acknowledgement has been made. This thesis contains no material which has been accepted for the award of any other degree or diploma in any university.

Pikky Atri
24 July 2020

“Well, I’m a bit of a fighter. I knew they’d made a mistake admitting me. I knew they were going to throw me out sooner or later. But I decided in the interim I would work my very hardest, so that when they threw me out, I wouldn’t have a guilty conscience. I’d know I’d done my best. And so I was being very diligent, very thorough, very conscientious, following up every anomaly that our new radio telescope turned up. And that’s what led to the discovery of pulsars. ”

— Professor Dame Jocelyn Bell Burnell

Acknowledgements

Three years and three months is how long it took to finish this thesis, but in reality the work towards this thesis started almost ten years ago - from my undergraduate. There is no way I would have lasted these ten years had it not been for the people that came in my life in the form of encouragement and support during this time, and I would like to take this space to thank them for getting me here.

I think the biggest and most special thanks has to go to my supervisory panel - James Miller-Jones, Arash Bahramian and Richard Plotkin. The three of you together make the best supervisory team a student can only dream of. I have brought the oddest problems and situations to you in the past three years, and have always been surprised at how well you have all handled them. You all have had to read and fix so many written documents of mine that I have lost count, and I am thankful for every suggestion you have ever made. I will terribly miss our weekly meetings, and I hope you will let me look to you for mentorship even after I am done with the PhD.

James, thank you for sowing the seed of this project and believing I was good enough to pull it off. I have no idea of what you saw in me that made you think ‘Oh, this student who claims to know X-ray astronomy would be a good fit to do a Very Long Baseline Interferometry based thesis’, all I know is that I will forever be grateful for your faith in me. Thanks for being so patient while

teaching me radio astronomy and *AIPS*, and for not only supporting but also encouraging me to participate in as many conferences and outreach activities as my time allowed. I also want to thank you for every word of encouragement and smiley emoticons in your emails, these little nuggets helped me persevere through some low self-confidence times.

Arash, you joining the supervisory team was the best thing that could have happened. You brought something to it that I didn't even know was missing, and now I cannot imagine it any other way. I have learnt so much from you, from something as basic as the difference between probability and probability density to the more complicated concepts like Bayesian hierarchical modelling. You always looked so excited and happy with all the plots I made, even though I knew that you could easily do a better job at making them. You never failed to tell me I was doing a good job, and hearing that was enough to make everything better during the lowest of times. I hope to one day imbue your love for visualising every problem with a code.

Rich, I was afraid you moving to the U.S would mean I would have only two supervisors, but you made sure you were present whenever you were needed and were up to date with my progress. I appreciate every evening you gave up so you could dial in to my supervisory meetings. Thanks for teaching me the art of talking to a room full of people, you understood my 'talks-too-fast' problem and your tips have helped me give presentations ever since. I am thankful for all the anecdotes you shared from your own life, which made me feel like I was not alone in making the mistakes I was making. This feeling has helped me not feel inadequate during the last three years.

I have been very lucky to have found support in many people at my institute. I would also like to thank J-P Macquart, Jess Broderick and Christene Lynch for agreeing to be my CIRA internal review panel. J-P, you made me believe in myself as a researcher by showing confidence in me and by taking the time to guide me through my PhD, even when you didn't have to. Had I known

this is all the guidance I was going to get from you, I would have typed down every single conversation we had. Jess, your guidance through the whole postdoc application process helped me a great deal. Cath Trott, thank you for taking the effort to come and congratulate me after my first-ever poster presentation. My supervisors were not able to attend the event, and you saying you liked my 30 seconds of fame meant the world to me. I would also like to thank Brian Crosse for the never ending banter, it made me feel like I was not far away from home. A huge thanks to the administration team at CIRA, Chamila Thrum, Emily Johnson, Tina Salisbury and Angela Dunleavy. I know I have always brought the most confusing and convoluted travel plans to you, but you all have always found a way to straighten them up.

Participating in various national and international conferences has been a great experience, and some of those conferences have given me a few surprising friendships. I would like to thank Zsolt Paragi for introducing me to the European VLBI Network support scientist team. They took me under their wing and have supported me in not just EVN data acquisition, but also in navigating through some difficult situations. Benito Marcote, Ross Burns, Katharina Immer, Jay Blanchard and Tatiana Bocanegra thanks for making me a part of your small family. I will always hold the memory of singing Abba songs with you all in the cobbled streets of Granada very close to my heart. Here's to hoping that we can have our *AIPS* retreat soon. I found a new love for outreach, and I have Kirsten Fredericksen to thank for that. You invited me to one event, and then there was no looking back. The experience would probably have been not as exciting had it not been the company of Gregory Rowbotham, Cassa Rowles, Robin Cook and Ronniy Joseph. I will always cherish every single trip of ours.

The PhD students cohort at my institute is one of the most fiercely supportive groups I have ever been a part of. I am grateful for all the friendships I have shared with this amazing group of people. To Ben Quici, Freya North-Hickey, David Scott and Mawson Sammons, thank you for helping me get through the

final, most-intense few months of my thesis. Every offer of help, whether it be to cook me food, do my laundry or smuggle things out of the office for me (*cough, cough, Ben*) is highly appreciated, and made me feel like I was not alone in this. I am really glad you all ‘love’ my great sense of humour and I look forward to meeting you all in a conference someday and keep up our tradition of happy hour and bikkies.

To Ryan Urquhart and Vlad Tudor, thank you for making sure I never missed my annoying siblings from back home in India. My first two PhD years would have been very dull (and probably more productive) if it were not for the constant entertainment you two provided from across the desk. To Ronniy, you have been the perfect friend - one I could have crazy times with but also someone I learnt a lot from. I am grateful for all the conferences we had the opportunity to attend together and not come back hating each other, all the times you were looking out for me and handing me water to drink even when I didn’t know I needed it, all the walks around the institute when it seemed like life did not have any answers anymore, and all the road trips and the hikes. I hope to see you soon in the Netherlands and we can go on biking trips (I promise I will try biking in that flat terrain).

There are a few friends in Perth that I would like to thank, who have now become family. To Abhi, Sakshi, Ritika and Sumit you had a huge part to play in making Perth my home. You opened your hearts and home to me and I would have not survived the last few years had it not been for your love and support. Whether it be a midnight medical emergency call or a ‘I need a hug’ call, you were there by my side at the drop of a hat. I wish I could have taken you all with me, but alas I will have to be content with the hope that you will see me when you come to Europe for vacations. To Kriti, thanks for being an amazing neighbour who loves to share her cooking. In my opinion, providing delicious food is one of the best ways one can help a person writing their thesis, so thanks a lot for that. To Teesta di and Luna, thanks for providing me with a space where I could just

unwind and spend hours laughing and talking, and I look forward to moving in with you two and giving Luna pats all day long. I would also like to thank Daksh and Swati for all the fun outings and picnics, you have helped me maintain my sanity.

I would have given up research a long time ago had it not been for my masters' mentors Prof. T. R. Seshadri and Prof. A. R. Rao. You both saw potential in me even when I had given up and when I was getting rejections from every corner. Thanks for keeping me involved in projects to make sure I never completely lose my motivation.

Living a continent away from my friends and family in India would have been so much more difficult had it not been for their undying support. To Arshdeep, Mikita, Suri and Sandhya, thanks for making my transition to Australia easier by always being only one-call-away. You are all very brave to stick with me through all these years and I will always be grateful for that. Talking to you all has always been a stress buster, even if it was 1 am for me, and I cannot wait to celebrate with you at the first chance we get. To Piyusha, we have been 'Snowy and Tintin' since we were toddlers, and just knowing that I will always have a Tintin by my side has been a great source of relief. To Vara, thanks for teaching me about unconditional friendship and for sharing your love of hiking with me. Hiking has helped me get through the many troughs of my PhD life, and my only regret is that I didn't get a chance to explore Australian trails with you before some random stranger on the road decided that you were too good for this planet.

I would like to thank my dad for making me fall in love with everything in the sky, whether it be planes or stars. Thanks papa, for taking me out to the runway as a child to gaze at the stars, searching for satellites in the night sky is one of my fondest childhood memories. Thanks for helping me look for dark areas whenever we went for vacations so I could star gaze to my heart's content. Thanks for making me stubborn enough to never give up, your advice 'run off the cold' somehow always works. I would like to thank my mom for giving up her

own career to take care of me and my sister. Ma, thanking you is never going to be enough and I will spend all my life trying to make you proud of your decision. You stood by me through every decision of mine, you supported my decision to pursue pure sciences even when I was being told it is not a good career path to earn a living. Even though we are separated by 6000 kilometers, you made sure I ate every single day. Thank you for everything ma pa, I am what I am because of you two. To my younger sister Manu, thank you for teaching me resilience, you are one of the bravest people I know. It took me a while to accept that I could take advice from you, but I am glad I came around and you have been an inspiration ever since.

Lastly, I would like to thank the 2017 Radio Astronomy School held at Narrabri, New South Wales, for helping me meet my partner. I would have never met him otherwise because we lived in different corners of the continent. Aditya, you have been my own personal sunshine, lighting up even the most darkest days of my life (the song 'My Girl' by The Temptations comes to mind). In this constantly changing world, your support and confidence in me has been the one constant I have relied on. Thank you, for never letting me feel alone even during the most isolated times. I am very excited to see what adventures we will embark on in the future and cannot wait to check out all the places in our travel list.

Abstract

This thesis demonstrates the different ways in which high precision radio astrometry can further our understanding of stellar mass black holes (BHs), especially BH birth mechanisms. In this thesis, we use black hole X-ray binaries (stellar-mass black holes accreting from a companion star) as a probe to study BHs. It is known that a stellar mass BH is born when a massive star runs out of fuel and dies, either with or without a supernova (SN) explosion. Differentiating between these two birth mechanisms by observing BHs while they are being formed is rare. Thus, we need to study a parameter that is indicative of the birth mechanism of a BH by observing them in the current epoch, after the BHXB has formed.

SN explosions impart a velocity to the BH remnant, which is referred to as a natal kick. Natal kicks affect BH binary merger rates and sites. Natal kicks are used in N-body simulations that estimate the number of BH systems that can be retained in globular clusters. Natal kicks are also integral to model SN explosion mechanisms that give birth to BHs. Until now, these codes have been using natal kick distributions that were not observationally constrained. Determining natal kicks can help differentiate between birth of a BH with or without a SN explosion.

To determine the natal kick velocity of a system, we must trace the 3D motion of the source in the Galaxy. This requires the measurement of the proper motion, the line-of-sight velocity and the distance to the source. Typical motions of BHXBs are of the order of a few milliarcseconds yr^{-1} and the parallax is a fraction of a milliarcsecond. Measuring this motion requires high resolution astrometry offered by Very Long Baseline Interferometry (VLBI) at radio wavelengths and by the *Gaia* satellite at optical wavelengths.

In this thesis, we first used VLBI to measure the proper motion and parallax

of a BHXB, MAXI J1820+070. We find that the high significance parallax measurement of MAXI J1820+070 when inverted to distance using Bayesian inference leads to a prior independent distance, which has been used to update other key system parameters of the BHXB (e.g., the mass of the BH).

We then extended this work to measure the proper motions of three more BHXBs. Combining the measured proper motions and distances with line-of-sight velocities from the literature, we developed a technique to estimate the potential kick velocity (PKV) of these four BHXBs. We also used the proper motions, distances and velocities of 12 other BHXBs that had been reported in the literature, giving a sample of 16 BHXBs with estimated PKV. Using these we were able to classify the BH birth mechanism of these systems. Out of the 16 BHXBs, we inferred that at least 75% of the systems had high PKV and thus likely strong natal kicks, indicating that BH birth by SN explosion was common in this sample of BHXBs. We used Bayesian hierarchical modelling to obtain the first observationally constrained PKV distribution of the BHXB population using these 16 PKV distributions. The best fit model of the PKV distribution of the BHXB population was unimodal, although a bimodal distribution could not be ruled out.

Building on this finding, we used proper motion measurements to differentiate between Galactic and extragalactic radio sources from a sample of 33 targets that were observed with the Very Long Baseline Array (VLBA). We were able to measure the proper motions of ten out of these 33 targets and found that at least six of them are Galactic. This demonstrates that this technique that can be used to discover new BHXBs in our Galaxy without relying on X-ray outbursts, providing a window into a new subset of the BHXB population.

This thesis underscores the importance of continuing radio astrometry programs for BHXBs to increase the sample size, remove observational biases affecting the estimated PKV of the BHXB population, and conduct astrometry for BHXBs that might not be accessible by *Gaia*.

Statement of contribution by others

Chapter 3 of this thesis, ‘Parallax of MAXIJ1820+070 : a case study’, has been adapted from an already published work Atri et al. 2020 (‘A radio parallax to the black hole X-ray binary MAXIJ1820+070’ *Monthly Notices of the Royal Astronomical Society*, Letters, Volume 493, Issue 1, p.L81-L86, DOI: 10.1093/mnrasl/slaa010). It is my own work, excepting the following. The Bayesian code to fit for the parallax and proper motion of MAXIJ1820+070 was written by A. Bahramian. Discussions on the data reduction and implications of the results were contributed to by my supervisory panel - J. C. A. Miller-Jones, A. Bahramian, and R. M. Plotkin. Discussions were also contributed to by A. T. Deller, P. G. Jonker, T. J. Maccaron, G. R. Sivakoff, R. Soria, D. Altamirano, T. Belloni, R. Fender, E. Koerding, D. Maitra, S. Markoff, S. Migliari, D. Russell, T. Russell, C. L. Sarazin, A. J. Tetarenko, and V. Tudose.

Chapter 4 of this thesis, ‘Black hole natal kicks and birth constraints’, has been adapted from an already published work Atri et al. 2019 (‘Potential Kick Velocity distribution of black hole X-ray binaries and implications for natal kicks’ *Monthly Notices of the Royal Astronomical Society*, Volume 489, Issue 3, p.3116-3134, DOI: 10.1093/mnras/stz2335). It is my own work, excepting the following. The Bayesian code to fit a distribution model for the potential kick velocity distribution of black hole X-ray binary population was written by A. Bahramian. The LBA data for the source GX 339-4 was reduced by J. C. A. Miller-Jones. The discussions to the implications of the results were contributed by J. C. A. Miller-Jones, A. Bahramian, R. M. Plotkin, P. G. Jonker, G. Nelemans, T. J. Maccarone, G. R. Sivakoff, A. T. Deller, S. Chaty, and M. A. P. Torres. S. Horiuchi, J. McCallum, T. Natusch, C. J. Phillips, J. Stevens, and S. Weston contributed to the acquisition of the LBA data of GX 33-4 and GRS 1716-249.

The content of Chapter 5, ‘A search for quiescent Galactic black hole systems’, is as yet unpublished. It is my own work, excepting the following. The Bayesian code to fit for the parallax and proper motion of the targets was written by A. Bahramian. Discussions were contributed to by my supervisory panel - J. C. A. Miller-Jones, A. Bahramian, and R. M. Plotkin. Discussions were also contributed by Craig Heinke, the P.I. of the VLBA observing campaign that provided the data for this chapter.

(Signature of candidate)

(Signature of supervisor)

Contents

Acknowledgements	vii
Abstract	xiii
List of Figures	xxv
1 Introduction	1
1.1 A series of unimaginable ideas	1
1.2 Looking for black holes	2
1.2.1 Supermassive black holes	3
1.2.2 Intermediate mass black holes	5
1.2.3 Stellar mass black holes	6
1.3 Black hole X-ray binaries	9
1.3.1 X-ray emission - accretion disc	9
1.3.2 Radio emission - jets	12
1.3.3 Geometry and emission during outburst	14
1.4 Stellar mass black hole birth and natal kicks	16
1.4.1 Different birth pathways	17
1.4.2 Natal kicks	19

1.4.2.1	Symmetric mass loss	21
1.4.2.2	Asymmetric kicks	25
1.5	Natal kick implications on BH studies	30
1.5.1	BH mass and natal kicks	30
1.5.2	BH-BH mergers	32
1.5.3	BH systems in GCs	35
1.5.4	Natal kicks and z -distribution	37
1.6	Measuring natal kicks	38
1.6.1	Peculiar velocity estimations	38
1.6.2	Existing natal kick constraints	39
1.7	Structure of thesis	42
2	Telescopes and Techniques	45
2.1	Radio interferometry	45
2.2	Observing the radio sky	46
2.2.1	Visibilities and Fourier transforms	46
2.2.2	The uvw plane	49
2.3	Obtaining radio data: VLBI	52
2.3.1	The VLBA	52
2.3.2	The EVN	54
2.3.3	The LBA	56
2.4	Reducing radio data	57
2.4.1	Calibration	57
2.4.1.1	Preliminary calibration	58
2.4.1.2	Fringe fitting	59
2.4.1.3	Phase referencing	60

2.4.2	Imaging and cleaning	61
2.4.2.1	Cleaning	61
2.4.2.2	Imaging	62
2.4.3	Reducing systematics	63
2.4.3.1	Geodetic blocks	63
2.4.3.2	Improving phase calibrator model	64
2.4.3.3	Tropospheric and Ionospheric errors	65
2.5	Velocities of BHXBs	66
2.5.1	Systemic radial velocity	67
2.5.2	BHXB astrometry	67
2.5.2.1	Gaia-DR2	67
2.5.2.2	Using VLBI	68
2.5.3	Distances	70
2.5.4	Measuring proper motion and parallax	71
2.5.5	Galactic motion and U, V, W velocities	72
2.6	Bayesian Inference	73
2.6.1	Applications	74
2.6.2	Computational method: HMC and NUTS	75
3	Parallax of MAXI J1820+070 : a case study	77
3.1	Importance of measuring distances	78
3.2	MAXI J1820+070	78
3.3	Observations and Data reduction	79
3.3.1	VLBA campaigns	81
3.3.2	Parallax campaign: EVN data	85
3.3.3	Mitigating systematic biases	86

3.3.3.1	Atmospheric errors	86
3.3.3.2	Reference frame shifts	89
3.4	Results and Analysis	90
3.4.1	A Bayesian approach for parallax fitting	90
3.4.2	Distance from parallax	92
3.4.2.1	Source density priors	92
3.4.2.2	Distance posterior distribution	95
3.5	Discussion	97
3.5.1	Transition and peak outburst luminosities	97
3.5.2	Jet parameters	97
3.5.3	Implications for BH mass	98
3.5.4	Peculiar velocity	100
3.6	Summary	100
4	Black hole natal kicks and birth constraints	103
4.1	Limitations of peculiar velocity for BHXBs	104
4.2	Data	105
4.2.1	BHXB sample	105
4.2.2	Sample biases	106
4.3	VLBI Observations and Data reduction	106
4.3.1	GX 339–4	108
4.3.2	GRS 1716–249	108
4.3.3	Swift J1753.5–0127	109
4.4	Results - Proper motion measurements	110
4.4.1	GX 339–4	112
4.4.2	GRS 1716–249	112

4.4.3	Swift J1753.5–0127	116
4.5	Distance and radial velocity estimates	117
4.5.1	Distance - Milky way prior	117
4.5.2	Systemic radial velocity estimates	118
4.6	Analysis - Potential kick velocity	119
4.6.1	Methodology and code for PKV	119
4.6.2	Potential kick velocity distributions of new VLBI sources	120
4.6.2.1	GX 339–4	121
4.6.2.2	GRS 1716–249	121
4.6.2.3	Swift J1753.5–0127	123
4.6.3	PKV distributions of <i>Gaia</i> DR–2 and archival sources . . .	125
4.7	Discussion	126
4.7.1	Potential kick velocity distribution - BHXB population . .	126
4.7.2	Potential Kick velocity interpretation	132
4.7.3	Comparison with NS natal kicks	134
4.7.4	Supernova mass loss	137
4.7.5	Natal kicks and z-distribution	138
4.7.6	Natal kicks and black hole mass	142
4.7.7	BHs in Globular clusters	142
4.7.8	Implications for BH-BH systems	145
4.7.9	BHXB spin-orbit misalignment	146
4.8	Summary	146
5	A search for quiescent Galactic black hole systems	149
5.1	Introduction	150
5.2	Observations	155

5.3	Data reduction	156
5.3.1	First order reduction	156
5.3.2	Second order reduction	158
5.3.3	Imaging	160
5.4	Results	162
5.5	Analysis	163
5.6	Discussion	174
5.6.1	Source classification	174
5.6.1.1	Galactic sources	176
5.6.1.2	Extragalactic/Inconclusive	178
5.6.2	Extinction limitations	179
5.6.3	Population comparison	181
5.7	Future Work	182
5.8	Summary	186
6	Discussion, Future Prospects and Conclusions	189
6.1	Discussion	189
6.1.1	A new technique: Improvements on previous studies	189
6.1.2	Natal kicks and beyond: implications	191
6.1.3	BHXB treasure unlocked with astrometry	194
6.1.3.1	Increase in proper motion sample size	194
6.1.3.2	Refined system parameters: MAXI J1820+070	195
6.1.3.3	Astrometry to search for BHXBs	197
6.1.4	The VLBI campaigns	198
6.1.5	PKV limitations and improvements	200
6.1.6	Upcoming instruments	203

6.2	Future Work	204
6.3	Conclusions	206
	Appendices	209
	A Publications	211
	B Co-author permissions	213
	Bibliography	243

List of Figures

1.1	Zooming into M87*, the SMBH at the centre of the galaxy Messier 87. Top left: HST image showing clear kpc scale optical jet of M87*. Top right: Radio image using East Asian Very Long Baseline Interferometry Network, a high resolution radio interferometry array, showing parsec scale jet of M87*. Bottom: Gravitationally lensed photon ring around M87* as seen by the EHT. <i>Image credits: Hada, 2019.</i>	4
1.2	Detections of gravitational wave events by LIGO compared with BHs and NSs that have been electromagnetically detected as of 16-05-2020. There appear to be a few NS merger candidates that lie in the mass gap a gap between $2-5 M_{\odot}$. <i>Credit: LIGO -Virgo/Frank Elavsky, Aaron Geller¹</i>	8
1.3	An artist's impression of the formation of accretion disc in binaries. Top panel: Formation of accretion disc in HMXBs due to strong stellar winds. Bottom panel: Accretion disc in LMXBs by stellar expansion and Roche Lobe overflow. <i>Image credits: Aditya Parthasarathy.</i>	10

1.4	The lightcurve of GX339-4 with a smoothed fit. This represents the X-ray lightcurve in the 2002-2003 outburst and the flux corresponds to the X-ray band of 0.1–200 keV. The hard X-ray spectral states are related to the increase in flux in the beginning and end of the outburst (see Section 1.3.3 for more details). <i>Image credits: Fender & Muñoz-Darias, 2016</i>	11
1.5	Image of radio jets in GRS 1915+105. This image is a colour version ² of the image from Mirabel & Rodríguez (1994). It represents bright radio lobes moving away from a stationary core. Six observations were taken a week apart from each other using the Very Large Array. <i>Image credits: Mirabel & Rodríguez, 1994.</i>	13
1.6	Variation in X-ray hardness ratio with X-ray luminosity during an outburst of GX 339–4. The images in the lower panel are artist’s impressions of the change in geometry of the accretion disc and the presence of a radio jet with a change in the X-ray spectrum. <i>Image credits: Fender & Muñoz-Darias, 2016.</i>	15
1.7	The first strong candidate of a direct collapse. Three epochs of images from the HST centred at the direct collapse candidate. The candidate is visible in 1994 (left panel) and vanishes in the image in 2001 (right panel). <i>Image credits: Reynolds et al., 2015.</i>	18
1.8	Chandra image of a pulsar, IGR J11014-6103, kicked away from its supernova remnant. The pulsar is estimated to have a transverse velocity of 2400-2900 km s ⁻¹ (Tomsick et al., 2012) and is attributed to an asymmetric natal kick at birth of the pulsar. <i>Image credits - NASA, Chandra X-ray Observatory, INTEGRAL Science Data Centre</i> ³	19

1.9 Representation of the process of a massive helium star undergoing an instantaneous SN explosion in a binary and the kick the system obtains due to symmetric mass loss. The first image is a representation of a helium star with mass M_{He} in a binary with a star of mass m and the binary has a semi-major axis of a_i . v_{He} represents the velocity of the primary and the SN remnant, and the arrow denotes the direction. a_f is the semi-major axis of the orbit after the primary undergoes an instantaneous SN explosion and v_{sys} is the kick velocity the system obtains from the SN explosion once the tidal forces have re-circularised the orbit, with the final semi-major axis of the orbit of the binary of $a_{\text{re-circ}}$ 22

1.10 Kick limits of six XRBs. Three dimensional recoil velocity estimates suggesting that velocities $<40 \text{ km s}^{-1}$ can be explained by symmetric mass loss. *Image credits: Nelemans et al., 1999.* 24

1.11 Model fit to the velocity distribution of 28 pulsars. A double Maxwellian model is preferred with a low and a high velocity peak. The grey is the single Maxwellian fit to all pulsars, the black and red solid lines are models for two Maxwellians for all and only young pulsars, respectively. The vertical dotted lines denote the median of the distributions. w is the fraction of pulsars in the lower velocity distribution and σ denotes the medians for the two Maxwellians. *Image credits: Verbunt et al., 2017.* 26

1.12	X-ray images using the Chandra X-ray Observatory and the ROentgen SATellite of six supernova remnants and pulsars. The green arrow denotes the direction from the estimated position of the supernova explosion to the dipole moment of the supernova remnant. The white arrow denotes the direction of the neutron star proper motion. Five out of the six neutron stars seem to have obtained kicks in the direction opposite to the direction of the dipole moment of the supernova remnant. <i>Image credits: Holland-Ashford et al., 2017.</i>	28
1.13	Spin-orbit misalignment due to symmetric and asymmetric mass loss. Left panel: Direction of the spin of the components and the orbital motion remains aligned after a Blaauw kick. Right panel: Direction of the spin of the components and orbital motion becomes misaligned after asymmetric mass loss. <i>Image Credits - Philipp Podsiadlowski.</i>	29
1.14	Measured momenta of BHXB systems as a function of the mass of the BH in the system. <i>Image credits: Mirabel, 2017</i>	32
1.15	BH-BH merger rates and effect on spin-orbit misalignment. Top panel: Simulations showing the effect of natal kicks on the rate of mergers. The orange and green lines represent the merger rate assuming the design parameter of LIGO and the actual parameters during LIGO's first and second observing runs. <i>Image credits: Wong & Gerosa, 2019.</i> Bottom panel : The misalignment that the binary will suffer after the first BH receives a natal kick with respect to the natal kick that the BH gets. The top axis depicts different natal kick input distribution models. The solid and shaded lines are the median, 68% and 95% confidence intervals. <i>Image credits: Wysocki et al., 2018.</i>	34

1.16	Radio image using the Very Large Array for the first BHXB candidates detected in the globular cluster M22. The source marked as ‘Pulsar’ is a known source, and M22-VLA1 and M22-VLA2 are the two candidate black hole X-ray binary candidates. <i>Image credits: Strader et al., 2012.</i>	36
1.17	Distribution of BHXB and Neutron Star X-ray binaries (NSXBs) in the Milky Way. The black filled-in markers denote the BHXBs and the transparent circle markers are the NSXBs. R is the distance from the Galactic centre. Based on the dispersion of BHXBs and NSXBs above and below the Galactic plane it was suggested that they obtain similar natal kicks. <i>Image credits: Repetto et al., 2012.</i>	37
1.18	Galactocentric orbit of BHXB, XTE J1118+480. Left panel: The face-on view of the Galaxy with the cross representing the Galactic centre. Right panel: The edge-on view of the Galaxy. Blue represents the Galactocentric orbit of the BHXB during its last orbital period and red represents the Galactocentric orbit of the BHXB since it crossed the Galactic plane ($z = 0$). <i>Image credits: Mirabel, 2017.</i>	39
1.19	Optical image of the sky to show the relationship between the BHXB Cyg X-1 and the stellar association Cyg OB3. The red and yellow arrows represent the magnitude and direction of the transverse velocity of Cyg X-1 and Cyg OB3, respectively. The motion in the plane of the sky suggests that Cyg X-1 was formed in the stellar association Cyg-OB3. <i>Image credits: Mirabel & Rodrigues, 2003.</i>	41

2.1	A basic two element radio interferometer. \mathbf{b} is the interferometer baseline. ω is the observing frequency ($2\pi\nu$) and τ_g is the time delay between the two elements of the interferometer. V_1V_2 is the correlated signal from the two antennas. <i>Image credits: Thompson et al., 2017.</i>	47
2.2	(u, v, w) coordinate system and the (l, m) plane. The source, $I(l, m)$ is being tracked and observed by a pair of antennas with a baseline length of D_λ . s_0 is the direction of the w component and also the delay tracking centre. <i>Image credits: Thompson et al., 2017.</i>	50
2.3	We have presented a comparison of the uv -tracks traced by the Very Long Baseline Array (see Section 2.3.1 for details about the array) for 80 minutes for two targets, MAXI J1820+070 (top figure) and MAXI J1813-095 (bottom figure) at a declination of $+07^\circ$ and -09° , respectively.	53
2.4	Locations of dishes that we used in the Very Long Baseline Array. The stations used in this thesis have been marked in this figure. BR - Brewster; FD - Fort Davis; HN - Hancock; KP - Kitt Peak; LA - Los Alamos; MK - Mauna Kea; NL - North Liberty; OV - Owens Valley ; PT - Pie Town; SC - St. Croix.	54
2.5	Locations of the dishes we used in the European VLBI Network. The stations used in this thesis have been marked in this figure. JB - Jodrell Bank; WB - Westerbork; EF - Effelsberg; MC - Medicina; NT - Noto; O8 - Onsala; T6 - Tianma65; TR - Torun; HH - Hartebeesthoek; YS - Yebes; IB - Irbene; CM - Cambridge; KN - Knockin; DE - Defford; PI - Pickmere.	55

2.6	Locations of the dishes that participate in LBA observations. AK - ASKAP; AT - phased up ATCA; CD - Ceduna; HO - Hobart; KE - Katherine; MP - Mopra; PA - Parkes; TD - Tidbinbilla; WA - Warkworth; YG - Yarragadee.	57
2.7	Phase slopes before and after removing delays. The slope across each IF of a pair of antennas flattens out.	60
2.8	Variation of astrometric accuracy in Right Ascension and Declination as a function of target-calibrator separation. <i>Image credits: Pradel et al., 2006.</i>	66
2.9	Proper motion and parallax of Cyg X-1 using VLBA and two phase calibrators. The change in position of the target when phase referenced to the two calibrators is depicted in two colours. Left panel: Positions on the sky of Cyg X-1 denoted by the square markers and circles indicate the expected position based on the proper motion and parallax fits. Middle panel: The east (top two lines) and north (bottom two lines) position offsets as a function of time. Right panel: Offsets in the north and east positions after removing the best fit proper motions. <i>Image Credits: Reid et al., 2011.</i> . . .	69

3.1	The X-ray and optical lightcurves of MAXI J1820. The range of the x-axis covers the duration of the main outburst (the one in which the target was first discovered) and the two refluers of the source. The bottom x-axis represent the dates in MJD and the top axis in yyyy/mm/dd. The top panel is the light curve from the Swifts Burst Area Telescope (BAT) light curve, the second panel from the top is the MAXI lightcurve, the third panel from the top is the lightcurve from the Swift X-ray Telescope (XRT) and the bottom panel is the ASAS-SN light curve. All the data in this figure are publicly available. The vertical dashed lines denote the epochs at which we observed at source using the VLBA and the EVN. <i>Image credits: Arash Bahramian.</i>	80
3.2	The positions of MAXI J1820, J1821 and J1813 in the plane of the sky. The separation between MAXI J1820 and J1813 is 1.7° and 0.92° in R.A and Dec, respectively. The separation between MAXI J1820 and J1821 is 0.27° and 1.37° in R.A and Dec, respectively. <i>Image credits: Arash Bahramian.</i>	82
3.3	The measured offsets of the positions of the check source when phase referenced to the calibrator. If the position of J1813 is labelled, then it was phase referenced to J1821, and vice-versa. The dashed ellipses represent the expected systematic error region in RA and Dec by combining the expected tropospheric and ionospheric errors in quadrature (see Table 3.3), assuming the mean offset as the centre.	87

3.4	Offsets in the measured position of MAXIJ1820 due to phase referencing to different calibrators. Different colours signify different observing epochs. The triangle and circle marker denotes the position of MAXIJ1820 when it was phase referenced to J1813 and J1821, respectively.	89
3.5	A cornerplot representing the posterior distributions of parameters fit for in our parallax estimation code. α_0 , δ_0 are the reference positions of MAXI J1820 in RA and Dec, respectively. δ RA (offset) and δ Dec (offset) represent the core offsets in the peak emissions of the phase calibrator when observed at 5 and 15 GHz. π represents the parallax. μ_α and μ_δ denote the proper motions in R.A and Dec. The dashed lines and the contours represent the 16 th , 50 th and 84 th percentiles of the probability distributions. Correlations between δ RA (offset) and μ_α , and between δ Dec (offset) and δ_0 are seen in the respective 2D histograms.	91
3.6	Astrometry of MAXI J1820, as phase referenced to J1821 at 5 GHz. The blue circles and red squares are the positions measured by the VLBA and the EVN, respectively. All marked positions have been corrected for the frame shift due to different calibrators and frequencies. The errors bars denote the statistical and systematic errors added in quadrature. Top panel: Motion in the plane of the sky relative to the fitted reference position, overlaid with the trajectory given by the best fitting proper motion and parallax (black dashed line). Bottom panel: Parallax signature of 0.348 (black dashed line) \pm 0.033 (grey dashed lines) mas isolated by removing our best fitting proper motion.	93

3.7	Distance posterior distributions of MAXI J1820, for both our new VLBI and the <i>Gaia</i> -DR2 parallax measurement. The <i>Gaia</i> -DR2 distance posterior has a higher median value for the Milky Way (MW) prior (5.1 ± 2.7 kpc) than for the exponentially-decreasing volume density (EDVD) prior (4.4 ± 2.4 kpc), whereas our VLBI distance distribution (2.96 ± 0.33 kpc) is insensitive to the prior chosen.	96
4.1	Proper motion fit for GX 339-4. GX 339-4 was tracked for three epochs over three different outbursts. Top panel: Offset of measured positions relative to the first epoch in Right Ascension. Bottom panel: Offset of measured positions in Declination relative to the first epoch.	114
4.2	Proper motion fits for GRS 1716-249. GRS 1716-249 was tracked for three epochs over one outburst using the LBA, with positions shown with respect to the first LBA epoch. Top panel: fits by considering position measurements of two epochs at a time in RA and Dec - epoch 1 and 2 (dashed line); epoch 2 and 3 (dotted line); epoch 1 and 3 (dotted dashed line). The three declination measurements do not lie on a straight line. Lower panel: fitting for proper motion by increasing the time baseline using the 1994 K-band image position measurement (dotted line), which breaks the degeneracy and shows that the epoch 1 LBA position is in error (blue and green dashed lines). This was then removed from the fit.	115

- 4.3 Proper motion fit for Swift J1753.5–0127. Swift J1753.5–0127 was observed for ten epochs spanning four years. The four observations in 2009 December were concatenated into one position measurement (MJD 55181 to MJD 55190). Top panel: offset of measured positions in Right Ascension of Swift J1753.5–0127 as a function of MJD relative to the first epoch. Bottom panel: offset of measured positions in Declination of Swift J1753.5–0127 as a function of MJD relative to the first epoch. 116
- 4.4 Potential kick velocity probability distribution of GX 339–4 with a median of 200 km s^{-1} (dashed line) and 5^{th} and 95^{th} percentile of 122 km s^{-1} and 258 km s^{-1} (in dotted lines), respectively. 121
- 4.5 Top panel: PKV probability distribution of GRS 1716–249 using Gaussian systemic radial velocity ($\bar{\gamma}$) distributions with means of -110 km s^{-1} , -60 km s^{-1} , -10 km s^{-1} , 40 km s^{-1} and 90 km s^{-1} all with a 1σ of 50 km s^{-1} . The medians of all the PKV distributions are the blue dashed vertical lines. The lowest PKV probability distribution median is of $\sim 70 \text{ km s}^{-1}$ and corresponds to the systemic radial velocity of $-10 \pm 50 \text{ km s}^{-1}$. Bottom panel: a 3-D visualisation of the Galactocentric orbit of GRS 1716–249, integrated for 1 Gyr for 20 orbit instances each of the lowest ($67_{-27}^{+41} \text{ km s}^{-1}$) and highest ($100_{-47}^{+68} \text{ km s}^{-1}$) PKV corresponding to systemic radial velocities of $-10 \pm 50 \text{ km s}^{-1}$ and $90 \pm 50 \text{ km s}^{-1}$, respectively. All three axes are in kpc. The system does not go beyond 1 kpc above the Galactic plane in both the cases. 122

4.6 Top panel: Posterior distribution function for the distance to Swift J1753.5–0127, constructed from the *Gaia*-DR2 parallax measurement using the Milky Way LMXB distribution prior (see §4.5.1 for details). The mode of the distribution is at 7.7 kpc. The 5th, 50th and 95th percentiles of the distance are at 4.8, 8.8 and 20.8 kpc respectively. Bottom panel: PKV probability distribution of Swift J1753.5–0127 using Gaussian systemic radial velocity ($\bar{\gamma}$) distributions with means of -7 km s^{-1} , 43 km s^{-1} , 93 km s^{-1} , 143 km s^{-1} and 193 km s^{-1} all with a 1σ of 50 km s^{-1} . The input distance distribution of $6 \pm 2 \text{ kpc}$ was used instead of the distance posterior distribution derived using the *Gaia* parallax as the former was more tightly constrained. The lowest median amongst all the PKV probability distributions is at 142 km s^{-1} and the 5th percentiles of all the PKV probability distributions are above 70 km s^{-1} 124

4.7 Realisations of the inferred unimodal (top) and bimodal (bottom) distributions for potential kick velocities (v), inferred from the data (d). The blue lines represent the model corresponding to the median values from the posterior sample for data from all the systems in the sample, while the red dashed lines represent the model based on the median from the posterior sample for data from the 13 systems with systemic radial velocity (γ) constraints. The faint gray lines are a small random subset from the posterior MCMC sample for all the systems, as a demonstration of uncertainty. 129

4.8 PKV probability distributions of the 16 BHXBs in our sample. It can be seen that no single system is responsible for either of the two most prominent peaks in the aggregated natal kick distribution. 131

- 4.9 Comparison of best fit unimodal and bimodal BHXB PKV distributions to the best pulsar kick velocity distribution. The BHXB PKV unimodal distribution is represented by the solid line and has a median of 110 km s^{-1} . The BHXB PKV bimodal distribution is represented by the dotted line. The best fit, two Maxwellian model for the peculiar velocities of pulsars (Verbunt et al., 2017) is denoted by the dashed line. The unimodal BHXB PKV distribution median is close to the low kick pulsar kick velocity component. There is a dearth of extremely high PKV BHs corresponding to the high velocity Maxwellian component for the pulsar velocity distribution. 135
- 4.10 The variation of PKV with the current height of the system above the Galactic plane. There are five systems with a PKV below 100 km s^{-1} are within 500 pc of the Galactic plane. There are two systems that are within 500 pc but have PKVs $>100 \text{ km s}^{-1}$. . . 139
- 4.11 The variation of PKVs with black hole mass. The systems marked with blue squares have had their proper motion measured by VLBI and the systems marked with pink diamonds had their proper motion measured by *Gaia*. The systems marked with yellow circles had their proper motions measured by VLBI, but we used the updated proper motions measured by *Gaia* for our simulations. We have assumed a BH mass of $8 M_{\odot}$ to represent the systems that do not have dynamical mass measurements (Kreidberg et al., 2012). The error bars are one standard deviation of the PKV probability distributions. No correlation between BH mass and potential kick velocity is seen, even after disregarding the systems without dynamical mass measurements. 143

5.1	Proper motion fits of Hi1and Mi. The top and bottom panels represent the motion in the plane of the sky relative to the fitted reference position in RA and Dec, respectively. The offset of the target positions relative to the reference position is denoted by the red markers and is overlaid with the trajectory given by the best fitting proper motion (black solid line). The yellow lines indicate the motion for a 1000 randomly-selected draws from the posterior distribution.	166
5.2	Proper motion fits of Di1and Ci. The top and bottom panels represent the motion in the plane of the sky relative to the fitted reference position in RA and Dec, respectively. The offset of the target position relative to the reference position is denoted by the red markers and is overlaid with the trajectory given by the best fitting proper motion (black solid line). The yellow lines indicate the motion for a 1000 randomly-selected draws from the posterior distribution.	167
5.3	Proper motion fits of Hii1and Ai. The top and bottom panels represent the motion in the plane of the sky relative to the fitted reference position in RA and Dec, respectively. The offset of the target positions relative to the reference position is denoted by the red markers and is overlaid with the trajectory given by the best fitting proper motion (black solid line). The yellow lines indicate the motion for a 1000 randomly-selected draws from the posterior distribution.	168

5.4	Proper motion and parallax fits of Ei1 and Eii. The top and bottom panels represent the motion in the plane of the sky relative to the fitted reference position in RA and Dec, respectively. The offsets of the target position from the reference position is denoted by the red markers and is overlaid with the trajectory given by the best fitting proper motion (black solid line). The yellow lines indicate the motion for a 1000 randomly-selected draws from the posterior distribution.	169
5.5	Proper motion fit of Ii1 and proper motion and parallax fit of Bii. The top and bottom panels represent the motion in the plane of the sky relative to the fitted reference position in RA and Dec, respectively. The offsets of the target position from the reference position is denoted by the red markers and is overlaid with the trajectory given by the best fitting proper motion (black solid line). The yellow lines indicate the motion for a 1000 randomly-selected draws from the posterior distribution.	170
5.6	A corner plot depicting the posterior distributions for the model parameters of Bii. The contour levels and the dashed lines represent the 16 th , 50 th and 84 th percentiles. Slight correlations are seen between π and μ_α , π and μ_δ , π and α_0 and, π and δ_0	171
5.7	Trace solutions of the MCMC code for Ei. The left panel shows the posterior distribution of the samples of the traces. The right panel reports the solution of each iteration and clearly shows that the sampler has converged effectively and has sampled the parameter space efficiently. The parallax posterior distribution shows that the maximum likelihood value could not be obtained but the likelihood increased towards smaller values of parallax, suggesting that values closer to zero are preferred.	172

5.8	Trace solutions of the MCMC code for Ai. The left panel shows the posterior distribution of the samples of the traces. The right panel reports the solution of each iteration and clearly shows that the sampler has converged effectively and has sampled the parameter space efficiently. The posterior distribution of the parallax shows that no value of parallax is preferred and the solution represents the prior itself. All targets with two position epochs had a similar shape of the parallax posterior distribution.	173
5.9	Top panel - A cumulative distribution of the total proper motions of a sample of Gaia sources (blue solid line), the radio sources in this work (red solid line) and the BHBs known in our Galaxy (black solid line). Bottom panel - A forest plot of the total proper motion of the known BHBs (black points), the sources for which proper motions was measured in this work (red points) and the Gaia proper motions depicted with the blue histogram.	183
6.1	Galactocentric orbit of MAXI J1820+070 overlaid on an optical map of the Milky Way Galaxy. (0,0) is the centre of the Galaxy. The starting conditions of the orbit are the current proper motion, distance and systemic radial velocity of the system, which are then integrated back in time for 500 Myr. MAXI J1820+070 is suggested to have been born with an asymmetric natal kick accompanied by a supernova explosion.	196

Chapter 1

Introduction

1.1 A series of unimaginable ideas

The idea of black holes (BHs) was first introduced by John Michell centuries ago (Michell, 1784), wherein the possibility of the existence of a star with gravity so strong that any light emitted from the star will not be able to escape this gravity was proposed. This idea was fairly ahead of its time and though not backed by mathematics then, proved its grit in the coming centuries. The framework that brought to light the possibility of spacetime curvature was published in a series of four papers by Albert Einstein in 1915 (Einstein, 1916). The theory, the General Theory of Relativity, outlines the relation between gravity and matter using Einstein's field equations and predicts that spacetime would not be flat in the presence of a massive object, but will instead be curved. This helped in visualising the Universe as a spacetime continuum and the understanding of gravity as an effect of spacetime curvature. Although the equations laid the foundation for the concept of BHs, they were deemed unsolvable by Einstein.

The step that made the connection from Einstein's equations to BHs was actually taken by Karl Schwarzschild (Schwarzschild, 1916), who solved Einstein's equations while serving on the battlefield of World War I. The solution suggested that objects that were massive enough would have a gravitational field around

them that would curve spacetime to the extent that the escape velocity of that curvature would be greater than the speed of light. He also discovered the existence of a radius around the mass (reduced to a point), or singularity, called the Schwarzschild radius that was the radius of no return. This radius was imagined as a sphere around the singularity, within which no object could exist in its known form and nothing could escape once it went beyond that radius. The reason why an object like this would exist in nature could not be explained by Karl Schwarzschild. This idea of the existence of an infinitely dense singularity in space time seemed so unfathomable and unimaginable that it was widely opposed by many scientists of the time, including Einstein himself.

Since then, theoretical and observational astrophysicists have worked either to prove the existence or the non-existence of BHs. Subramanyan Chandrasekhar in the 1930s presented his work where he combined quantum physics and general relativity to suggest that a massive star, once it has fused all its hydrogen would remain stable only until the mass of the star is $<1.4 M_{\odot}$ (Chandrasekhar, 1931). If the mass of the star is greater than this limit, later dubbed the ‘Chandrasekhar limit’, the electron degeneracy pressure would not be able to support the star against its own gravity, resulting in the collapse of the star on itself (Landau, 1932). This gave birth to the world of neutron stars and BHs as ‘completely collapsed gravitational objects’. Along with Penrose’s theorem of singularity that showed that singularities would always occur for a star that was massive enough, the scientific community was finally open to the idea of BHs and the search for these objects became all the more important to validate this theoretical framework.

1.2 Looking for black holes

Confirming the existence of BHs meant finding these objects in the Universe. As the basic property of these objects is that they do not let any emission escape their event horizon, astronomers were perplexed on how to observe an object

that is invisible. Through a series of chance discoveries and very well executed experiments and observations, we now have a few ways in which BHs are being studied. Other than one method wherein the shadow of a BH has been directly imaged under very specific conditions (see discussion about the Event Horizon Telescope below), we are studying BHs by their effects on their surroundings. Through decades of observations, different kinds of BHs have been discovered that have enabled the classification of BHs into three categories depending on their masses.

1.2.1 Supermassive black holes

Supermassive black holes (SMBHs) are the most massive class of BHs with a mass range of 10^6 - $10^{10} M_{\odot}$. They are present at the centres of most large galaxies, and are associated with influencing the dynamics and evolution of the galaxy that they are hosted in (e.g., Lynden-Bell & Rees, 1971; Fabian, 2012; Kormendy & Ho, 2013). SMBHs can be seen exerting their influence on their environment in the form of an accretion disc, which is a disc of gas and matter spiralling around the BH due to the gravitational pull of the BH (e.g., Shakura & Sunyaev, 1973; Ilić & Popović, 2014; Murchikova et al., 2019). This disc of matter may exist due to the dense environment of SMBHs, due to winds from massive stars in the vicinity of the SMBH or due to tidal disruption events, an event where a star gets caught in the tidal forces of a SMBH and is ripped apart. This stripped matter from the star forms the accretion disc. SMBHs are thought to fuel most Active Galactic Nuclei (AGN), the central extremely bright region of a galaxy.

Accreting SMBHs can be detected throughout the electromagnetic spectrum, with non-thermal processes giving rise to X-rays and thermal emission from the inner disk being responsible for UV emission (e.g., Richards et al., 2006; Elvis et al., 1994). A small fraction (10-20%) of SMBHs may launch bipolar jets (McKinney et al., 2012) that emit in radio wavelengths, and sometimes also in optical wavelengths, and hence they are called radio-loud SMBHs (e.g., Kellermann et al.,

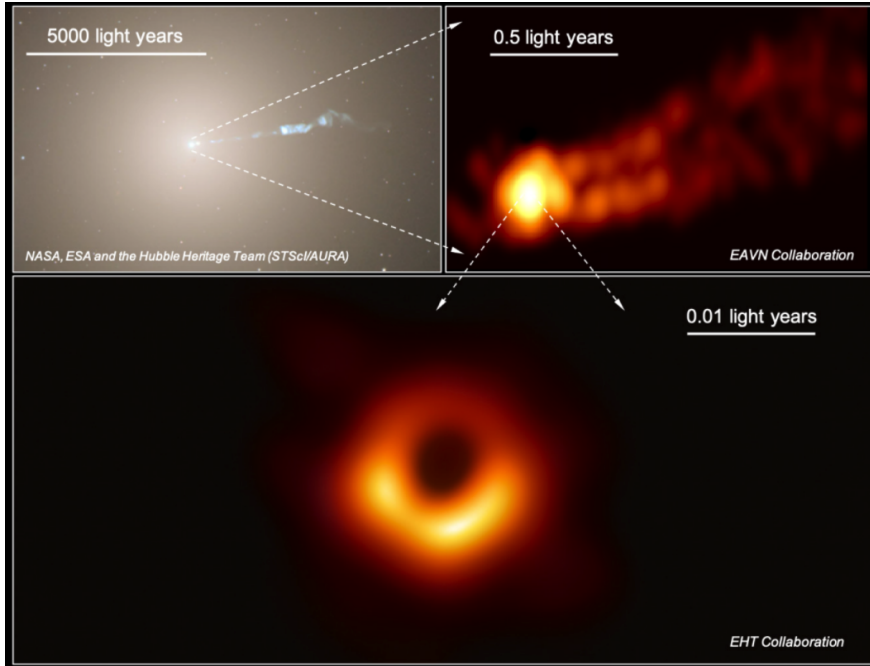


Figure 1.1: Zooming into M87*, the SMBH at the centre of the galaxy Messier 87. Top left: HST image showing clear kpc scale optical jet of M87*. Top right: Radio image using East Asian Very Long Baseline Interferometry Network, a high resolution radio interferometry array, showing parsec scale jet of M87*. Bottom: Gravitationally lensed photon ring around M87* as seen by the EHT. *Image credits: Hada, 2019.*

1989; Urry & Padovani, 1995). As can be seen in Figure 1.1, studying the SMBH at different wavelengths and scales reveals different structures and properties of the SMBH (Hada, 2019).

SMBHs influence the orbits of the stars in their vicinity and estimates about the mass of the SMBH are made by studying the orbits of the stars around the SMBH (e.g., Wolfe & Burbidge, 1970; Ghez et al., 2000, 2003). In the case of the SMBH at the centre of our Galaxy (Sgr A*), the proper motion measurements of the stars in the innermost parsec over a period of two years led to the estimation of the minimum density and hence the minimum mass being held inside that region, providing strong evidence for the existence of a SMBH at the centre of our Galaxy (Ghez et al., 1998). In the following years, tracking the orbits of a few of those stars over a period of ~ 20 years has resulted in a strongly constrained

mass of Sgr A* (Boehle et al., 2016).

The closest we have come to imaging a BH is by imaging the shadow of M87* (Event Horizon Telescope Collaboration et al., 2019a,b), a SMBH that is 53 million light years away from us, and was imaged by the Event Horizon Telescope (EHT, Figure 1.1, Bottom panel). The EHT is a collaboration of radio telescopes around the world providing enough resolution to image the event horizon of SMBHs (Event Horizon Telescope Collaboration et al., 2019c,d). This method of studying SMBHs is very restrictive as it requires certain combination of distance and mass of the SMBH. Nevertheless, it has led to the estimation of the mass and the gravitational radius of M87* with high accuracy (Event Horizon Telescope Collaboration et al., 2019e,f) and has the promise of revealing new details about Sgr A*.

1.2.2 Intermediate mass black holes

Intermediate mass BHs (IMBHs) form a class of BHs hypothesised to lie between masses of $100 - 10^5 M_{\odot}$. A few IMBH candidates are have been reported, although there is still ambiguity on the properties and demographics of these objects. IMBHs are theoretically expected to exist at some point in the Universe and behave as seeds for the more massive BHs that we observe i.e., SMBHs (e.g., Bañados et al., 2018). This has supported the continued search for these objects (see Greene et al., 2019 for a complete review). Attempts have been made to look for IMBHs in the centres of globular clusters, AGN, dwarf galaxies and even our own Galaxy by studying stellar dynamics near the centres of these galaxies. These studies have suggested ~ 10 IMBH candidates (see Figure 2 of Greene et al., 2019 for a summary of current mass constraints of IMBH candidates using stellar dynamics). Estimating masses of BHs from AGN radiative signatures have given large samples of possible IMBH candidates (e.g., Greene & Ho, 2007; Reines et al., 2013).

Studies are also looking into the high velocities of hypervelocity stars, and

one such star has been claimed to have interacted with an IMBH to then attain its escape velocity (e.g., Edelman et al., 2005; Gualandris et al., 2005; Erkal et al., 2019). X-ray flashes from far away galaxies have also been used to search for IMBHs. In 2003, researchers used the ESA’s XMM-Newton space observatory to identify two strong, distinct X-ray sources in the nearby starburst galaxy NGC 1313. By pinpointing NGC 1313’s X-ray sources and studying how they periodically flash, in 2015, researchers suggested that the one of the X-ray systems, NGC1313 X–1, could fall in the mass range of an IMBH (Pasham et al., 2015; Jang et al., 2018). Similar studies of X-ray variations of a source called HLX-1 (Hyper-Luminous X-ray source 1) at the edge of the galaxy ESO 243-49 revealed another possible intermediate mass BH with a mass range of $500\text{--}20000 M_{\odot}$ (Farrell et al., 2009).

1.2.3 Stellar mass black holes

Stellar mass black holes are a class of BHs in the mass regime of $< 100 M_{\odot}$. These BHs are believed to have been born when a massive star runs out of fuel and dies. There are an estimated $>10^9$ stellar-mass BHs in our Galaxy alone (Agol & Kamionkowski, 2002). The first observational evidence of the existence of BHs was provided by Bolton when he discovered the BH in Cyg X-1 (Bolton, 1972). Cyg X-1 was first detected as an X-ray source and was also found to have emission in radio wavelengths (Hjellming & Wade, 1971). The optical counterpart of Cyg X-1, HDE226868, was observed and its high orbital velocity suggested that an object more compact and dense than a neutron star (NS) was the source of the gravitational potential in which HDE226868 was moving (Bolton, 1975). This was the first time any collapsed object heavier than a NS ($>2\text{--}3 M_{\odot}$) had been observed, and this opened up a whole new field of black hole X-ray binary (BHXB) studies. Since then, BHXBs have been usually discovered as X-rays or optical transients in the sky. There are now ~ 60 BHXBs candidates out of which ~ 20 have a dynamical mass measurement (Tetarenko et al., 2016b, and

references therein).

Another way in which BHs have been observed is through microlensing events. These events occur when an object with strong gravity (BH in this case) passes in front of a background star. This gravitationally strong object bends the light of the background star around it, making it look brighter and multiple snapshots of this event can help estimate the size of the object that is bending the light. The first event of this kind was observed in 1996 and 1998 by the Massive Compact Halo Object (MACHO) collaboration that used the optical telescope at Mt. Stromlo. This event was followed up with the Hubble telescope and it was found that the mass of the lensing object was heavy enough to be classified as a BH (Bennett et al., 2002). The fact that isolated BHs do not have any strong emissions that are detectable, and one has to wait for these chance one-off lensing events to study these systems is very challenging and makes the study of isolated BHs very difficult. Thus instead of directly studying isolated BHs, we can study the effect these stellar mass systems have on their surroundings by using BH systems in a binary to understand and constrain BH physics. BHs in binary systems are the subject of this thesis and will be explained in detail in §1.3.

In the past decade, the Laser Interferometer Gravitational wave Observatory (LIGO) has been established that detects gravitational waves and is based on the principle of the Michelson Interferometer. A gravitational wave is detected as a change in the interference pattern caused due to change in the path length the laser has to travel in different directions at LIGO. These waves are like ripples through space and can be caused due time-varying quadruple moment, which can occur due to massive accelerating objects that also undergo changes in their mass e.g., energetic events like mergers of compact objects. LIGO detected its first merging BHs in September 2015 (Abbott et al., 2016b,a), followed by 18 BH binary mergers and one NS-NS merger in the first two observing runs (2015–2017 Venumadhav et al., 2019). The preliminary report for the third observing run

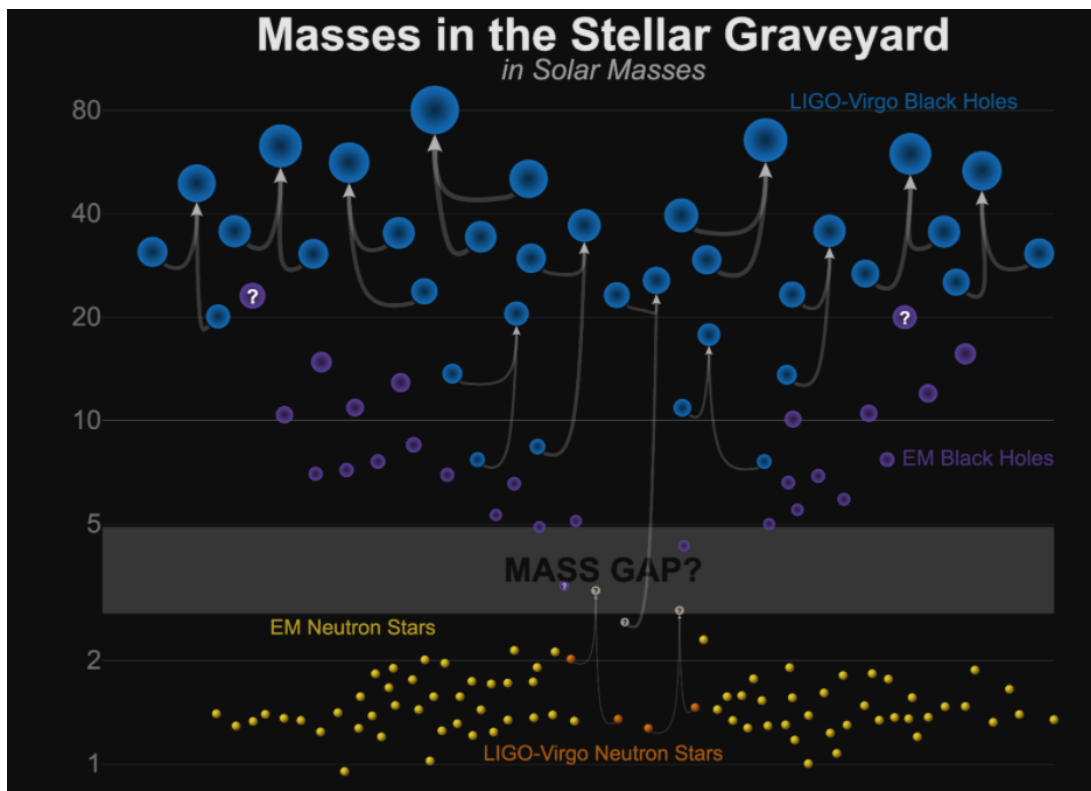


Figure 1.2: Detections of gravitational wave events by LIGO compared with BHs and NSs that have been electromagnetically detected as of 16-05-2020. There appear to be a few NS merger candidates that lie in the mass gap a gap between $2\text{--}5 M_{\odot}$. *Credit: LIGO -Virgo/Frank Elavsky, Aaron Geller²*

has suggested the detections of a few BHNS mergers¹, that were not observed in the first two runs. This way of studying BHs has given us a window into a mass regime of stellar BHs that have never been detected by electromagnetic searches in our Galaxy, as can be seen in Figure 1.2. GWs provide another tool to study stellar-mass BHs, but we might not detect a Galactic BH merger (Olejak et al., 2019) as the current synthetic BH population estimations of our Galaxy suggest that the merger rate is low enough ($3\text{--}81 \text{ Myr}^{-1}$). Thus, we rely on another class of BH binary systems to study Galactic BHs as discussed in the next section.

¹<https://gracedb.ligo.org/superevents/public/03/>

²<https://media.ligo.northwestern.edu/gallery/masses-in-the-stellar-graveyard>

1.3 Black hole X-ray binaries

Black hole X-ray binaries (BHXBs) are binary systems of a BH and a star where the BH is accreting mass from the star. A stellar binary system where the mass difference between the two stars is large i.e one star is more massive than the other and one star is massive enough to form a BH, the binary system can evolve to form a BHXB. Two common classes of such objects are low mass X-ray binaries (LMXBs) where a BH is in binary system with a sub-solar mass star ($<1M_{\odot}$) that is slightly evolved and off the main sequence, and high mass X-ray binaries (HMXBs) where the BH is in a binary system with a more massive star ($>10M_{\odot}$). Matter from the star falls towards the compact object and forms a disc, called the accretion disc, to conserve angular momentum as it falls in. In the case of LMXBs this disc is formed once the stellar companion expands and fills the Roche Lobe to the limit of the equipotential point called the first Lagrangian point (L1; see Figure 1.3). HMXBs usually transfer matter by a process called wind-accretion, where the massive star expels away matter by stellar winds and this matter is captured by the gravity of the compact object and might form an accretion disc (see Figure 1.3). The dissipation of energy from the infalling matter from an accretion disc can sometimes take the form of bipolar jets that get launched from these systems.

BHXBs can be detected at various wavelengths during different phases of their outburst cycle, which is a phase of heightened activity from these sources. The period of an outburst could last from weeks, to months and in some cases years (e.g., the BHXB Swift J1753.5-0127, see details in Chapter 4). Below, we discuss the emission from BHXBs where most BHXBs are first discovered i.e., X-rays, and the emission that is used in this thesis to study BHXBs i.e., radio.

1.3.1 X-ray emission - accretion disc

The signature emission of BHXBs (X-rays) are usually emitted from the inner regions of the accretion disc, where the temperature of the infalling material gets

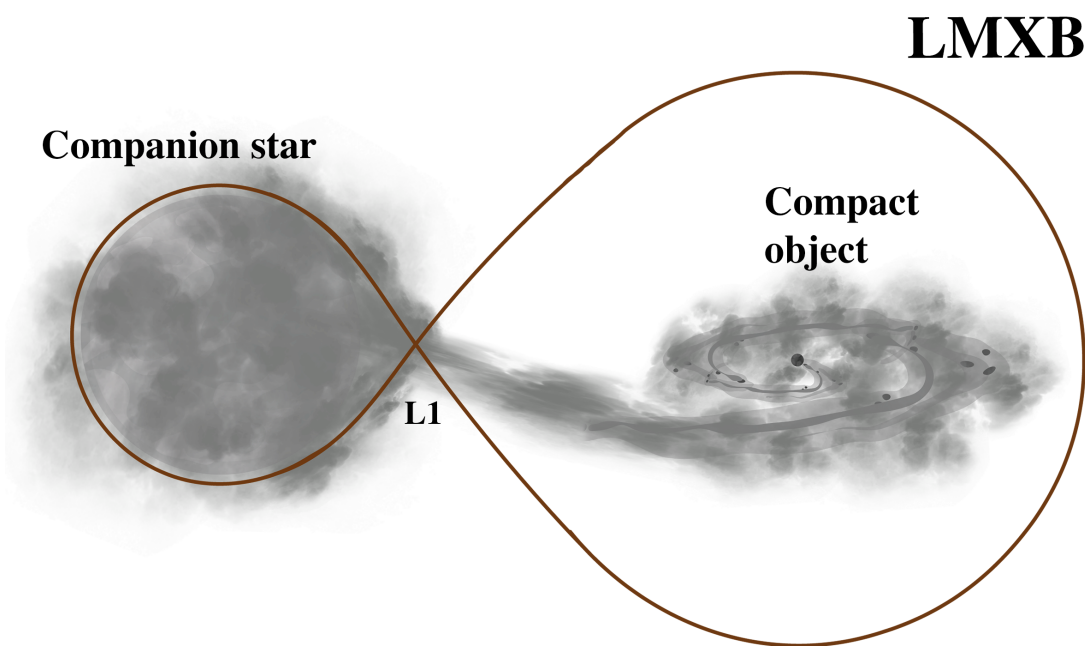
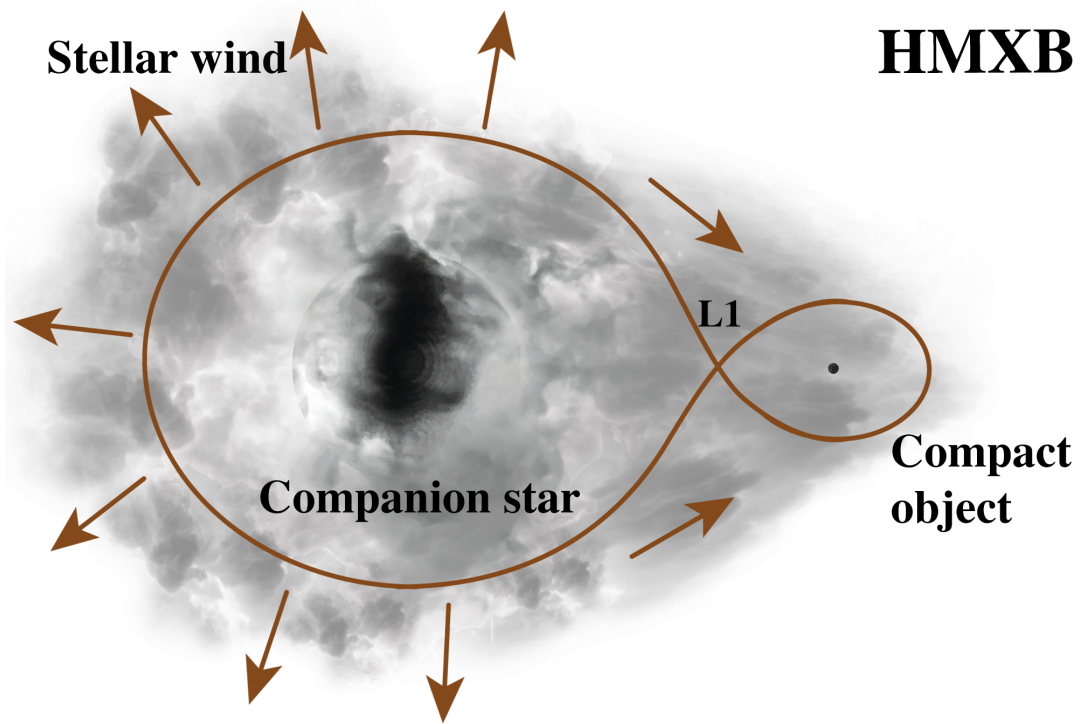


Figure 1.3: An artist's impression of the formation of accretion disc in binaries. Top panel: Formation of accretion disc in HMXBs due to strong stellar winds. Bottom panel: Accretion disc in LMXBs by stellar expansion and Roche Lobe overflow. *Image credits: Aditya Parthasarathy.*

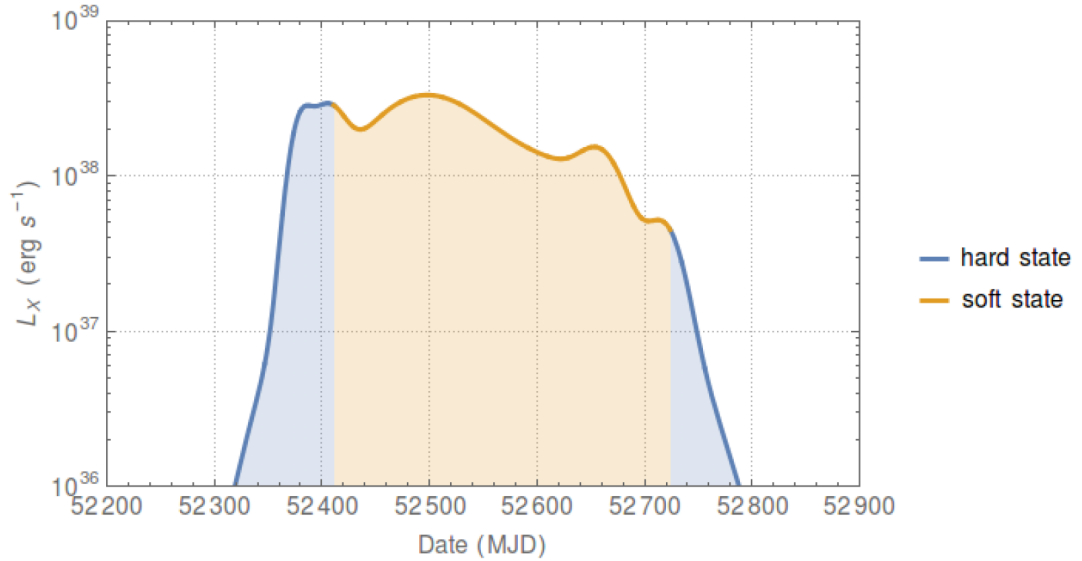


Figure 1.4: The lightcurve of GX339-4 with a smoothed fit. This represents the X-ray lightcurve in the 2002-2003 outburst and the flux corresponds to the X-ray band of 0.1–200 keV. The hard X-ray spectral states are related to the increase in flux in the beginning and end of the outburst (see Section 1.3.3 for more details). *Image credits: Fender & Muñoz-Darias, 2016*

high enough due to increased friction closer to the compact object. This emission is theoretically limited by the mass accretion rate onto the compact object (for a given compact object mass), and is called the Eddington limit. This limit is the maximum luminosity that can be reached due to the accretion rate where the gravity and the radiation pressure can balance each other. If the luminosity exceeds this limit, then the matter will be pushed away from the accreting object rather than falling inwards. The Eddington luminosity for a spherically symmetric (for hydrogen) radiating object is given by $1.38 \times 10^{38} (M/M_{\odot}) L_{\odot} \text{ erg s}^{-1}$, where M is the mass of the accreting object, and M_{\odot} and L_{\odot} are the solar mass and luminosity.

BHXBs spend most of their time in a quiescent phase where this X-ray emission is $< 10^{34} \text{ erg s}^{-1}$ (Plotkin et al., 2013). Sometimes due to instabilities in the accretion disc, there is a sudden increase in the accretion rate and the accretion in some cases can even reach close to (or beyond) the Eddington (Lasota et al., 1996). These events of sudden increase in accretion rate are called outbursts,

and BHXBs appear as transients in the X-ray sky that usually last for weeks or months. These outbursts are associated with an order of magnitude increase in the X-ray flux from these objects (see Figure 1.4 for an example), and also at radio and optical wavelengths in some cases.

Some BHXBs may also be persistent sources of X-rays if the viscosity and temperature of the accretion disc is maintained and requires the mass transfer rate from the companion to remain above a certain limit (Coriat et al., 2012; van Paradijs, 1996). Very few persistent BHXBs have been observed to date (ten; Tetarenko et al., 2016b). The persistent nature of these sources could also mean that these sources have a long quiescent phase before they go into outburst, and we just haven't observed the X-ray sky for long enough to catch the outburst of these long-quiescent-phase BHXBs. It has also been shown that all BHXBs with a period of < 2 days should behave as transients (King et al., 1996). The first BHXB that was observed, Cyg X-1, is a persistent source (Bolton, 1972, 1975) and the first transient BHXB, A0620-00 (Elvis et al., 1975), was observed just a couple of years after Cyg X-1.

1.3.2 Radio emission - jets

Relativistic outflows or jets are usually associated with an accreting object, and hence also with BHXBs. Any accreting body that is radiating in X-rays from its accretion disc can also have outflow of energy in the jets with a radiative signature in radio wavelengths, and usually along the BH spin axis (Blandford & Rees, 1978). Two kinds of radio jets have been observed in BHXBs, steady and transient radio jets with the transient jet existing for a short time and ultimately giving way to steady jets (see Massi, 2011 for a review).

Transient jets are characterised by a spectral index of < 0 . These have been resolved in a few BHXBs as plasmoids moving away from a central core with relativistic speeds. In 1994, a radio image of the BHXB GRS 1915+105 revealed such a relativistic radio jet (Mirabel & Rodríguez, 1994; Fender et al., 1999) as

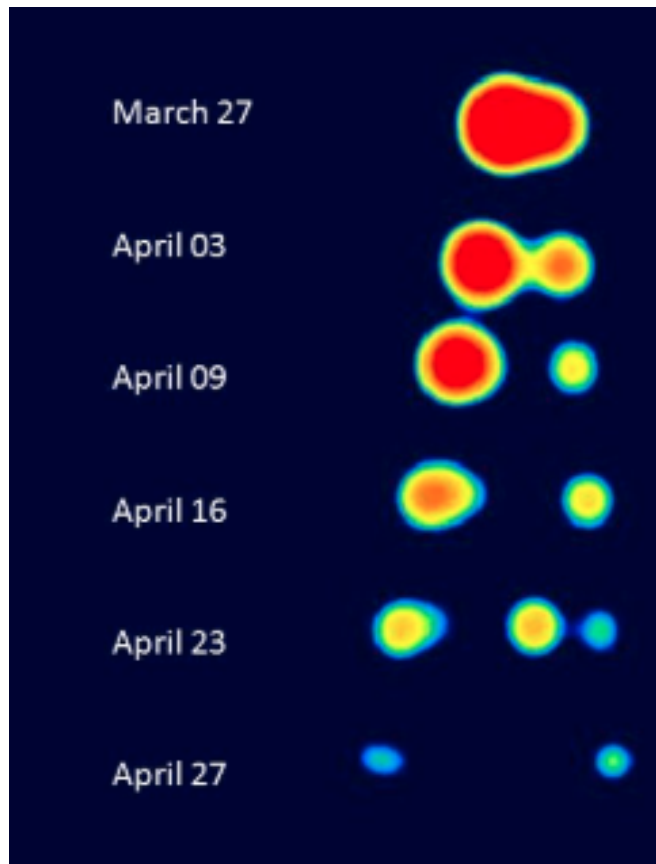


Figure 1.5: Image of radio jets in GRS 1915+105. This image is a colour version³ of the image from Mirabel & Rodríguez (1994). It represents bright radio lobes moving away from a stationary core. Six observations were taken a week apart from each other using the Very Large Array. *Image credits: Mirabel & Rodríguez, 1994.*

can be seen in Figure 1.5. A similar structure was later observed in a second BHXB, GRO J1655-40 (Hjellming & Rupen, 1995). These jets are assumed to be perpendicular to the plane of the binary system, though in some cases these radio jets have been seen to precess, with their inclination angle towards the line-of-sight changing over time. This has been notably reported in SS 433 (Hjellming & Johnston, 1981), GRO J1655-40 (Hjellming & Rupen, 1995) and V404 Cyg (Miller-Jones et al., 2019), and has been attributed to a slight misalignment between the plane of the binary and the BH spin.

Steady jets are another kind of radio jets often observed from accreting ob-

³<https://www.nrao.edu/pr/2000/vla20/background/superlum/>

jects. Steady jets act as compact radio sources, which when spatially resolved appear as continuous jets (e.g., Stirling et al., 2001). Steady jet sources have a flat or inverted radio spectrum. Compact radio sources are assumed to consist of a system of core and relativistic electrons and plasma moving with constant velocity and are assumed to be constrained in a conical geometry (Blandford & Rees, 1978; Blandford & Königl, 1979). The size of this core depends on the inverse of the observing frequency. This model has been used to explain the compact radio emission from sources and has stood the test of time and observations with Active Galactic Nuclei (e.g., Reynolds, 1982; O’Sullivan & Gabuzda, 2009) and BHXBs alike (Fender et al., 2004; Stirling et al., 2001).

1.3.3 Geometry and emission during outburst

The outbursts in BHXBs indicate changes in the accretion disc and the current theories suggest the outburst cycle of a BHXB is related to the geometry of its inner accretion disc. This has been diagrammatically represented in Figure 1.6 using the BHXB GX339-4 as an example. A BHXB spends most of its time in quiescence and is possibly devoid of X-ray emission from the accretion disc (Bildsten & Rutledge, 2000; Lasota, 2000; Bernardini et al., 2015). In the beginning of an outburst, as the X-rays from the system rise the BHXB is said to be in a low hard state. In this state the X-ray emission from the system is mostly in high energy photons and is coming from either the hot corona of electrons that fill the inner region of the accretion disc or from a possible advection dominated accretion flow (A to B in Figure 1.6, Top panel). As the inner edge of the accretion disc moves in closer to the innermost stable circular orbit (ISCO), the X-ray spectrum starts changing to be dominated by thermal blackbody emission from the disc and is called the soft state (B to D in Figure 1.6, Top panel). The source reaches its peak X-ray luminosity either at the peak of the hard state (B in Figure 1.6, Top panel) or once the source has completely entered the soft state (D in Figure 1.6, Top panel), depending on the shape of the hardness intensity

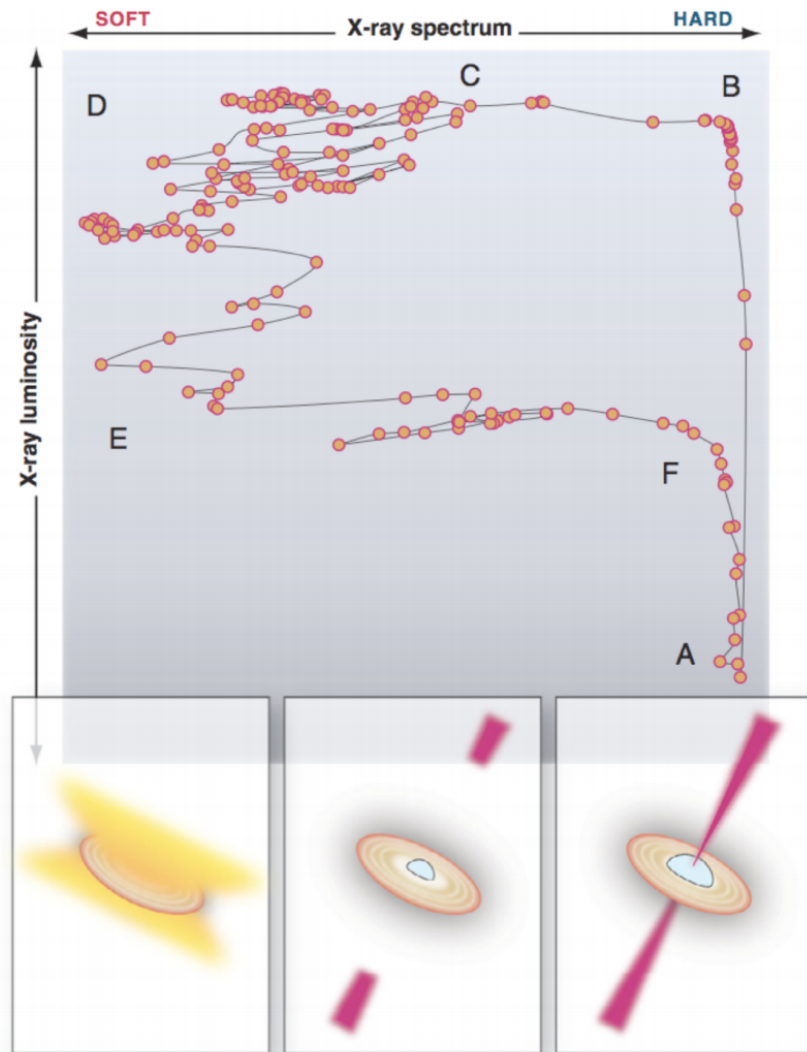


Figure 1.6: Variation in X-ray hardness ratio with X-ray luminosity during an outburst of GX 339-4. The images in the lower panel are artist's impressions of the change in geometry of the accretion disc and the presence of a radio jet with a change in the X-ray spectrum. *Image credits: Fender & Muñoz-Darias, 2016.*

diagram (e.g., Muñoz-Darias et al., 2013). After reaching peak X-ray luminosity, the X-rays from the system start to decay with the inner edge of the accretion disc moving away from the ISCO (E to F in Figure 1.6, Top panel). The source then either goes into quiescence again (F to A in Figure 1.6, Top panel), or goes into a reflare. This reflare may or may not completely reach the soft state (e.g., Stiele & Kong, 2016).

Through decades of following outburst cycles of BHXB, it has been observed that the X-ray spectral state changes are related to the changes in the radio emission coming from these systems. It has been shown that a BHXB has a steady compact jet associated with it even in the low accreting quiescent phase (Gallo et al., 2003). In the low hard state, a compact steady radio jet that is causally connected to the BHXB is seen (Figure 1.6, Bottom right panel). During the transition from hard to the soft state (B to D in Figure 1.6, Top panel), multiple radio ejection events from close to the compact object are often observed (Figure 1.6, Bottom middle panel). These ejection events are the transient jets discussed in §1.3.2 and are highly relativistic. By the time the BHXB fully enters the soft state, the radio jet is quenched and turned off (Figure 1.6, Bottom left panel). The steady radio jets switch back on in the hard decay state along E to F in Figure 1.6 and can exist at a fainter state when the source might go into quiescence again.

1.4 Stellar mass black hole birth and natal kicks

BHXBs can be used as probes to understand the birth mechanism of BHs in binary systems. In the following section, I will highlight the current BH birth theories and the strides that are being made in order to draw a coherent picture of BH birth mechanisms.

1.4.1 Different birth pathways

Theoretical models suggest the formation of a stellar mass black hole (BH) could take place either by :

- (a) Direct collapse (DC) - whereby the massive progenitor star collapses directly into a BH with almost no mass ejection. (e.g., Reynolds et al., 2015; Adams et al., 2017a; Kalogera, 1998).
- (b) delayed formation in a supernova (SN), wherein matter ejected during the SN falls back onto the proto-neutron star, creating a BH (e.g., Gourgoulhon, 1991; Woosley & Weaver, 1995; Brandt et al., 1995).

When an iron core is too massive for the degeneracy pressure to stabilise the gravity of the star, the core starts collapsing. This iron core collapse leads to the formation of a proto-neutron star and the system is in equilibrium, until the collapsed proto-neutron star core rebounds and sends a shock wave through the stellar layers surrounding the core. If this shock wave is energetic enough, it results in the outer layers of the stars being blown away in a supernova explosion leaving behind a BH after further fallback of matter (Colgate, 1971). On the other hand, if the shock wave is less energetic and the star is difficult to explode then the outer layers fall back onto the core and collapse into a BH in a failed SN.

The hunt for stars collapsing and becoming BHs has been ongoing (Kochanek et al., 2008; Adams et al., 2017a), but the probability of observing such a rare event is quite low. A direct link between BHs and a SN has not been observed, but there is one strong candidate of a BH formed from a SN explosion (Iwamoto et al., 1998). This conclusion is based on supernova modelling and energetics, wherein the amount of various metals ejected during the explosion that were estimated by spectral studies could only be explained if the progenitor was massive enough to give rise to a BH. Based on modelling, the mass of the remnant was found to be $2.9 M_{\odot}$, which is greater than the most massive NS ($2.14 \pm 0.1 M_{\odot}$) observed

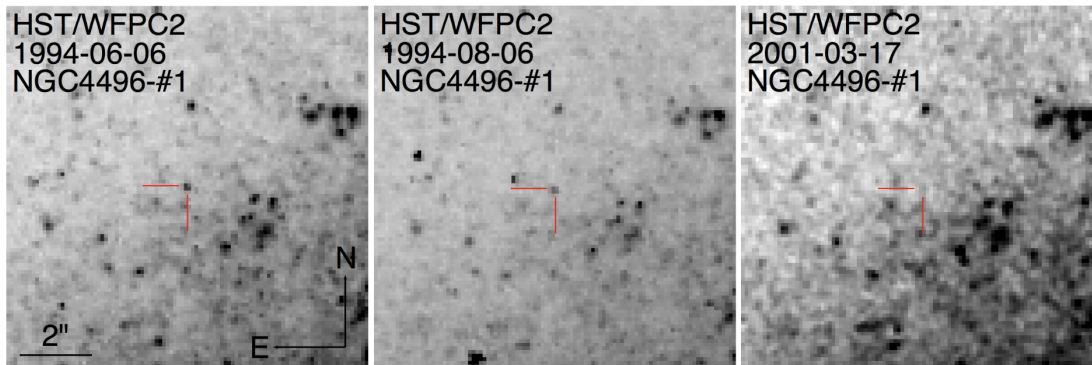


Figure 1.7: The first strong candidate of a direct collapse. Three epochs of images from the HST centred at the direct collapse candidate. The candidate is visible in 1994 (left panel) and vanishes in the image in 2001 (right panel). *Image credits: Reynolds et al., 2015.*

till date (Cromartie et al., 2020). There are two strong candidates for BHs being formed with a failed SN and the massive star disappearing without a trace. These candidates have been identified by looking for massive stars in nearby galaxies that disappear without an optical SN counterpart. One failed SN (direct collapse) candidate (see Figure 1.7) was found in the analysis of HST images of targets where at least 3 epochs were compared in a survey that spanned 20 years (1994–2003; Reynolds et al., 2015).

A similar search by the Large Binocular Telescope (LBT; Hill & Salinari, 2000) found a direct collapse candidate that had a stable luminosity for two years of observations after which it went into an outburst in 2009 and then faded (Gerke et al., 2015). This source was followed up using the HST and the disappearance and a delayed faint emission in near infrared suggested the possible direct collapse of a massive red supergiant star into a BH and the fallback of material onto the BH that is emitting in the near-IR (Adams et al., 2017b). Clearly, searching for massive dying stars that become BHs either by direct collapse or with a SN explosion requires comparing years of high-resolution data from multiple telescopes and even then the success rate of finding such candidates is very low. Beyond the theoretical framework, this direct approach of imaging dying stars and looking for their optical SN counterpart is not currently able to give us a big

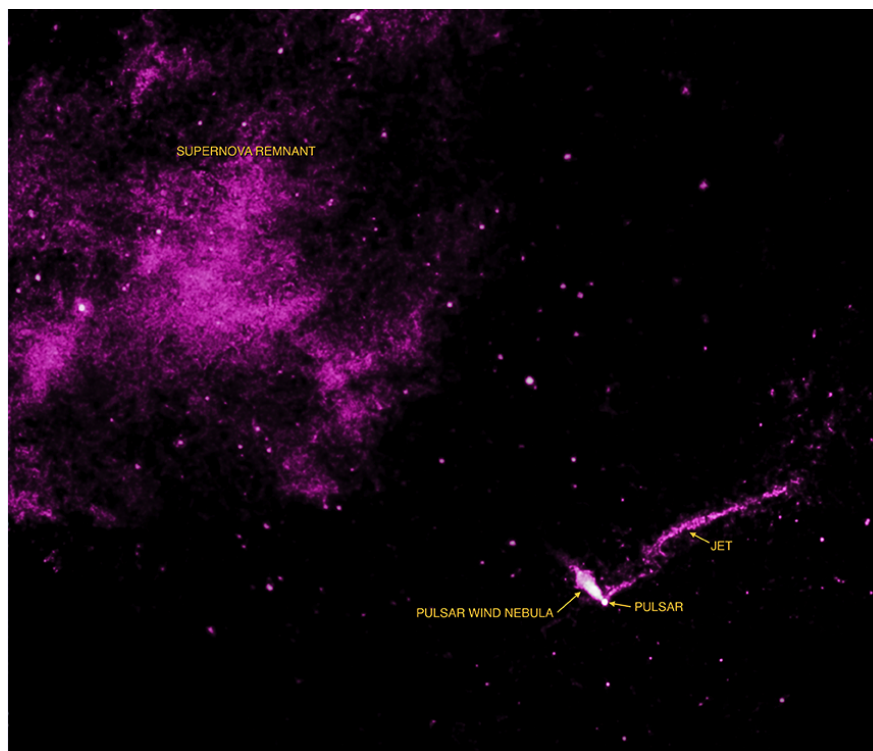


Figure 1.8: Chandra image of a pulsar, IGR J11014-6103, kicked away from its supernova remnant. The pulsar is estimated to have a transverse velocity of $2400\text{-}2900\text{ km s}^{-1}$ (Tomsick et al., 2012) and is attributed to an asymmetric natal kick at birth of the pulsar. *Image credits - NASA, Chandra X-ray Observatory, INTEGRAL Science Data Centre*⁴.

sample set to obtain a deep understanding of the birth mechanism of the stellar mass BH population. This thesis is an attempt to use another line of attack to find possible BH candidates that were born with either the DC or SN pathways by using BHXBs as probes.

1.4.2 Natal kicks

The sudden mass loss from a massive star in a binary could result in either the binary obtaining large velocities or unbinding the binary and its components obtaining large velocities (e.g., Tomsick et al., 2012). This large velocity that a binary acquires is called the natal kick (see Figure 1.8). The idea of objects

⁴<https://apod.nasa.gov/apod/ap140221.html>

obtaining velocities that were high as compared to their environment was born out of the observation of run-away stars or high velocity stars moving around in the Galaxy (e.g., Blaauw, 1956a,b). Specifically, instantaneous mass loss due to supernova explosions was suggested as the cause of the high velocities of stars that could have been part of a binary system (Zwicky, 1957). If the instantaneous mass loss from the more massive star in a binary is greater than half the initial mass of the binary system, the binary will get unbound and will release the secondary on a hyperbolic orbit relative to the primary (Blaauw, 1961). Thus, if the instantaneous mass loss from the primary is less than half the total mass of the initial binary system the binary will remain bound. If a compact object (BH or NS) in a binary system is formed due to a SN explosion, the sudden mass loss in the form of SN ejecta from the binary system will change the centre of mass of the remnant binary system. The ejected mass continues to move in the initial direction of motion of the progenitor with the same velocity and to conserve momentum the centre of mass of the binary system changed that, giving the remnant binary system a recoil kick. This kick is referred to as the Blaauw kick (Blaauw, 1961).

This kick is expected to speed the binary system to velocities higher than its local environment. In addition to this recoil kick (Blaauw kick) due to the sudden mass loss from the binary, the binary could pick up more momentum depending on the morphology of the ejected mass in the SN. Asymmetries in neutrino emission could also give additional velocity to the compact object formed, as discussed in §1.4.2.2. Hence compact objects that are formed accompanied by a SN explosion without getting unbound can be found as high velocity X-ray binaries in our Galaxy. On the contrary, a compact object that formed with a failed SN and without any major ejection of matter will not receive such a kick and will have velocities comparable to the local environment of the system. This thesis aims to test this hypothesis by conducting a systematic study of the velocities of multiple BHXBs in our Galaxy and determine whether kicks are imparted to BHs on

formation and if so, their magnitude. This will lead to the identification of the birth mechanism of the BH in the BHXBs that are studied and help in obtaining a model to suggest the requirements of a massive star to use either the SN birth pathway or have a failed SN.

1.4.2.1 Symmetric mass loss

As discussed above, sudden mass loss in binaries can result in speeding up the binaries to high velocities or unbinding the binary. If a BH is then formed with a SN explosion, the remnant binary system will suffer a recoil kick even if the SN is symmetric in the frame of reference of the progenitor. This symmetric SN will not change the spin axis of the remnant BH and the orbital axis of the binary. Consider a binary with a massive helium star (M_{He}) and a less massive secondary star (m). The primary helium star undergoes an instantaneous SN and loses ΔM in the process, which gets unbound from the remnant binary system. The remnant binary system ($M_{\text{BH}}+m$) itself remains bound as long as $\Delta M < (M_{\text{He}} + m)$. This process changes the centre of mass, the orbital period, the eccentricity and the semi-major axis of the binary system. As shown by Boersma (1961), the semi-major axis (a_i) of a binary after a SN changes to a_f where a_f is related to a_i by

$$a_f = \frac{\mu_f}{2\mu_f - 1} a_i \quad (1.1)$$

where μ_f is the ratio of the total mass of the system after the SN explosion ($M_{\text{BH}}+m$) to the mass of the system before the SN ($M_{\text{He}} + m$). In order to find out how the orbital period of the binary will be affected due to the SN explosion, we can combine the above equation with Kepler's third law (Kepler et al., 1619) given by $a_f = P_f^{2/3} \mu_f^{1/3}$. Here P_f is the orbital period of the binary after the SN. Thus, substituting equation (1.1) in Kepler's third law we obtain

$$P_f = P_i \frac{\mu_f}{(2\mu_f - 1)^{3/2}} \quad (1.2)$$

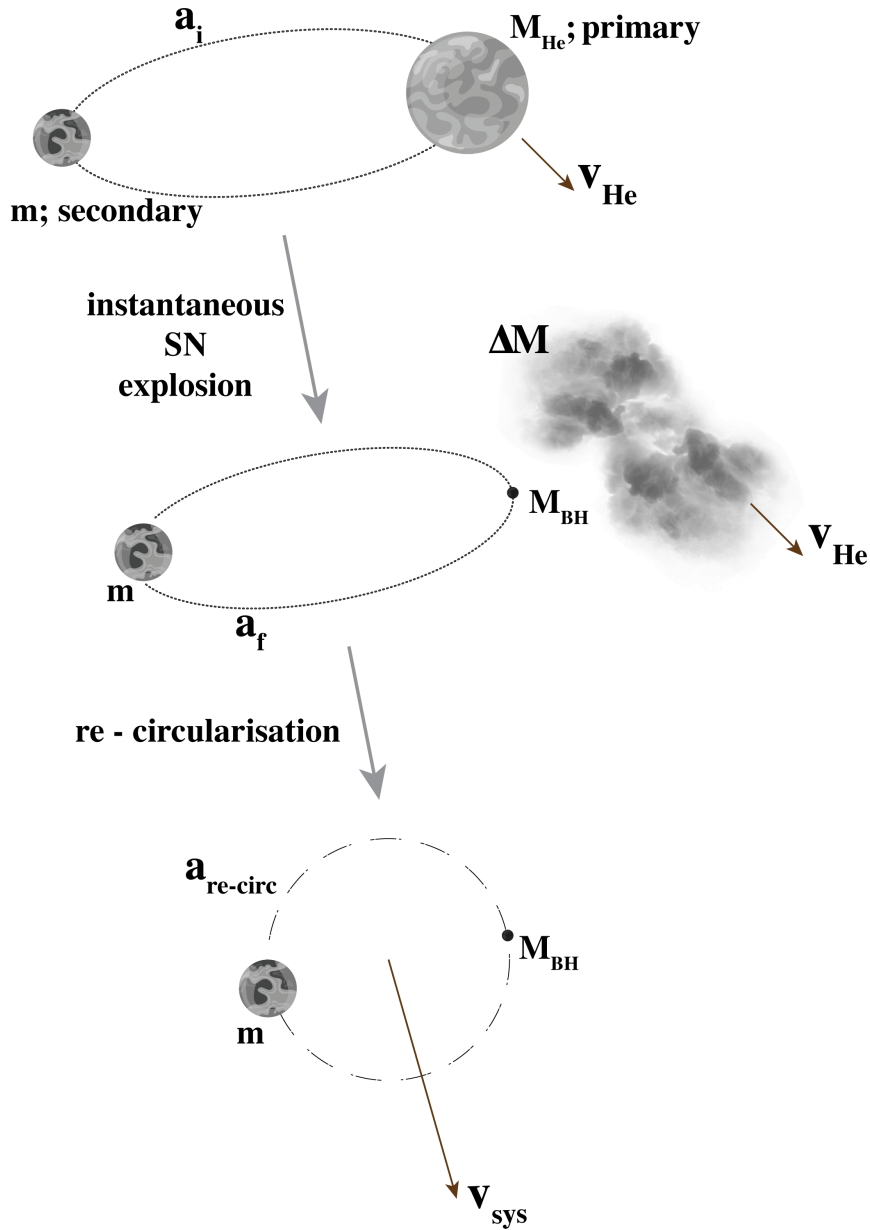


Figure 1.9: Representation of the process of a massive helium star undergoing an instantaneous SN explosion in a binary and the kick the system obtains due to symmetric mass loss. The first image is a representation of a helium star with mass M_{He} in a binary with a star of mass m and the binary has a semi-major axis of a_i . v_{He} represents the velocity of the primary and the SN remnant, and the arrow denotes the direction. a_f is the semi-major axis of the orbit after the primary undergoes an instantaneous SN explosion and v_{sys} is the kick velocity the system obtains from the SN explosion once the tidal forces have re-circularised the orbit, with the final semi-major axis of the orbit of the binary of $a_{\text{re-circ}}$.

Flannery & van den Heuvel (1975) report a relation to find the eccentricity of an orbit if the post (a_f) and pre-SN (a_i) semi-major axis are given.

$$(1 - e)a_f = a_i \quad (1.3)$$

Substituting equation (1.1) in equation (1.3) gives the eccentricity, e , of the post-SN orbit in terms of μ_f .

$$e = \frac{1 - \mu_f}{\mu_f} e = \frac{\Delta M}{M_{BH} + m} \quad (1.4)$$

After the SN, the orbit tends to re-circularise due to tidal forces keeping the orbital angular momentum conserved (Hurley et al., 2002; Witte & Savonije, 2002). In this case, the semilatus rectum stays conserved i.e $l_f = a(1 - e^2)$ (Halbwachs et al., 2005). This becomes the radius of the final re-circularised orbit

$$a_{re-circ} = a_f(1 - e^2) \quad (1.5)$$

Substituting equation (1.3) and equation (1.4) in equation (1.5) we get a relation between the re-circularised orbital radius and the reduced mass μ

$$a_{re-circ} = \frac{a_i}{\mu} \quad (1.6)$$

Using Kepler's third law in equation (1.5) gives the re-circularised orbital period as

$$P_{re-circ} = P_f(1 - e^2)^{3/2} \quad (1.7)$$

Combine equation (1.7) with equation (1.2) and (1.4)

$$P_{re-circ} = \frac{P_i}{\mu^2} \quad (1.8)$$

The ejected mass continues to move with the original velocity of the progenitor (v_{He}) and using conservation of momentum we can derive the velocity imparted

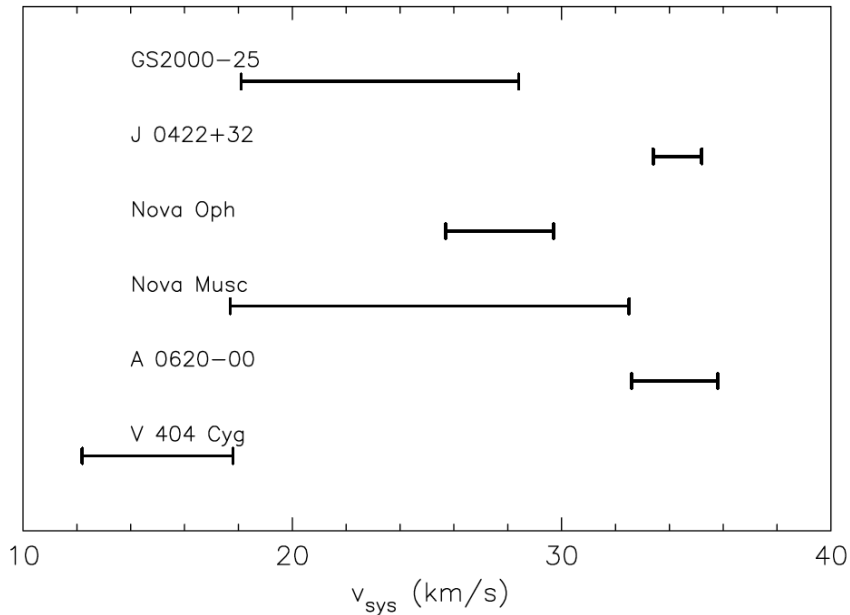


Figure 1.10: Kick limits of six XRBs. Three dimensional recoil velocity estimates suggesting that velocities $<40 \text{ km s}^{-1}$ can be explained by symmetric mass loss. *Image credits: Nelemans et al., 1999.*

to the remnant system (v_{sys})

$$v_{sys} = \frac{\Delta M v_{He}}{M_{BH} + m} \quad (1.9)$$

The above equation, along with equation (1.6), (1.8) and Kepler's third law gives us

$$v_{sys} = (G2\pi)^{1/3} \Delta M P_{re-circ}^{-1/3} (M_{BH} + m)^{-5/3} \quad (1.10)$$

For an equation with standard astronomy units

$$v_{sys} = 213 \frac{\Delta M}{M_{\odot}} \frac{P_{re-circ}}{\text{day}}^{-1/3} \frac{(M_{BH} + m)^{-5/3}}{M_{\odot}} \text{ km s}^{-1} \quad (1.11)$$

Hence, the magnitude of the recoil kick due to symmetric mass loss in a SN can be estimated if the orbital period just after the re-circularisation, the masses of the components of the binary and the mass ejected away in the SN are known. These parameters are difficult to estimate as the systems as observed in the

current epoch might have undergone mass transfer that will change the orbital parameters and the component masses in the system. Limits on the velocity of the system (the symmetric kick velocity) can still be placed by modelling the change in the orbital parameters due to mass transfer in a BHXB (e.g., Nelemans et al., 1999; Miller-Jones et al., 2009b). Nelemans et al. (1999) assumed a mass loss fraction ($\Delta M/M_{\text{He}}$) of 0.35 and found that kick velocities of up to $< 40 \text{ km s}^{-1}$ can be explained by symmetric mass loss from a SN during the formation of a compact object for the six systems they studied (see Figure 1.10). Thus the kick velocity that a binary system can obtain due to a symmetric SN is a few tens of km s^{-1} , depending on the binary mass, progenitor velocity, orbital period, and ejected mass of the system.

1.4.2.2 Asymmetric kicks

BHXBs or neutron stars that have velocities higher than the Blaauw kick that the system could have acquired due to symmetric mass loss, need some other mechanism to explain the high velocities. The space velocity distribution of pulsars was shown to have a mean of 450 km s^{-1} with a high-velocity tail (Lyne & Lorimer, 1994), with the highest velocities reaching up to $>1000 \text{ km s}^{-1}$ (Hobbs et al., 2005). Verbut et al. (2017, V17 hereafter) updated the work by Hobbs et al. (2005) by using a bigger sample, accurately measured pulsar proper motions and parallaxes, and applying a Bayesian method to estimate distances from parallaxes. They found that the velocity distribution was wider than can be fit by a single Maxwellian, and has two prominent peaks, at 120 km s^{-1} and 540 km s^{-1} (see Figure 1.11). With the advancement in observations, modelling and simulating the process of SN explosions, we are starting to see how the initial asymmetries in the supernova explosion could affect the nature of the system left behind. The high velocity kicks have been attributed to possible asymmetry during the SN explosion (see Figure 1.12) owing to three possible mechanisms:

- Asymmetric mass ejection - The hydrodynamical instabilities in the pro-

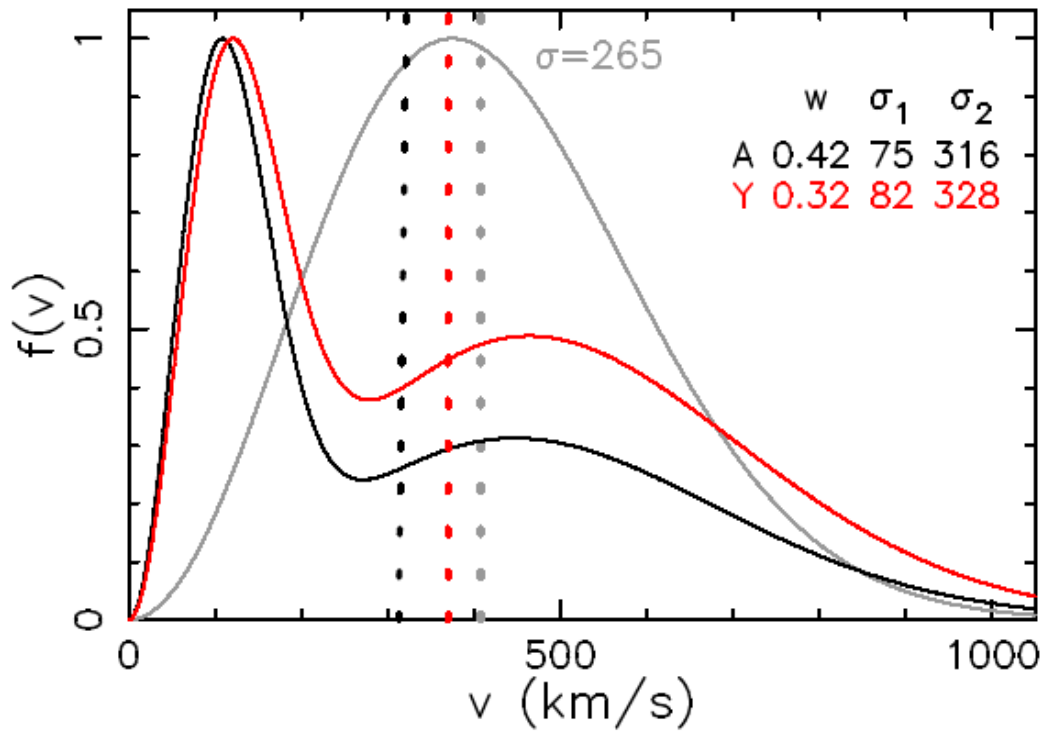


Figure 1.11: Model fit to the velocity distribution of 28 pulsars. A double Maxwellian model is preferred with a low and a high velocity peak. The grey is the single Maxwellian fit to all pulsars, the black and red solid lines are models for two Maxwellians for all and only young pulsars, respectively. The vertical dotted lines denote the median of the distributions. w is the fraction of pulsars in the lower velocity distribution and σ denotes the medians for the two Maxwellians. *Image credits: Verbunt et al., 2017.*

genitor for the SN leads to the preferential ejection of mass in a SN in a particular direction and can give rise to an additional kick imparted in the opposite direction to conserve linear momentum. This asymmetrically ejected matter can speed the compact object to $\sim 200 \text{ km s}^{-1}$ and all velocities above this need another mechanism. This large fraction of asymmetry requires a unipolar asymmetry in the hydrodynamics of the SN progenitor, but simulations show that such a model is unstable and a star will usually have multipolar asymmetry. A study comparing the morphology of 18 supernova remnants and the direction of motion of their associated neutron stars (see Figure 1.12) claimed that ejecta asymmetries were the dominant cause for asymmetric natal kicks in the sample (Holland-Ashford et al., 2017).

- Asymmetric neutrino emission - The process of SN explosion is accompanied by strong neutrino emission as the final supernova process involves capturing of electrons for the production of neutrons. The neutrino emission accompanying the collapse of a proto-neutron star into a BH could in principle be detected by the neutrino detectors on earth. However, simulations show that the maximum energy and luminosity of such a neutrino burst will still be too faint to be captured by the neutrino detectors (Gourgoulhon & Haensel, 1993) unless the SN explosion is very nearby as was the case with SN1987A (e.g., Aglietta et al., 1987). Asymmetry in the direction of neutrino emission can give rise to high velocity kicks to the remnant compact core (Chugai, 1984; Sagert & Schaffner-Bielich, 2008). Simulations have shown that even an anisotropy of 1% in the neutrino emission could kick the compact core up to a velocity of 300 km s^{-1} .
- c. Tug-boat mechanism - 3D simulations of SN mechanisms and the birth of neutron stars show that there is a part of the expelled gas that expands quickly and interacts with the core only for a very short period of time (Wongwathanarat et al., 2013). This is able to push the compact core in the

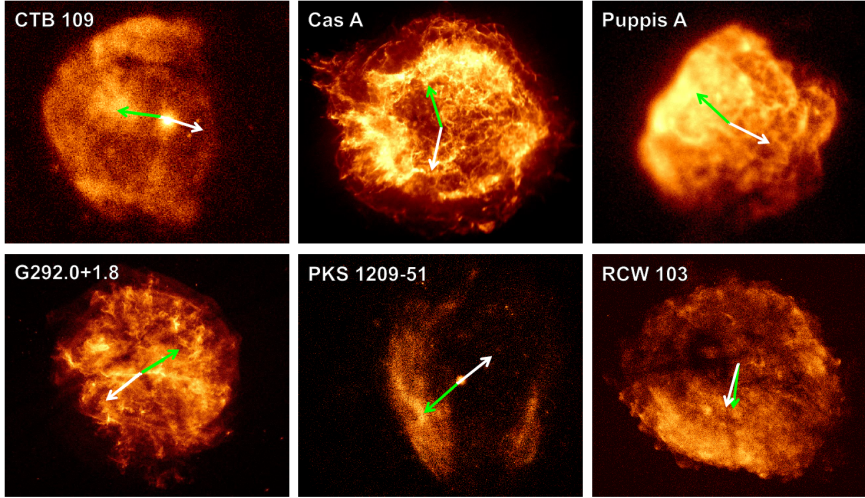


Figure 1.12: X-ray images using the Chandra X-ray Observatory and the ROentgen SATellite of six supernova remnants and pulsars. The green arrow denotes the direction from the estimated position of the supernova explosion to the dipole moment of the supernova remnant. The white arrow denotes the direction of the neutron star proper motion. Five out of the six neutron stars seem to have obtained kicks in the direction opposite to the direction of the dipole moment of the supernova remnant. *Image credits: Holland-Ashford et al., 2017.*

opposite direction, though the high kicks observed in pulsars need a stronger effect. Modelling has shown that the slower expanding asymmetric part of the expelled gas interacts with the compact core long enough to effectively drag the compact core with it by transferring momentum to the compact core. This effect was termed as the tug-boat mechanism and can in some cases kick the compact core to up to 1000 km s^{-1} . Thus the gravitational pull of the asymmetric mass ejected can accelerate the compact core to the observed velocities.

If the SN progenitor was in a binary system and if the binary system remains bound after the SN, the rest of the binary system gets a part of the natal kick imparted to the compact core formed from the SN. The maximum kick velocity imparted to the system is given by (Brandt et al., 1995)

$$v_{\text{sys,max}} = \frac{(\mu \Delta M_1 / M_1) v_{\text{orb,max}} + M'_1 v_{\text{kick}}}{M'_1 + M_2} \quad (1.12)$$

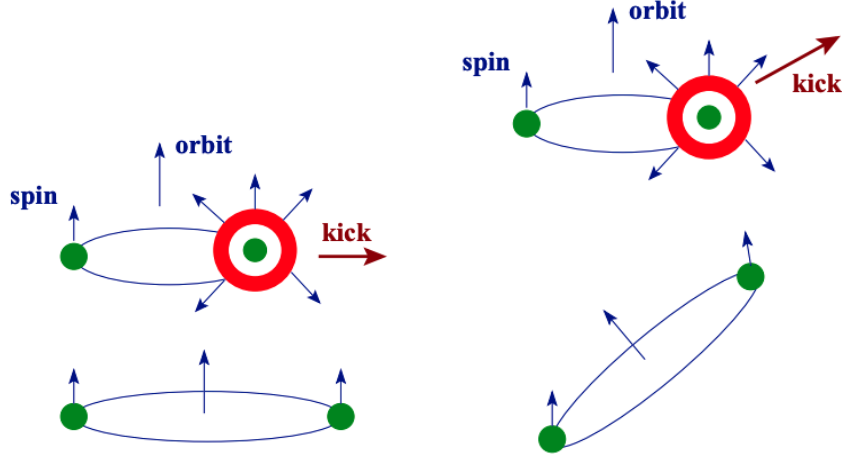


Figure 1.13: Spin-orbit misalignment due to symmetric and asymmetric mass loss. Left panel: Direction of the spin of the components and the orbital motion remains aligned after a Blaauw kick. Right panel: Direction of the spin of the components and orbital motion becomes misaligned after asymmetric mass loss. *Image Credits - Philipp Podsiadlowski.*

where $v_{\text{sys,max}}$ is the maximum kick imparted to the binary system, μ is the reduced mass $M_1 M_2 / (M_1 + M_2)$, M_1 and M_2 are the masses of the pre-SN binary stars where M_1 experiences the SN explosion, $v_{\text{orb,max}}$ is the maximum initial orbital velocity that the binary can have to ensure that Roche lobe overflow occurs, M'_1 is the mass of the remnant produced after the SN and v_{kick} is the kick received by the remnant. Further, an asymmetric kick to the SN progenitor can lead to the misalignment of the spin axis of the compact core with the original orbital axis of the binary. The spin axis of the stars in a primordial binary system are mostly aligned and thus any asymmetry in the SN kick can perturb this alignment (see Figure 1.13).

Since these kick mechanisms occur prior to the fallback of matter on the proto-neutron star and consequent BH formation (Gourgoulhon & Haensel, 1993), it is plausible that BHs formed by the fallback process should also receive such strong natal kicks. It is expected that the velocity of the kicks BHs receive will be smaller than NS velocity kicks because BHs are more massive than NSs ($v_{\text{BH}} = v_{\text{NS}}(M_{\text{NS}}/M_{\text{BH}})$), and so the anchoring effect of this more massive compact object will lead to the remnant binary obtaining less velocity due to conservation

of momentum. On the other hand, fallback of slower moving ejecta from the SN explosion could accelerate the BH by gravitationally pulling the compact object with it for a longer time (see tug-boat mechanism above; Janka, 2013). This would imply that BHs born in a SN explosion could also get large kicks at birth. BHs born by direct collapse are expected to receive kicks lower than those obtained due to birth in SN explosion (Belczynski et al., 2002). Hence, natal kick measurements could provide effective probes to differentiate between the SN and direct collapse birth pathways. This thesis is reporting the results of a study of the velocities of a population of BHXBs to relate the velocity of the BHXB to the natal kick and finally to the BH birth mechanism. This study will address the long standing issue of whether natal kicks are indeed imparted to BHXBs on the birth of the BH and how they stand in comparison to NS kicks. This will help in constraining the SN mechanism and the symmetry or asymmetry of matter ejected during a SN.

1.5 Natal kick implications on BH studies

Further from indicating the birth mechanism of a BH, natal kicks significantly impact many other aspects of BH studies. Natal kicks influence the internal properties of a binary and also the position and existence of binaries in their host galaxies or clusters. The following section discusses the various aspects of binaries that natal kicks can affect and the implications of studying natal kicks on the understanding of those aspects.

1.5.1 BH mass and natal kicks

The distribution of observed BH masses gives an idea of the masses of the BH progenitors. The Chandrasekhar mass limit, i.e. the limit of the mass for a stable white dwarf beyond which the star collapses into a neutron star is well known (Chandrasekhar, 1931). Such a clear limit is not known between the mass of the

progenitor for a NS and a BH, although a soft limit of $2.1 M_{\odot}$ is usually quoted. The mass plane of compact objects has also not been sampled enough to make out the mass distinction between NSs and BHs. The lack of BHs observed in the mass range of $3\text{--}5 M_{\odot}$ is appearing like a 'mass-gap' in the BH mass distribution, which could either be a real mass gap or due to observational biases (e.g., Kreidberg et al., 2012).

On a similar path, the mass distinction between stars that collapse into BHs with or without a SN is not clear. These mass limits will also help in determining beyond what progenitor mass the star does not undergo a SN. There is a dearth of observed massive red supergiants that have been associated with a SN explosion (Gerke et al., 2015). A possible explanation is that the massive red supergiant ends its life in a direct collapse without a SN explosion, thus explaining the lack of an observed SN association. Obtaining a cut-off mass for BHs that are formed with SN might also give an input in this problem and has been attempted in the past (Mirabel, 2017). Even though it was a very small sample set and there are large error bars on the velocities and masses of the systems, an anti-correlation between momentum of the BHXB and mass of the BH was suggested (see Figure 1.14). Increasing the sample size can help obtain meaningful statistics to test this relation. Studying compact object mass distributions will tell us about the SN explosion mechanisms as it has a direct link to how much fallback happened, the energy of the explosion that decides the amount of mass ejected, and the different kinds of compact objects that can exist.

The theoretical mass distribution of BHs in BHXBs derived by Fryer & Kalogera (2001) suggests that beyond a critical progenitor mass of $40 M_{\odot}$ (assuming no mass loss through winds), BHs form via direct collapse (DC) and a SN explosion does not occur. However, more recent work suggests that the formation of BHs by direct collapse (implosion) has a wider progenitor mass range, interspersed by narrow pockets of progenitor masses that undergo a supernova explosion to become a BH (Sukhbold et al., 2016). Natal kicks could suggest

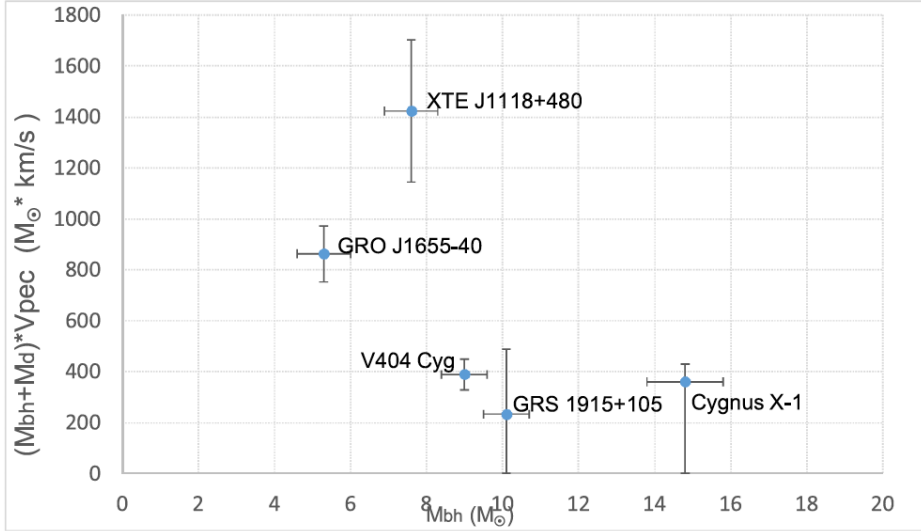


Figure 1.14: Measured momenta of BHXB systems as a function of the mass of the BH in the system. *Image credits: Mirabel, 2017*

if the BH was born with a SN explosion or by DC. Hence, if the natal kicks of a large enough sample of BH masses are determined and are in turn related to the BH birth mechanism, this could lead to the estimation of a mass cut-off for BHs that are formed by SN explosion. This approach to finding the cut-off mass for birth has been tried but due to very few BHXBs for which the possible kick velocity was estimated and due to the large error bars on the measured BH mass, a conclusive relation between BH mass, BH natal kick and BH birth pathway could not be established (Mirabel, 2017). This thesis is attempting to solve this problem by increasing the sample size of BHXBs with estimated natal kicks and hence measured momenta of a larger sample of BHXBs.

1.5.2 BH-BH mergers

With the discovery of BH mergers from gravitational wave (GW) events (Abbott et al., 2016b), we are achieving new insights into the stellar-mass BH mass distribution (The LIGO Scientific Collaboration & The Virgo Collaboration, 2018; Abbott et al., 2016a) and stellar-mass BH formation. According to theoretical

models, BH-BH binaries can be formed due to dynamical interactions in high density clusters (e.g., Fabian et al., 1975; Goodman & Hut, 1993; Sigurdsson & Hernquist, 1993; Sigurdsson & Phinney, 1993; Benacquista & Downing, 2013) e.g., in globular clusters (GCs) (Rodriguez et al., 2016) and Galactic nuclear clusters, or can be formed due to hierarchical three body interactions (Antonini et al., 2019). These interactions occur owing to the high stellar density in the above mentioned environments, which increases the probability that a single star that has evolved into a BH can become gravitationally bound to another BH. BH-BH binaries could also be formed in the Galactic field, which hosts the astrophysical stellar binaries that evolve into BH-BH binaries and would require the progenitors to be of low metallicity (Belczynski et al., 2002; Postnov & Yungelson, 2014).

Strong natal kicks could lead to the BHs being kicked out of a GC before they could become BH-BH binaries, or result in unbinding the binary system. This would hinder BH-BH binary formation and in turn reduce the rate of BH-BH mergers. Comparing the evolutionary models of BHs that form BH-BH binaries it was found that models that suggested strong natal kicks, of the order of 200 km s^{-1} , to the first born BH in a binary were preferred (Wysocki et al., 2018). Simulating a population of BH binaries while considering different natal kicks showed that the rate of GW events would decrease drastically with the increase in the kick imparted to the first born BH. Simulations using machine learning to learn from the observed events in the first and the second run of the LIGO detector were used to estimate the net rate of GW events that would be expected using different natal kick models (see Figure 1.15, top panel; Wong & Gerosa, 2019).

Natal kicks were also seen to affect the parameters of the observed BH-BH binaries. Simulations suggested that the amount of misalignment of BHs in BH-BH binaries to the orbital angular momentum vector of the binary would be dependent on the strength of the natal kick that the first BH that is born in the binary received, if the BH-BH binary has evolved from a stellar binary in isolation

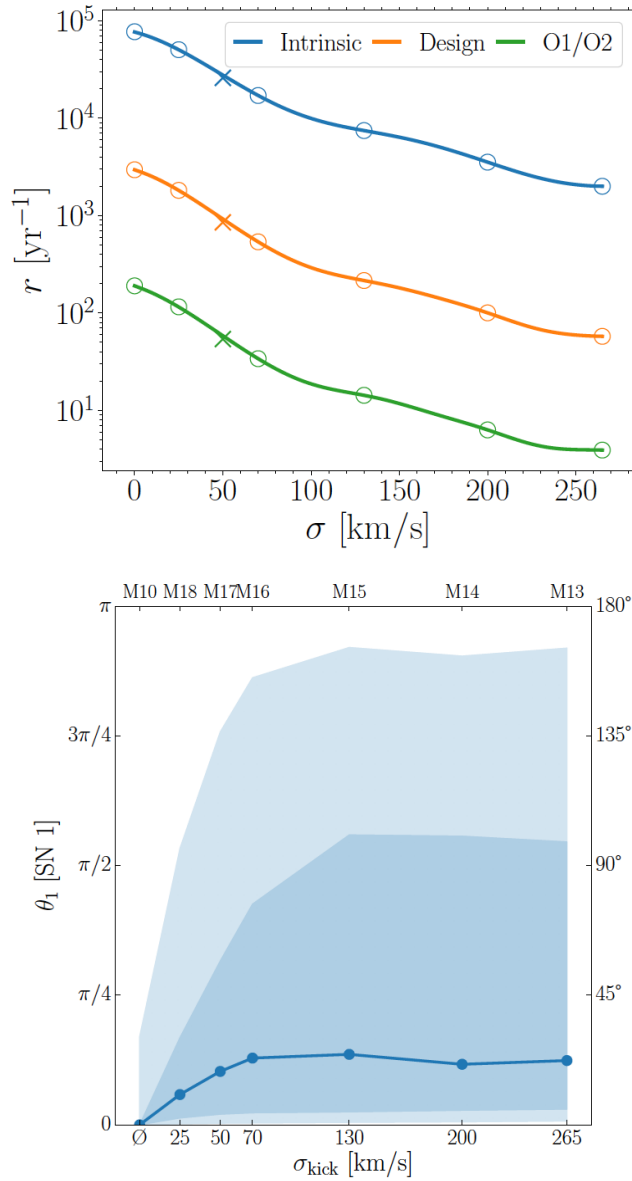


Figure 1.15: BH-BH merger rates and effect on spin-orbit misalignment. Top panel: Simulations showing the effect of natal kicks on the rate of mergers. The orange and green lines represent the merger rate assuming the design parameter of LIGO and the actual parameters during LIGO’s first and second observing runs. *Image credits: Wong & Gerosa, 2019.* Bottom panel : The misalignment that the binary will suffer after the first BH receives a natal kick with respect to the natal kick that the BH gets. The top axis depicts different natal kick input distribution models. The solid and shaded lines are the median, 68% and 95% confidence intervals. *Image credits: Wysocki et al., 2018.*

(see Figure 1.15, bottom panel; Wysocki et al., 2018). The most massive BH in the first BH-BH binary detected by LIGO, GW 151226, was estimated to have a spin axis that is slightly misaligned from the direction of the orbital angular momentum of the binary. This misalignment suggested that a kick of $> 50 \text{ km s}^{-1}$ is needed to explain the estimated properties of the BH binary (O’Shaughnessy et al., 2017).

The sites of GW merger events are also affected by the strength of kicks that the BH binary obtains. This was shown by using standard Maxwellian distribution kicked BH-BH binaries and letting them evolve in their host Galaxy. It was found that the density of BH-BH binaries is usually more concentrated a few Mpc away from the halo of the host Galaxy (Kelley et al., 2010). All the above mentioned modelling and simulations use various kick distributions that are either derived from pulsar kick distributions or use a flat distribution up to 100 km s^{-1} . This increases the need to have a well constrained kick distribution that is specifically for BHs and this thesis is attempting to obtain an observationally constrained kick velocity distribution for BHBs as a probe for kick velocities that BHs can obtain. The natal kicks will also be probed by future observations of GW events, though the model dependency of the estimation of parameters for these will need a huge increase in observed events. Estimating natal kicks by using BHBs and using GW events will help sample different populations of BH systems, thus complementing each other to obtain kick estimations of a well sampled space of BH masses.

1.5.3 BH systems in GCs

Globular clusters (GC) are high stellar density clusters and many of them are within the limits of our Galaxy (Harris, 2010). It is expected that BHs formed in GCs could get ejected out of the GC when formed due to the natal kick imparted to the BH. Any BHs that do not get kicked out will eventually sink towards the core of the GC by dynamical friction. These BHs will undergo dynamical

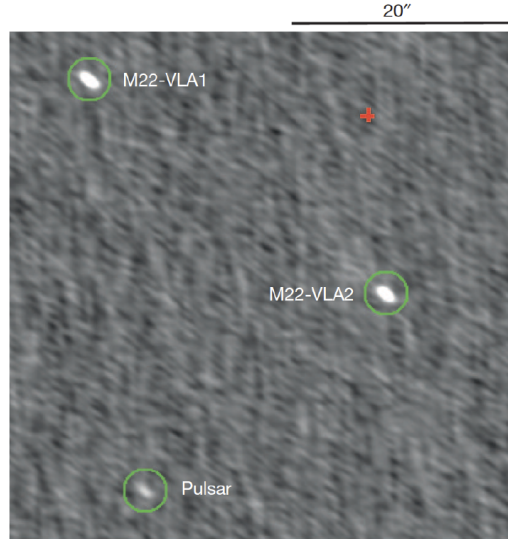


Figure 1.16: Radio image using the Very Large Array for the first BHXB candidates detected in the globular cluster M22. The source marked as ‘Pulsar’ is a known source, and M22-VLA1 and M22-VLA2 are the two candidate black hole X-ray binary candidates. *Image credits: Strader et al., 2012.*

interactions, which was thought to eject most of the BHs from the cluster (e.g., Kulkarni et al., 1993; Sigurdsson & Hernquist, 1993). This continued kicking-out of BHs from GCs was initially thought to leave GCs with no BHs or BH binaries. The lack of observed BHXBs in GCs backed this claim. Dynamical simulations of GCs showed that there could still be many BHs retained in GCs (e.g., Mackey et al., 2008; Morscher et al., 2013; Sippel & Hurley, 2013). The discovery of BHXB candidates in extragalactic (e.g. Maccarone et al., 2007) and Galactic (e.g., Strader et al., 2012; Chomiuk et al., 2013, see Figure 1.16) GCs has reignited the interest in not only looking for more such candidates, but also understanding how natal kicks are affecting the retention fraction of BHs in GCs.

While it is currently poorly constrained, the BH natal kick distribution is a key parameter in N-body simulations of GCs, used to estimate the number of BHs that are retained or ejected upon formation and due to subsequent dynamical interactions (e.g., Giesler et al., 2018). Thus, the natal kick distribution has important implications for the likelihood of finding BH-BH binaries, and also BHXBs in GCs. The current N-body simulations assume random flat natal kick

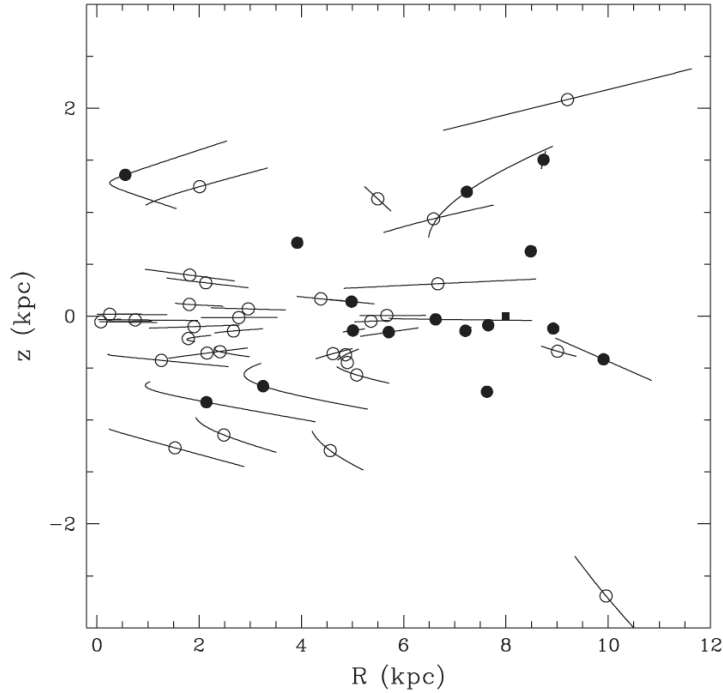


Figure 1.17: Distribution of BHXB and Neutron Star X-ray binaries (NSXBs) in the Milky Way. The black filled-in markers denote the BHXBs and the transparent circle markers are the NSXBs. R is the distance from the Galactic centre. Based on the dispersion of BHXBs and NSXBs above and below the Galactic plane it was suggested that they obtain similar natal kicks. *Image credits: Repetto et al., 2012.*

distribution of BHs of up to 100 km s^{-1} (Sippel & Hurley, 2013) or kick distributions derived from NS kick distributions (Giesers et al., 2019). Thus, obtaining an observationally constrained natal kick distribution for BHs is important for well-informed GC N-body simulations that estimate BH retention fractions in GCs.

1.5.4 Natal kicks and z -distribution

The effect of any natal kick during BH birth is seen in simulating the BH population in GCs, and a similar effect is expected in our Galaxy. Most BHXBs are assumed to have been born in the Galactic plane due to its high stellar density. In the absence of direct kick measurements, the height of known BHXBs above

the Galactic plane has been used as a proxy (e.g., White & van Paradijs, 1996; Jonker & Nelemans, 2004) given that the majority of the progenitor systems are closely confined to the plane. Various natal kick distributions were used to simulate BHXB populations and it was found that natal kicks are essential to explain the large displacement of a number of systems from the Galactic plane (Repetto et al., 2012; Repetto & Nelemans, 2015; Repetto et al., 2017, ; see Figure 1.17). However, Mandel (2016) showed that for extreme assumptions (i.e. all systems are currently at maximum $|z|$) BH kicks of $>100 \text{ km s}^{-1}$ are not required to explain the observed distribution of heights ($|z|$) above the Galactic plane. Measuring space velocities and positions of BHXBs provides extra information that helps to relate the $|z|$ -distribution to the natal kicks received by the BHs and in turn resolve this discrepancy.

1.6 Measuring natal kicks

Estimating the velocity that the BH received at birth requires the knowledge of multiple system parameters before and after the stellar collapse (Equation (1.11) and (1.12)). Simulating the exact values of these parameters needs accurate models of the SN mechanism and stellar binary evolution, which are currently not well known. This has motivated astronomers to use the current peculiar velocity i.e. the current three-dimensional velocity of the BHXB as compared to its local environment, as a proxy to the kick the BHXB received at the birth of the BH (see §1.6.2 for details on current constraints).

1.6.1 Peculiar velocity estimations

In order to measure the peculiar velocity of a system we need to know the proper motion (the motion in the plane of the sky), the radial velocity (the line-of-sight velocity) and the distance to the system. Combining the proper motion, the radial velocity and the distance to the source and subtracting the motion of the local

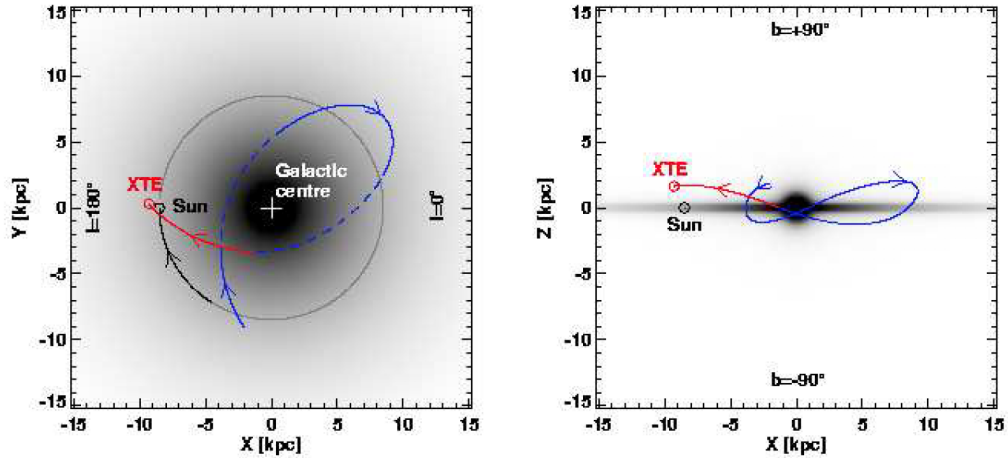


Figure 1.18: Galactocentric orbit of BHBX, XTE J1118+480. Left panel: The face-on view of the Galaxy with the cross representing the Galactic centre. Right panel: The edge-on view of the Galaxy. Blue represents the Galactocentric orbit of the BHBX during its last orbital period and red represents the Galactocentric orbit of the BHBX since it crossed the Galactic plane ($z = 0$). *Image credits: Mirabel, 2017.*

standard of rest, we can determine the current peculiar velocity of the system. Using this current peculiar velocity and a model of the Galactic potential, we can track the motion of the system as it makes its way around the Galaxy to the time when the BH was born, if the age of the system is known. This gives the full three-dimensional Galactocentric orbit of the system in our Galaxy (see Figure 1.18). Measuring peculiar velocity of systems away from the Galactic plane implies comparing their velocity with that of the local standard of rest, which is not ideal. Since many BHBXs are found away from the Galactic plane (see Figure 1.17), peculiar velocity of BHBXs might not always be meaningful.

1.6.2 Existing natal kick constraints

While we know of ~ 60 strong candidate BH systems in our Galaxy (Tetarenko et al., 2016b; Corral-Santana et al., 2016), only seven BHBX candidates have been analysed to determine if they were born in a supernova with substantial mass ejection, rather than a direct collapse. System parameters like component masses,

orbital period, donor effective temperature and the three dimensional motion of BHXBs need to be well constrained if the complete evolutionary history of these BHXb systems is to be mapped (Nelemans et al., 1999). The Galactocentric orbits of such systems with well known parameters could be integrated back to a reasonable range of their ages, thus the velocity of the system immediately after the BH birth could be determined. Such an analysis has been conducted for three systems, namely, XTE J1118+40 (Willems et al., 2005), GRO J1655–40 (Fragos et al., 2009) and Cyg X–1 (Wong et al., 2012).

These studies involved simulating five evolutionary phases of the BHXb starting from the current observed values of component masses, orbital period and donor effective temperature. An accreting system is modelled and with the help of simulations allowed to evolve to a time when the Roche lobe overflow had not started. The motion of the system through the Galaxy is then modelled during this mass transfer phase, up to a time when the Roche lobe overflow started. The phase of tidal circularisation of the system after the BH formation is also modelled along with scenarios for core collapse and hydrodynamic modelling during the supernova explosion that gives possible connections to the system before the SN occurred. This connection is able to estimate the natal kick imparted to the BH when it is formed.

This technique helped in estimating the post SN peculiar velocity of XTE J1118+40, and with the assumption that the system was born in the Galactic plane this velocity indicated that the system received an asymmetric natal kick (Fragos et al., 2009). The high peculiar velocity could also mean that the system was a GC escapee (Mirabel et al., 2001; Gualandris et al., 2005), in which case the assumption that it was born in the Galactic plane would not hold. It was suggested that GRO J1655–40 was born in a SN and received a kick when the BH was formed (Brandt et al., 1995; Mirabel et al., 2002; Willems et al., 2005), though the strength of the kick did not require an asymmetric explosion (Nelemans et al., 1999). Cyg X–1 was found to have received a small kick velocity at birth (Mirabel

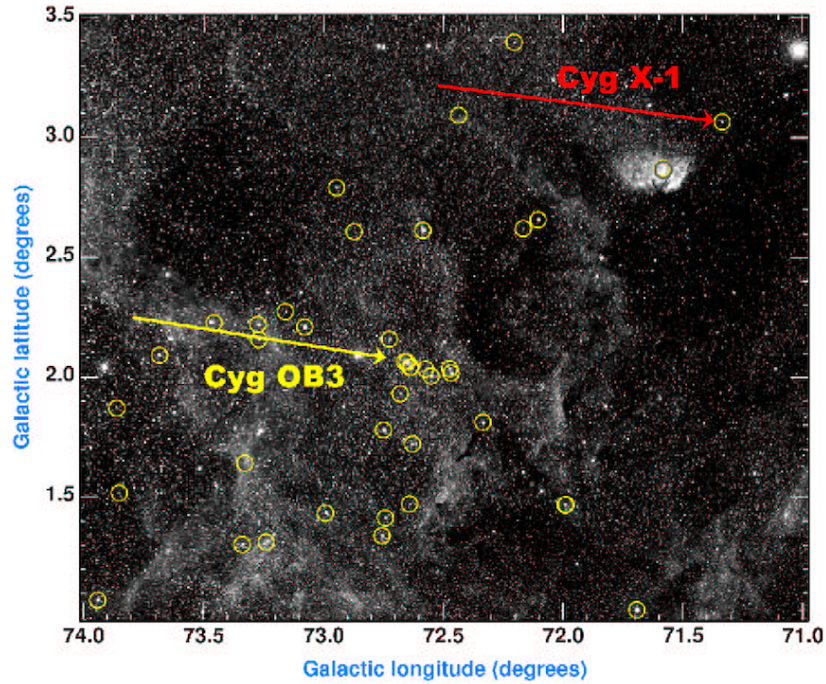


Figure 1.19: Optical image of the sky to show the relationship between the BHXB Cyg X-1 and the stellar association Cyg OB3. The red and yellow arrows represent the magnitude and direction of the transverse velocity of Cyg X-1 and Cyg OB3, respectively. The motion in the plane of the sky suggests that Cyg X-1 was formed in the stellar association Cyg-OB3. *Image credits: Mirabel & Rodrigues, 2003.*

& Rodrigues, 2003; Wong et al., 2012). This system has been associated with an OB association (Cyg OB3) and appears to move with velocities comparable to this association (see Figure 1.19).

Only the peculiar velocities were used to infer whether the kicks BHXB systems received were high enough to suggest a SN origin for the other four systems (e.g., Mirabel et al., 2001; Mirabel & Rodrigues, 2003; Dhawan et al., 2007; Miller-Jones et al., 2009b). This has been done by measuring the proper motions of the BHXBs, and combining them with the line-of-sight velocities and the distances to the systems to measure the velocities of the systems with respect to the local standard of rest. A low peculiar velocity was measured for GRS 1915+105 (Dhawan et al., 2007; Reid et al., 2014), which suggested that the system could have been born by direct collapse. The inferred peculiar veloc-

ities of V404 Cyg (Miller-Jones et al., 2009b), VLA J2130+12 (Tetarenko et al., 2016a) and MAXI J1836–194 (Russell et al., 2015) were more consistent with a symmetric SN explosion. This is a small sample size, with estimations of the minimum natal kick having been made using different methods. Thus in order to draw statistically robust conclusions about the natal kick distribution of BHs, we need to increase this sample size and adopt a more systematic approach. In this thesis, we increase the sample size of estimated kick velocities of BHXBs to 16, by combining measured proper motions, systemic radial velocities and distances to these systems and a new technique to estimate the kick velocities.

1.7 Structure of thesis

This thesis consists of 6 chapters and one appendix, with the current chapter being the first one and the one that introduces and motivates the thesis. The majority of the research in this thesis (Chapters 3 and 4) is adapted from two published papers, and the final piece of research (Chapter 5) is under preparation to be submitted for publication. A complete list of publications has been presented in the Appendix A to this thesis, including my coauthored publications.

Chapter 2 states and explains the instruments and techniques that are used in this thesis. Specifically, it details the methods of radio interferometry and Bayesian inference and these techniques are the foundation of the work carried out in this thesis.

Chapter 3 demonstrates the successful use of the technique of Very Long Baseline Interferometry (VLBI) to measure a high significance parallax distance to a BHXB, MAXI J1820+070. The chapter also discusses the impact of this high significance distance measurement to improve on other estimated properties of the system.

Chapter 4 reports the proper motion measurements of three BHXBs using VLBI. It lays down a new methodology to estimate potential natal kick distributions of BHXBs. Finally, the chapter uses this analysis to estimate the potential

kick velocity distribution of the BHXB population, and discuss its influence on various BH studies and parameters.

Chapter 5 reports a search for BHXB candidates that have not yet been detected as transients, and showcasing the use of proper motion measurement as a tool to differentiate between Galactic and extragalactic sources.

Chapter 6 presents a brief discussion of the implications of the work done in this thesis and an exploration of the possible future work. The chapter ends with reviewing the conclusions derived from the work.

Telescopes and Techniques

This chapter provides a brief discussion of all the instruments, concepts and techniques that have been used in this thesis. Since this thesis for the most part uses radio data and the technique of Very Long Baseline Interferometry, the chapter starts with discussing some standard formalism used in radio interferometry. The chapter then goes into the details of astrometry and measuring velocities of black hole X-ray binaries. The chapter ends with a discussion on Bayesian Inference, which is a statistical technique that has been used in this thesis to fit models and obtain probability distributions of fitted parameters.

2.1 Radio interferometry

Radio emission from astronomical objects can be detected and studied on earth with the use of radio telescopes. Radio wavelengths provide a unique view into objects and phenomena that are not typically accessible in optical wavelengths, e.g., pulsars and HI regions. The fact that our atmosphere allows radio emission of wavelengths >30 MHz to reach the surface of the earth, although with some slight distortions due to the tropospheric and ionospheric variations, allows astronomers to study these wavelengths without having to send detectors and satellites into space. Radio telescopes range from single one dimensional conducting wires to

large area parabolic dishes. Large parabolic dishes have the advantage of having large collecting area and this thesis uses the data provided by such dishes. The resolution of a telescope is limited by the diffraction limit given by $\theta = \lambda/D$, where λ is the observing frequency and D is the diameter of the radio dish. Thus, for radio wavelengths really large dishes are needed for decent resolution. The largest known radio telescope, The Five-hundred-meter Aperture Spherical radio Telescope (FAST), is 500 metres in diameter, but is embedded in a valley thus restricting the steering capabilities. Resolution higher than what a single dish can provide is attained by using a technique called interferometry, where a number of small dishes are spread across a large distance, thus changing the effective resolution to λ/B_{max} where B_{max} is the length of the longest baseline.

2.2 Observing the radio sky

The radio sky can be studied and imaged by using basic radio interferometry principles. Radio interferometers measure visibilities, by correlating electric signals from two or more radio telescopes. Below is a brief discussion on the use of a two element interferometer to study the radio sky and most of it is drawn from Taylor et al. (1999), Thompson et al. (2017) and National Radio Astronomy Observatory online lectures for Essential Radio Astronomy¹.

2.2.1 Visibilities and Fourier transforms

The measured visibilities are a representation of the Fourier transform of the radio brightness in the sky. Using a two element interferometer, a radio wavefront from an astronomical source will reach element two after a time delay of τ_g relative to when it reaches element one, which will be dependent on the separation of the two elements (\mathbf{b}) and the angle the radio source makes with baseline separating the two elements (θ , see Figure 2.1). The superposition of the signal from the

¹<https://science.nrao.edu/opportunities/courses/era>

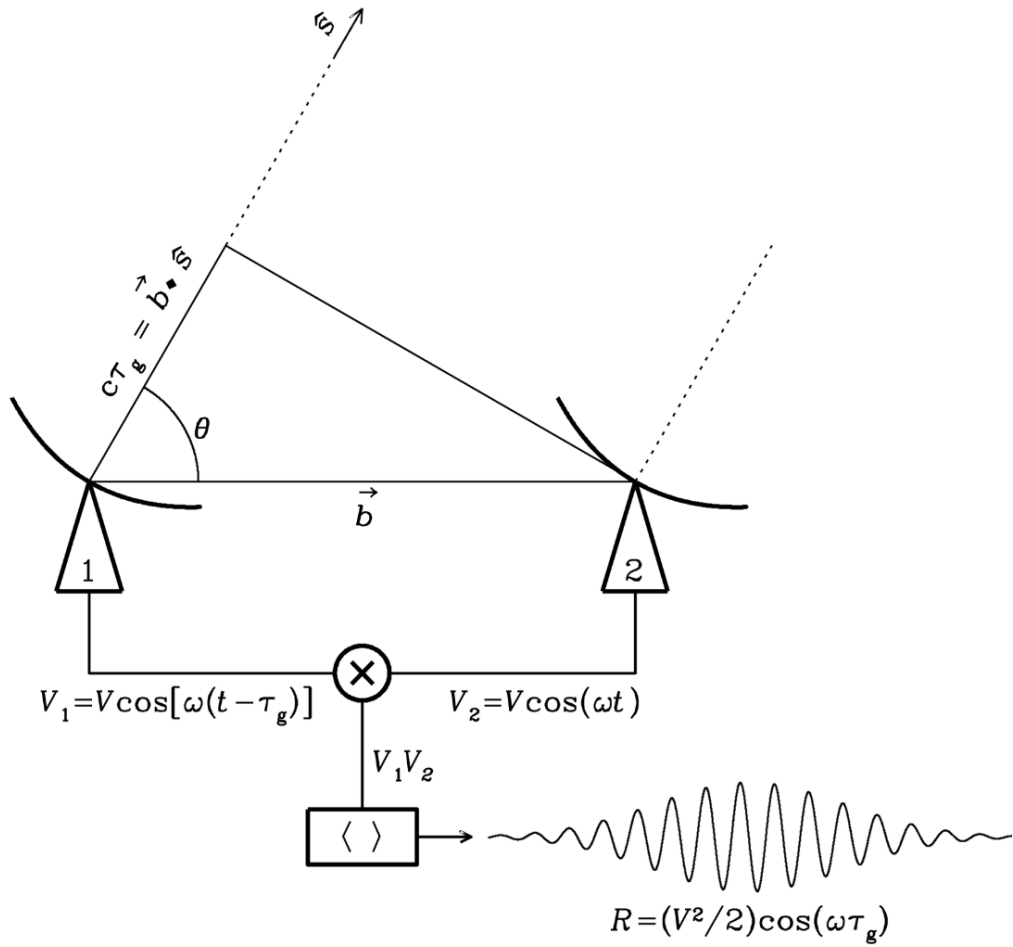


Figure 2.1: A basic two element radio interferometer. \mathbf{b} is the interferometer baseline. ω is the observing frequency ($2\pi\nu$) and τ_g is the time delay between the two elements of the interferometer. $V_1 V_2$ is the correlated signal from the two antennas. *Image credits: Thompson et al., 2017.*

two elements produces interference fringes where the fringe spacing is given by $\lambda/b \sin \theta$. Combining the voltage signals at the two elements using a correlator that multiplies the signals, we get a response that is varying as the cosine of the time delay (τ_g) and the central observing frequency (ν) i.e $r(\tau_g) \propto \cos 2\pi\nu\tau_g$.

The power received by this two element radio interferometer, with each antenna having an effective collecting area of $A(s)$ in the direction \mathbf{s} , from a solid angle $d\Omega$ in the sky is dependent on the radio brightness of the source, $I(s)$, in the direction of s at a frequency ν and an observing bandwidth $\Delta\nu$ and can be represented as

$$r = \Delta\nu \int_S A(\mathbf{s}) I(\mathbf{s}) \cos \frac{2\pi\nu\mathbf{b} \cdot \mathbf{s}}{c} d\Omega \quad (2.1)$$

Assuming that the synthesized radio image is tracking $\mathbf{s} = \mathbf{s}_0 + \boldsymbol{\sigma}$, where \mathbf{s}_0 is the centre of the image and is the delay tracking centre (see Figure 2.2), also called the phase centre, equation (2.1) can be written as

$$\begin{aligned} r = & \Delta\nu \cos \left(\frac{2\pi\nu\mathbf{b} \cdot \mathbf{s}_0}{c} \right) \int_S A(\boldsymbol{\sigma}) I(\boldsymbol{\sigma}) \cos \frac{2\pi\nu\mathbf{b} \cdot \boldsymbol{\sigma}}{c} d\Omega \\ & - \Delta\nu \sin \left(\frac{2\pi\nu\mathbf{b} \cdot \mathbf{s}_0}{c} \right) \int_S A(\boldsymbol{\sigma}) I(\boldsymbol{\sigma}) \sin \frac{2\pi\nu\mathbf{b} \cdot \boldsymbol{\sigma}}{c} d\Omega \end{aligned} \quad (2.2)$$

Complex *visibility* (\mathcal{V}) and is related to the separation between the two points by a Fourier transform as

$$\mathcal{V} = |\mathcal{V}| e^{i\phi_V} = \int_S A(\boldsymbol{\sigma}) I(\boldsymbol{\sigma}) e^{-2\pi i \nu \mathbf{b} \cdot \boldsymbol{\sigma} / c} d\Omega \quad (2.3)$$

where $A(\boldsymbol{\sigma})$ is the antenna response on the sky, $I(\boldsymbol{\sigma})$ is the source intensity distribution on the plane of the sky and ϕ_V is the phase of the visibility. Expanding the exponential part of equation (2.3) into real and imaginary cosine and sine counterparts and substituting in equation (2.2)

$$r = A_0 \Delta\nu |\mathcal{V}| \cos \left(\frac{2\pi\nu\mathbf{b} \cdot \mathbf{s}_0}{c} - \phi_V \right) \quad (2.4)$$

where A_0 is the effective collecting area of the antenna in the direction s_0 . Specifically for the data in this thesis, this correlation from the signals in individual antennas to combine and Fourier transform is done by either the DiFX correlator (Deller et al., 2007) or the SFXC correlator (Keimpema et al., 2015). The cosine term in equation (2.4) gives rise to a fringe pattern that can be studied by interpreting the interferometer measurements.

The radio observations are carried out in a band. This implies that the response of the antenna is recorded not just at a central frequency, but over a range of frequencies. This bandwidth manifests itself as modulations to the amplitude of the fringe pattern as a sinc function. By combining the measurement made by a baseline at a frequency for a specific time, we can measure the amplitude and phase of the visibilities. The Fourier transform relation (equation (2.3)) between the measured visibilities and the brightness distribution of the radio source is key to then obtain position and flux information of the radio source.

2.2.2 The uvw plane

Creating images and measuring positions of radio sources using the Fourier transform equations and a radio telescope requires a coordinate system. The (u, v, w) coordinate system is chosen such that u points in the east direction, v points in the direction of the north pole and w points in the direction of the phase centre of the synthesised image. The magnitude of (u, v, w) are measured in wavelengths at the central observing frequency. The position of the tracked source in the sky are represented in (l, m, n) , where (l, m, n) are direction cosines of the u, v and w axes. The (l, m) coordinate system helps to project the celestial sphere onto a 2D plane. Using the change of coordinates to (u, v, w) and (l, m, n) , the solid angle element and the baseline projection in the direction of the phase centre can

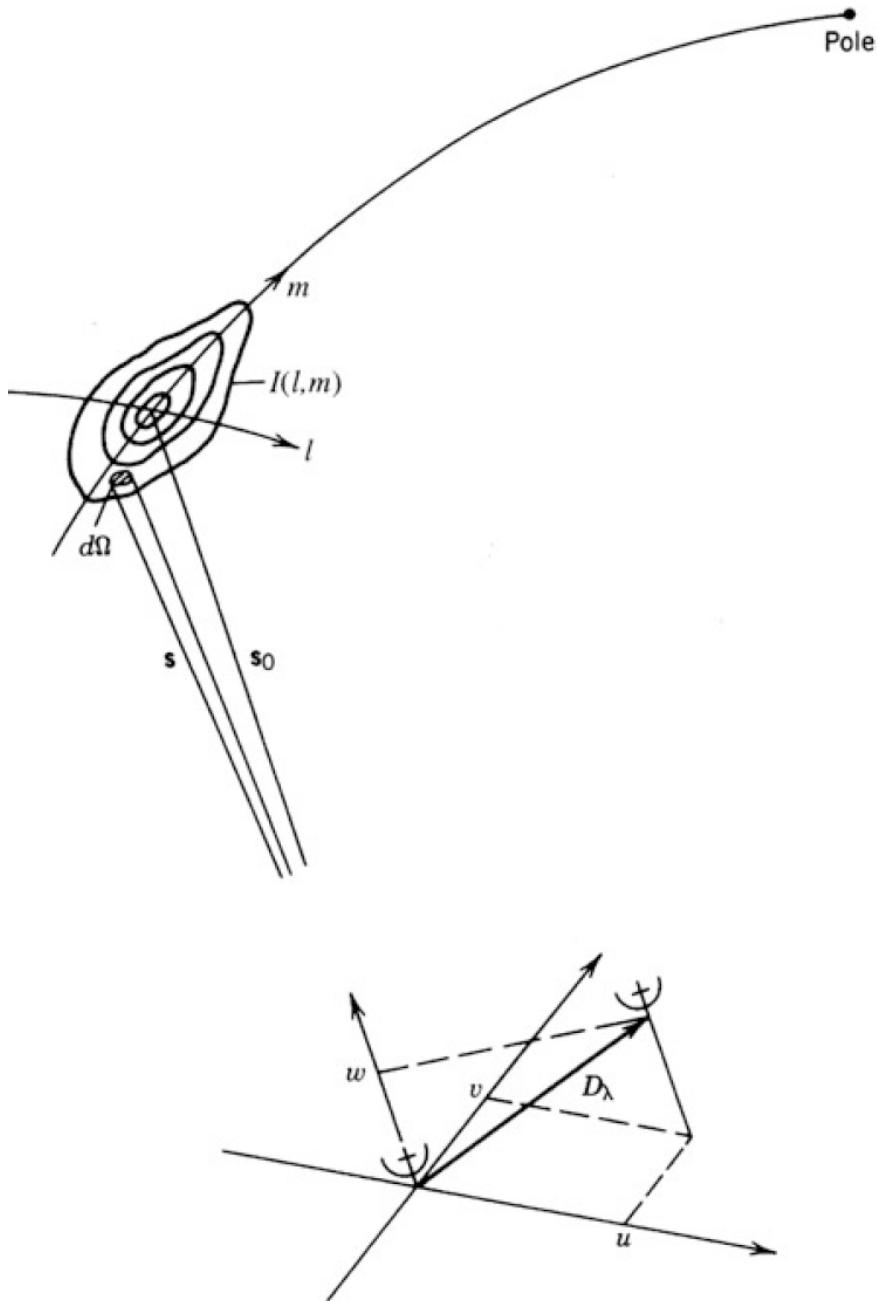


Figure 2.2: (u, v, w) coordinate system and the (l, m) plane. The source, $I(l, m)$ is being tracked and observed by a pair of antennas with a baseline length of D_λ . s_0 is the direction of the w component and also the delay tracking centre. *Image credits: Thompson et al., 2017.*

be written as

$$\begin{aligned}\frac{\nu \mathbf{b} \cdot \mathbf{s}}{c} &= ul + vm + wn \\ \frac{\nu \mathbf{b} \cdot \mathbf{s}_0}{c} &= w \\ d\Omega &= \frac{dldm}{\sqrt{1 - l^2 - m^2}}\end{aligned}\tag{2.5}$$

We can then obtain a practical Fourier transform formula for the visibilities in terms of the antenna separation and wavelengths by substituting the above in equation (2.3).

$$\begin{aligned}\mathcal{V}(u, v, w) &= \int_{-\infty}^{\infty} \int_{-\infty}^{\infty} A(l, m) I(l, m) \times \\ &\quad \exp\{-2\pi i[ul + vm + w(\sqrt{1 - l^2 - m^2} - 1)]\} \frac{dldm}{\sqrt{1 - l^2 - m^2}}\end{aligned}\tag{2.6}$$

This results in every point in the (l, m) plane having a corresponding data point in the (u, v) plane. If the synthesised field is not large, such that for some range of (l, m) the w term in the above integral can be neglected, the integral then becomes a Fourier transform in two dimensions.

$$\frac{A(l, m) I(l, m)}{\sqrt{1 - l^2 - m^2}} = \int_{-\infty}^{\infty} \int_{-\infty}^{\infty} \mathcal{V}(u, v) e^{2\pi i(ul + vm)} dudv\tag{2.7}$$

This inverse Fourier transform then gives the sky brightness distribution of the radio source that has been imaged. The assumption that the w term can be ignored places limits on the (l, m) size, which in turn puts limits on the size of the field that can be imaged. If b_{\max} is the maximum baseline in the telescope array and λ is the central observing wavelength then the minimum half-power width of the synthesised beam is given by $\theta_{\text{HPBW}} = \lambda/b_{\max}$. The maximum baseline along with the observing frequency determine the angular resolution to which the radio emission can be imaged. The baseline vector between two telescopes will trace out an ellipse centred at the origin of the (u, v) plane due to the rotation of the earth. When an array with more than two antennas is used the (l, m) coordinate can be transferred to a coordinate system with hour angle (or LST Right Ascension)

and declination (δ) the base with the X-axis pointing in the direction of $h=0$, $\delta = 0$. The aim of multiple antennas array radio interferometry observations is to get a wide and uniform (u, v) coverage and use it to determine the sky brightness distribution. A longer observation will result in a better uv -coverage, which gives more information that can be used to infer the sky brightness distribution (see Figure 2.3).

2.3 Obtaining radio data: VLBI

Radio interferometry using two antennas can be extended to multiple disconnected antennas spread across a large area to achieve a resolution limited by the maximum baseline of this multi-antenna array, and this interferometry technique is called Very Long Baseline Interferometry (VLBI). The increase in the effective collecting area also increases the sensitivity. The main aim of this thesis is to measure the natal kick velocities of radio bright objects called black hole X-ray binaries (BHXBs), and measuring proper motions (velocity of the object in the plane of the sky) and parallaxes is a key aspect of that. The proper motion of typical BHXBs is of the order of a few mas yr^{-1} and the parallax is $< 1 \text{ mas}$. To achieve this resolution at radio wavelengths, baselines as long as a few thousand kilometres are needed. In some cases the distribution of dishes is spread across continents providing resolution of sub-milliarcseconds, such as in the case of the Very Long Baseline Array (VLBA) spread across the US. The work in this thesis also used the European VLBI Network (EVN) that has dishes spread across Europe, parts of Asia and South Africa; and the Long Baseline Array (LBA) with dishes located in Australia, New Zealand and one dish in South Africa.

2.3.1 The VLBA

The VLBA is an array of ten homogeneous dishes spread across the US and operated by the National Radio Astronomy Observatory (NRAO; see Figure 2.4).

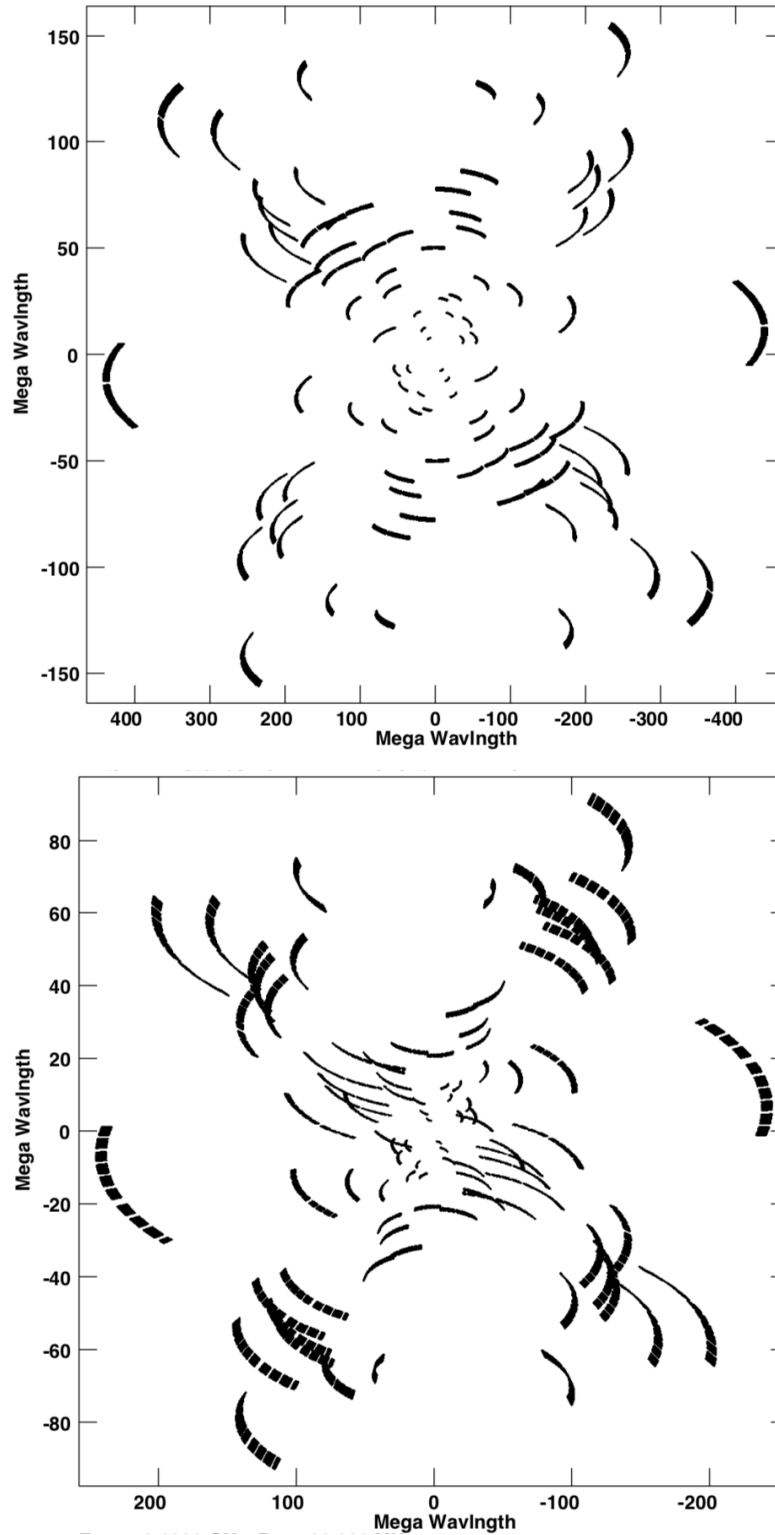


Figure 2.3: We have presented a comparison of the uv -tracks traced by the Very Long Baseline Array (see Section 2.3.1 for details about the array) for 80 minutes for two targets, MAXI J1820+070 (top figure) and MAXI J1813-095 (bottom figure) at a declination of $+07^\circ$ and -09° , respectively.



Figure 2.4: Locations of dishes that we used in the Very Long Baseline Array. The stations used in this thesis have been marked in this figure. BR - Brewster; FD - Fort Davis; HN - Hancock; KP - Kitt Peak; LA - Los Alamos; MK - Mauna Kea; NL - North Liberty; OV - Owens Valley ; PT - Pie Town; SC - St. Croix.

The longest baseline is in the east-west direction with the two dishes separated by 8611 km. All the dishes in the VLBA are identical in construction and have a diameter of 25 m. The VLBA is equipped to observe at a wide range of frequencies and has receivers that can observe from 3 mm to 90 cm. The minimum angular resolution depends on the observing frequency, and ranges from 0.17 mas to 22 mas. Since the dishes are dedicated to VLBI, one can observe using the VLBA at any time of the year. The data are recorded on disks that are later shipped to the NRAO facility in Socorro, where the data get correlated.

2.3.2 The EVN

The EVN is an inhomogenous array, with most of the dishes having different dimensions. In a usual EVN run, at least 10 of the dishes participate (see Figure 2.5). The addition of other dishes depends on availability. The fact that all the dishes are of different sizes then gives different slew times for all the dishes to get to the target of interest, making observations that require quick switching between targets difficult. The large number of dishes that can participate

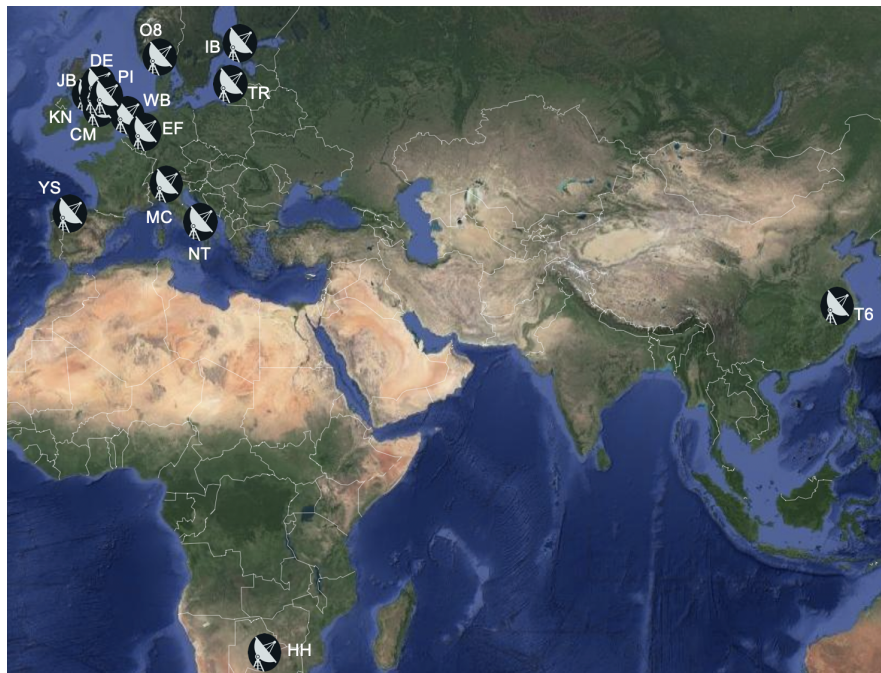


Figure 2.5: Locations of the dishes we used in the European VLBI Network. The stations used in this thesis have been marked in this figure. JB - Jodrell Bank; WB - Westerbork; EF - Effelsberg; MC - Medicina; NT - Noto; O8 - Onsala; T6 - Tianma65; TR - Torun; HH - Hartebeesthoek; YS - Yebes; IB - Irbene; CM - Cambridge; KN - Knockin; DE - Defford; PI - Pickmere.

in the observations, especially the bigger EVN dishes (EF, T6, YS), makes the EVN more sensitive than the VLBA, caveat the participation of the bigger EVN dishes. The EVN has three scheduled runs per year of twenty days each, during which most of the telescopes from Europe and Asia participate. There is also the possibility of having observations outside of these scheduled runs, but the observations have to be adequately justified and the facility only allows a maximum of 144 hours of such observations in a year.

There are also calls for proposals to observe using the EVN with the e-Multi-Element Radio Linked Interferometer Network (eMERLIN) telescopes. eMERLIN is an array of seven telescopes in the UK, which give added sensitivity to the EVN array and the increase in the number of short baselines can help pick up more diffuse structure. We used five of these seven dishes in the observations in this thesis (CM, PI, KN, DE and JB). The EVN offers observations in various bands from 0.7 cm to 92 cm. The data are correlated after the observations at the The Joint Institute for Very Long Baseline Interferometry European Research Infrastructure Consortium located in the Netherlands, unless the observations were taken during a scheduled e-VLBI run. e-VLBI offers data transfer over the internet and a real-time correlation of observations. This is a favourable mode of observation if the data are needed immediately after the observations to obtain successful science from the data, as is the case in transient science.

2.3.3 The LBA

The LBA is an ad-hoc array of ten antennas that are controlled by different institutes (see Figure 2.6). These telescope facilities, managed by The Commonwealth Scientific and Industrial Research Organisation (CSIRO), come together a few times a year to conduct VLBI observations. LBA is the only facility in the southern hemisphere that can observe at milliarcsecond resolutions. If the observations are conducted outside of the standard observing runs, then all ten telescopes may not be able to take part in the observations. One of the ten sta-



Figure 2.6: Locations of the dishes that participate in LBA observations. AK - ASKAP; AT - phased up ATCA; CD - Ceduna; HO - Hobart; KE - Katherine; MP - Mopra; PA - Parkes; TD - Tidbinbilla; WA - Warkworth; YG - Yarragadee.

tions is the Australia Telescope Compact Array (ATCA), which consists of six dishes with a maximum baseline of 6 km. When ATCA is participating in the VLBI observations, the array usually observes a bright flux calibrator in the sky to phase-up all the dishes and make sure the signals add coherently. The LBA offers radio observations over a range of frequencies from 1.4 GHz to 22 GHz. Due to differing sizes of the dishes in the LBA array and different slew times, observing projects with quick target switching is not considered efficient. A-priori amplitude calibration may not always be feasible due to the absence of system temperature measurements and gain curves for all antennas in the LBA. The data are observed and correlated after the fact, however real time data correlation have been possible in a few cases (e.g., Phillips et al., 2007; Moin et al., 2016). The data are correlated at the Pawsey Supercomputing Centre ².

2.4 Reducing radio data

2.4.1 Calibration

Once the data have been correlated and are acquired by the user, they will need to be appropriately calibrated to correct for the effect the troposphere, ionosphere, and antenna positional errors have on the fringe pattern of the data from the

²<https://pawsey.org.au/about-us/about-pawsey/>

antennas. I will discuss some of the important calibration steps and techniques I carried out on the data that have been used in this thesis. Since the main aim of my thesis is to measure proper motions and parallaxes of BHXBs, I taken special steps to maximise the astrometric accuracy. The Astronomical Image Processing System (AIPS 31DEC17; Greisen, 2003) is a software whose development started in 1978 and it is still being used to successfully reduce and calibrate VLBI data. I have used AIPS for the data reduction in my thesis and discuss those steps below. More details can be found in VLBA Scientific Memos³, present in an online archive maintained by NRAO.

2.4.1.1 Preliminary calibration

The correlator corrects for the time delay between different antennas by using geometric delays during correlation. Other than the standard rotation of earth, slight precession and other effects change the earth's orientation parameters. At the time of correlation this correction is done using a predicted value of the orientation on the day of the observation. This might be slightly different from the true values, and so before any other calibration of the data it is advisable to correct for the earth's orientation parameters. A procedure called 'VLBAEOPS' in AIPS allows for this correction by fetching the file containing the parameter values from the NASA website⁴. This step is particularly important for high precision astrometry experiments.

The signal coming to individual antennas goes through the ionosphere while making its way to earth. This causes a frequency-dependent delay in the radio signal that should be corrected for. One way to do that is by using a global model of the total electron content (TEC)⁵, which is being measured by global positioning (GPS) networks around the world. The GPS system measures the delay caused at different frequencies in the same band and estimates the dispersive

³<https://library.nrao.edu/vlbas.shtml>

⁴http://gemini.gsfc.nasa.gov/solve_save/usno_finals.erp

⁵<https://science.nrao.edu/facilities/vlba/publications/memos/sci/index/sci23memo.ps>

delay caused by the ionosphere. As the ionospheric delay scales with wavelength squared, it is more problematic at lower frequencies (especially below 5 GHz). The task ‘TECOR’ in AIPS has been designed to read the file containing the TEC information (available on the NASA website⁶) and extrapolate it to the time and place of the individual antenna. The procedure ‘VLBATECR’ has been made to automatically download the file and run ‘TECOR’ to correct for the ionospheric delays.

In the case of the VLBA, the errors in the sampler voltage offsets due to some errors in the digitizer at the correlator are not removed before sending the data to the user. The sampler offsets will need to be corrected for using autocorrelations (task ‘ACCOR’ in AIPS), and then a-priori amplitude calibration is carried out by using the system temperature information at individual antennas. The system temperature information is available as a table (TY) along with the correlated data provided by NRAO. The EVN conducts this a-priori amplitude calibration as a product of their pipeline and puts it as a calibration (CL) table in the data. As an alt-az mount telescope tracks the motion of a source in the sky, the telescope feeds rotate with respect to the sky. This effect in the phases are corrected by using a AIPS procedure, ‘VLBAPANG’.

2.4.1.2 Fringe fitting

Once the initial calibration is done, small instrumental delays that are still present in the data due to imperfectly known delays from a combination of telescope and correlator models need to be fixed. A very bright, known calibrator is observed preferably every few hours, with the recommended time being every three hours. This calibrator, called the fringe finder, is used to correct the instrumental delays and rates for all antennas. The instrumental delays show up as a phase slope with frequency through the bandwidth and a delay rate will result in a change in the phase slope with time. Fringe fitting is a self calibration process that fits for

⁶cddis.gsfc.nasa.gov

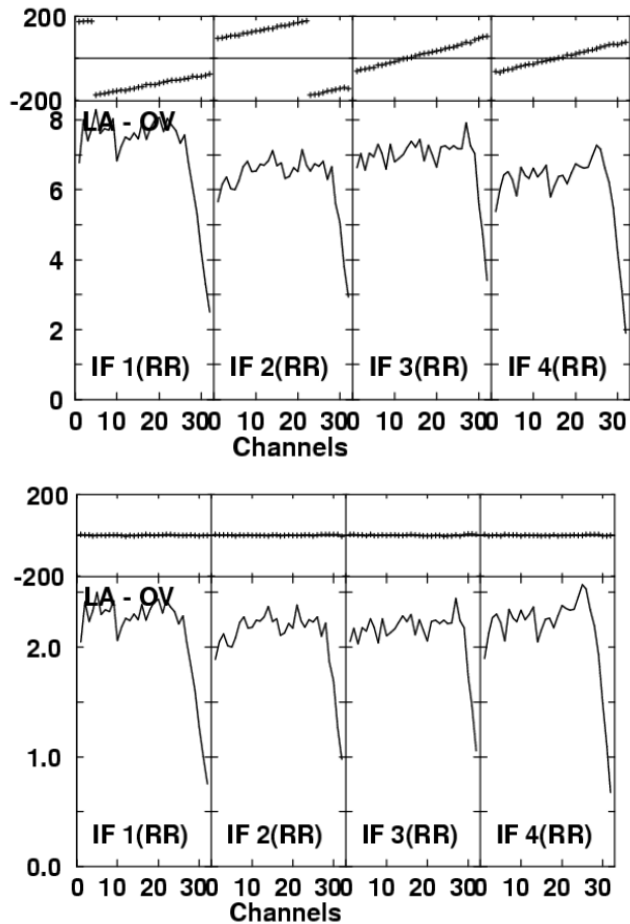


Figure 2.7: Phase slopes before and after removing delays. The slope across each IF of a pair of antennas flattens out.

these delays and rates. The AIPS task ‘FRING’ can do this procedure.

2.4.1.3 Phase referencing

Coherence time, the time for which the phases are coherent, is dependent on the observing frequency and the atmospheric conditions at the time of observing. The usual VLBI observing runs are far longer than this coherence time, and the phase drifts during the observation will need to be solved for using fringe fitting. Fringe fitting requires a high signal to noise ratio to work well, and so a technique called phase referencing has been developed to solve for phases of weak radio sources. In this technique, the phase drifts are tracked on a nearby bright

calibrator source (preferably very close to the target, <2) and interpolated to the target. Observations should be designed so that the observing time between two scans of this phase calibrator is less than the estimated average coherence time at the observing frequency for different kinds of weathers.

One can solve for the phases, delays and rates, and assuming that the atmospheric models change slowly across the sky and are mostly the same between the target and the phase calibrator the solutions on the phase calibrators are then transferred onto the target. Phase referencing also helps in strong detections of faint targets by increasing the integration time on target from a few minutes (the coherence time) to hours (the observation time). The sensitivity improves by $\sqrt{N_b \times \frac{T_{\text{int}}}{T_{\text{scan}}}}$, where N_b is the number of baselines, T_{int} is the extended integration time due to phase referencing to a phase calibrator and T_{scan} is the duration of each scan (Lestrade et al., 1990) Residual delays even after fringe fitting might result in amplitude reduction when the data are averaged in time or frequency for the purposes of imaging.

2.4.2 Imaging and cleaning

Once the radio source has been observed using a combination of antennas, and the data correlated and well-calibrated, it is ready for imaging.

2.4.2.1 Cleaning

The complex visibilities are Fourier transformed to give the flux density distribution in the sky. Initially, a dirty image is produced that has artefacts due to the sparse sampling of the wavefront and limited number of antennas. In order to obtain clean components from this dirty image that truly represents the flux density distribution of the source, the structure of the dirty beam is subtracted from the image around the brightest point in the image. This process is repeated iteratively to remove all the bright points in the image until the image only consists of residual noise. The clean components are convolved with the main lobe

of the synthesised beam and the residual noise is added to give the final image.

A model of the intensity of the source can be used to estimate source structure and visibilities $\mathcal{V}(u, v)$. This model is sampled from the visibility measurements made in the u, v space and can be represented as

$$\mathcal{V}(u, v) = W(u, v)\hat{V}(u, v) + \epsilon(u, v) \quad (2.8)$$

where $\mathcal{V}(u, v)$ is the image visibility, $W(u, v)$ is the weighting function and $\epsilon(u, v)$ is the normally distributed random error. The weighting function used in the reduction of data in this thesis is based on local data density in a specific symmetric region of (u, v) space. Two extreme weighting options are present and the weighting can be scaled towards either of the two extremes based on requirement.

- *natural* weighting - where all data points in the (u, v) plane are treated the same. Since the data clumping is more dense near the (u, v) origin, natural weighting has the effect of up-weighting the shorter baselines. The weighting maximises the sensitivity of the image and is good to image faint radio sources.
- *uniform* weighting - this weighting adjusts the data by $(1/N_s)$ where N_s is the number of data points within a symmetric region of (u, v) of width s . The weighting will thus change based on the size of the pixels and the image and can be controlled by these parameters.

2.4.2.2 Imaging

The target data to be imaged are usually averaged in all spectral channels and then split off from the main dataset to reduce the data size. The imaging involves iterative deconvolution of the bright pixels in the image from a dirty image as discussed in §2.4.2.1. In this thesis targets have been imaged to conduct astrometry i.e to measure the position of the core of the radio emission. For astrometry, the positions have to be measured prior to self-calibration as self-calibration can shift

the centroid of the target to the assumed centroid of the starting model. This was done by obtaining the cleaned image and using the task ‘JMFIT’, which fits Gaussian components to the target whose position is being measured and reports their parameters like peak flux with density, source size in case of a resolved source and centroid with errors of the Gaussian components. The position measurements in this thesis were mostly fit with a point source model.

2.4.3 Reducing systematics

Various data reduction and observing techniques have been used to mitigate the systematic errors arising in the position measurements of the radio sources of interest in this thesis, thus improving the accuracy and precision of the measurements. Where possible, the same array, frequency and calibrator was used to observe a target. Any corrections needed due to use of different arrays, observing frequency or calibrators were considered after the process of data reduction, especially in Chapter 3 where we had to observe the target using a combination of the VLBA and the EVN at two different frequencies and using two different phase calibrators.

2.4.3.1 Geodetic blocks

The phase solutions and fringe fitting on the phase calibrator and transferring the solutions onto the target are limited by the atmospheric effects. The errors introduced by varying atmospheric models scale as $\sec Z$, where Z is the zenith angle. This error then increases as the source gets lower in elevation. The ionospheric models to solve for these atmospheric variations are using the GPS system that estimates the total electron content in the line-of-sight as discussed in Section 2.4.1.1. The troposphere also affects the time delay and hence the phase slopes, and mostly affect frequencies >5 GHz. Clock errors are also the most pronounced at higher frequencies. In order to mitigate the residual delay and clock errors, geodetic blocks are observed. A geodetic block is a half-an-hour chunk of time

that is spent observing strong calibrator sources at various elevations all over the sky. This observation is usually carried out at the beginning and end of the observing run. If the observations are long enough observing an additional geodetic block in the middle of the observing run helps in solving for the quadratic multi-band delay over time, rather than a linear one. Since the tropospheric errors are a function of the the elevation angle, measuring the phases of various strong calibrator sources at various elevations can help model this error and determine the tropospheric offsets for all antennas. In this thesis, this observing technique has been implemented only while using the VLBA as the dishes are similar (and appropriately) sized, in contrast to the dishes in the EVN and the LBA. Hence the quick switching between multiple targets in the case of the VLBA is not as time costly as compared to the LBA and the EVN.

2.4.3.2 Improving phase calibrator model

Other than using imaging as a tool to obtain the position and flux density of the target, it has also been used to get the best possible model of the phase calibrator by iteratively self calibrating the image. This will help improve the antenna-specific delay and phase solutions by using a more accurate model of the calibrator source. In this thesis, I have used a technique called 'hybrid mapping'. The phase calibrator, after initial calibration and global fringe fitting, is split off from the main dataset. This global fringe fitting is done by assuming that the phase calibrator is a point source, which in the case of VLBI observations is not always true. Thus, using a model informed by what the phase calibrator actually looks like in our observations, will give better fringe fitting solutions. Thus, the split dataset is imaged and the clean components from the image are compared with the visibility data to determine the corrections needed to best match the measured visibilities to the model. This new model is then used to image the dataset again and with an decreased integration time to solve for short term phase variations. This process is repeated until a best model for the phase

calibrator is achieved. This process is carried until the difference between the subsequent models becomes minimal and thus the best possible model of the phase calibrator is obtained. This best model is then used to run fringe fitting again on the phase calibrator and the solutions thus derived and interpolated to the target.

One of the aims of this thesis is to measure the motion of the radio sources in the plane of the sky, which involves measuring their positions at multiple epochs. The same phase calibrator has been used for multiple observations of the same target. The phase calibrators used in this work did not show intrinsic structural changes between epochs, although the differing uv-coverage between epochs could have introduced variation between the clean component models used for calibration. To minimise the differences arising in the positions of the targets because of slight changes in the phase calibrator model used, we stacked the phase calibrator data in all the available epochs and then found the best model for this stacked phase calibrator data using the same procedure as discussed in the above paragraph. We then used this model for the fringe fitting in all epochs.

2.4.3.3 Tropospheric and Ionospheric errors

Astrometric observations with VLBI have to be carefully scheduled with correct choice of phase calibrators. The astrometric accuracy is limited by the ionosphere, troposphere and by the target-calibrator separation. The astrometric accuracy due to the different tropospheric conditions scales with the target-calibrator separation (see Figure 2.8; Pradel et al., 2006). The systematics due to the ionosphere are estimated to be directly proportional to the target-calibrator throw and inversely proportional to the square of the observing frequency (Reid et al., 2017). In order to test the extent of the systematic errors being introduced in the astrometry of a target, a bright nearby extragalactic compact radio source is usually observed along with the target and is called the check source. All the calibration that is applied to the target is also applied to this check source, and this check

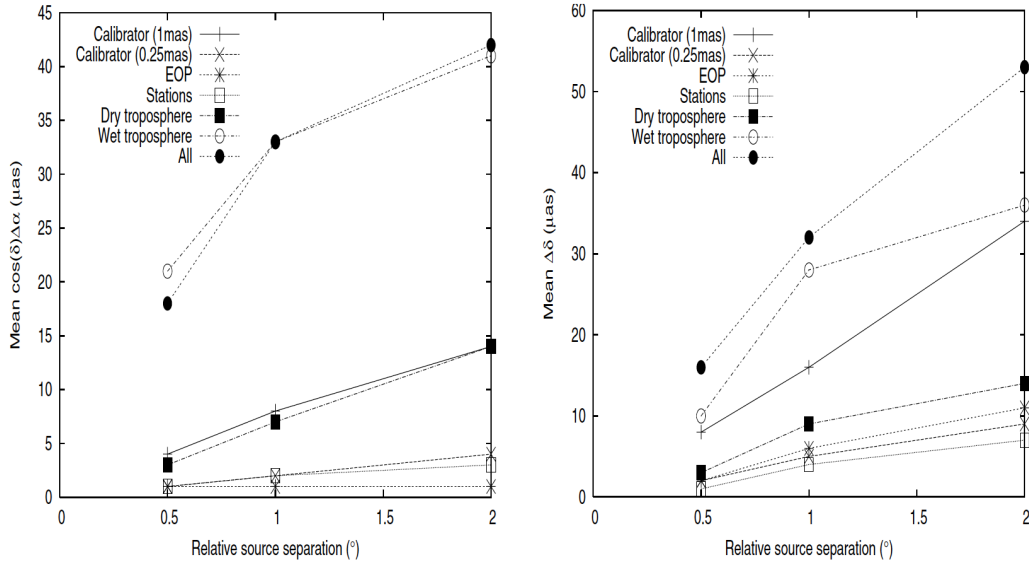


Figure 2.8: Variation of astrometric accuracy in Right Ascension and Declination as a function of target-calibrator separation. *Image credits: Pradel et al., 2006.*

source should not be moving with respect to the International Celestial Reference Frame. Any deviation from the fixed position assumption of this check source points towards systematic errors that have affected the data.

2.5 Velocities of BHXBs

The aim of this thesis is to estimate the natal kick velocities of BHXBs by measuring their peculiar velocities. Peculiar velocity represents the current motion of an object through its local standard of rest and is measured by determining the three dimensional velocity of the system, along with the position and the distance of the source. The net velocity of a system has two components - the total proper motion and the systemic radial velocity. Combining the proper motion, systemic velocity, the distance to the source, and the location of the system in the Galaxy, the magnitude and direction of its motion is known. As the main goal of this thesis is to understand the motion and hence birth mechanisms of BHs (discussed in Chapter 1), we need to know their proper motions and distances.

2.5.1 Systemic radial velocity

The systemic radial velocity of BHXB is measured by studying the optical/near-infrared spectra of the donor star. These measurements can be performed if the system is bright enough for optical (or infrared) telescopes and also when the emission from the donor star is strong enough that we are able to detect the absorption lines from the stellar atmosphere. The velocity of lines in the absorption spectra of a donor star is traced. Doppler red-shifting and blue-shifting gives the velocity of the absorption line a sinusoidal motion, which gives the projected magnitude of the orbital motion of the BHXB. The mean value of the velocity shift gives the line-of-sight (or systemic radial) velocity of the BHXB system. Systemic radial velocities are being measured routinely by a couple of collaborating teams and their measurements have been used to infer the full three dimensional velocities of our systems.

2.5.2 BHXB astrometry

To measure the typical proper motions of BHXBs (a few mas yr^{-1}) and their parallaxes, high-precision astrometry is required. This high precision astrometry can be conducted by optical satellites like *Gaia* or using radio interferometry, specifically VLBI.

2.5.2.1 Gaia-DR2

Gaia is a satellite that was launched in 2013 by the European Space Agency and has been surveying the optical sky since then (Gaia Collaboration et al., 2016). The second data release of *Gaia* was published in April, 2018 and it reports the astrometric parameters of around a billion stars, thus enabling high precision parallax measurements of bright stars (Gaia Collaboration et al., 2018b). The data is accessible on their online archive⁷ and using just the position or name of the target, proper motions and in some cases the parallax of the targets of interest

⁷<https://gea.esac.esa.int/archive/>

can be obtained. In quiescence, where BHXBs spend most of their time, most systems are too faint for detection by *Gaia* and its astrometric capabilities drop drastically as the target of interest reaches the instrument’s magnitude limit (20th magnitude in G band). *Gaia* is a satellite that continuously maps out sections of the sky, and so the chances of a BHXB in a particular location in the sky undergoing an outburst when the satellite is scanning that portion of the sky are low. Some BHXBs, even in a heightened state of radio and X-ray emission are still too faint for precision astrometry by *Gaia*. This leaves VLBI as the only reliable way to conduct astrometry of some BHXBs and thus triggered VLBI astrometric campaigns are crucial.

2.5.2.2 Using VLBI

Radio VLBI is also capable of measuring the proper motions and parallaxes of BHXBs and there are a few systems for which this has already been done (e.g., Miller-Jones et al., 2009a; Dhawan et al., 2007; Reid et al., 2011). High precision astrometry also becomes highly challenging for extremely faint sources even with VLBI. Astrometric studies of BHXBs must therefore be performed during outbursts, when both optical and radio emission coming from the system are enhanced. During an outburst, BHXBs go through a hard X-ray spectral state in both the rising and decaying phases of the outburst. Canonically, this hard spectral state is associated with radio emission that is dominated by partially self-absorbed emission from compact jets, which are causally connected to the BH. This emission is known to reach levels of a few mJy for a source at a typical BHXB distance of a few kpc. This brightness is sufficient for astrometric VLBI observations. The hard-state radio emission is centred a little downstream in the radio jet of the binary system. Reid et al. (2011) demonstrated that even for the brightest compact jets, any scatter along the jet axis does not hinder high-precision astrometry and could successfully measure the proper motion and parallax of Cyg X-1 (see Figure 2.9).

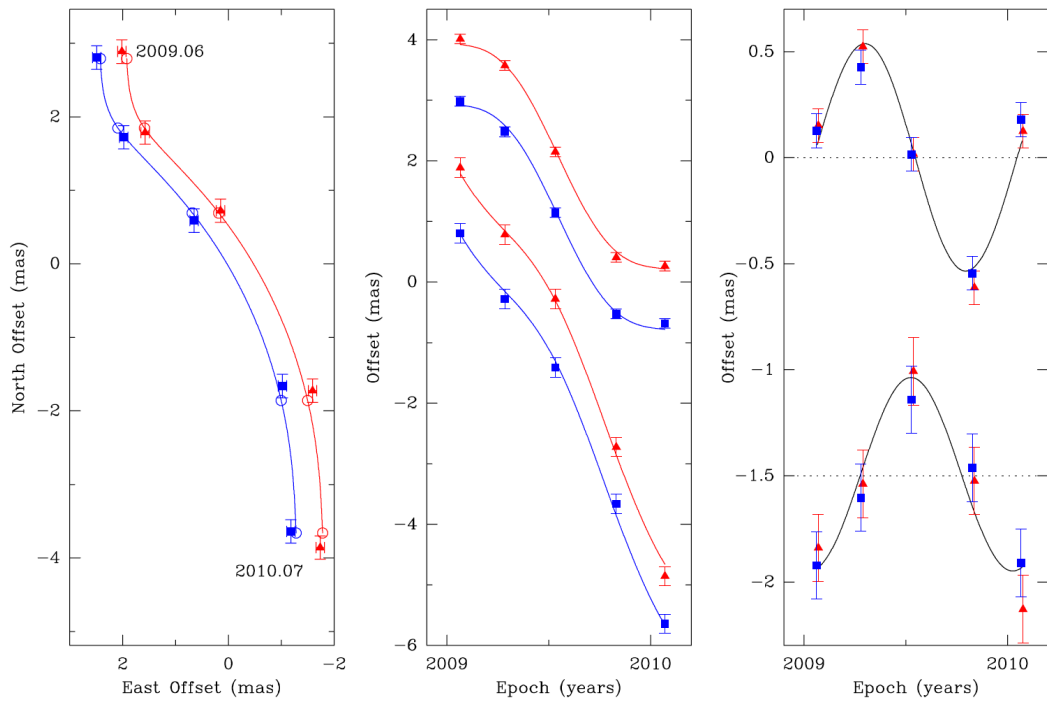


Figure 2.9: Proper motion and parallax of Cyg X-1 using VLBA and two phase calibrators. The change in position of the target when phase referenced to the two calibrators is depicted in two colours. Left panel: Positions on the sky of Cyg X-1 denoted by the square markers and circles indicate the expected position based on the proper motion and parallax fits. Middle panel: The east (top two lines) and north (bottom two lines) position offsets as a function of time. Right panel: Offsets in the north and east positions after removing the best fit proper motions. *Image Credits: Reid et al., 2011.*

The outburst recurrence timescales of BHXBs vary from 1–2 years to several decades. While at least 2 (and preferably 3) observations are required to determine a proper motion, the rising and decaying hard states during BH outbursts are typically separated by several months, giving a sufficiently long time baseline to measure a proper motion. Alternatively, for recurrent systems we can increase the time baseline by triggering on multiple outbursts. In this thesis I have measured the proper motions of four BHXBs using VLBI arrays from around the world. I led astrometric campaigns for three years with the VLBA, the EVN and the LBA. Whenever a source went into outburst and if it was in the southern hemisphere, we would observe the source using ATCA. We would trigger our LBA program if the target was brighter than our proposed triggering threshold ($>0.3 \text{ mJy beam}^{-1}$) in the ATCA observations. A similar protocol was followed to observe using the VLBA and the EVN, with the difference being that ATCA may not have been able to observe all northern hemisphere sources and so we relied on flux density measurements by the Very Large Array or the Arcminute Microkelvin Imager.

2.5.3 Distances

Distances to BHXBs are often estimated by studying the optical/infrared spectra of the donor star (Jonker & Nelemans, 2004). The proper motions of the receding and approaching jets can also be used to place an upper limit on the distance of the BHXBs (Mirabel & Rodríguez, 1994). Lower limits on the distance can be estimated by measuring either the interstellar extinction (Zdziarski et al., 1998, 2004) or the velocities of H I absorption (e.g. Chauhan et al., 2019) towards the source. X-ray dust scattering haloes have also been used to constrain the distance to some BHXBs (e.g. Xiang et al., 2011). However, these methods are all model-dependent, involving certain assumptions. The only model-independent method of distance determination is measuring a high significance trigonometric parallax. If the parallax is measured in mas, the distance is given by $(1/\text{parallax}) \text{ kpc}$.

However, given their typical distances (several kpc), such high-precision observations can only be carried out using Very Long Baseline Interferometry (VLBI) or by satellites like *Gaia* (Gaia Collaboration et al., 2018a). *Gaia*'s ability to conduct high precision astrometry of BHXBs in the Galactic plane can be limited due to high extinction and low optical brightness outside of outburst. *Gaia* also has a global zeropoint offset in its parallax measurements, the magnitude of which is still under debate (Chan & Bovy, 2020). Therefore, targeted VLBI astrometry campaigns on outbursting BHXBs remain crucial. Of the ~ 60 BHXB candidates (Tetarenko et al., 2016b), only V404 Cyg (Miller-Jones et al., 2009a), Cyg X-1 (Reid et al., 2011; Gaia Collaboration et al., 2018a) and GRS 1915+105 (Reid et al., 2014) have a directly measured parallax at $>5\sigma$ significance.

2.5.4 Measuring proper motion and parallax

The proper motion and parallax of the target manifest themselves as the change in position of the target with every epoch (see Figure 2.9 as an example). The position of the target at any given time can be predicted with the help of proper motions, positions and parallax of the target and is given by (Loinard et al., 2007)

$$\begin{aligned}\alpha(t) &= \alpha_0 + (\mu_\alpha \cos \delta) t + \pi f_\alpha(t) \\ \delta(t) &= \delta_0 + \mu_\delta t + \pi f_\delta(t)\end{aligned}\tag{2.9}$$

where $\alpha(t)$ and $\delta(t)$ are the Right Ascension (RA) and Declination (Dec) components of the position of the target at time t , α_0 and δ_0 are the RA and Dec components at a reference epoch, μ_α and μ_δ are the proper motions in RA and Dec, π is the parallax of the target, and f_α and f_δ are the projections of the parallax ellipse in RA and Dec, respectively. f_α and f_δ are in turn given by-

$$\begin{aligned}f_\alpha(t) &= (X \sin \alpha_1 - Y \cos \alpha_1) / (15 \cos \delta_1) \\ f_\delta(t) &= X \cos \alpha_1 \sin \delta_1 + Y \sin \alpha_1 \sin \delta_1 - Z \cos \delta_1\end{aligned}\tag{2.10}$$

where X , Y , Z are the barycentric coordinates of the Earth relative to the solar system barycentre, $\alpha_1 = \alpha - \pi f_\alpha(t)$ and $\delta_1 = \delta - \pi f_\delta(t)$.

We obtained the barycentric coordinates of the Earth from the JPL Horizons webpage⁸. The above set of equations can be solved analytically by using Singular Value Decomposition. They can also be solved by taking a Bayesian approach and fitting the multiple parameters at the same time using Monte Carlo simulations (see §2.6).

2.5.5 Galactic motion and U, V, W velocities

The structure of our Galaxy is like a thick disc with a bulge towards the centre, and the midplane of the disc is called the Galactic plane. The Galactic plane has a high stellar density, and is responsible for the birth of most binaries in our Galaxy. The stars in our Galaxy go around the centre of the Galaxy in almost circular orbits with an average orbital velocity of ~ 220 (e.g., Kerr & Lynden-Bell, 1986; Karachentsev & Makarov, 1996). The study of the motion of various objects in our Galaxy is called Galactic dynamics and a velocity coordinate system (U, V, W) is defined centred on the sun to study Galactic dynamics. Taking the sun as the origin, U points in the direction of the Galactic centre, V points in the direction of the Galactic rotation and W points in the direction of the North Galactic pole. We are measuring the proper motions of BHXBs in the (RA, Dec) coordinate system and one can transform the (RA, Dec) proper motion values and systemic radial velocity measurements to velocities in U, V, W as given in Johnson & Soderblom (1987)

$$\begin{bmatrix} U \\ V \\ W \end{bmatrix} = \mathbf{B} \cdot \begin{bmatrix} \rho \\ k\mu_\alpha/\pi \\ k\mu_\delta/\pi \end{bmatrix} \quad (2.11)$$

⁸<https://ssd.jpl.nasa.gov/?horizons>

where ρ is the systemic radial velocity, μ_α is proper motion in RA, μ_δ is proper motion in Dec, π is the parallax to the system, $k=4.74057$ and B is the transformation matrix (details can be found in Johnson & Soderblom, 1987). These U , V , W components of the velocity of a BHXB can be used to measure the peculiar velocity given by

$$V_p^2 = (U - U_c)^2 + (V - V_c)^2 + (W - W_c)^2 \quad (2.12)$$

where V_p is the peculiar velocity of the system, and (U_c, V_c, W_c) are U , V , W velocity components of the local standard of rest.

The peculiar velocity of the system can be used to integrate the motion of the BHXB back in time to the time of birth of the BH in the system (e.g., Mirabel et al., 2001; Miller-Jones et al., 2009b). This requires a good model of the Galactic potential, so that the orbit of the BHXB can be traced through the Galaxy as a function of time. A simple and accurate Milky Way gravitational potential model was derived by fitting a variety of Milky Way data and has been incorporated in a python package for Galactic dynamics called *galpy*⁹ (Bovy, 2015). This thesis uses this potential, named MWPotential2014, to integrate the orbit of the BHXB as it moves in the Galaxy and to trace its Galactocentric orbit using *galpy*.

2.6 Bayesian Inference

Bayesian inference is a statistical framework to determine the probability distribution of a parameter based on observed data and a prior distribution model of the parameter space. This approach is in contrast to the frequentist approach, where the estimations about a parameter are tested based only on the data and is dependent on the number of times the experiment is carried out. In this thesis, we have used the technique of Bayesian inference to fit models to data using prior information on the parameters being fit, and we prefer it above the frequentist

⁹<https://docs.galpy.org/en/v1.6.0/>

approach for the following two reasons:

1. Uncertainties or probabilities in a frequentist inference are properties of the procedure and not the results or the data, while in the Bayesian inference probabilities or uncertainties are associated with the data.
2. Bayesian inference techniques allows the use of prior knowledge available about the parameter being inferred, in the form of probability distributions. For the purpose of this thesis, this gives it an edge over frequentist approach, which does not have provision for including priors.

Below, we briefly discuss the overarching concept of Bayesian Inference (Gelman & Rubin, 1992) and its use in this thesis.

2.6.1 Applications

The Bayesian inference technique is based on Bayes theorem (Bayes & Price, 1763), which can be used to determine the probability distribution of a parameter (θ) given an observed value or data (D) when some prior information about the behaviour of the prior is known.

$$P(\theta|D) = \frac{1}{P(D)} P(D|\theta) P(\theta) \quad (2.13)$$

where $P(\theta|D)$ is called the parameter posterior distribution, $P(D|\theta)$ is called the likelihood, $P(\theta)$ is called the prior and $P(D)$ is the data probability and is the normalisation factor in most cases. Likelihood, or $P(D|\theta)$ above, is the density function in the form of a conditional probability of obtaining data D given the hypothesis θ is true. Likelihood is the link between the data and the hypothesis. A prior, or $P(\theta)$, encapsulates any known information about the parameter. A prior can take various forms ranging from complicated models to uniform distributions. We have specified the priors in the following chapters wherever they have been used. Finally, the posterior probability distribution, or $P(\theta|D)$, is a probability

distribution that summarises all that we can infer about our data after taking the information of the prior in consideration. Bayesian inference is thus an effective tool to update the prior known distribution of the inferred parameter when more data becomes available.

Bayesian inference has been used in Chapter 3 and 5 primarily for two tasks - to estimate the distance probability distribution of a BHXB from its measured parallax and for fitting for proper motion and parallax, given measured positions of the source. Other than obtaining posterior distributions of parameters by fitting them to models, this thesis also uses Bayesian inference to fit a probability distribution to a sample of distributions (see Chapter 4). This technique is called Bayesian Hierarchical modelling, wherein an initial prior that is chosen is updated through modelling. A specific application of Bayesian Hierarchical modelling as laid out by Mandel (2010) enables a test to determine the relative probability of the consistency of a chosen population distribution with the observed data. This technique assumes that although the posterior probability distributions of the individual measurements were obtained independently, the parameters that describe these distributions can share a common distribution.

2.6.2 Computational method: HMC and NUTS

Bayesian inference for a single parameter (θ) is a simple task of estimating the posterior probability distribution ($P(\theta|D)$) as a function of the parameter (θ). Once the number of parameters included in the prior model and the likelihood function increases, it becomes more complicated to derive the posterior probability distribution and the Bayesian analysis depends on methods like Markov Chain Monte Carlo (MCMC) for efficient sampling the posterior's parameter space. Hamiltonian Monte Carlo (HMC; Neal, 2012; Betancourt, 2019) is a type of MCMC that is a computational tool to determine the most likely value to define a distribution. In this technique, the system is defined via a hamiltonian as a function of position and velocity, and the least energy point of this hamiltonian

is derived by sampling the complete parameter space defined by it. A popular analogy is of a friction-less bowl with a ball. This ball when pushed randomly in any direction will move across the surface of the bowl for a long time. If this act is repeated multiple times, the whole surface of the bowl can be traced and the least energy location can be pointed out. We used HMC because it can be significantly more efficient at sampling continuous parameter spaces with rather high number of dimensions, compared to many other methods. Also, the converged values using HMC are mostly in the highest probability region of the posterior probability distribution and the chain can travel to a larger sampling area thus covering a more possible values, while also being faster.

In this thesis, we have used a No-U-Turn sampler (NUTS; Hoffman & Gelman, 2011) to decide the number of steps and the length of those steps for the Monte Carlo chains. Taking the analogy of the bowl again, once the ball is given some initial energy in a random direction it can in principle move forever. The number of steps and how long those steps are decide how long one chain goes on for. Using few or too many steps both have the issue of giving rise to sampling one area more. Hence, the NUTS uses an algorithm that lets the chain path continue for as long as it turns around. If the path turns around it is possible that it will sample the same steps again and this inefficiency can be avoided by stopping the chain once it turns around. The NUTS does this by extending the path in both directions to make sure both directions are sampled at the same time and that is a more time efficient way.

The code written to estimate the potential kick velocity distribution using Bayesian inference, HMC and NUTS is available at the github link <https://github.com/pikkyatri/BHnataalkicks>.

Parallax of MAXI J1820+070 : a case study

Adapted from:

P. Atri, J. C. A. Miller-Jones, A. Bahramian, R. M. Plotkin, A. T. Deller, P. G. Jonker, T. J. Maccarone, G. R. Sivakoff, R. Soria, D. Altamirano, T. Belloni, R. Fender, E. Koerding, D. Maitra, S. Markoff, S. Migliari, D. Russell, T. Russell, C. L. Sarazin, A. J. Tetarenko, and V. Tudose (2020), ‘A radio parallax to the black hole X-ray binary MAXI J1820+070’ *Monthly Notices of the Royal Astronomical Society*, Letters, Volume 493, Issue 1, p.L81-L86,

DOI: 10.1093/mnrasl/slaa010

In this chapter, we present a precise measurement of the radio parallax and proper motion of a black hole X-ray binary, MAXI J1820+070. We have used the technique of Very Long Baseline Interferometry and utilised the Very Long Baseline Array and the European Very Long Baseline Interferometry Network to observe the source for nine epochs. We have used the parallax to provide a model-independent distance to the source using Bayesian inference. Using this distance we are able to determine the fraction of the Eddington luminosity reached by the source reached at the peak of its 2018 outburst. Further, we also report refined estimates of the jet inclination angle, jet velocity and the mass of the black hole.

3.1 Importance of measuring distances

The distances to astronomical systems are essential quantities that allow us to draw a connection between observed and physical parameters (e.g., flux and luminosity, angular and physical speeds). In particular, for black hole X-ray binaries (BHXBs) the relation between different accretion phases and Eddington luminosity fractions can then be studied (Maccarone, 2003), and the systems can be accurately placed on the X-ray/radio luminosity plane (Gallo et al., 2018) to probe jet/accretion coupling. Peak luminosities of BHXBs during outburst can also be a window into the low-luminosity end of ultra-luminous X-ray sources. With accurate distances, we can break the degeneracy between the inclination angles of radio jets and their speeds (Fender et al., 2003). A well constrained inclination angle can also help in obtaining accurate mass estimates of the black hole (BH) from the mass function of the system (Cantrell et al., 2010). An accurate distance helps in obtaining a well constrained three dimensional space velocity and hence the potential kick velocity (PKV) distribution of the system (Atri et al., 2019), providing clues as to the BH formation mechanism (Nelemans et al., 1999).

3.2 MAXI J1820+070

MAXI J1820+070 (ASASSN-18ey, hereafter MAXI 1820), a BHXB, was first discovered when it went into an outburst in March 2018 (MJD 58188). The source was discovered when it was detected as a bright X-ray transient by the Monitor of All-sky X-ray Image (MAXI) instrument on board the International Space Station (Kawamuro et al., 2018) and as a bright optical source by the All-Sky Automated Survey for SuperNovae (ASAS-SN; Tucker et al., 2018), reportedly a week before the MAXI detection. Archival photographic plates show two past outbursts of MAXI 1820 in 1898 and 1934 (Grindlay et al., 2012), suggesting an outburst recurrence timescale of ~ 40 years for this source (Kojiguchi et al., 2019). In its

March 2018 outburst, the transient made a complete hard (until MJD 58303.5) to soft (MJD 58310.7–58380.0) to hard state (from MJD 58393.0) outburst cycle (Shidatsu et al., 2019). Radio observations during and after the transition from hard to soft state revealed an apparently superluminal approaching jet (Bright et al., 2020).

The source almost faded to quiescence in February 2018 (Russell et al., 2019), enabling optical spectroscopic studies (Torres et al., 2019) to dynamically confirm the presence of a BH in the system. These spectroscopic studies led to the determination of the systemic radial velocity and the orbital period of the system as

$$\begin{aligned}\gamma &= -21.6 \pm 2.3 \text{ km s}^{-1} \\ P_{orb} &= 0.68549 \pm 0.00001 \text{ d}\end{aligned}\tag{3.1}$$

MAXIJ1820 subsequently showed two reflares beginning on MJD 58552 and MJD 58691. Both the reflares (see Figure 3.1) lasted a couple of months each (Ulowetz et al., 2019; Zampieri et al., 2019). *Gaia* measured a proper motion of the system based on optical astrometry of $\mu_\alpha \cos \delta = -3.14 \pm 0.19 \text{ mas yr}^{-1}$ and $\mu_\delta = -5.9 \pm 0.22 \text{ mas yr}^{-1}$. *Gaia* also reported a parallax for the system, but the measurement was only of 3σ significance. The distance inferred from the *Gaia* parallax depended heavily on the priors used to invert the parallax (2.1–7.2 kpc; Gandhi et al., 2019). Thus, to obtain a more accurate parallax of MAXIJ1820 we carried out a targeted VLBI campaign while the source was in the hard X-ray spectral state, emitting steady compact radio jets. As the source went into multiple reflares, there were opportunities to observe the source in this desired state multiple times.

3.3 Observations and Data reduction

We monitored MAXIJ1820 (see Table 3.2) with the Very Long Baseline Array (VLBA), using both the Jet Acceleration and Collimation Probe of Transient

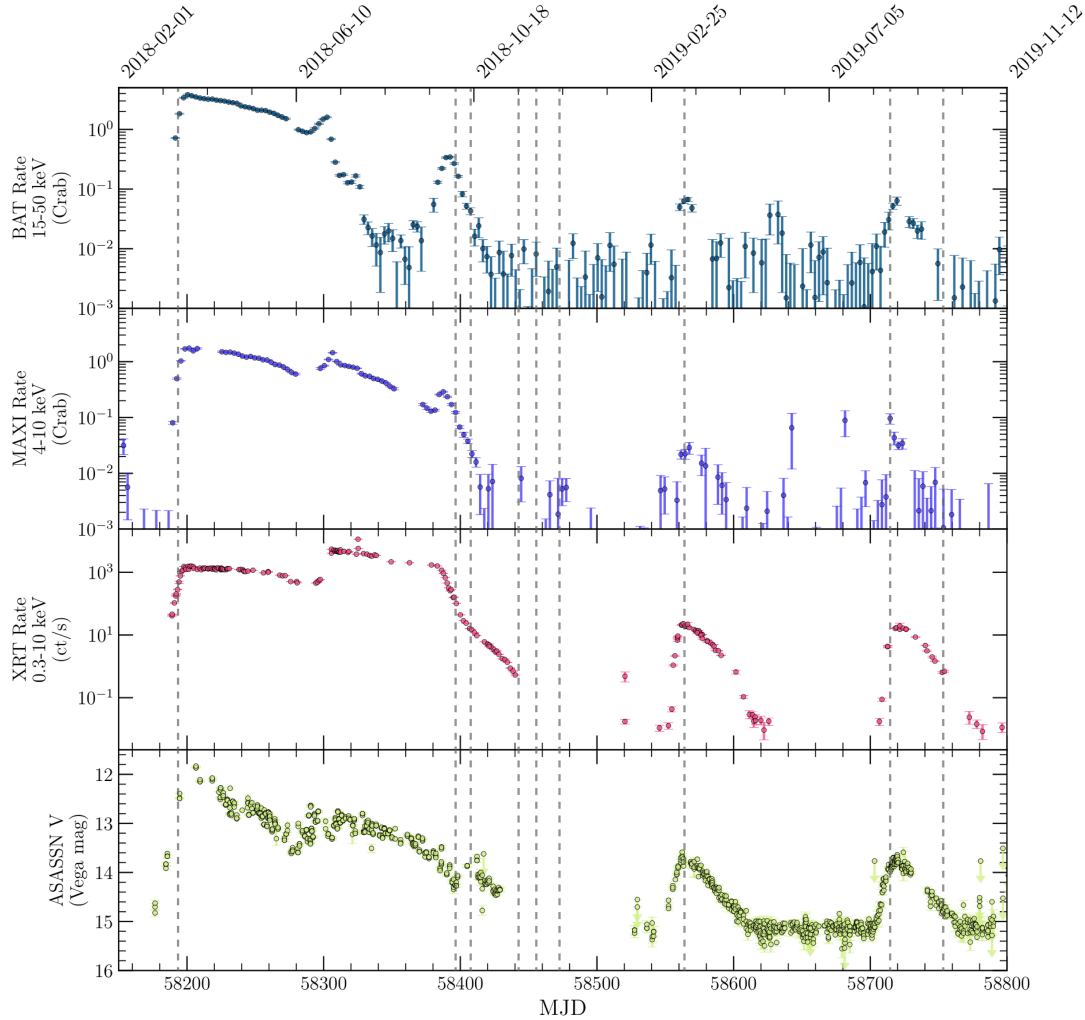


Figure 3.1: The X-ray and optical lightcurves of MAXI J1820. The range of the x-axis covers the duration of the main outburst (the one in which the target was first discovered) and the two reflares of the source. The bottom x-axis represent the dates in MJD and the top axis in yyyy/mm/dd. The top panel is the light curve from the Swifts Burst Area Telescope (BAT) light curve, the second panel from the top is the MAXI lightcurve, the third panel from the top is the lightcurve from the Swift X-ray Telescope (XRT) and the bottom panel is the ASAS-SN light curve. All the data in this figure are publicly available. The vertical dashed lines denote the epochs at which we observed at source using the VLBA and the EVN. *Image credits: Arash Bahramian.*

X-ray Binaries (JACPOT-XRB) program (e.g., Miller-Jones et al., 2012, 2019, proposal code BM467), and a long-running astrometry program (proposal code BA130), supplemented with a targeted European VLBI Network (EVN) campaign (proposal code EA062). All observations used a combination of J1821+0549 (J1821 hereon) and J1813+065 (J1813 hereon) as the phase reference and astrometric check sources. A bright extragalactic radio source that is close to the target and the phase calibrator is usually chosen to be a check source. The phase solutions that are applied to the target are also applied to the check source. Since the check source is an extragalactic source it should not show any motion between various epochs, and any measured motion can be attributed to systematics affecting the data. Both J1821 and J1813 are strong extragalactic radio sources and so can be used as either the phase calibrator or the check source.

The calibrator positions were taken from the Radio Fundamental catalogue (rfc2015a¹). Our assumed positions (J2000) were RA = 18^h21^m27^s.305837, Dec = 05°49′10″.65156 for J1821, and RA = 18^h13^m33^s.411619, Dec = 06°15′42″.03366 for MAXI J1813 (see Figure 3.2). The data were correlated using DiFX (Deller et al., 2011) and standard calibration steps were followed using the Astronomical Image Processing System (AIPS 31DEC17; Greisen, 2003). We imaged the calibrated data and determined the target position by fitting a point source in the image plane for every epoch.

3.3.1 VLBA campaigns

In the hard state at the start and end of an outburst, the radio jets are compact and ideal for astrometry. We took four epochs of observations in March (MJD 58193), October (MJD 58397), November (MJD 58441) and December 2018 (MJD 58474) via the JACPOT-XRB program. The first three epochs (proposal codes BM467A, BM467O and BM467R) were observed at 15 GHz. These observations used J1813 (1.93° away from MAXI J1820) as the phase calibrator (being brighter

¹http://astrogeo.org/vlbi/solutions/rfc_2015a/rfc_2015a_cat.html

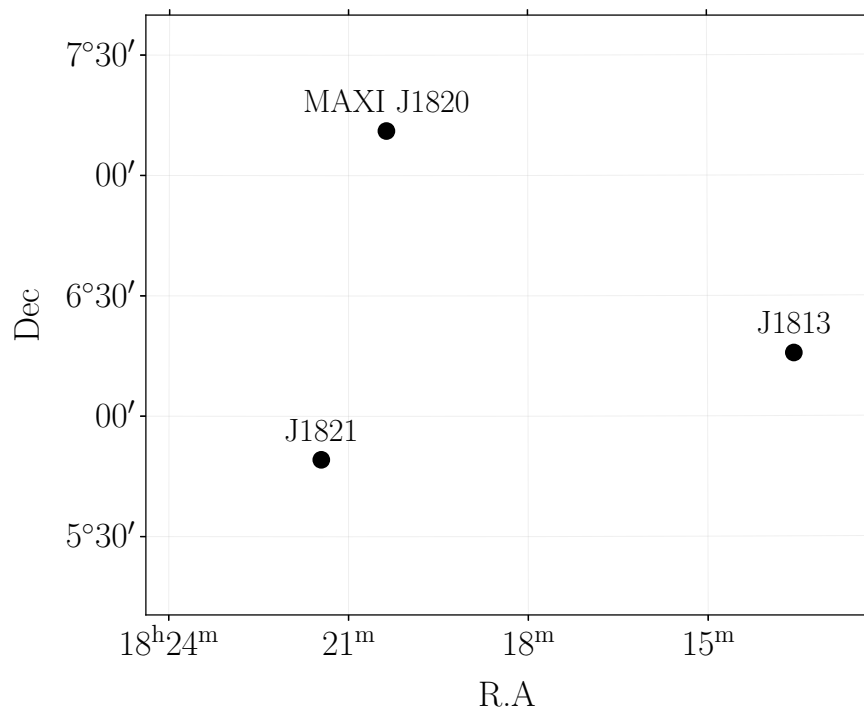


Figure 3.2: The positions of MAXI J1820, J1821 and J1813 in the plane of the sky. The separation between MAXI J1820 and J1813 is 1.7° and 0.92° in R.A and Dec, respectively. The separation between MAXI J1820 and J1821 is 0.27° and 1.37° in R.A and Dec, respectively. *Image credits: Arash Bahramian.*

Table 3.1: Summary of the observations of MAXI J1820+070. The observing bandwidth was 32 MHz for both the VLBA and the EVN. JB - Jodrell Bank; WB - Westerbork; EF - Effelsberg; MC - Medicina; NT - Noto; O8 - Onsala; T6 - Tianna65; TR - Torun; HH - Hartebeesthoek; YS - Yebes; IB - Irbene; CM - Cambridge; KN - Knockin; DE - Defford; PI - Pickmere.

Project Code	Date	Array	Frequency (GHz)	Stations
BM467A	March 16, 2018	VLBA	15	BR, HN, KP, LA, MK, NL, OV, PT, SC
BM467O	October 05, 2018	VLBA	15	BR, FD, HN, KP, LA, MK, NL, OV, PT, SC
EA062A	October 16, 2018	EVN	5	JB, WB, EF, MC, NT, O8, T6, TR, HH, YS, IB, CM, KN, DE
BM467R	November 19, 2018	VLBA	15	BR, FD, HN, KP, LA, MK, NL, OV, PT, SC
EA062B	December 04, 2018	EVN	5	JB, WB, EF, MC, NT, O8, TR, YS, HH, IB, CM, DA, DE, KN, PI
BM467S	December 22, 2018	VLBA	5	BR, FD, HN, KP, LA, MK, NL, OV, PT, SC
EA062C	March 03, 2019	EVN	5	JB, WB, EF, MC, NT, O8, T6, TR, YS, HH, IB, CM, DA, DE, KN, PI
BA130B	August 23, 2019	VLBA	5, 15	BR, FD, HN, KP, LA, MK, NL, OV, PT, SC
BA130C	September 29, 2019	VLBA	5, 15	BR, FD, HN, KP, LA, MK, NL, OV, PT, SC

Table 3.2: Measured positions and flux densities of MAXI J1820+070. The observing bandwidth was 32 MHz for both the VLBA and the EVN. We give the measured target positions for each epoch. When both J1813 and J1821 were observed as phase calibrators, we give target positions phase referenced to 1821. The error bars denote the statistical errors in the position measurement of the targets.

Project Code	MJD	Array	Phase Calibrator	Check source	RA (J2000) ($18^{\text{h}}20^{\text{m}}$)	Dec (J2000) ($07^{\circ}11'$)	Peak Intensity (mJy bm^{-1})
BM467A	58193.65	VLBA	J1813	J1821	$21^{\text{s}}.9386536(1)$	$07''.170025(4)$	31.6 ± 0.2
BM467O	58397.01	VLBA	J1813	J1821	$21^{\text{s}}.9384875(4)$	$07''.166302(10)$	5.84 ± 0.08
EA062A	58407.71	EVN	J1821	J1813	$21^{\text{s}}.9384883(33)$	$07''.166075(27)$	1.55 ± 0.05
BM467R	58441.73	VLBA	J1813	J1821	$21^{\text{s}}.9384770(9)$	$07''.165549(31)$	0.56 ± 0.03
EA062B	58457.04	EVN	J1821	J1813	$21^{\text{s}}.938437(16)$	$07''.16485(12)$	0.16 ± 0.03
BM467S	58474.86	VLBA	J1821, J1813	J1813, J1821	$21^{\text{s}}.938462(14)$	$07''.16498(41)$	0.13 ± 0.02
EA062C	58562.25	EVN	J1821	J1813	$21^{\text{s}}.9384324(12)$	$07''.163533(10)$	3.86 ± 0.05
BA130B	58718.06	VLBA	J1821, J1813	J1813, J1821	$21^{\text{s}}.9382958(8)$	$07''.160872(21)$	4.09 ± 0.05
	58718.14	VLBA	J1821, J1813	J1813, J1821	$21^{\text{s}}.9383011(3)$	$07''.160709(14)$	4.32 ± 0.12
BA130C	58755.04	VLBA	J1821, J1813	J1813, J1821	$21^{\text{s}}.9382761(28)$	$07''.159845(93)$	1.00 ± 0.05
	58755.12	VLBA	J1821, J1813	J1813, J1821	$21^{\text{s}}.9382730(22)$	$07''.160090(74)$	1.20 ± 0.12

than J1821 at 15 GHz), and cycled every ~ 2 min between it and the target, observing the check source J1821 (1.39° away from MAXI J1820) once every eight cycles. We observed geodetic blocks (Reid et al., 2009) for half an hour at the beginning and end of each observation to better model the troposphere. As the source faded in December 2018 (Proposal Code BM467S), we took the final epoch in the more sensitive 5 GHz band with the observing scheme J1821–J1813–MAXI J1820.

We also observed under the astrometry program BA130 during the August 2019 reflare. We cycled through J1813, J1821 and MAXI J1820 at 5 GHz for 1.5 hrs, and then at 15 GHz for 2.5 hrs, with geodetic blocks at the start and end of the observation. This cycling process lets us use any of the bright sources as phase calibrator or check source. We followed standard calibration techniques within AIPS (31DEC17). MAXI J1820 was phase referenced separately to J1821 and J1813.

3.3.2 Parallax campaign: EVN data

We were also approved to observe with the EVN at 5 GHz during the expected peaks of parallax offset in RA in the months of March and September, and in Dec in the months of June and December. The source was observed in October 2018, December 2018 and March 2019, but faded below the detection capability of the EVN before the scheduled June 2019 epoch. J1821 was chosen as the phase reference source due to its close proximity to MAXI J1820 and was observed every 4 minutes, with J1813 used as a check source. The data were reduced using AIPS (31DEC17). We used the bandpass, a-priori amplitude and parallactic angle corrections produced by the EVN pipeline, and corrected for ionospheric dispersive delays. We then performed phase, delay and rate calibration using standard procedures in AIPS and extrapolated the phase and delay solutions derived from J1821 to both J1813 and MAXI J1820.

3.3.3 Mitigating systematic biases

Since the observations were carried out at different frequencies and the target position was measured using different calibrators, we need to account for the systematic uncertainties associated with different frequencies and different reference frames. We thus fixed our frame of reference to be that defined by using J1821 as a phase calibrator at 5 GHz, and shifted the other measurements by the amount that was needed based on the combination of the observing frequency and the phase calibrator. The details of these corrections are in the following sections. Below we also discuss the steps taken to mitigate different atmospheric errors affecting the different observations and also the amount of shift that was needed because of calibration using different phase calibrators.

3.3.3.1 Atmospheric errors

To mitigate against systematic errors arising from low elevations, we removed all data below 20° in elevation. We also removed half an hour of data around the sunrise/sunset times at each station when the ionosphere could be changing rapidly. The AIPS task ‘UVFLG’ was used to flag the times when the data were suspected to be noisy. Data from the Mauna Kea dish were removed for the complete duration of BA130B due to very high dispersive delays that were calculated by the task TECOR. This was realised as the check source position (J1813) between the epochs BA130B and BA130C differed by 0.3 mas. Once the check source in BA130B was imaged without MK and the position measured, the check source positions in the two epochs coincided within error bars. To prevent source structure sampled with differing *uv*-coverage from affecting our astrometry, we made global models of the two phase reference sources by stacking all EVN data at 5 GHz, and all VLBA data at each of 5 and 15 GHz. These global models were used to derive our final phase and delay solutions for each epoch, which were then extrapolated to MAXI J1820 and the relevant check source.

The check source is observed in each epoch to test the quality of phase solu-

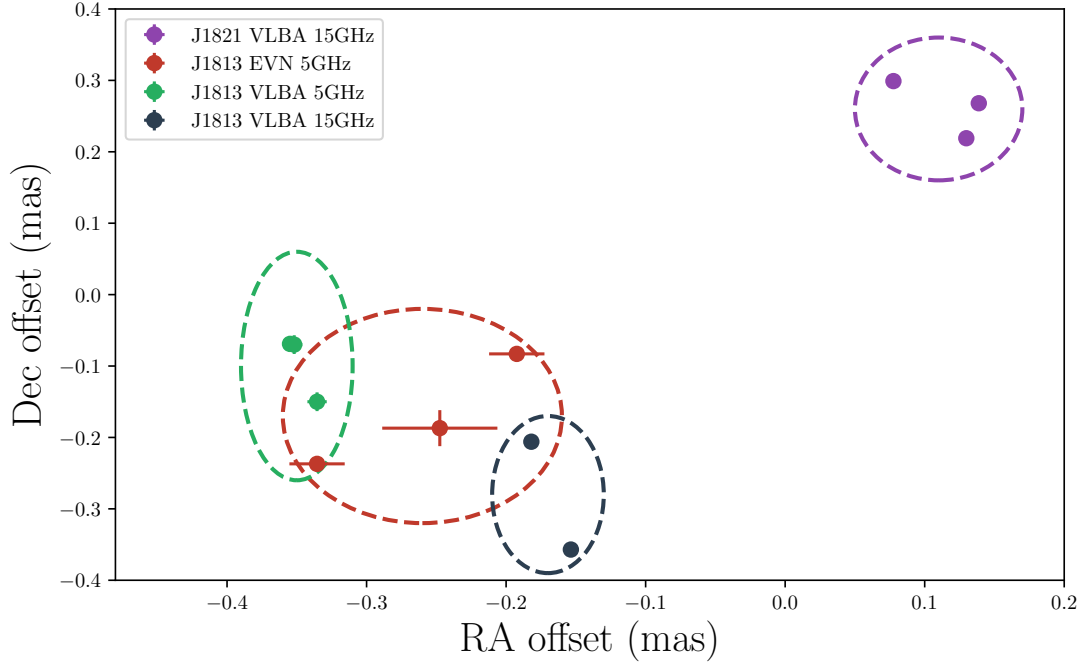


Figure 3.3: The measured offsets of the positions of the check source when phase referenced to the calibrator. If the position of J1813 is labelled, then it was phase referenced to J1821, and vice-versa. The dashed ellipses represent the expected systematic error region in RA and Dec by combining the expected tropospheric and ionospheric errors in quadrature (see Table 3.3), assuming the mean offset as the centre.

Table 3.3: This table represents the expected errors the troposphere and ionosphere can introduce in the measurement of the position of a target. Estimates have been determined using the relations in Pradel et al. (2006) and Reid et al. (2017) for the troposphere and ionospheric systematics, respectively.

Calibrator	Frequency (GHz)	Troposphere ($\sigma_{\text{sys,trop}}$)				Ionosphere ($\sigma_{\text{sys,ion}}$)	
		VLBA		EVN		RA	Dec
		RA (μas)	Dec (μas)	RA (μas)	Dec (μas)	RA (μas)	Dec (μas)
J1821	5	36	110	72	24	24	122
	15	36	110	72	24	3	14
J1813	5	56	102	96	55	152	82
	15	56	102	96	55	17	10

tions that are transferred to the target. The variation in the position of the check source between different epochs can be used to determine the systematic offsets caused by the ionosphere and troposphere. We could measure the offset of J1821 when phase referenced to J1813 and vice-versa for a few observations (BM467S, BA130B and BA130C) at 5 GHz, and at 15 GHz too for observations BA130B and BA130C. Since only J1813 was used as the check source in the JACPOT observations (BM467A, BM467O and BM467R), we measured the offset of J1813 when phase referenced to J1821 for these observations. We also measured the offset of J1821 when phase referenced to J1813 at 5 GHz for the observations with the EVN. The measured offsets can be seen in Figure 3.3. We checked these offsets against the model predictions for the errors introduced in the position of the target when phase calibrated to J1813 and J1821. To estimate the systematics arising from the troposphere ($\sigma_{\text{sys,trop}}$), we used the simulations of Pradel et al. (2006) for both the VLBA and EVN measurements, as appropriate for our target-phase calibrator angular separation and target declination (see Figure 3.2). $\sigma_{\text{sys,trop}}$ is dependent on calibrator-target separation, declination of the target and also the array (see table 3.3 for detailed values). To this, we added in quadrature a conservative estimate of the ionospheric systematics (Reid et al., 2017), taken as

$$\sigma_{\text{sys,ion}} = 50 \mu\text{as} \left(\frac{\nu}{6.7 \text{GHz}} \right)^{-2} \left(\frac{\theta}{1^\circ} \right), \quad (3.2)$$

where ν is the observing frequency and θ is the angular separation between target and phase reference calibrator. The rms of the positions of our check source (J1821 for BM467A, BM467O, BM467R and J1813 for the remaining data sets) was in all cases less than the conservative upper limits calculated from the combined effect of $\sigma_{\text{sys,trop}}$ and $\sigma_{\text{sys,ion}}$. This can be clearly seen in Figure 3.3, where the dashed ellipses have the dimensions of $\sqrt{\sigma_{\text{sys,trop}}^2 + \sigma_{\text{sys,ion}}^2}$ in RA and Dec and are centred on the measured mean of the check source position. We thus used the conservative upper limits as the systematic errors on the position measurement in order to make sure that the significance of our parallax detection was

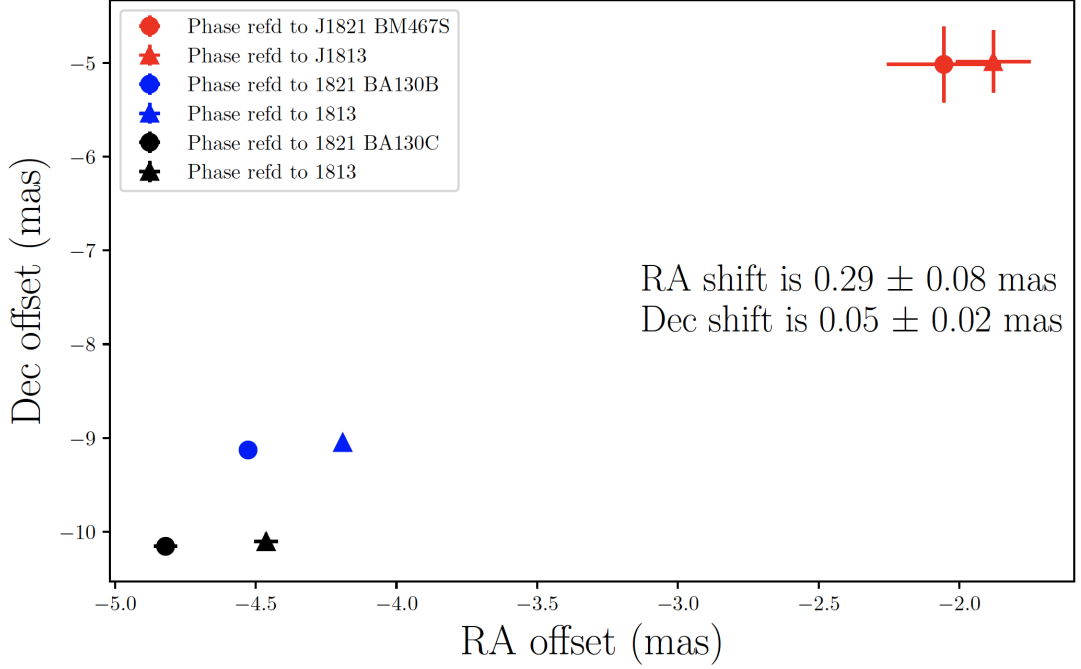


Figure 3.4: Offsets in the measured position of MAXIJ1820 due to phase referencing to different calibrators. Different colours signify different observing epochs. The triangle and circle marker denotes the position of MAXIJ1820 when it was phase referenced to J1813 and J1821, respectively.

not overestimated.

3.3.3.2 Reference frame shifts

The JACPOT-XRB program (see § 3.3.1) and the EVN parallax campaign (see § 3.3.2) observed different extragalactic sources as phase calibrators. Hence, we scheduled the BHXB astrometry program observations (BA130B and BA130C, see § 3.3.1) such that MAXIJ1820 could be independently phase referenced to both J1813 and J1821. We measured the shift in the position of MAXIJ1820 when it was phase referenced to J1813 as compared to when it was phase referenced to J1821 (see Figure 3.4) at a frequency of 5 GHz as we have defined J1821 at 5 GHz as our base reference frame. This was done with the three epochs for which the observing scheme allowed simultaneous phase referencing to J1813 and J1821 at 5 GHz, i.e, BM467S, BA130B and BA130C. We measured an average shift of $+0.29 \pm 0.08$ mas in RA and $+0.05 \pm 0.02$ mas in Dec in the position of

MAXIJ1820 when it was phase referenced to J1813 as compared to when it was phase referenced to J1821. To account for this astrometric frame shift, we shifted the target positions measured when phase referenced to J1813 by -0.29 ± 0.08 mas and -0.05 ± 0.02 mas in RA and Dec, respectively. The combination of two different observing campaigns with different goals was responsible for some of the epochs being observed at 15 GHz and others at 5 GHz. We fit for any potential change in the frame of reference due to different observing frequency in our parallax fitting code (see § 3.4.1).

3.4 Results and Analysis

3.4.1 A Bayesian approach for parallax fitting

To derive the proper motion $(\mu_\alpha \cos \delta, \mu_\delta)$, parallax (π) and reference position (α_0, δ_0) of MAXIJ1820, we fit the position as a function of time (e.g. Loinard et al., 2007), with a reference date equivalent to the midpoint of the observing campaign (MJD 58474). To perform the fit, we adopted a Bayesian approach, using the PYMC3 python package (Salvatier et al., 2016) to implement a Hamilton Markov Chain Monte Carlo (MCMC; Neal, 2012) technique with a No-U-Turn Sampler (NUTS; Hoffman & Gelman, 2011). The *Gaia*-DR2 proper motion and parallax measurements were used as priors in the procedure. We had observations at 5 and 15 GHz and so fit for any potential core shift in the calibrator peak emission from 5 GHz to 15 GHz (δ RA, δ Dec), and used a flat prior from -1 mas to 1 mas for both δ RA and δ Dec. We checked for convergence in our MCMC using the Gelman-Rubin diagnostic (Gelman & Rubin, 1992). The posterior distributions for all parameters are Gaussian, and the median and the 68 per cent confidence interval of each of the fitted parameters are given in Table 3.4. All error bars reported hereafter are at 68% confidence, unless otherwise stated. The corner plot representation of the results of the Bayesian fitting code that shows the best fit values and the correlations of the different parameters being fit for is shown

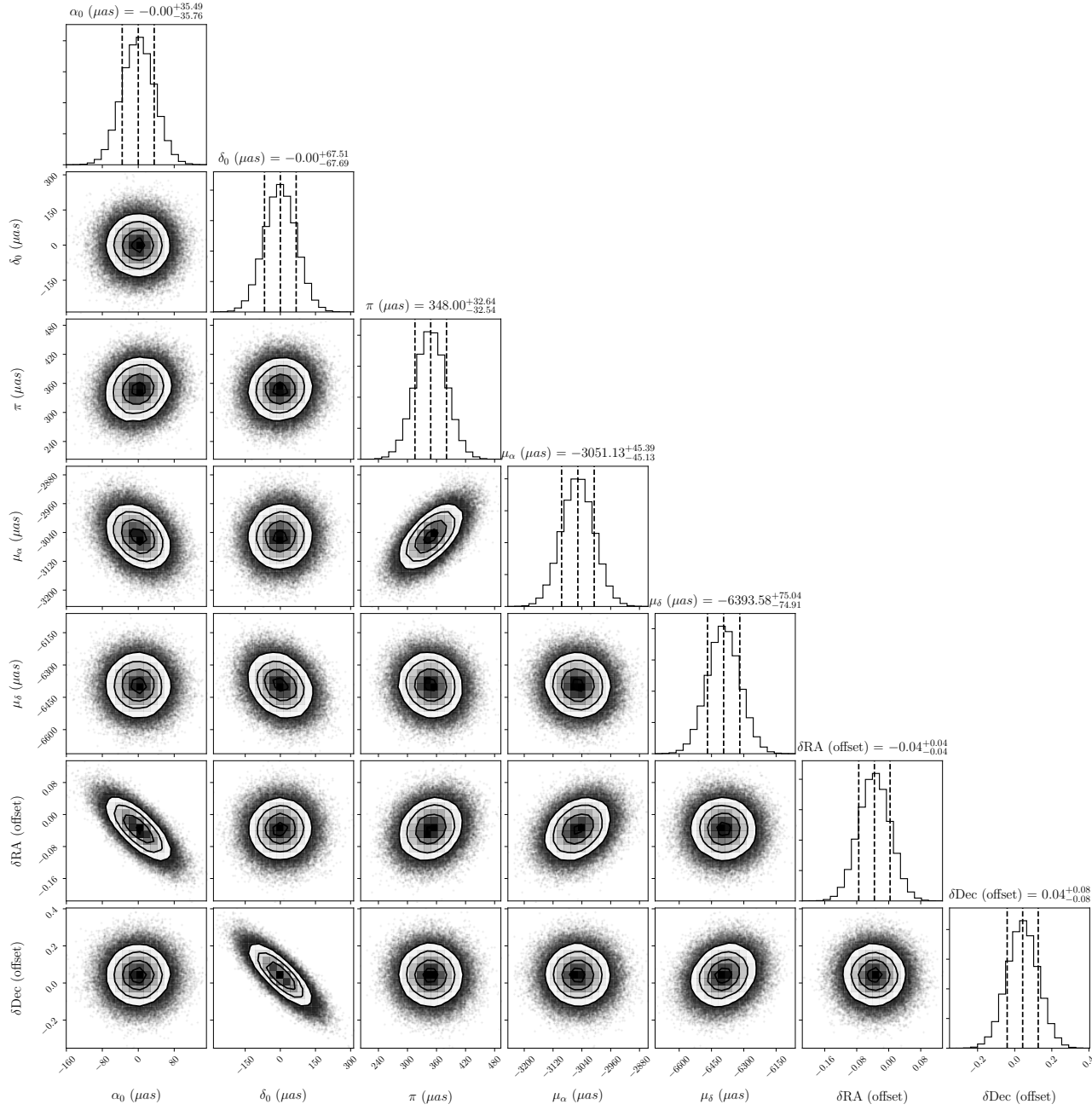


Figure 3.5: A cornerplot representing the posterior distributions of parameters fit for in our parallax estimation code. α_0 , δ_0 are the reference positions of MAXI J1820 in RA and Dec, respectively. $\delta\text{RA (offset)}$ and $\delta\text{Dec (offset)}$ represent the core offsets in the peak emissions of the phase calibrator when observed at 5 and 15 GHz. π represents the parallax. μ_α and μ_δ denote the proper motions in R.A and Dec. The dashed lines and the contours represent the 16th, 50th and 84th percentiles of the probability distributions. Correlations between $\delta\text{RA (offset)}$ and μ_α , and between $\delta\text{Dec (offset)}$ and δ_0 are seen in the respective 2D histograms.

Table 3.4: The results of the Bayesian fitting algorithm. α_0 , δ_0 are the reference positions of MAXI J1820 in RA and Dec, respectively. δ RA and δ Dec represent the core offsets in the peak emissions of the phase calibrator when observed at 5 and 15 GHz. π represents the parallax. μ_α and μ_δ denote the proper motions in R.A and Dec. Here we report the median and 68% confidence intervals from the posterior distributions of the fitted parameters.

Parameter	Value
RA ₀	18 ^h 20 ^m 21 ^s 9384568 ± 0.0000024
Dec ₀	07°11′07″1649624 ± 0.0000680
$\mu_\alpha \cos \delta$ (mas yr ⁻¹)	-3.051 ± 0.046
μ_δ (mas yr ⁻¹)	-6.394 ± 0.075
π (mas)	0.348 ± 0.033
δ RA (mas)	-0.04 ± 0.04
δ Dec (mas)	0.04 ± 0.08

in Figure 3.5. The resulting fits to the sky motion are shown in Figure 3.6.

3.4.2 Distance from parallax

Any parallax measurement that has large error bars could lead to an over or underestimated distance. Distances inferred by inverting low significance parallax measurements also suffer from Lutz-Kelker bias (Lutz & Kelker, 1973). Lutz-Kelker bias suggests that parallaxes tend to be overestimated leading to underestimated distances. This is because given a uniform stellar density, there is more volume in a shell at a larger radius and hence more stars in a larger shell. Thus there is more chance of a star being scattered into an inner shell due to uncertainty than of being scattered into an outer shell. This increases the possibility of the parallax being overestimated resulting in an underestimated distance. Thus the use of appropriate priors is essential to obtain meaningful distances (Bailer-Jones, 2015; Astraatmadja & Bailer-Jones, 2016).

3.4.2.1 Source density priors

In order to make sure that the errors from the measured quantity are appropriately propagated to the inferred quantity, we use a Bayesian inference approach

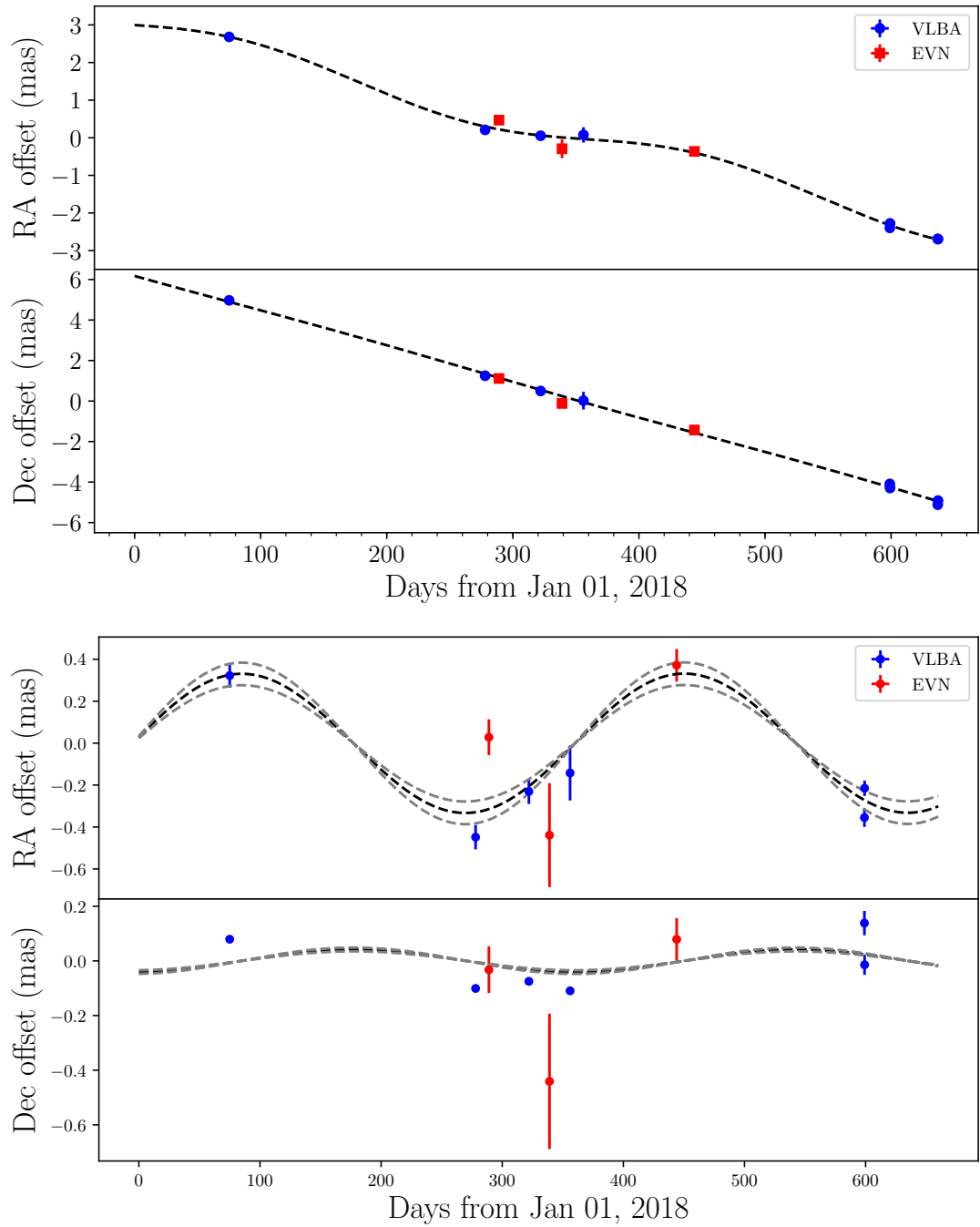


Figure 3.6: Astrometry of MAXI J1820, as phase referenced to J1821 at 5 GHz. The blue circles and red squares are the positions measured by the VLBA and the EVN, respectively. All marked positions have been corrected for the frame shift due to different calibrators and frequencies. The errors bars denote the statistical and systematic errors added in quadrature. Top panel: Motion in the plane of the sky relative to the fitted reference position, overlaid with the trajectory given by the best fitting proper motion and parallax (black dashed line). Bottom panel: Parallax signature of 0.348 (black dashed line) ± 0.033 (grey dashed lines) mas isolated by removing our best fitting proper motion.

(Astraatmadja & Bailer-Jones, 2016). We use the likelihood function as described in Bailer-Jones (2015). The likelihood distribution is defined as a Gaussian function of a measured parallax (p) with a standard deviation of σ_p with an unknown mean $1/r$

$$P(p|r, \sigma_p) = \frac{1}{\sqrt{2\pi}\sigma_p} \exp \left[-\frac{1}{2\sigma_p^2} \left(p - \frac{1}{r} \right)^2 \right] \quad (3.3)$$

We first use a simple prior, where we assume that the volume density of the stellar distribution is exponentially decreasing with distance (r) and is given by

$$\rho_{\text{exp}}(r) = \begin{cases} \frac{1}{2L^3} r^2 e^{-r/L} & \text{if } r > 0 \\ 0 & \text{otherwise} \end{cases} \quad (3.4)$$

Combining the prior and the likelihood mentioned above, a posterior distance distribution was obtained that was solved analytically with the help of a code.

To set a more physically motivated prior, we follow the work by Grimm et al. (2002, GR02 hereafter) to make an analytical model of the X-ray binary density distribution in our Galaxy to use as the prior, called Milky Way (MW) prior hereon. This considers the density of the bulge, disc and spheroid of the Galaxy, as described by the following equations (equations 4,5,6 in GR02).

$$\begin{aligned} \rho_{\text{Bulge}} &= \rho_{0,\text{Bulge}} \cdot \left(\frac{\sqrt{r^2 + \frac{z^2}{q^2}}}{r_0} \right)^{-\gamma} \cdot \exp \left(-\frac{r^2 + \frac{z^2}{q^2}}{r_t^2} \right), \\ \rho_{\text{Disk}} &= \rho_{0,\text{Disk}} \cdot \exp \left(-\frac{r_m}{r_d} - \frac{r}{r_d} - \frac{|z|}{r_z} \right), \\ \rho_{\text{Sphere}} &= \rho_{0,\text{Sphere}} \cdot \frac{\exp \left(-b \cdot \left(\frac{R}{R_e} \right)^{\frac{1}{4}} \right)}{\left(\frac{R}{R_e} \right)^{\frac{7}{8}}}. \end{aligned} \quad (3.5)$$

Here r is the distance from the Galactic centre of the projected position of the source on the Galactic plane, z is the height of the source above the Galactic plane, and R is the distance of the source from the Galactic centre. q , r_0 , r_t , r_d , r_m , r_z and R_e are scale parameters. GR02 derived these scale parameters for LMXBs by

constructing the X-ray luminosity function of these systems. We use the values of these constants as summarised in Table 4 of GR02. $\rho_{0,\text{Bulge}}$, $\rho_{0,\text{Disk}}$ and $\rho_{0,\text{Sphere}}$ are normalisation constants. We estimate the density constants $\rho_{0,\text{Bulge}}$, $\rho_{0,\text{Disk}}$ and $\rho_{0,\text{Sphere}}$ for LMXBs using the Disk:Bulge:Sphere mass ratio of 2:1:0.5 as derived by GR02, and assuming the mass of the bulge as $1.3 \times 10^{10} M_{\odot}$ (GR02). This gave the values of $\rho_{0,\text{Bulge}}$, $\rho_{0,\text{Disk}}$ and $\rho_{0,\text{Sphere}}$ as $1.1 M_{\odot} \text{pc}^{-3}$, $2.6 M_{\odot} \text{pc}^{-3}$ and $13.1 M_{\odot} \text{pc}^{-3}$ respectively. We note that the spatial distribution model of GR02 is not exclusively for BHXBs as their work considered neutron star X-ray binaries as well, but GR02 is currently the best available model for the spatial distribution of X-ray binaries as typical stellar spatial distributions do not account for kicks.

3.4.2.2 Distance posterior distribution

With our new and more precise parallax measurement (0.348 ± 0.033 mas) and the MW prior, we determined the distance posterior distribution (Figure 3.7), finding a median of 2.96 kpc and a 68 per cent confidence interval of ± 0.33 kpc. We compared this distance posterior distribution to that obtained using the parallax measurement made by *Gaia*-DR2, which gave a larger median value and a wider distribution (5.1 ± 2.7) kpc. The mode and the 68 per cent higher density interval values (Bailer-Jones, 2015) of this distribution are $4.1^{+2.6}_{-1.5}$ kpc. We also tested the exponentially decreasing volume density (EDVD) prior (Equation (3.3)) using the scaling length parameter L (2.17 kpc) for BHXBs from Gandhi et al. (2019) and find that unlike the *Gaia*-DR2 distance posterior distribution (median of 4.4 ± 2.4 kpc; mode of $3.5^{+2.1}_{-1.1}$ kpc), our new distance measurement is unaffected by the chosen prior (see Figure 3.7). This shows that the high significance of our parallax measurement has led to a model-independent distance to the source.

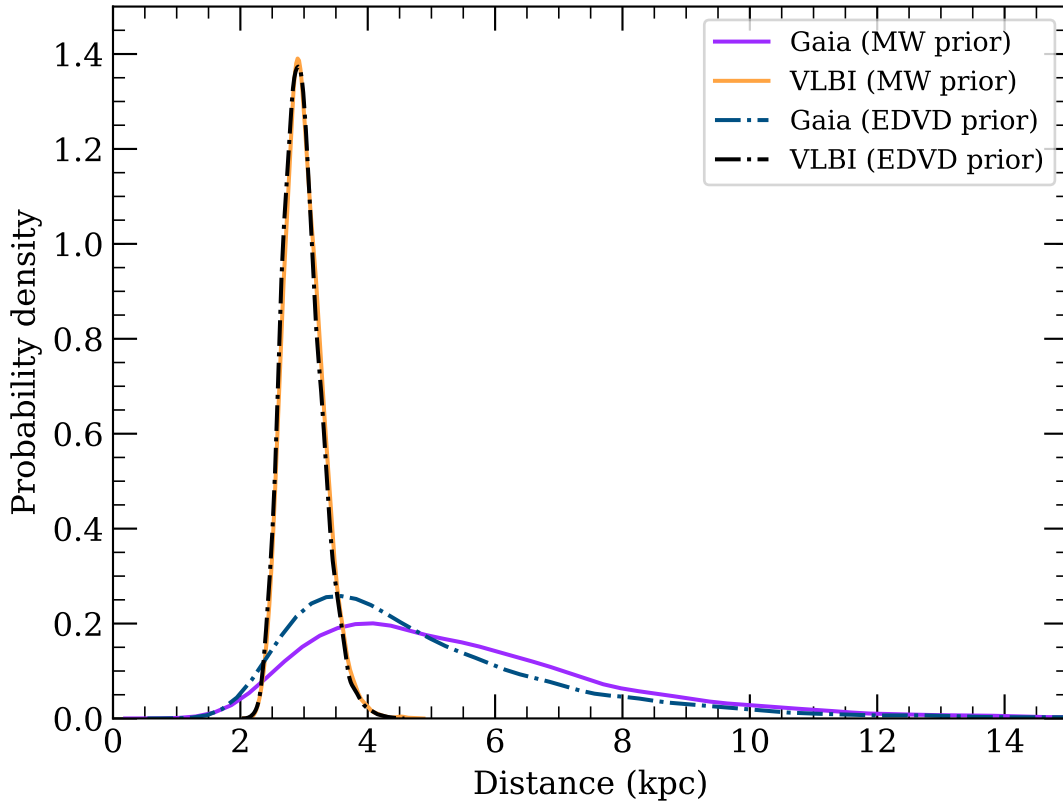


Figure 3.7: Distance posterior distributions of MAXI J1820, for both our new VLBI and the *Gaia*-DR2 parallax measurement. The *Gaia*-DR2 distance posterior has a higher median value for the Milky Way (MW) prior (5.1 ± 2.7 kpc) than for the exponentially-decreasing volume density (EDVD) prior (4.4 ± 2.4 kpc), whereas our VLBI distance distribution (2.96 ± 0.33 kpc) is insensitive to the prior chosen.

3.5 Discussion

With our much improved distance measurement for MAXI J1820, we now consider the physical implications of our result.

3.5.1 Transition and peak outburst luminosities

One of the unsolved puzzles about BHXBs is the correlation of the X-ray and radio behaviour during an outburst. A correlation between X-ray and radio luminosities has been reported (e.g., Gallo et al., 2018). Measuring luminosities for various systems at different stages of their outburst thus becomes crucial in order to successfully fit X-ray models to the emission region. The changes in spectral distribution and luminosities have been related to the change in the geometry of the accretion disc. As mentioned earlier, an accurate distance is a necessity when estimating luminosities.

The main outburst of MAXI J1820 was observed to have a peak X-ray flux of $(14 \pm 1) \times 10^{-8} \text{ erg cm}^{-2} \text{ s}^{-1}$ in the 1–100 keV band (Shidatsu et al., 2019). A distance of $2.96 \pm 0.33 \text{ kpc}$ implies that the system only reached $0.15 \pm 0.03 L_{\text{Edd}}$ at the peak of its outburst, where L_{Edd} is the Eddington luminosity for a $10M_{\odot}$ BH (see §3.5.3). The soft-to-hard state transition luminosity, from a flux of $(2.5 \pm 0.4) \times 10^{-8} \text{ erg cm}^{-2} \text{ s}^{-1}$, implies that the system made this transition at 3 ± 1 per cent L_{Edd} , in agreement with the average luminosity fraction of 1.58 ± 0.93 per cent L_{Edd} for BHXBs (Vahdat Motlagh et al., 2019; Maccarone, 2003). This average luminosity fraction in many cases is used to estimate a lower limit on the distance to a BHXB when more accurate parallax measurements are not available (Maccarone, 2003; Kalemci et al., 2013).

3.5.2 Jet parameters

The intermediate state during the hard to soft state transition of a BHXB during an outburst is associated with the ejection of jet knots that emit at radio

wavelengths. These radio emitting ejecta move away from the BH and measuring their proper motions can determine the time of zero separation, which can be used to determine the state of the accretion flow at the time, giving insights into the reasons for the jet ejection. Assuming intrinsic symmetry, the measured proper motions of corresponding approaching and receding jet ejecta along with a distance can be used to uniquely determine the jet speed and inclination angle between the jet and the line of sight (Mirabel & Rodríguez, 1994; Fender et al., 1999), via

$$\beta \cos i = \frac{\mu_{\text{app}} - \mu_{\text{rec}}}{\mu_{\text{app}} + \mu_{\text{rec}}}; \tan i = \frac{2d}{c} \frac{\mu_{\text{app}} \mu_{\text{rec}}}{\mu_{\text{app}} - \mu_{\text{rec}}} \quad (3.6)$$

where β is the velocity of the jet (normalised to the speed of light c), μ_{app} and μ_{rec} are the proper motions of the approaching and receding components of the jet, i is the inclination angle of the jet to the line of sight, and d is the distance to the system. Bright et al. (2020) measured the proper motions of corresponding jet ejecta during the transition phase of MAXI J1820 to be $\mu_{\text{app}} = 77 \pm 1 \text{ mas d}^{-1}$, $\mu_{\text{rec}} = 33 \pm 1 \text{ mas d}^{-1}$. We use this with our distance constraint to estimate $\beta = 0.89 \pm 0.09$ and $i = (63 \pm 3)^\circ$. We note that even with the highly precise distance, possible apparent superluminal motion of the jets cannot be ruled out.

3.5.3 Implications for BH mass

According to Kepler’s third law, the orbital velocities, period and the mass of a binary are related. Measuring the orbital velocity and period can thus give an estimate of the masses of the objects in the binary. The velocity is measured by optical spectroscopy and measuring the Doppler shift of a spectral line. The orbital plane of the binary might be inclined to the line-of-sight, which will manifest as a sinusoidal variation in the velocity. The masses in the orbit are then related to the velocity by the ‘mass function’. Once the mass ratio and the inclination angle of the orbital plane are known, the masses of both the components in the binary can be estimated. Torres et al. (2019) conducted optical spectroscopy on

MAXI J1820 and reported a mass function of

$$f(M) = \frac{(M_1 \sin i)^3}{(M_1 + M_2)^2} = 5.18 \pm 0.15 M_\odot \quad (3.7)$$

where $f(M)$ is the mass function, i is the inclination angle, and M_1 and M_2 are the masses of the BH and its companion. Assuming a mass ratio $q \equiv M_2/M_1 = 0.12$, they constrained the inclination angle to be $69^\circ < i < 77^\circ$, and the BH mass to be $7\text{--}8 M_\odot$. Using our derived inclination angle of $(63 \pm 3)^\circ$, we re-calculated the BH mass to be $(9.2 \pm 1.3) M_\odot$. Torres et al. (2019) suggested that the value $q = 0.12$ needs confirmation, so we also calculated the mass of the BH for the full suggested range of q (0.03–0.4) to be $(10 \pm 2) M_\odot$.

In the high/soft state it is assumed that the accretion disc reaches the innermost stable circular orbit (R_{ISCO} ; see Chapter 1 for details). It has been shown that R_{ISCO} scales with the BH spin parameter, a_* (Bardeen et al., 1972; McClintock et al., 2014), and thus determining R_{ISCO} can help estimating a_* . The inner disc radius is related to the photon flux and accretion disc temperature for a given distance (D) and inclination angle (i) of the source (Shidatsu et al., 2018). Fitting accretion disc models to the X-ray spectrum of MAXI J1820+070 during the high/soft state, Shidatsu et al. (2019) arrived at the best fit values for the photon flux and the inner accretion disc temperature. They concluded that the inner disc radius should then take the form

$$R_{in} = 77.9 \pm 1.0 \frac{D}{3 \text{ kpc}} \frac{\cos i}{\cos 60^\circ} \text{ km} \quad (3.8)$$

Equating (3.8) to the inner most stable orbit of the BH, we find that $R_{\text{ISCO}} = 62 \pm 8 \text{ km}$. The physical radius of the disc is then given by $1.19 R_{\text{ISCO}}$ (Kubota et al., 1998). Thus, the ratio of $1.19 R_{\text{ISCO}}$ and $R_g (= GM/c^2)$ is 5.3 ± 1.0 . From the monotonic relation between this ratio and a_* (Bardeen et al., 1972), the BH in MAXI J1820 is likely slowly spinning ($a_* = 0.20^{+0.27}_{-0.20}$) under the assumptions that the disk flux vanishes at the R_{ISCO} and the orbit of particles around a rotating

BH at R_{ISCO} is circular. See McClintock et al. (2014) for more details.

3.5.4 Peculiar velocity

The peculiar velocity of BHXBs has been used to indicate the natal kick the system might have received on the birth of the BH (Mirabel et al., 1993; Mirabel, 2017; Nelemans et al., 1999; Fragos et al., 2009; Janka, 2017). Measuring peculiar velocity requires good constraints on the proper motion, systemic radial velocity and the distance to the system. We used the parallax and proper motion measured in this work, combined with the systemic radial velocity of $(-21.6 \pm 2.3) \text{ km s}^{-1}$ (Torres et al., 2019) to determine a peculiar velocity (relative to the local standard of rest) of $68 \pm 10 \text{ km s}^{-1}$, where the error bar represents the 5th and 95th percentile of the resultant peculiar velocity distribution. This velocity is slightly higher than the typical velocity dispersion of stars in the Galaxy (50 km s^{-1} for older stars and lower for younger stars; Mignard, 2000) indicating a natal kick at birth, but $< 50 \text{ km s}^{-1}$ within a 3σ limit suggesting the lack of a natal kick. Thus, we are not able to conclude the birth mechanism of the BH in MAXI J1820 based on its peculiar velocity probability distribution. Since MAXI J1820 is at a height of $\sim 0.5 \text{ kpc}$ above the Galactic plane, the local standard of rest is not as well defined as it would be for a system in the Galactic Plane. Hence, estimating the peculiar velocity of this system by comparing it with the local standard of rest is not ideal. We have hence developed a new methodology in Chapter 4 to circumvent this limitation of using peculiar velocity to get an idea about the natal kick of the system.

3.6 Summary

We have used VLBI to conduct high precision astrometry of MAXI J1820+070 to measure its proper motion and parallax.

- We observed using the VLBA and the EVN, at 5 and 15 GHz at nine epochs.

- We carefully considered the systematics that arose due to the ionosphere, the troposphere, and the phase referencing to different phase calibrators.
- We used a Bayesian inference approach and MCMC to fit the parallax and proper motion to the corrected positions.
- We report a precise VLBI parallax measurement of (0.348 ± 0.033) mas to the BHXB MAXI J1820+070.
- Using this parallax and a Milky Way specific Bayesian prior, we inferred a distance of (2.96 ± 0.33) kpc. We compared it to the distance obtained using the *Gaia* parallax and also using another simpler prior, an exponentially decreasing volume density prior.
- We showed that MAXI J1820+070 reached (15 ± 3) per cent Eddington luminosity at the peak of its outburst.
- We constrained the jet inclination angle and velocity to be $(63 \pm 3)^\circ$ and $(0.89 \pm 0.09)c$, respectively.
- We also report an updated BH mass estimate of $(9.2 \pm 1.3) M_\odot$, and suggest the BH is slowly spinning.
- Using the newly constrained proper motion, systemic radial velocity and distance, we measured the peculiar velocity of the system and suggest that the BH in the system could have been born with a SN explosion.

Black hole natal kicks and birth constraints

Adapted from:

P. Atri, J. C. A. Miller-Jones, A. Bahramian, R. M. Plotkin, P. G. Jonker, G. Nelemans, T. J. Maccarone, G. R. Sivakoff, A. T. Deller, S. Chaty, M. A. P. Torres, S. Horiuchi, J. McCallum, T. Natusch, C. J. Phillips, J. Stevens, S. Weston (2019), ‘Potential Kick Velocity distribution of black hole X-ray binaries and implications for natal kicks’ *Monthly Notices of the Royal Astronomical Society*, Volume 489, Issue 3, p.3116-3134,

DOI: 10.1093/mnras/stz2335

Having used the proper motion, parallax, and systemic radial velocity of a single BHXB to determine its peculiar velocity in Chapter 3, and recognising the limitations of using peculiar velocity to infer the birth mechanism of the BH we now expand this work to a larger sample of BHXBs and present a methodology to estimate the potential kick velocities of BHXBs. In this chapter, we use Very Long Baseline Interferometry (VLBI) to measure the proper motions of three black hole X-ray binaries (BHXBs). Using these results together with data from the literature and *Gaia*-DR2 to collate the best available constraints on proper motion, parallax, distance and systemic radial velocity of 16 BHXBs, we determined

their three dimensional Galactocentric orbits. We extended this analysis to estimate the probability distribution for the potential kick velocity (PKV) a BHXB system could have received on formation. Constraining the kicks imparted to BHXBs provides insight into the birth mechanism of black holes (BHs). We suggest the birth pathway that the 16 BHXBs in our sample could have taken based on their kick velocity distributions. We used a Bayesian hierarchical methodology to analyse the PKV distribution of the BHXB population and explore the effect of the resulting natal kicks on BH-BH merger rates, merger sites, and binary evolution, spin-orbit misalignment in BH binary systems and BH retention fraction in globular clusters. Finally, we test for a correlation between the BH mass and PKV and also the PKV and height of the BHXB above the Galactic plane. Our Python code allows the estimation of the PKV for any system with sufficient observational constraints.

4.1 Limitations of peculiar velocity for BHXBs

The literature reports the use of current peculiar velocity to suggest the possibility of the BHXB receiving a kick when the BH was born (See Chapter 1). Using the current peculiar velocity of a system to infer the strength of the kick the system might have received at birth has a few limitations. Peculiar velocity is the current three dimensional velocity of a system relative to the local standard of rest and thus changes based on the epoch of observation. Also, using peculiar velocity relative to that expected from Galactic rotation as an indicator of natal kick velocity could be misleading for sources that are far away from the Galactic plane. Our analysis tries to minimise these shortcomings by instead using the peculiar velocity of the system when it crosses the Galactic plane, which we refer to as the potential kick velocity (PKV).

4.2 Data

4.2.1 BHXB sample

To determine the three dimensional motion of BHXBs, we need to combine the proper motion, systemic radial velocity and distances to these systems. The literature already contains estimates of the current peculiar velocity for seven of our systems, XTE J1118+480 (Mirabel et al., 2001), GRO 1655–40 (Mirabel et al., 2002), Cyg X–1 (Mirabel & Rodrigues, 2003), GRS 1915+105 (Dhawan et al., 2007), V404 Cyg (Miller-Jones et al., 2009b), MAXI J1836–194 (Russell et al., 2015) and VLA J2130+12 (Tetarenko et al., 2016a). *Gaia* in its second data release (DR2) measured the proper motions of 11 BHXBs, three of which were improvements on previous measurements (Cyg X–1, GRO J1655–40 and XTE J1118+480; Mirabel et al., 2001, 2002; Mirabel & Rodrigues, 2003). Gandhi et al. (2019) estimated the current peculiar velocities for BHXBs for which *Gaia*-DR2 (Gaia Collaboration et al., 2018a) measured proper motions and parallaxes. We use these proper motion and parallax measurements along with the Very Long Baseline Interferometry (VLBI; Shapiro et al., 1979; Reid & Honma, 2014) measurements present in the literature (based on whichever was more precise) for our analysis.

Typical BHXBs have proper motions of a few mas yr^{-1} , which can be measured by the *Gaia* satellite (Lindgren et al., 2016) or with VLBI. The quiescent optical brightness of BHXBs is usually near to or below the limiting magnitude of the *Gaia* satellite, and they only get bright enough for high precision astrometry with *Gaia* when they are in outburst. This makes proper motion measurements challenging for many of these sources. *Gaia* would also not be able to detect BHXBs towards the Galactic bulge due to high extinction. Thus, triggered VLBI observations when a BHXB goes into an outburst can probe systems not accessible to *Gaia*. We used VLBI to measure the proper motions of three new sources; GX 339–4, Swift J1753.5–0127 and GRS 1716–249.

4.2.2 Sample biases

Our sample set of 16 BHXBs suffers from certain observational biases. There are a few systems in our sample that are not dynamically confirmed BHs but are BHXB candidates (see Tetarenko et al. (2016a) for a summary of all BHXB candidates). Notably, the nature of VLA J2130+12 that is a BHXB detected in quiescence (Kirsten et al., 2014) is still under debate (Tetarenko et al., 2016b). We include Cyg X-1 in our analysis even though it is a younger, high mass X-ray binary (HMXB) with a potentially more massive donor star than that of a typical low mass X-ray binary. This is because it has well constrained parameters and thus is a good test source.

We note that almost all BHXBs in our sample have been in outburst at some point, except VLA J2130+12. During outbursts typical BHXBs reach X-ray peak luminosities of $>10^{37-39}$ ergs s⁻¹. Thus the sample is devoid of any very faint X-ray transients (Wijnands et al., 2006), which have peak luminosities of 10^{36-37} ergs s⁻¹ (Heise, 1999). We are biased against observing BHs that received kicks strong enough to unbind the binary system, as we can only observe BHs in X-ray binaries. We may also be observationally biased against distant, low kick systems as they will be very close to the Galactic plane and therefore will be highly extinguished.

4.3 VLBI Observations and Data reduction

To measure the proper motions of GX 339-4, GRS 1716-249 and Swift J1753.5-0127, we used the Very Long Baseline Array (VLBA), the European VLBI Network (EVN) and the Australian Long Baseline Array (LBA). The observational setups are summarised in Table 4.1. The hard X-ray spectral state of BHXBs is associated with the rising and decaying phases of the outbursts (Belloni & Motta, 2016). The radio jets during the hard spectral state are compact, steady and are causally connected to the BH (Fender et al., 2009). Thus the hard state is an

ideal phase during the outburst to conduct astrometry. High precision astrometry can be conducted even if the target image is resolved (Reid et al., 2011). The observations need to be separated in time by at least a couple of months to provide a sufficient time baseline for a proper motion measurement. Thus, depending on how long the source stays in a hard state, we need to observe it over one or multiple outbursts.

The data were correlated using the DiFX software correlator (Deller et al., 2011) and reduced using the Astronomical Image Processing System (AIPS 31DEC17; Greisen, 2003). Observations of bright fringe finder sources were used to correct for non-zero instrumental delays and rates. The observations of the target were bracketed by shorter observations of a phase reference calibrator, located as close to the target as possible (preferably $<2^\circ$; Pradel et al., 2006). The details of the calibrators used for each target are summarised in Table 4.2.

For observations made at frequencies higher than 5 GHz using the VLBA, numerous widely separated calibrators were observed in quick succession (geodetic blocks) for ~ 30 minutes at the start and end of each observing run. Geodetic blocks help in determining any error in the estimated zenith tropospheric delay and thus improve astrometric accuracy. The multi-band delays were corrected using standard *AIPS* procedures (*AIPS* Memo 110). The overheads associated with observing a geodetic block with the LBA and the EVN were high due to the large dish sizes and consequent slow slew rates of the dishes involved, and hence we did not observe geodetic blocks with the LBA and the EVN. The stations included in the LBA and the EVN are not solely for the purpose of VLBI, and so have infrequent formal VLBI observing sessions. For any transients that have to be observed out of the standard observing sessions, the source is observed with whatever stations are available. This gives varying sensitivity and resolution from epoch to epoch.

4.3.1 GX 339–4

GX 339–4 is a low mass black hole X-ray binary (LMXB), which was first detected in 1973 (Markert et al., 1973). This system goes into frequent outbursts, with 20 outbursts since its detection (Tetarenko et al., 2016b). Hence, astrometry over multiple outbursts is possible. The optical emission from the accretion disc of the system even during the low luminosity quiescent phase makes the detection of the donor star difficult (Shahbaz et al., 2001). Recently, NIR spectra of GX 339–4 were obtained using the VLT/X-Shooter during quiescence, which led to a systemic radial velocity measurement of $\gamma = 26 \pm 2 \text{ km s}^{-1}$ (Heida et al., 2017) and a distance estimate of $9 \pm 4 \text{ kpc}$ for the system. GX 339–4 was observed on three epochs (Table 4.1) using the LBA during the hard states of three different outbursts (Homan & Belloni, 2005; Buxton et al., 2013; Yan et al., 2014) spanning over 4 years. We observed at a frequency of 8.4 GHz in all three epochs for maximum sensitivity.

4.3.2 GRS 1716–249

GRS 1716–249 (Nova Oph 1993) was discovered (Ballet et al., 1993) as an X-ray transient in Ophiuchus in 1993. della Valle et al. (1994) conducted a photometric and spectroscopic analysis of GRS 1716–249 and concluded that the source is at a distance of $2.4 \pm 0.4 \text{ kpc}$. The mass of the primary in the system is $> 4.9 M_{\odot}$ (Masetti et al., 1996). The systemic radial velocity of this system is not yet known. After a prolonged quiescent period (Negoro et al., 2016) following some renewed activity in 1995 (Karitskaya & Goranskij, 1995), the source went into outburst again in December 2016, but did not reach a soft state. The source was observed at three epochs under the LBA program V447 (Table 4.1 and Table 4.2), and the observations were spaced a few months apart. The last two observations were taken right after the source finished brief softening periods (Bassi et al., 2019). Ceduna did not have valid data for three hours of observations for the first epoch. The last epoch was obtained during a scheduled VLBI run and hence

had access to all telescopes in the LBA other than Hartebeesthoek.

4.3.3 Swift J1753.5–0127

Swift J1753.5–0127 is a high Galactic latitude system which was first discovered when it went into outburst in 2005 (Palmer et al., 2005). It has one of the shortest known orbital periods (3.2443 ± 0.001 hr) for a BHXB (Zurita et al., 2008). This system remained in outburst for 11 years before it ultimately faded to quiescence in 2016 November (Russell et al., 2015). The distance to this source is not well known; the best available estimation being 4–8 kpc (Cadolle Bel et al., 2007). The mass of the BH in this system is $> 7.4 M_{\odot}$ (Shaw et al., 2016).

Swift J1753.5–0127 was observed using the EVN, the VLBA and the HSA (High Sensitivity Array) for a total of nine epochs. The four VLBA observations in December 2009 were conducted with the dual 13/4-cm recording mode (2.3 and 8.4 GHz), but we only use the 8.4 GHz data to measure the position due to reduced scattering, reduced ionospheric effects that could give rise to systematic errors in astrometry, and higher sensitivity (Table 4.1). In addition to the standard calibration steps, a global model of the phase calibrator was made by stacking the calibrated data sets of the phase calibrator from all four epochs to prevent minor differences in the model (due to varying uv-coverage) from introducing astrometric systematics. The calibrated data sets of the target from 2008 were also stacked, as the array does not have the capability to detect a week’s motion of the system. Swift J1753.5–0127 was detected in the stacked image with a significance of $\sim 5.2\sigma$. GBT was a part of the HSA in addition to the standard VLBA dishes for the 8.4 GHz observations in March 2010, where the target was strongly detected ($\sim 124\sigma$).

The EVN observations of Swift J1753.5–0127 were taken as part of a parallax measurement campaign (EM101) in 2012–2013, and consisted of 5 epochs taken over a period of one year. The phase calibrator J1743–0350, which was used in the earlier VLBA observations, was suitable for measuring the proper motion

of the target but not the parallax, due to its large angular separation (3.36°) from the target. We therefore conducted an X-ray binary calibrator survey on the VLBA (program code BS206) to find closer compact calibrators. We used the multi-phase centre capability of the DiFX software correlator (Deller et al., 2011) to correlate on the positions of all NVSS sources within $30'$ of the target, observing at 1.6 GHz to give a field of view such that only four pointings were required to cover the desired sky area. Within $30'$ of Swift J1753.5–0127 we detected two potential calibrators, J1752–0147 ($17^{\text{h}}52^{\text{m}}18.364^{\text{s}}$, $-01^\circ47'16.685''$) and J1753–0102 ($17^{\text{h}}53^{\text{m}}10.4488^{\text{s}}$, $-01^\circ02'48.854''$). While the latter turned out to be a widely-separated double, the former was a compact, single source of peak flux density 6–9 mJy, and was therefore adopted as a secondary phase calibrator for our EVN parallax campaign, and was 0.44° away from our target.

To make sure that we were using the same source models to solve for the delays and rates, we concatenated the calibrated data sets of the primary calibrator for all epochs. This model was then used to derive (epoch-wise) the phase, delay and rate solutions that were interpolated to the secondary calibrator and the target. The secondary calibrator was then imaged and the data were stacked to obtain a global model (e.g., Miller-Jones et al., 2018; Atri et al., 2020). The global model was again used to derive epoch-wise phase solutions that were applied to the target data, which were then imaged. The target positions were then measured by fitting a point source model in the image plane.

4.4 Results - Proper motion measurements

Our VLBI data were used to find the proper motions of GX 339–4 and GRS 1716–249 for the first time. We also measured the proper motion of Swift J1753.5–0127, for which *Gaia* also had made a measurement. The position measurements of the three sources at all epochs are summarised in Table 4.3.

Table 4.1: Summary of the VLBI observations. Station codes: Ak - ASKAP; At - phased up ATCA; Br - Brewster; Cd - Ceduna; Ef - Effelsberg; Fd - Fort Davis; Gb - Green Bank; Hh - Hartebeesthoek; Hn - Hancock; Ho - Hobart; Jb - Jodrell Bank Mk II; Ke - Katherine; Kp - Kitt Peak; La - Los Alamos; Mc - Medicina; Mk - Mauna Kea; Mp - Mopra; Nl - North Liberty; Nt - Noto; On - Onsala; Ov - Owens Valley ; Pa - Parkes; Pt - Pie Town; Sc - St. Croix; Td - the 34m DSS36 antenna at Tidbinbilla; Ti - the 70m DSS43 antenna at Tidbinbilla; Tr - Torun; Wa - Warkworth 30m (Woodburn et al., 2015); Wb - Westerbork; Ww - Warkworth 12m; Yg - Yarragadee; Ys - Yebees

Target	Array	Code	Date	MJD (UTC)	Freq. (GHz)	Time on Source (mins)	Stations
GX 339-4	LBA	V430A	2011 Apr 03	55654.84	8.4	368.2	At, Cd, Ho, Mp, Pa, Ti
		V486B	2013 Aug 15	56520.20	8.4	193.9	Ak, At, Cd, Hh, Ho, Ke, Mp, Pa, Ti, Ww, Yg
		V447A	2014 Nov 22	56983.17	8.4	254.4	At, Cd, Ho, Mp
GRS 1716-249	LBA	V447D	2017 Feb 21	57805.41	8.4	283.0	At, Cd, Ho, Mp
		V447E	2017 Apr 22	57865.73	8.4	329.3	At, Cd, Ho, Mp
		V447F	2017 Aug 13	57978.48	8.4	279.5	At, Cd, Ho, Ke, Mp, Pa, Td, Ti, Wa, Yg
Swift J1753.5-0127	VLBA	BM331A	2009 Dec 16	55181.81	8.4	149.7	Br, Fd, Hn, Kp, La, Mk, Nl, Ov, Pt, Sc
		BM331B	2009 Dec 19	55184.79	8.4	147.9	Br, Fd, Hn, Kp, La, Mk, Nl, Ov, Pt, Sc
		BM331C	2009 Dec 22	55187.81	8.4	148.6	Br, Fd, Hn, Kp, La, Mk, Nl, Ov, Pt, Sc
		BM331D	2009 Dec 24	55189.79	8.4	147.9	Br, Fd, Hn, Kp, La, Mk, Nl, Ov, Pt, Sc
		BM326	2010 Mar 30	55285.47	8.4	189.1	Br, Fd, Gb, Hn, Kp, La, Mk, Nl, Ov, Pt, Sc
	VLBA+GBT EVN	EM101A	2012 Nov 13	56245.03	5.0	156.9	Ef, Jb, Mc, Nt, On, Tr, Ys, Wb, Hh
		EM101B	2013 Mar 20	56371.18	5.0	117.4	Ef, Jb, Mc, Nt, On, Tr, Ys, Wb, Hh
		EM101C	2013 Jun 18	56461.99	5.0	174.2	Ef, Jb, Mc, Nt, On, Tr, Ys, Wb, Hh
		EM101D	2013 Sep 17	56552.74	5.0	192.1	EF, Jb, Mc, Nt, On, Tr, Ys, Wb, Hh
		EM101E	2013 Dec 03	56629.75	5.0	220.8	Ef, Jb, Mc, Nt, On, Tr, Ys, Wb, Hh

Table 4.2: Information about the calibrators used. The R. A. and Dec. positions of the calibrators are those mentioned in the Astrogeo VLBI calibrator search website <http://astrogeo.org/calib/search.html> (rfc2019a catalogue). The integrated flux density is the average of the cleaned flux of all epochs of the calibrator. θ_{sep} is the angular separation of the target from the calibrator. [1] Murphy et al. (2010); [2] Condon et al. (1998); [3] Johnston et al. (1995)

Target	Array	Calibrators	R. A. (J2000) (h m s)	Dec. (J2000) ($^{\circ}$ ' ")	θ_{sep} $^{\circ}$	Integrated flux density (Jy)
GX 339–4	LBA	J1711–5028 ^[1]	17 ^h 11 ^m 40 ^s .9927	-50 $^{\circ}$ 28'17".409	2.21	0.08
GRS 1716–249	LBA	J1711–2509 ^[2]	17 ^h 11 ^m 23 ^s .1020	-25 $^{\circ}$ 09'01".564	1.87	0.1
Swift J1753.5–0127	VLBA	J1743–0350 ^[3]	17 ^h 43 ^m 58 ^s .8591	-03 $^{\circ}$ 50'04".617	3.36	3
	EVN	J1743–0350	17 ^h 43 ^m 58 ^s .8591	-03 $^{\circ}$ 50'04".617	3.36	2.4
		J1752–0147	17 ^h 52 ^m 18 ^s .3640	-01 $^{\circ}$ 47'16".685	0.45	0.14

4.4.1 GX 339–4

As shown in Figure 4.1, for GX 339–4 a linear fit for the proper motion of the system gives:

$$\begin{aligned}\mu_{\alpha} \cos \delta &= -3.95 \pm 0.07 \text{ mas yr}^{-1} \\ \mu_{\delta} &= -4.71 \pm 0.06 \text{ mas yr}^{-1}.\end{aligned}\tag{4.1}$$

This gives an overall proper motion for GX 339–4 of $6.15 \pm 0.06 \text{ mas yr}^{-1}$.

4.4.2 GRS 1716–249

The measured offsets of GRS 1716–249 in RA and Dec for our three epochs of LBA observations have been plotted in Figure 4.2. Measured declinations in these epochs do not appear to follow a linear trend (Top panel of Fig. 4.2). Choosing different subsets of measurements yield drastically different results. The proper motions of the different fits (considering two epochs at a time) in RA agree with each other within the 1σ error limit. On the contrary, the proper motion fits in Dec vary between $-41.4 \text{ mas yr}^{-1}$ and -2.5 mas yr^{-1} . This suggests that the measured position in Declination for one out of the three epochs is unreliable.

To ascertain which of the epochs were giving accurate positions, we obtained an archival position measurement of GRS 1716–249 from a near infrared observation to increase the time baseline. We use the position of GRS 1716–249 as

Table 4.3: Summary of the detections of GX 339–4, GRS 1716–249 and Swift J1753.5–0127. MJD is taken as the middle of the observing run and the error on MJD is calculated as half the length of the observation. The positions, peak intensities and errors on each parameter are calculated by fitting an elliptical Gaussian to the target in the image plane.

Target	Project Code	MJD (UTC)	R. A. (J2000) (h m s)	Dec. (J2000) ($^{\circ}$ ' ")	Peak Intensity (μ Jy bm^{-1})
GX 339–4	V430A	55654.84 \pm 0.25	17 ^h 02 ^m 49 ^s .38260 \pm 0.00004	-48 $^{\circ}$ 47'23".1413 \pm 0.0003	197 \pm 18
	V486B	56520.21 \pm 0.24	17 ^h 02 ^m 49 ^s .38164 \pm 0.00001	-48 $^{\circ}$ 47'23".1534 \pm 0.0001	2280 \pm 163
	V447A	56983.17 \pm 0.16	17 ^h 02 ^m 49 ^s .38114 \pm 0.00001	-48 $^{\circ}$ 47'23".1591 \pm 0.0001	2629 \pm 203
GRS 1716–249	V447D	57805.41 \pm 0.31	17 ^h 19 ^m 36 ^s .92008 \pm 0.00002	-25 $^{\circ}$ 01'04".1215 \pm 0.0005	1488 \pm 156
	V447E	57865.73 \pm 0.23	17 ^h 19 ^m 36 ^s .92003 \pm 0.00001	-25 $^{\circ}$ 01'04".1286 \pm 0.0001	1135 \pm 105
	V447F	57978.48 \pm 0.19	17 ^h 19 ^m 36 ^s .91994 \pm 0.00003	-25 $^{\circ}$ 01'04".1294 \pm 0.0002	290 \pm 42
Swift J1753.5–0127	BM331	55186.05 \pm 0.10	17 ^h 53 ^m 28 ^s .29060 \pm 0.00001	-01 $^{\circ}$ 27'06".2916 \pm 0.0002	290 \pm 56
	BM326	55285.47 \pm 0.14	17 ^h 53 ^m 28 ^s .29061 \pm 0.000003	-01 $^{\circ}$ 27'06".2919 \pm 0.0001	2614 \pm 21
	EM101A	56245.03 \pm 0.48	17 ^h 53 ^m 28 ^s .29074 \pm 0.00002	-01 $^{\circ}$ 27'06".3011 \pm 0.0003	280 \pm 27
	EM101B	56371.18 \pm 0.08	17 ^h 53 ^m 28 ^s .29077 \pm 0.00005	-01 $^{\circ}$ 27'06".3037 \pm 0.0006	161 \pm 31
	EM101C	56461.99 \pm 0.09	17 ^h 53 ^m 28 ^s .29078 \pm 0.00003	-01 $^{\circ}$ 27'06".3036 \pm 0.0004	141 \pm 20
	EM101D	56552.74 \pm 0.13	17 ^h 53 ^m 28 ^s .29081 \pm 0.00002	-01 $^{\circ}$ 27'06".3053 \pm 0.0004	207 \pm 27
EM101E	56629.75 \pm 0.10	17 ^h 53 ^m 28 ^s .29082 \pm 0.00004	-01 $^{\circ}$ 27'06".3054 \pm 0.0006	109 \pm 21	

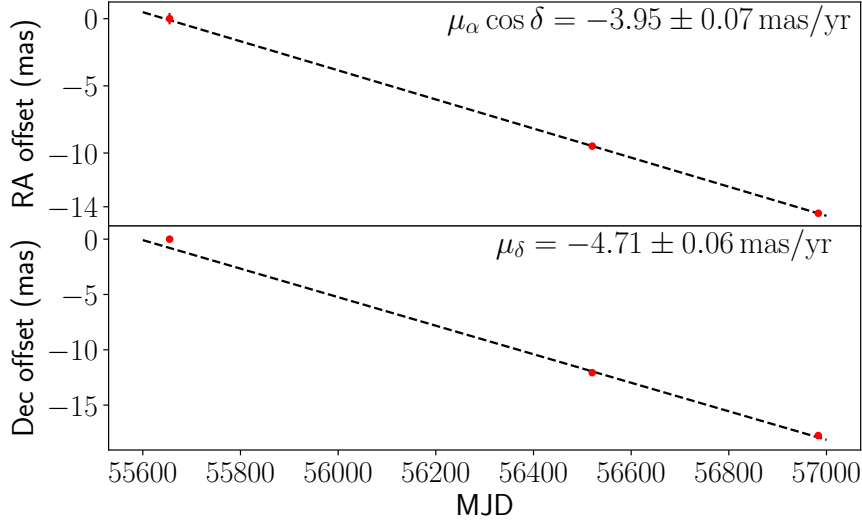


Figure 4.1: Proper motion fit for GX 339–4. GX 339–4 was tracked for three epochs over three different outbursts. Top panel: Offset of measured positions relative to the first epoch in Right Ascension. Bottom panel: Offset of measured positions in Declination relative to the first epoch.

measured from the K-band image taken on MJD 49263 during the 1994 outburst (Chaty et al., 2002). We fixed the image astrometry to the *Gaia*-DR2 frame by cross matching it with ~ 140 sources from the *Gaia*-DR2 catalogue using *PyRAF*. The proper motions of these sources as reported by *Gaia*-DR2 were used to correct the positions of the sources. The position of GRS 1716–249 was determined with an uncertainty of ~ 0.2 arcsec. This shows that the position from the first LBA epoch is the cause of the discrepancy. As mentioned in §4.3.2, Ceduna was not available for observing during most of that observing run. Thus the uv coverage was sparse and could explain the wrong position measurement. To determine the true proper motion, we therefore fit using the last two LBA epochs (V447E and V447F) and the position measurement from the 1994 K-band image. We obtain the following proper motion

$$\begin{aligned} \mu_{\alpha} \cos \delta &= -3.83 \pm 1.25 \text{ mas yr}^{-1} \\ \mu_{\delta} &= -2.64 \pm 0.75 \text{ mas yr}^{-1}. \end{aligned} \tag{4.2}$$

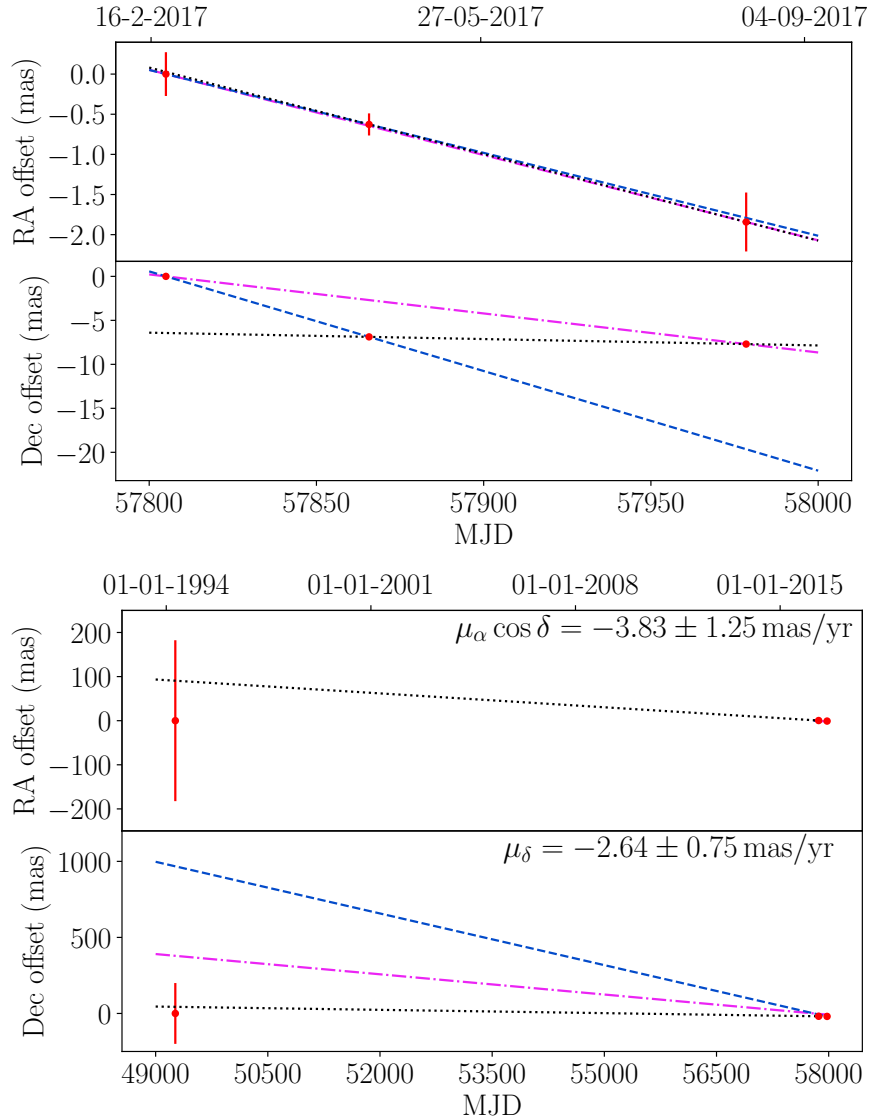


Figure 4.2: Proper motion fits for GRS 1716–249. GRS 1716–249 was tracked for three epochs over one outburst using the LBA, with positions shown with respect to the first LBA epoch. Top panel: fits by considering position measurements of two epochs at a time in RA and Dec - epoch 1 and 2 (dashed line); epoch 2 and 3 (dotted line); epoch 1 and 3 (dotted dashed line). The three declination measurements do not lie on a straight line. Lower panel: fitting for proper motion by increasing the time baseline using the 1994 K-band image position measurement (dotted line), which breaks the degeneracy and shows that the epoch 1 LBA position is in error (blue and green dashed lines). This was then removed from the fit.

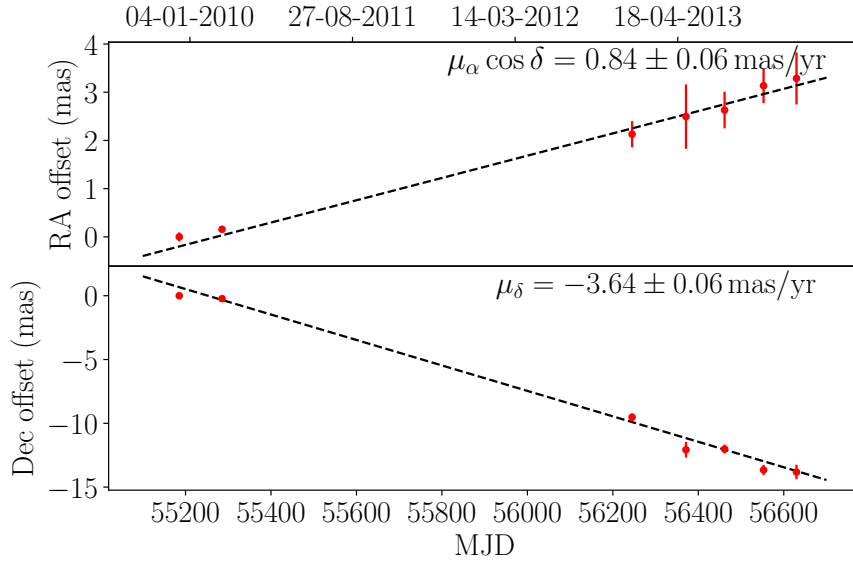


Figure 4.3: Proper motion fit for Swift J1753.5–0127. Swift J1753.5–0127 was observed for ten epochs spanning four years. The four observations in 2009 December were concatenated into one position measurement (MJD 55181 to MJD 55190). Top panel: offset of measured positions in Right Ascension of Swift J1753.5–0127 as a function of MJD relative to the first epoch. Bottom panel: offset of measured positions in Declination of Swift J1753.5–0127 as a function of MJD relative to the first epoch.

This gives an overall proper motion of $4.65 \pm 1.12 \text{ mas yr}^{-1}$ for GRS 1716–249.

4.4.3 Swift J1753.5–0127

Figure 4.3 shows a linear fit to the measured positions of Swift J1753.5–0127 over a span of 4 years. Although we used a different calibration scheme for the VLBA and EVN epochs, the nearby secondary calibrator used for the EVN (J1752–0147) was observed using the VLBA primary calibrator J1743–0350 as a phase reference source, such that the two data sets should be referenced to the same absolute reference frame. The absolute astrometric systematics should therefore be of order 0.09 and 0.27 mas, respectively in R.A. and Dec. The fit gives a proper motion of

$$\begin{aligned} \mu_{\alpha} \cos \delta &= 0.84 \pm 0.06 \text{ mas yr}^{-1} \\ \mu_{\delta} &= -3.64 \pm 0.06 \text{ mas yr}^{-1}. \end{aligned} \tag{4.3}$$

This gives a net proper motion of $3.73 \pm 0.06 \text{ mas yr}^{-1}$. The proper motion determined above agrees within 2σ error limits with that reported by *Gaia*-DR2, which is

$$\begin{aligned}\mu_\alpha \cos \delta &= 1.13 \pm 0.16 \text{ mas yr}^{-1} \\ \mu_\delta &= -3.53 \pm 0.15 \text{ mas yr}^{-1}.\end{aligned}\tag{4.4}$$

4.5 Distance and radial velocity estimates

We will fold the proper motions measured by our VLBI data for the three systems as reported in §4.4, and those available in archival data (using VLBI and *Gaia*) with distance and systemic radial velocities of these systems to get their potential kick velocity distribution.

4.5.1 Distance - Milky way prior

The distances to some of the sources in our sample have been inferred from a parallax measurement made by *Gaia*-DR2 (Gaia Collaboration et al., 2018a) or VLBI. Every *Gaia* measurement of a parallax has an uncertainty associated with it. The fractional errors associated with these measurements are significant, even if they are small in absolute value. Thus, it is essential that these errors are properly considered when converting parallax to distance. In order to make sure that the errors from the measured quantity are appropriately propagated to the inferred quantity, we use a Bayesian inference approach (Astraatmadja & Bailer-Jones, 2016; Bailer-Jones, 2015; Gandhi et al., 2019). We use the Milky Way prior described in Chapter 3 to derive the distance posterior distributions of sources.

The parallaxes measured by *Gaia*-DR2 have a global zero-point offset of -0.029 mas (Luri et al., 2018). Hence the parallax values from *Gaia* were corrected before being used for the distance estimation using the Milky Way prior. These corrected parallax values along with the estimated values of distances of 11 BHBs for which *Gaia*-DR2 measured parallaxes has been reported in Table

4.4 and Table 4.5. There are also reports that the *Gaia*-DR2 parallaxes on average have a systematic offset of -0.075 ± 0.029 mas (Xu et al., 2019), but we use the more established -0.029 mas offset (Luri et al., 2018) for the correction of the parallaxes. 11 of the 16 systems in our sample also have distance estimations in the literature (see Table 4.4 and 4.5 for more details), and *Gaia*-DR2 measured the parallax of six of those systems (1A 0620-00, XTE J1118+480, GS 1124-684, GRO J1655-40, Swift J1753.5-0127 and SAX J1819-2525). We compare the distance estimates derived from *Gaia* parallaxes to the ones available in the literature and use the better constrained distance for determining and analysing the PKV distributions.

4.5.2 Systemic radial velocity estimates

We have three systems with poorly constrained systemic radial velocities (Swift J1753.5-0127, VLA J2130+12 and GRS 1716-249). Using the best distance estimates for these systems, we project them onto the Galactic plane. We estimate the expected systemic radial velocity ($\bar{\gamma}$) of the system at this projected distance onto the Galactic plane and assuming that the system is undergoing pure Galactic rotation about the Galactic centre. We note that this estimated value of systemic radial velocity is not a true indicator of the systemic radial velocity of the system as it might have received kicks, and thus is probably not following a pure Galactic rotation about the Galactic centre. Thus for each system, we estimate five probable systemic radial velocity Gaussian distributions with medians of $\bar{\gamma}$, $\bar{\gamma} \pm 50$ km s⁻¹ and $\bar{\gamma} \pm 100$ km s⁻¹ (see Table 4.5). We limit our assumed distributions of the systemic radial velocities based on the fact that out of the systems for which systemic radial velocity is measured, the values lie between -142 ± 1.5 km s⁻¹ for GRO J1655-40 (Shahbaz et al., 1999) and 107 ± 2.9 km s⁻¹ for SAX J1819.3-2525 (Orosz et al., 2001).

4.6 Analysis - Potential kick velocity

As explained in §4.1, peculiar velocity of a system when it crosses the Galactic plane is a better probe to understand the kick a BHXB received when the BH was born. Since all the parameters, namely proper motion, systemic radial velocity and parallax (or distance), have error bars associated with them, it is crucial to propagate these errors appropriately to estimate the Galactocentric orbits of the systems. The age of most BHXBs is not known, which makes integrating the Galactocentric orbits back to the time of birth of the BH uncertain. We thus developed a Monte Carlo (MC) methodology that accounts for the errors on the measured quantities and determines the peculiar velocity every time the system crosses the Galactic plane.

4.6.1 Methodology and code for PKV

The code integrates the Galactocentric orbit of every system in our sample back for 10 Gyrs and records the velocity of the system at every plane crossing. Instead of a delta function for the measurement, it involves using Gaussian distributions of the measured parameters with reported uncertainties as standard deviation. Random values are picked from these Gaussian distributions as inputs to *galpy*¹ (Bovy, 2015) to create instances of Galactocentric orbits for ~ 5000 random draws to make sure we have sampled the input distribution properly. We assume a Galactic potential given by the *galpy* model MWPotential2014 (see Bovy, 2015). The Galactocentric orbits are integrated back in time for 10 Gyrs, which exceeds the likely ages of LMXB systems. GRO J1655–40 (Shahbaz, 2003), GS 1354–64 (Casares et al., 2009) and SAX J1819–2525 (MacDonald et al., 2014) are intermediate-mass systems and may have a shorter lifetime than standard LMXBs. Cyg X-1 is a HMXB and has not lived long enough to cross the Galactic plane (Wong et al., 2012). So this calculation, while indicative of the kick, does not represent the system’s true history. To check if the integration of the

¹<https://docs.galpy.org/en/v1.6.0/>

systems back for 10 Gyrs is valid for these systems, we integrated the orbits of these systems back in time for 1 Gyr with 50,000 random draws and found that our results were not affected and were the same as those using 5000 draws and 10 Gyr orbits. Thus, for uniformity we have used a time integration of 10 Gyrs for all systems.

The peculiar velocity at each Galactic plane crossing (i.e. $z=0$, where z is the height above the Galactic plane) is calculated as

$$v_{\text{peculiar}} = [(U - U_0)^2 + (V - V_0)^2 + (W - W_0)^2]^{0.5} \quad (4.5)$$

Here U , V and W are Galactic space velocities towards the Galactic centre, in the direction of Galactic rotation and towards the North Galactic Pole respectively (Johnson & Soderblom, 1987). U_0 , V_0 and W_0 are the U , V , W components of the Galactocentric space velocities of the local standard of rest at a time when the system crosses the Galactic plane.

This approach allows us to estimate potential kick velocity distributions even if all the parameters required to construct the three dimensional motion are not accurately known. This will also help in estimating the potential kick velocities for newly discovered BHXBs that go into outburst, and when uncertain parameters of known systems are updated with new measurements. The code detailing the MC simulation methodology for estimating the potential kick velocity probability distribution and the distance estimation using our Milky way prior is available at the github link <https://github.com/pikkyatri/BHnataalkicks>.

4.6.2 Potential kick velocity distributions of new VLBI sources

We estimated the potential kick velocity (PKV) probability distributions for the three sources for which we made proper motion measurements; GX 339–4, Swift J1753.5–0127 and GRS 1716–249. The proper motion input for the MC

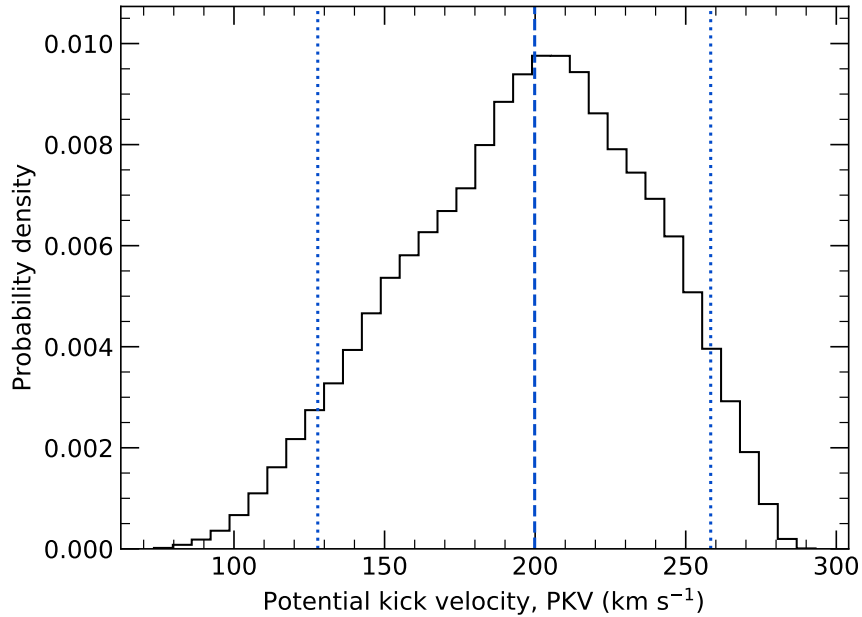


Figure 4.4: Potential kick velocity probability distribution of GX 339–4 with a median of 200 km s^{-1} (dashed line) and 5^{th} and 95^{th} percentile of 122 km s^{-1} and 258 km s^{-1} (in dotted lines), respectively.

simulation is a Gaussian distribution based on the measured proper motion and error bars.

4.6.2.1 GX 339–4

Gaia could not make a parallax measurement for GX 339–4. For the distance input we used a uniform distribution between 5 and 13 kpc as estimated by Heida et al. (2017). The system velocity input for the code was a Gaussian distribution based on the measurement of Heida et al. (2017) (Table 4.4). Running MC simulations for these distributions gives a PKV probability distribution as shown in Figure 4.4 with a median of 200 km s^{-1} and the 5^{th} percentile at 122 km s^{-1} .

4.6.2.2 GRS 1716–249

della Valle et al. (1994) estimated the distance to GRS 1716–249 as $2.4 \pm 0.4 \text{ kpc}$, which we used as a Gaussian input prior. The systemic radial velocity of this

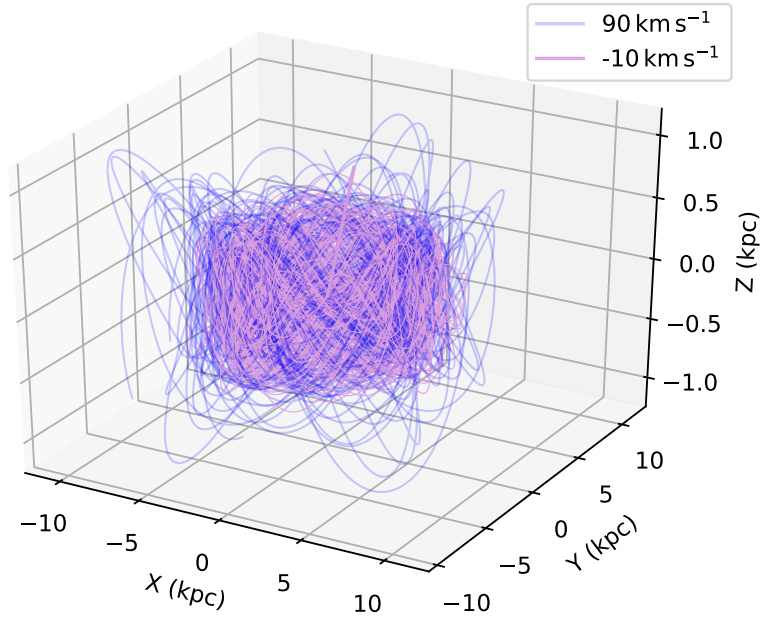
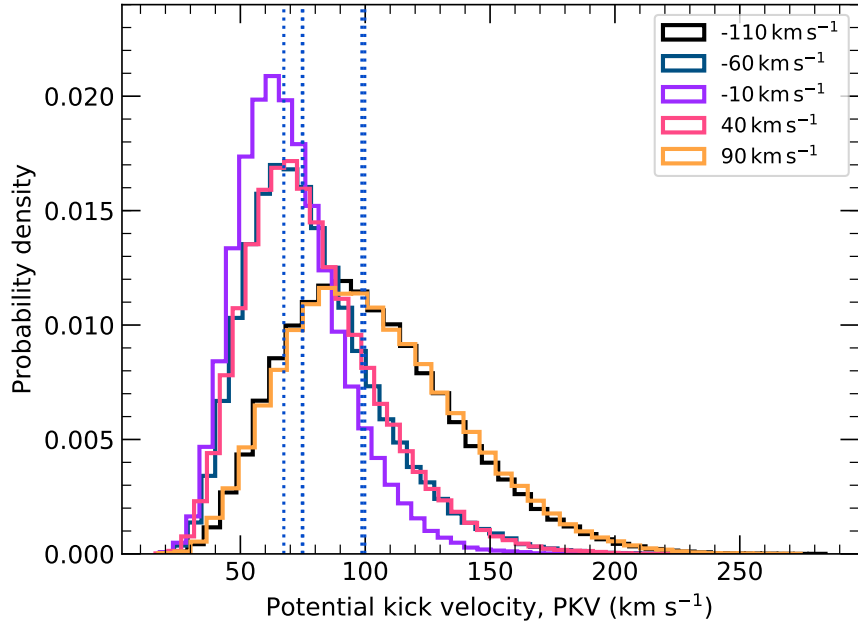


Figure 4.5: Top panel: PKV probability distribution of GRS 1716–249 using Gaussian systemic radial velocity ($\bar{\gamma}$) distributions with means of -110 km s^{-1} , -60 km s^{-1} , -10 km s^{-1} , 40 km s^{-1} and 90 km s^{-1} all with a 1σ of 50 km s^{-1} . The medians of all the PKV distributions are the blue dashed vertical lines. The lowest PKV probability distribution median is of $\sim 70 \text{ km s}^{-1}$ and corresponds to the systemic radial velocity of $-10 \pm 50 \text{ km s}^{-1}$. Bottom panel: a 3-D visualisation of the Galactocentric orbit of GRS 1716–249, integrated for 1 Gyr for 20 orbit instances each of the lowest ($67^{+41}_{-27} \text{ km s}^{-1}$) and highest ($100^{+68}_{-47} \text{ km s}^{-1}$) PKV corresponding to systemic radial velocities of $-10 \pm 50 \text{ km s}^{-1}$ and $90 \pm 50 \text{ km s}^{-1}$, respectively. All three axes are in kpc. The system does not go beyond 1 kpc above the Galactic plane in both the cases.

system has not been measured yet. A system at the Galactocentric radius of GRS 1716–249 and in the Galactic plane is expected to have a systemic radial velocity $\bar{\gamma}$ of $\sim -10 \text{ km s}^{-1}$. We thus run the MC simulations assuming five different Gaussian systemic radial velocity distributions with means of -110 km s^{-1} , -60 km s^{-1} , -10 km s^{-1} , 40 km s^{-1} and 90 km s^{-1} , all with a 1σ of 50 km s^{-1} . All five PKV probability distributions have a median above $\sim 70 \text{ km s}^{-1}$ (see Figure 4.5, left panel and Table 4.4). In figure 4.5 (right panel) we plotted twenty orbits for the maximum ($100_{-47}^{+68} \text{ km s}^{-1}$) and minimum ($67_{-27}^{+41} \text{ km s}^{-1}$) PKVs corresponding to systemic radial velocities of 90 km s^{-1} and -10 km s^{-1} , respectively. The orbits stay within the vertical thick stellar disc limits of $\sim 1 \text{ kpc}$ (Gilmore & Reid, 1983).

4.6.2.3 Swift J1753.5–0127

Gaia–DR2 measured a parallax of $-0.01 \pm 0.13 \text{ mas}$ for this system. As there is a zero-point offset in all *Gaia* parallax measurements of -0.029 mas (Luri et al., 2018), we use the corrected parallax of $0.02 \pm 0.13 \text{ mas}$ for our simulations. We determined a posterior distribution for the distance as shown in Figure 4.6-Left panel. Comparing this with the distance estimated for this source in the literature ($6 \pm 2 \text{ kpc}$) (Cadolle Bel et al., 2007) suggests that the poorly constrained *Gaia* parallax may be overestimating the distance. We thus use a Gaussian distance distribution centred at 6 kpc with a 1σ of 2 kpc as input for the simulations rather than the distance distribution derived using *Gaia* parallax. Along with the distance distribution, we use Gaussian distributions of the proper motion and five different Gaussian distributions (see §4.5.2 and Table 4.5) as systemic radial velocity (γ) inputs to calculate the PKV probability distribution (Figure 4.6-Right panel). Even the lowest median amongst the five PKV probability distributions is at 142 km s^{-1} , with the 5^{th} and 95^{th} percentiles as 76 km s^{-1} and 243 km s^{-1} , respectively (see Table 4.4). Over the past 10 Gyrs, the system has reached as high as 1.5 kpc above the Galactic plane.

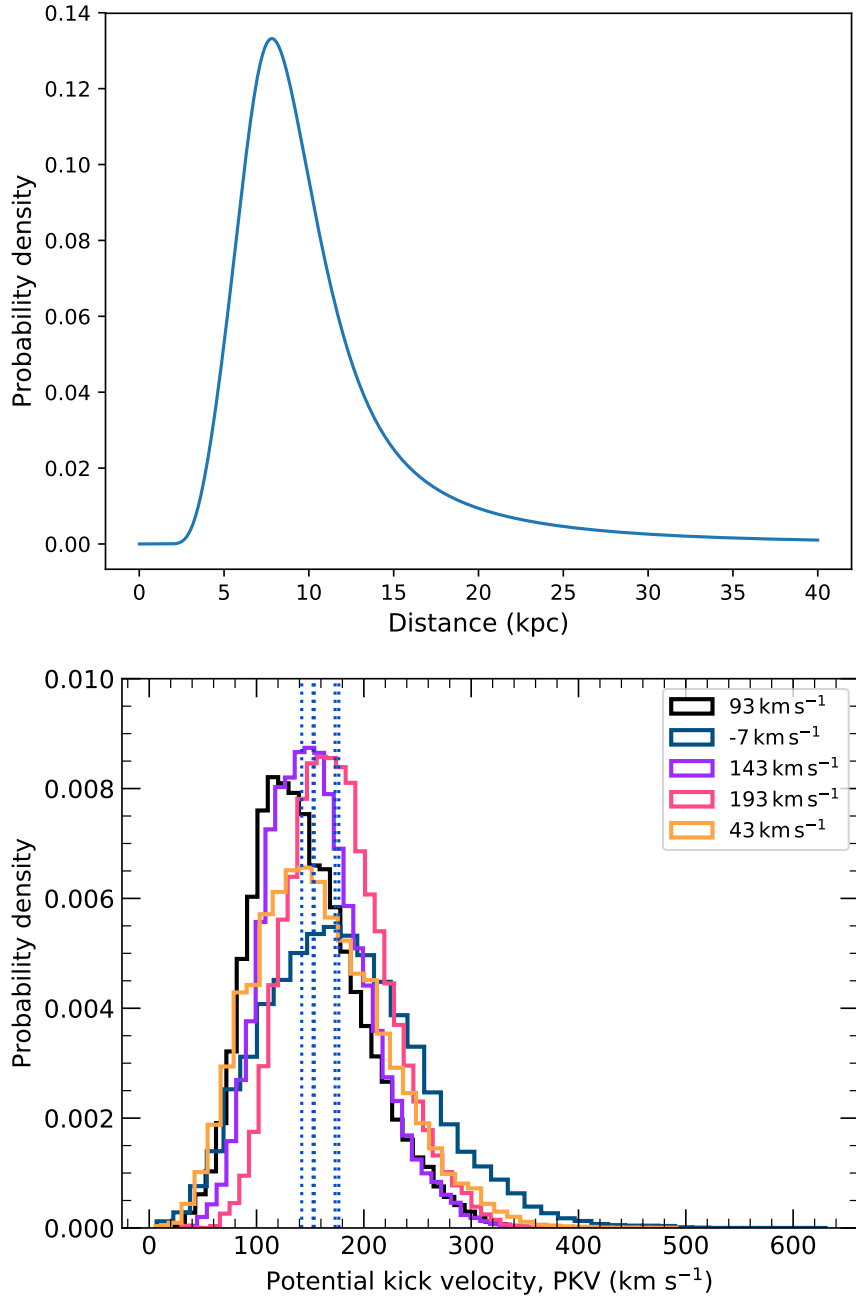


Figure 4.6: Top panel: Posterior distribution function for the distance to Swift J1753.5–0127, constructed from the *Gaia*-DR2 parallax measurement using the Milky Way LMXB distribution prior (see §4.5.1 for details). The mode of the distribution is at 7.7 kpc. The 5th, 50th and 95th percentiles of the distance are at 4.8, 8.8 and 20.8 kpc respectively. Bottom panel: PKV probability distribution of Swift J1753.5–0127 using Gaussian systemic radial velocity ($\bar{\gamma}$) distributions with means of -7 km s^{-1} , 43 km s^{-1} , 93 km s^{-1} , 143 km s^{-1} and 193 km s^{-1} all with a 1σ of 50 km s^{-1} . The input distance distribution of $6 \pm 2 \text{ kpc}$ was used instead of the distance posterior distribution derived using the *Gaia* parallax as the former was more tightly constrained. The lowest median amongst all the PKV probability distributions is at 142 km s^{-1} and the 5th percentiles of all the PKV probability distributions are above 70 km s^{-1} .

4.6.3 PKV distributions of *Gaia* DR–2 and archival sources

We used our methodology (see §4.5.1) to invert the *Gaia*–DR2 parallaxes for eight systems that *Gaia*–DR2 measured parallaxes, and for two sources (V404 Cyg and VLA J2130+12) that had archival parallax measurements. We also used the proper motion and parallax of MAXI J1820+070 from Chapter 3 to determine the distance posterior distribution of MAXI J1820+070. We have summarised the results for these simulations in Table 4.4. Out of these 11 systems, six also had distance constraints in the literature. We used the distance estimations from the literature (d_{lit}) as inputs for the MC simulations to obtain another set of PKV probability distributions for these six systems (1A 0620-00, GS 1124–684, GRO J1655–40, Swift J1753.5–0127, SAX J1819–2525 and XTE J1118+480). We thus obtain two PKV probability distributions each for these seven systems, but use the PKV probability distributions determined using the literature distance estimates (d_{lit}) for further analysis of these systems as they were more tightly constrained.

We used the distance posterior derived from parallax measurements for our PKV probability distributions for four systems, namely GS 1354–64, Cyg X–1, V404 Cyg and VLA J2130+12, as they did not have better distance estimates in the literature (See Table 4.4 and Table 4.5). We tested the sensitivity of the PKV distribution of these four systems to the prior we are using to calculate the distance posterior, using an exponentially decreasing volume density prior (Astraatmadja & Bailer-Jones, 2016; Gandhi et al., 2019) to determine a revised PKV distribution. The only system showing a marked difference in the PKV distributions from the two priors was GS 1354–64, with a revised median PKV of 183_{-64}^{+102} km s^{–1} as compared to 213_{-78}^{+88} km s^{–1} from the Milky Way prior. However, even this difference was within the uncertainties of the PKV distribution using the Milky Way prior.

For V404 Cyg, we use the archival VLBI proper motion and parallax measurements (Miller-Jones et al., 2009b) as they were more precise than the *Gaia*–DR2

measurements. The parallax and proper motion for VLA J2130+12 were measured by Kirsten et al. (2014), though there is no available estimate of its systemic radial velocity. We thus used the expected radial velocity of a source at the Galactocentric distance of VLA J2130+12 but in the Galactic plane as the input for estimating its PKV probability distribution. For systems that did not have measured parallaxes, we use the best estimates on distance present in the literature (Table 4.5). *Gaia*-DR2 did not measure proper motions for MAXI J1836-194 and GRS 1915+105, so we also use archival VLBI proper motion measurements for these systems. We have reported the 5th, 50th and 95th percentiles for both the distance distribution that we determined using the LMXB Milky Way prior described in §4.5.1, and for the potential kick velocities for these systems.

4.7 Discussion

4.7.1 Potential kick velocity distribution - BHBX population

We investigated the distribution of the potential kick velocities in BHBX systems based on the results in §4.6.2 and §4.6.3. Given the probabilistic nature of these results (probability distributions for the predicted velocity of each system), we follow the Bayesian hierarchical methodology outlined by Mandel (2010) and Hogg et al. (2010) for fitting a distribution model. We evaluate the distribution of posteriors with unimodal (with mean of μ and standard deviation of σ) and bimodal (with means of μ_1, μ_2 , standard deviations of σ_1, σ_2 , and weights of w_1 and $w_2 = 1 - w_1$) gaussian models. For this purpose, we used a Hamiltonian Markov chain Monte Carlo (MCMC) algorithm (Neal, 2012; Betancourt, 2019) with No U-Turn Sampling (NUTS; Hoffman & Gelman, 2011) as implemented in PyMC3 (Salvatier et al., 2016). We assumed uninformative priors for all parameters in the models and verified convergence in the final samples for all parameters using the Gelman-Rubin diagnostic test (Gelman & Rubin, 1992), with $\hat{R} < 1.001$ for

Table 4.4: PKV distributions for systems that have a systemic radial velocity measurement (γ) in the literature. The measured quantities are the various parameters for the BHXB systems that were available in the literature, and the estimated quantities are the values that have been determined in this work using the MC simulations code described in §4.6.1. d_{lit} is the best distance estimate available in the literature for some of these systems. The *Gaia* offset corrected parallax measurement and the distance distribution (d_{post}) estimated using the LMXB Milky way density prior are reported. The 5th and 95th percentiles of these distributions are the upper and lower limits on the distance estimated using the Milky Way prior. For distances in the literature that were just a range, a uniform distribution was used as the input to the MC code. For the distances in literature that have been reported with error bars, the input to our MC code was a Gaussian distribution. The PKV is reported as the median of the PKV probability distribution with the lower and upper limits representing the 5th and 95th percentiles. PKV_{post} and PKV_{lit} are the potential kick velocity distributions using the d_{post} and the d_{lit} as input distance distributions, respectively. The last column is the suggested birth pathway for the BH in each system and could be SN (Supernova), DC (Direct collapse) or U (Unsure). Refer to §4.7.1 and §4.7.4 for the explanation of the suggested birth pathway. References: [1] Gaia Collaboration et al. (2018a); [2] González Hernández & Casares (2010); [3] Cantrell et al. (2010); [4] González Hernández et al. (2008a); [5] Gelino et al. (2006); [6] Orosz et al. (1996); [7] Hynes (2005); [8] Casares et al. (2004); [9] Shahbaz et al. (1999); [10] Hjellming & Rupen (1995); [11] Orosz et al. (2001); [12] MacDonald et al. (2014); [13] Gies et al. (2008); [14] Miller-Jones et al. (2009a); [15] Casares & Charles (1994); [16] Orosz et al. (1998); [17] Heida et al. (2017); [18] Russell et al. (2014); [19] Reid et al. (2014); [20] Steeghs et al. (2013); [21] Atri et al. (2020); [22] Torres et al. (2019); [23] This work.

Source	Measured quantities					Estimated quantities in this work				
	$\mu_{\alpha} \cos \delta$ (mas yr ⁻¹)	μ_{δ} (mas yr ⁻¹)	γ (km s ⁻¹)	d_{lit} (kpc)	Parallax (mas)	d_{post} (kpc)	PKV_{post} (km s ⁻¹)	PKV_{lit} (km s ⁻¹)	Birth	
1A 0620-00	-0.09±0.25 ^[1]	-5.20±0.30 ^[1]	8.5±1.8 ^[2]	1.06±0.1 ^[3]	0.67±0.16 ^[1]	1.9 ^{+2.0} _{-0.7}	60 ⁺⁵⁵ ₋₂₁	34 ⁺⁰⁸ ₋₀₈	DC	
XTE J1118+480	-17.57±0.34 ^[1]	-6.98±0.43 ^[1]	2.7±1.1 ^[4]	1.72±0.10 ^[5]	0.30±0.40 ^[1]	13 ⁺²¹ ₋₁₁	212 ⁺³⁴⁷ ₋₁₀₉	186 ⁺³⁹ ₋₅₅	SN	
GS 1124-684	-2.44±0.61 ^[1]	-0.71±0.46 ^[1]	16±5 ^[6]	5.9±0.3 ^[7]	0.64±0.34 ^[1]	5.3 ^{+7.7} _{-3.5}	101 ⁺⁸⁴ ₋₅₄	133 ⁺³⁵ ₋₃₄	SN	
GS 1354-64	-9.38±2.22 ^[1]	-5.70±2.26 ^[1]	103±4 ^[8]	—	1.86±0.58 ^[1]	7.4 ^{+9.6} _{-6.3}	213 ⁺⁸⁸ ₋₇₈	—	SN	
GRO J1655-40	-4.20±0.13 ^[1]	-7.44±0.09 ^[1]	-1.42±1.5 ^[9]	3.2±0.2 ^[10]	0.27±0.08 ^[1]	6.4 ^{+4.6} _{-3.2}	137 ⁺⁴⁷ ₋₃₆	140 ⁺²⁸ ₋₂₆	SN	
SAX J1819.3-2525	-0.73±0.07 ^[1]	0.42±0.06 ^[1]	107±2.9 ^[11]	6.2±0.7 ^[12]	0.18±0.04 ^[1]	7.5 ^{+1.9} _{-2.2}	189 ⁺¹⁸² ₋₈₇	122 ⁺⁶⁴ ₋₂₈	SN	
Cyg X-1	-3.88±0.05 ^[1]	-6.17±0.05 ^[1]	-5.1±0.5 ^[13]	—	0.42±0.03 ^[1]	2.3 ^{+0.2} _{-0.3}	30 ⁺¹⁰ ₋₁₀	—	DC	
V404 Cyg	-4.99±0.19 ^[14]	-7.76±0.21 ^[14]	-0.4±2.2 ^[15]	—	0.418±0.024 ^[14]	2.4 ^{+0.3} _{-0.2}	43 ⁺⁰⁸ ₋₀₉	—	DC	
4U1543-475	-7.41±0.14 ^[1]	-5.33±0.10 ^[1]	-87±3 ^[16]	7.5±1.0 ^[16]	—	—	—	124 ⁺²⁷ ₋₂₇	SN	
GX 339-4	-3.95±0.07 ^[23]	-4.71±0.06 ^[23]	26±2 ^[17]	5-13 ^[17]	—	—	—	200 ⁺⁵⁸ ₋₇₂	SN	
MAXI J1836-194	-2.3±0.6 ^[18]	-6.1±1.0 ^[18]	61±15 ^[18]	4-10 ^[18]	—	—	—	162 ⁺⁴² ₋₄₇	SN	
GRS 1915+105	-2.86±0.07 ^[19]	-6.20±0.09 ^[19]	11±4.5 ^[20]	8.6±2.0 ^[19]	—	—	—	49 ⁺³⁷ ₋₂₈	DC	
MAXI J1820+070	-3.05 ± 0.05 ^[21]	-6.39 ± 0.08 ^[21]	22±2 ^[22]	—	0.348 ± 0.033 ^[21]	2.96 ^{+0.33} _{-0.33}	120 ⁺²⁵ ₋₂₉	—	SN	

Table 4.5: PKV distributions for systems that do not have a systemic radial velocity measurement (γ) in the literature. For these systems, we calculated the predicted systemic radial velocity ($\bar{\gamma}$) for pure Galactic rotation at a projected distance on the Galactic plane (see §4.5.2 for more details). We run the MC simulations code for five possible systemic radial velocity distributions. The measured quantities are the various parameters for the BHXB systems that were available in the literature, and the estimated quantities are the values that have been determined in this work using the MC simulations code described in §4.6.1. d_{lit} is the best distance estimate available in the literature for some of these systems. The *Gaia* offset corrected parallax measurement (as described in §4.5.1) and the distance distribution (d_{post}) estimated using the LMXB Milky Way density prior are reported. The 5th and 95th percentiles of these distributions are the upper and lower limits on the distance estimated using the Milky Way prior. For distances in the literature that were just a range, a uniform distribution was used as the input to the MC code. For the distances in literature that have been reported with error bars, the input to our MC code was a Gaussian distribution. The PKV is reported as the median of the PKV probability distribution with the lower and upper limits representing the 5th and 95th percentiles. PKV_{post} and PKV_{lit} are the potential kick velocity distributions using the d_{post} and the d_{lit} as input distance distributions, respectively. The last column is the suggested birth pathway for the BH in each system and could be SN (Supernova), DC (Direct collapse) or U (Uncure). We have stated that just for the central predicted systemic radial velocity. Refer to §4.7.1 and §4.7.4 for the explanation of the suggested birth pathway. References: [1] This work; [2] della Valle et al. (1994); [3] Cadolle Bel et al. (2007) [4] Gaia Collaboration et al. (2018a); [5] Kirsten et al. (2014)

Source	Measured quantities			Estimated quantities in this work					Birth
	$\mu_\alpha \cos \delta$ (mas yr ⁻¹)	μ_δ (mas yr ⁻¹)	d_{lit} (kpc)	Parallax (mas)	d_{post} (kpc)	$\bar{\gamma}$ (km s ⁻¹)	PKV_{post} (km s ⁻¹)	PKV_{lit} (km s ⁻¹)	
GRS 1716-249	-1.7 \pm 1.25 ^[1]	-2.48 \pm 0.75 ^[1]	2.4 \pm 0.4 ^[2]	—	—	-110 \pm 50	—	99 $^{+68}_{-45}$	U
						-60 \pm 50	—	75 $^{+54}_{-31}$	
						-10 \pm 50	—	67 $^{+41}_{-27}$	
						40 \pm 50	—	75 $^{+54}_{-32}$	
						90 \pm 50	—	100 $^{+68}_{-47}$	
Swift J1753.5-0127	0.84 \pm 0.06 ^[1]	-3.64 \pm 0.06 ^[1]	6 \pm 2 ^[3]	0.02 \pm 0.13 ^[4]	8.8 $^{+12}_{-4.0}$	-7 \pm 50	212 $^{+114}_{-104}$	154 $^{+116}_{-84}$	
						43 \pm 50	196 $^{+118}_{-89}$	142 $^{+101}_{-66}$	
						93 \pm 50	240 $^{+128}_{-115}$	177 $^{+135}_{-103}$	SN
						143 \pm 50	192 $^{+118}_{-82}$	153 $^{+88}_{-63}$	
						193 \pm 50	204 $^{+115}_{-77}$	173 $^{+86}_{-65}$	
						-90 \pm 50	146 $^{+116}_{-74}$	—	
						-40 \pm 50	101 $^{+95}_{-47}$	—	
						10 \pm 50	82 $^{+63}_{-32}$	—	U
						60 \pm 50	86 $^{+60}_{-34}$	—	
VLA J2130+12	-0.07 \pm 0.13 ^[5]	-1.26 \pm 0.29 ^[5]	—	0.45 \pm 0.08 ^[5]	2.4 $^{+3.4}_{-1.8}$	110 \pm 50	111 $^{+79}_{-49}$	—	

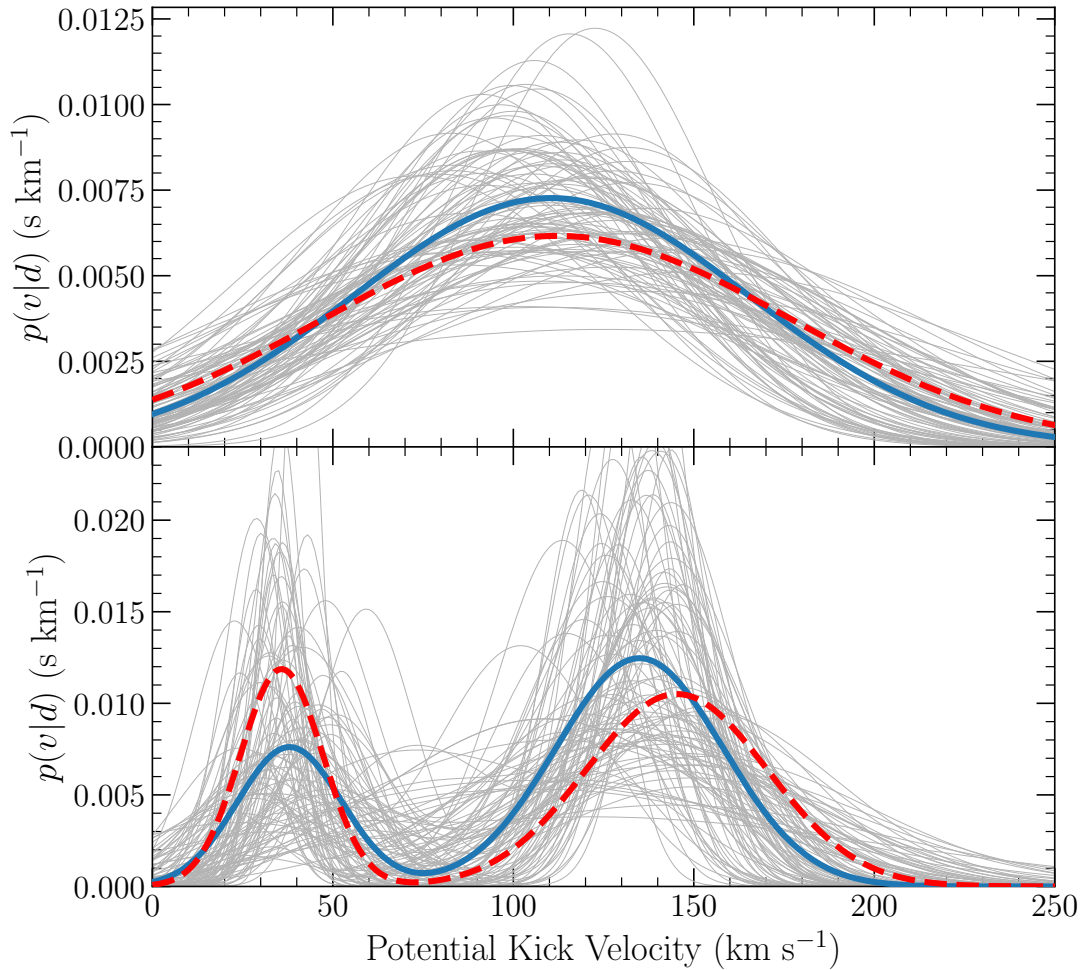


Figure 4.7: Realisations of the inferred unimodal (top) and bimodal (bottom) distributions for potential kick velocities (v), inferred from the data (d). The blue lines represent the model corresponding to the median values from the posterior sample for data from all the systems in the sample, while the red dashed lines represent the model based on the median from the posterior sample for data from the 13 systems with systemic radial velocity (γ) constraints. The faint gray lines are a small random subset from the posterior MCMC sample for all the systems, as a demonstration of uncertainty.

Table 4.6: Model estimates for the potential kick velocity distribution using unimodal and bimodal gaussian models when all systems are considered and when only systems with well constrained radial systemic velocity (γ) are considered. Reported values are medians (μ) of the posterior distributions, along with uncertainties (σ) and all values are in km s^{-1} . w_1 is the weight of the Gaussian distribution with the mean μ_1 . AICc is the corrected Akaike information criterion. A smaller AICc suggests that the model is more favourable.

		μ_1	σ_1	μ_2	σ_2	w_1	AICc
All systems	Unimodal	110±16	55±14	-	-	-	-16.6
	Bimodal	38±12	14±10	135±13	23±15	0.3±0.1	-4.4
Systems with γ	Unimodal	112±22	65±20	-	-	-	-2.4
	Bimodal	36±10	11±9	145±15	25±17	0.3±0.1	10.7

all parameters (\hat{R} closer to one indicates certainty of convergence of the chains).

We evaluated the distribution with both models over two sets of velocities, with one set containing all the BHXB systems in our sample (16 systems), and a second set containing only the systems with systemic radial velocities that have been measured in the literature (13 systems). The results for both models in both cases are tabulated in Table 4.6 and plotted in Fig. 4.7.

Due to the low number of “events” (number of systems for which we have kick velocity PDFs), we used the corrected Akaike information criterion (AICc; Akaike, 1974; Cavanaugh, 1997; Burnham & Anderson, 2002) to compare the models. As tabulated in Table 4.6, the unimodal distribution is clearly favoured in both cases (a smaller AICc suggests a better model). Removal of systems with loose systemic radial velocity constraints provides a marginal relative improvement to the bimodal model, as the difference between the AICc parameter reduced when evaluated for a sample devoid of loose systemic radial velocity constraints as compared to a sample that consisted of all 16 systems. It is worth noting however, that the clear separation of posterior constraints for μ_1 and μ_2 in the bimodal model (given the uninformative priors) hints at the possibility of a bimodal nature for the distribution of the potential BHXB kicks, but testing this model is currently hampered by the low number of BHXB systems with potential

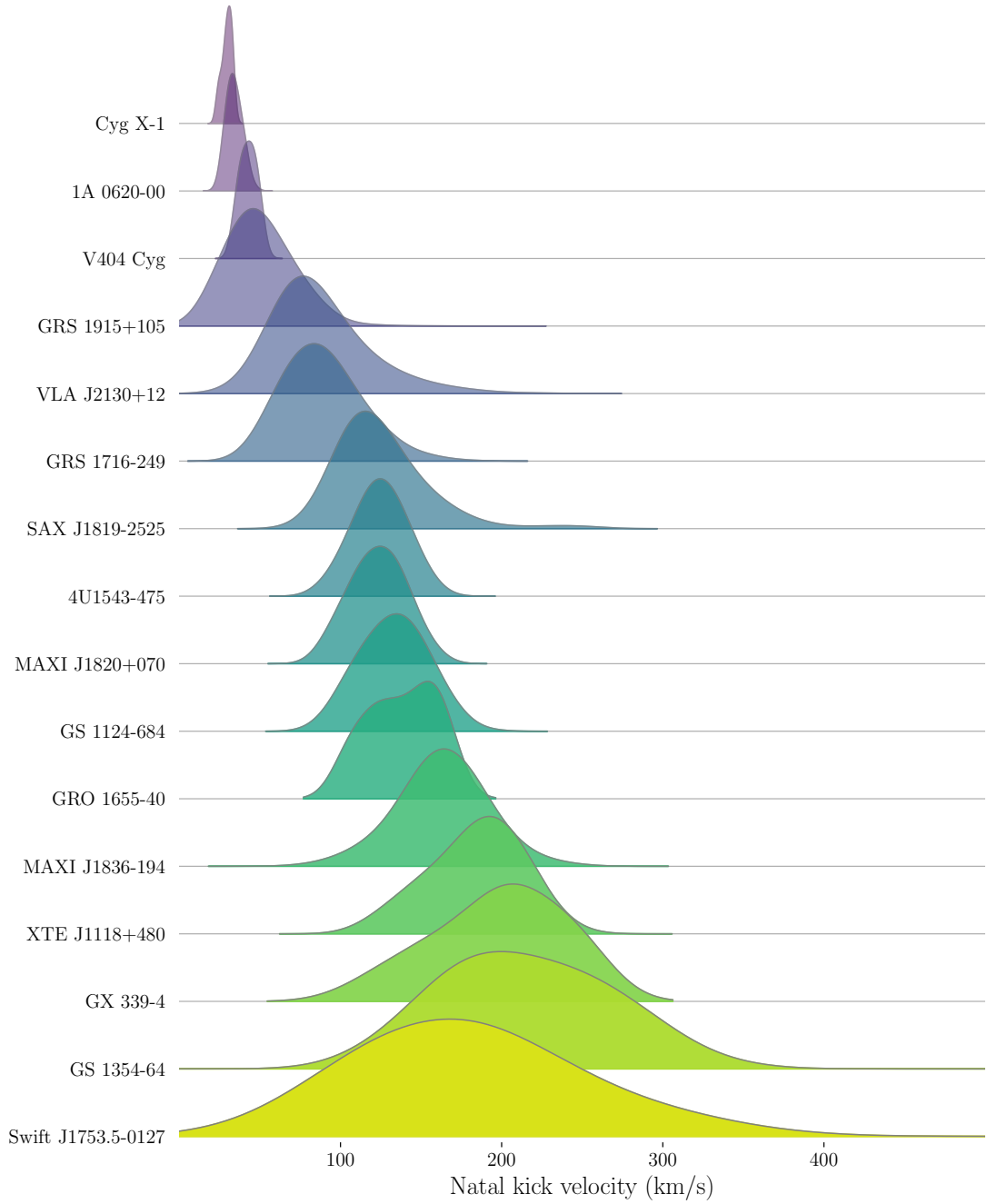


Figure 4.8: PKV probability distributions of the 16 BHXBs in our sample. It can be seen that no single system is responsible for either of the two most prominent peaks in the aggregated natal kick distribution.

kick velocity constraints.

To demonstrate that neither of the two components in the bimodal model are caused by a single source, we plot all individual distributions in Figure 4.8. We find that there are at least four systems (first four systems in Figure 4.8) contributing to the lower velocity peak (41 km s^{-1}), which could be consistent with birth of the BH by direct collapse. We find at least ten systems (SAX J1819–2525 to Swift J1753.5–0127 in Figure 4.8) clearly contributing to the higher velocity peak (135 km s^{-1}). Better constraints on some of the measured parameters for systems like GS 1124-684, VLA J2130+12, GS 1352–64, Swift J1753.5–0127 and SAX J1819–2525 might help in tightening their PKV probability distributions, which could change the form (and interpretation) of the PKV distribution of BHB population. With the current available data on BHBs, our results provide the best constraint we can obtain for the PKV distribution of BHBs.

4.7.2 Potential Kick velocity interpretation

The potential kick velocity (PKV) that we estimate here is not the actual natal kick the BH receives when it is born, but is the potential peculiar velocity of the system, with which it may have been kicked out of the Galactic plane. Calculating the actual BH natal kick from the BHB peculiar velocity at Galactic plane crossing is complex and depends on modelling the system (Repetto et al., 2012, 2017), taking into account the orbital period, the component masses of the binary system, the direction of the kick and the mass ejected in the SN explosion (Nelemans et al., 1999). It also involves simulating the subsequent dynamical interaction of the sources and evolution of the binary system. These parameters are currently not well constrained for most systems, and thus simulating the evolution of these systems to determine the actual BH natal kick is out of the scope of this paper. Hence the peculiar velocity of the system at Galactic plane crossing is currently the best proxy that we can use for BH natal kicks in a population-wide analysis such as this one. Since most star forming regions are in the Galactic

plane, it is probable that most BHXBs form in the Galactic plane. Since we do not know the time of BH birth, we instead consider the velocity of the system every time it crosses the Galactic plane as a potential velocity kick the system might have received.

According to Mignard (2000), stellar velocity dispersions due to Galactic interactions are the order of $\sim 50\text{km s}^{-1}$ for old systems (and lower for younger systems). Since BHXBs are more massive than these systems, they will suffer even lower velocity dispersions. Thus we classify systems with potential kick velocities higher than the $\sim 50\text{km s}^{-1}$ limit as systems that might have received strong kicks, and hence the BH in the BHXB might have formed in a SN explosion. We suggest that the systems with a median PKV of less than $\sim 50\text{km s}^{-1}$ are systems with weak potential kicks, and thus could well have formed by direct collapse rather than a SN explosion. Systems that have a PKV distribution such that their median is $>50\text{ km s}^{-1}$ but the 5th is lower than 50 km s^{-1} do not clearly fall into either category, and hence we could not deduce their likely birth mechanism. We find two such sources in our sample, namely VLA J2130+12 and GRS 1716–249. Ten systems in our sample are likely to have been formed in a SN explosion, whereas four systems could plausibly have formed by direct collapse. We summarise the results of our analysis in Tables 4.4 and 4.5.

The PKV probability distribution of GRS 1915+105 (median $\sim 49\text{ km s}^{-1}$) suggests that it could have been born via direct collapse, as the PKV is within the velocity dispersion limits for Galactic scattering ($\sim 50\text{ km s}^{-1}$ for late type stellar systems; Mignard 2000). According to our results the v_{95} values for V404 Cyg and 1A 0620-00 are lower than the v_{95} for GRS 1915+105, suggesting that V404 Cyg and 1A 0620–00 might also have been born without a strong natal kick. The probability of a compact object receiving a kick between angle θ and $\theta + d\theta$ during a SN explosion varies as $\frac{1}{2} \sin \theta d\theta$, where θ is the angle the kick makes with the direction of the peculiar velocity of the system before the explosion. Thus it is also possible that these low PKV systems were born with a SN explosion but

their velocity was reduced due to an asymmetry in the explosion counteracting the recoil kick. For Cyg X-1, the median of the PKV we obtain is in agreement with the estimation of Wong et al. (2012) and suggests a direct collapse birth (albeit with the caveat that this is a high mass X-ray binary and has never crossed the Galactic plane in its lifetime, so our methodology is not strictly applicable).

For our interpretation of PKV as the BH natal kick, we are assuming that none of the systems in our sample were born in GCs. There have been no confirmed BHXBs in GCs, though there are some candidates (Strader et al. 2012; Camilo et al. 2000; Chomiuk et al. 2013; Miller-Jones et al. 2015). GCs only contain 5–10% of the total number of known Galactic X-Ray binaries (Clark, 1975; Bahramian et al., 2014), so this population is likely to be a small fraction of the total BHXBs in the Galaxy.

The Galactocentric orbits in the past 10 Gyrs also show that only four (GRO 1655–40, SAX J1819–2525, GX 339–4 and MAXI J1836–194) out of the 16 systems ever get within 2 kpc of the Galactic centre, which is the truncation radius for a spheroidal bulge model (Dehnen & Binney, 1998). We note that we have classified these systems as having a SN birth, but due to their possible association with being bulge objects we cannot rule out the high PKV as being due to bulge formation and/or interactions.

4.7.3 Comparison with NS natal kicks

The kick velocity distribution of pulsars has been extensively studied (e.g. Hobbs et al., 2005; Fryer et al., 1998; Arzoumanian et al., 2002), whereas there is no well documented kick velocity measurement catalogue for neutron star X-ray binaries (NS XRBs). Thus to understand the relation between NS and BH natal kicks, we compare our BHXB PKV distribution with the pulsar kick velocity distribution (Verbunt et al., 2017). BHXBs and pulsars suffer from different observational biases. The distance to pulsars is usually smaller than the distance to BHXBs, and thus their detection is less affected by extinction. Pulsars just have their two

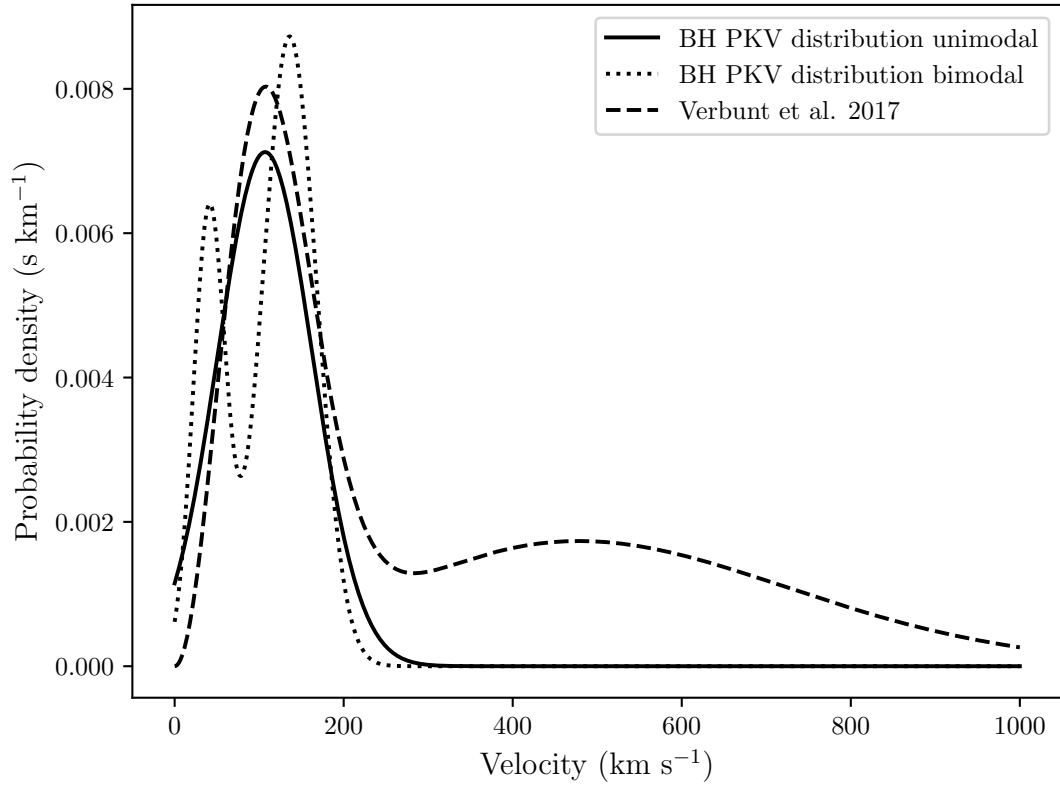


Figure 4.9: Comparison of best fit unimodal and bimodal BHXB PKV distributions to the best pulsar kick velocity distribution. The BHXB PKV unimodal distribution is represented by the solid line and has a median of 110 km s^{-1} . The BHXB PKV bimodal distribution is represented by the dotted line. The best fit, two Maxwellian model for the peculiar velocities of pulsars (Verbunt et al., 2017) is denoted by the dashed line. The unimodal BHXB PKV distribution median is close to the low kick pulsar kick velocity component. There is a dearth of extremely high PKV BHs corresponding to the high velocity Maxwellian component for the pulsar velocity distribution.

dimensional velocities measured, there are no systemic velocity measurements for pulsars. Also, it is possible to observe pulsars that might have received strong enough kicks to disrupt the binary they were a part of, whereas our data sample only consists of BHs that are in binaries. Keeping these biases in mind, we compare BHB and pulsar kick velocities.

Theory suggests that fallback of matter ejected in a SN onto the proto-neutron star can give rise to BHs, so we expect similarities in the kick distributions of BHs and NSs. The most recent NS peculiar velocity distribution is fit better with two Maxwellian components than one (V17). Our bimodal Gaussian (Figure 4.9) fit to the data shows that the medians of the two Gaussians in the BHB PKV distribution ($38 \pm 12 \text{ km s}^{-1}$ and $135 \pm 13 \text{ km s}^{-1}$) are lower than the NS peculiar velocity peaks (120 km s^{-1} and 540 km s^{-1}) for the best fit model by V17 by a factor of 3–4. This may suggest that BHs receive weaker natal kicks as compared to NSs by a factor that is similar to the mass ratios of standard BHs and NSs. This is in contrast to the conclusion of Repetto et al. (2012), where it was shown that BHs and NSs get equally strong kicks. This mismatch of the medians of the two components of the BHB PKV distribution and pulsar kick velocity distribution could also be because of different kick mechanisms in BHs and NSs. For BHs the low velocity kick is probably due to formation by direct collapse, whereas low NS kicks have been attributed to various mechanisms like ultra-stripped SNe (Tauris et al., 2015), electron capture SNe (Gessner & Janka, 2018) and collapse of low iron mass cores (Podsiadlowski et al., 2004).

Our unimodal fit to the BHB PKV data matches the lower Maxwellian component of the pulsar kick velocity distribution (Figure 4.9). However, we are biased against stronger kicks, since they can unbind BHBs and make them unobservable whereas pulsars can be observed even in an unbound state. Due to this selection bias, we expected the BHB PKV distribution kicks to be lower than the V17 peculiar velocities.

4.7.4 Supernova mass loss

We find that there are at least nine systems of the 16 in our sample set that clearly received strong natal kicks ($>50\text{km s}^{-1}$). This makes SN birth more probable for these systems than direct collapse BH birth. We note that our sample set may be biased against observing direct collapse BHs. This is because they will not receive strong kicks and will be located close to the Galactic plane, where detecting distant BHXBs is challenging due to high extinction and scattering.

Symmetric mass loss (ΔM) during a SN explosion is one of the reasons for a natal kick. However, this mass loss has to be $< 0.5(M_{\text{He}}+m)$ for the binary to remain bound (Blaauw, 1961), where M_{He} is the mass of the progenitor helium star and m is the mass of the donor star. Thus the maximum possible recoil velocity due to symmetric mass loss can be estimated by constraining the maximum possible mass ejected in the BHXB system without unbinding the binary. This was given by Nelemans et al. (1999) as

$$v_{\text{sys}} = 213 \left(\frac{\Delta M}{M_{\odot}} \right) \left(\frac{m}{M_{\odot}} \right) \left(\frac{P_{\text{re-circ}}}{\text{days}} \right)^{-1/3} \left(\frac{(M_{\text{BH}} + m)}{M_{\odot}} \right)^{-5/3} \text{ km s}^{-1} \quad (4.6)$$

where ΔM , M_{BH} and m are the mass ejected in the SN, mass of the BH and mass of the donor immediately after the SN, respectively. $P_{\text{re-circ}}$ is the period of the re-circularised orbit of the system after the formation of the BH, and it is assumed that no mass transfer occurs until the re-circularisation of the orbit is complete. v_{sys} is the recoil kick velocity the system should have received due to the symmetric mass loss in the SN explosion. Nelemans et al. (1999) estimated the maximum possible recoil kick velocities for GS 1124–684 and GRO 1655–40 and found that they were limited to $<40 \text{ km s}^{-1}$. Our estimated PKV for all these systems is greater than those estimated by Nelemans et al. (1999) in the case of only symmetric mass ejection. We thus suggest that the observed kick velocity of these systems is not only because of symmetric mass loss in a SN explosion, but due to these systems receiving additional acceleration due to asymmetries

associated with the SN explosion (Janka, 2017).

Gualandris et al. (2005) suggested that XTE J1118+480 received an asymmetric kick that put the system in its current Galactocentric orbit. We measured a PKV of $186 \pm 28 \text{ km s}^{-1}$ for XTE J1118+480, which agrees with the peculiar velocity measurement of Gualandris et al. (2005). Systems like 4U1543–475, GS 1354–64, SAX J1819.3–2525 and MAXI J1820+070 also have high enough PKVs to suggest asymmetries in the SN explosions, keeping in mind that we are assuming that these systems are similar to the ones already studied in the literature (e.g. Nelemans et al., 1999; Gualandris et al., 2005). The observed metal abundances in XTE J1118+480 (González Hernández et al., 2006), GRO J1655–40 (González Hernández et al., 2008a) and SAX J1819.3–2525 (Orosz et al., 2001) also point towards contamination of these sources by a SN and support the hypothesis that they were probably born in SN explosions.

4.7.5 Natal kicks and z-distribution

In the past, the distribution of the distance from the Galactic plane ($|z|$) has been used to determine the strength of BH natal kicks (e.g. van Paradijs & White, 1995; Jonker & Nelemans, 2004; Repetto et al., 2017). We plot the median of the current height probability distributions of all BHBs in our sample using our distance posterior distributions (Table 4.7) in Figure 4.10. It can be seen that all systems with a potential kick velocity $< 100 \text{ km s}^{-1}$ are within 500 pc of the Galactic plane, other than VLA J2130+12. We conducted Pearson and Spearman rank correlation tests to check the correlation of the distance to the Galactic plane ($|z|$) with PKVs of BHBs. We found a potential correlation between the two, with correlation coefficients of 0.51 ± 0.15 ($p=0.02$) and 0.56 ± 0.13 ($p=0.02$) for Pearson and Spearman Rank tests respectively. This, however does not suggest that systems at small heights from the Galactic plane received low kick velocities because of the two outliers GRO J1655–40 and GS 1354–64. This could be because the systems are passing through the Plane at the present time, which is the case

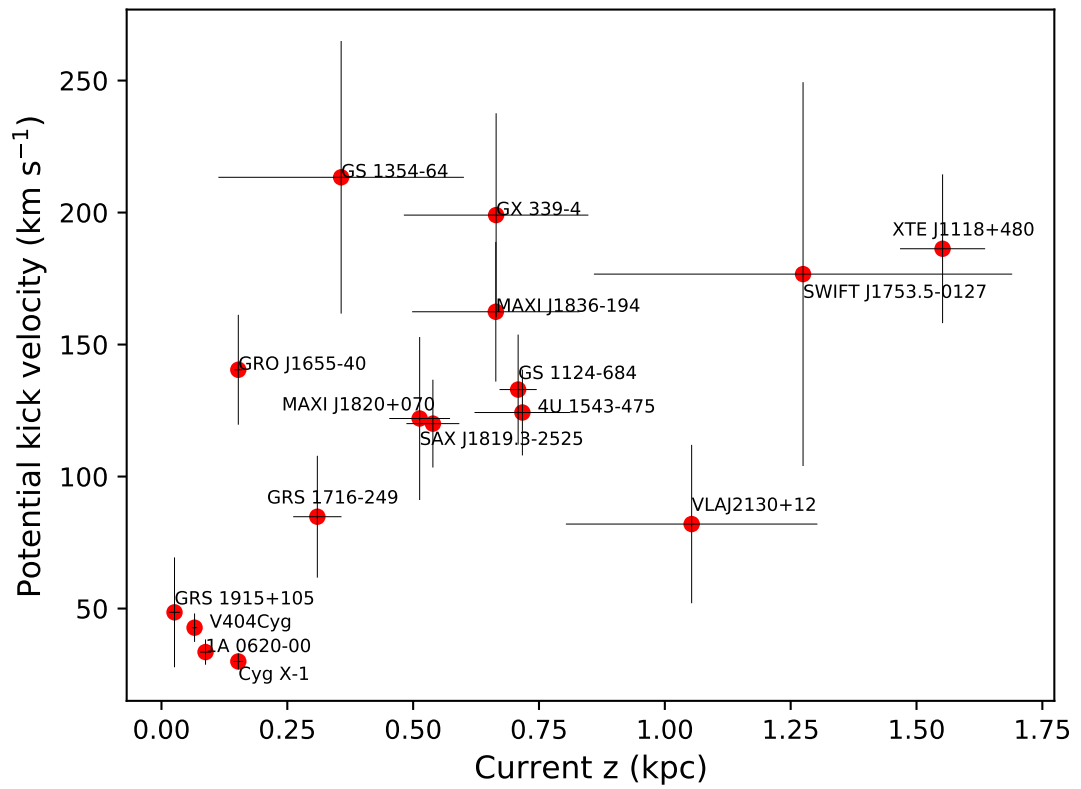


Figure 4.10: The variation of PKV with the current height of the system above the Galactic plane. There are five systems with a PKV below 100 km s^{-1} are within 500 pc of the Galactic plane. There are two systems that are within 500 pc but have PKVs $>100 \text{ km s}^{-1}$

Table 4.7: Current $|z|$ and PKV estimates for every source, along with the assumed mass used for the correlation test. The PKV is the median of the PKV probability distribution and the error bar is the 1σ deviation of the distribution. Current $|z|$ is the median of the current $|z|$ distribution for the estimated distance distributions for each BHXB and the errors are the 1σ of the distributions. GS 1354–64, MAXI J1836–194, GRS 1716–249, MAXI J1820+070 and VLA J2130+12 do not have dynamical mass measurements, so we assumed BH masses of $8M_{\odot}$ (Kreidberg et al., 2012).

Source	PKV (km s^{-1})	Current $ z $ (kpc)	BH mass (M_{\odot})	mass Ref
1A 0620–00	34 ± 5	0.09 ± 0.01	6.6 ± 0.3	van Grunsven et al. (2017)
XTE J1118+480	186 ± 28	1.55 ± 0.09	7.55 ± 0.65	Khargharia et al. (2013)
GS 1124–684	133 ± 21	0.71 ± 0.04	7 ± 0.6	Casares (2007)
GS 1354–64 (BW Cir)	213 ± 52	0.36 ± 0.24	–	–
4U 1543–475	124 ± 16	0.72 ± 0.1	2.7–7.5	Orosz et al. (1998)
GRO J1655-40	140 ± 21	0.15 ± 0.01	6.6 ± 0.5	Casares (2007)
GX 339–4	199 ± 39	0.66 ± 0.18	8.28–11.89	Sreehari et al. (2018)
GRS 1716–249	67 ± 21	0.31 ± 0.05	–	Masetti et al. (1996)
Swift J1753.5–0127	177 ± 73	1.3 ± 0.42	$> 7.4 \pm 1.2$	Shaw et al. (2016)
SAX J1819.3–2525	122 ± 31	0.51 ± 0.06	6.4 ± 0.6	MacDonald et al. (2014)
MAXI J1820+070	120 ± 25	0.54 ± 0.05	9.2 ± 1.3	Atri et al. (2020)
MAXI J1836–194	162 ± 27	0.66 ± 0.17	–	Russell et al. (2014)
GRS 1915+105	49 ± 21	0.03 ± 0.01	10.1 ± 0.6	Steeghs et al. (2013)
Cyg X–1	30 ± 3	0.15 ± 0.01	14.8 ± 1.0	Orosz et al. (2011)
V404 Cyg	43 ± 5	0.07 ± 0.01	9 ± 0.6	Khargharia et al. (2010)
VLA J2130+12	82 ± 30	1.05 ± 0.25	–	–

for GRO J1655–40 as it is on a path towards the Galactic plane in its orbit (Gandhi et al., 2019). The distance estimate of GS 1354–64 is poorly constrained and could be the reason for a misleading current height above the Galactic plane. Thus, the strength of PKV a BHXB receives cannot be determined solely by the current $|z|$. Hence, the approach that we take is currently the best that can be done to estimate natal kick distributions.

Comparisons between the root mean square distance from the Galactic plane (z_{rms}) for BHXBs and NSs have led to contrasting claims about BH natal kicks. NSs and BHs have different observational biases and these contrasting claims could be an artefact of that. White & van Paradijs (1996) suggested that BHs get reduced kicks as compared to NSs. Jonker & Nelemans (2004) updated the distances to these systems and showed that BH natal kicks are as strong as those of NSs. We now update the z_{rms} as we have new distances (in some cases better constrained distances) for BHXBs. Our analysis gives the z_{rms} of BHXBs as ~ 700 pc, which is higher than those estimated by White & van Paradijs (1996) (~ 410 pc) and Jonker & Nelemans (2004) (~ 625 pc), but lower than the most recent estimate by Repetto et al. (2017) (~ 980 pc). If we exclude the halo object XTE J1118+480, the z_{rms} for BHXBs drops down to 595 pc. If we are to believe the relation between z_{rms} and BHXB kick distribution, this would then suggest that NSXBs ($z_{rms}=1$ kpc (van Paradijs & White, 1995)) receive stronger kicks as compared to BHXBs. We arrived at a similar conclusion when we compared pulsar kick velocities with BHXB PKVs in §4.7.3, but with the caveat of the selection bias of our sample of BHXBs. Hence, even though the current $|z|$ of the BHXBs in our data sample is not a strong proxy for the PKV of individual systems, z_{rms} is a good way to compare the PKV distributions of our sample of BHXBs to the NSs. This could be because systems spend most of their time close to the orbit extrema, and when we average the current heights of a sample, we remove the bias of the epoch of observation.

4.7.6 Natal kicks and black hole mass

Attempts have been made to understand if there is any relation between BH mass and the natal kick it receives (Mirabel, 2017). This could assist in understanding the correlation between the final pathway a progenitor takes to become a BH and the mass of the BH. The current theoretical understanding does not show a direct correlation and suggests that there is no clean mass cut off for direct collapse formation (Sukhbold et al., 2016). We have obtained observational constraints on the potential kicks of 16 BHBs (Figure 4.10), which increases the sample size and updates the estimations of BHB kicks by Mirabel (2017) and Gandhi et al. (2019) (current peculiar velocity used as proxy in both works). We conducted correlation tests, which indicated negligible correlation between BH mass and kick, with a Pearson Rank coefficient of -0.24 ± 0.16 ($p=0.20$) and a Spearman Rank coefficient of -0.19 ± 0.17 ($p=0.40$). We used a standard mass of $8 \pm 3 M_{\odot}$ (Kreidberg et al., 2012) for the systems that do not have a dynamically measured mass (see Table 4.7 for a summary of masses used). Removing these systems from the test sample gave Pearson and Spearman rank coefficients of -0.35 ± 0.16 ($p=0.18$) and -0.30 ± 0.17 ($p=0.25$), respectively. Using BHB potential kick velocities as an indicator of BH natal kick, we suggest that there is no significant dependency of BH mass on natal kick. This is the first time there has been observational evidence to support the simulations of Sukhbold et al. (2016), although we stress that the large error bars in the masses of the BHs (e.g. Zilkowski, 2008) are a caveat.

4.7.7 BHs in Globular clusters

XTE J1118+480 is argued to be a GC escapee because of its high peculiar velocity and high Galactic latitude. We find at least five systems with PKVs comparable to XTE J1118+480, making this system non-unique. However, most LMXBs are relatively old systems and thus may have come from low metallicity environments like GCs. So a GC origin of these high PKV systems cannot be ruled out. Since

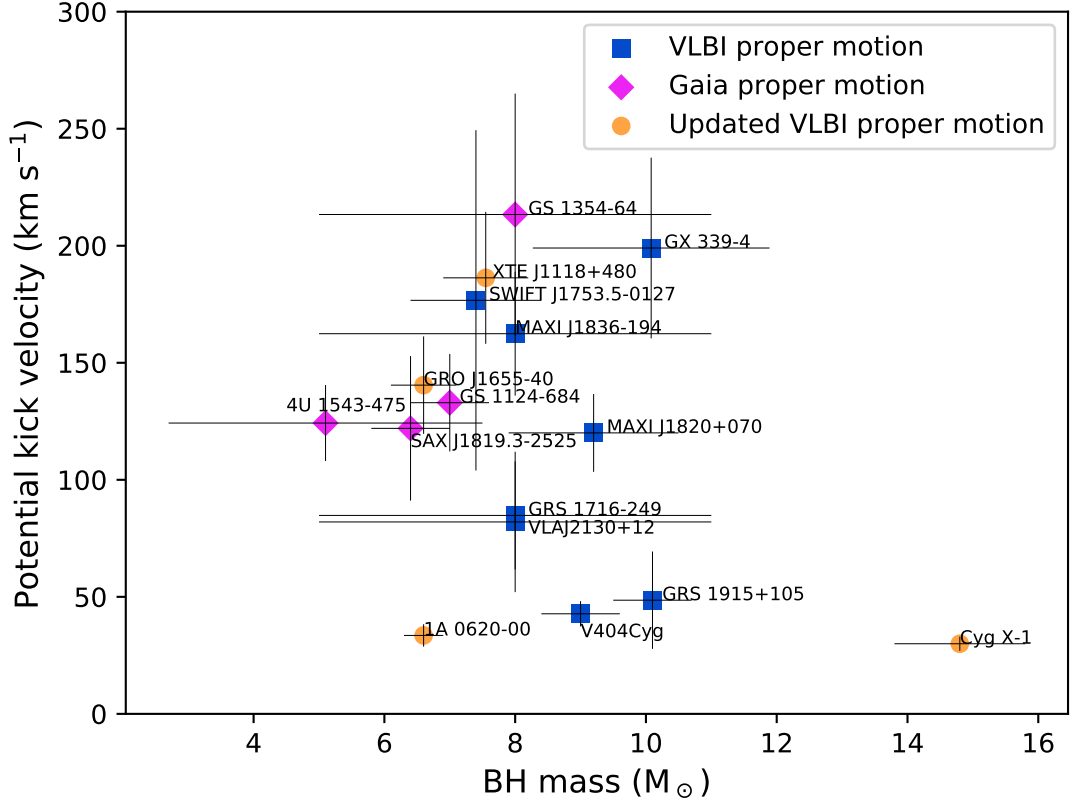


Figure 4.11: The variation of PKVs with black hole mass. The systems marked with blue squares have had their proper motion measured by VLBI and the systems marked with pink diamonds had their proper motion measured by *Gaia*. The systems marked with yellow circles had their proper motions measured by VLBI, but we used the updated proper motions measured by *Gaia* for our simulations. We have assumed a BH mass of $8 M_{\odot}$ to represent the systems that do not have dynamical mass measurements (Kreidberg et al., 2012). The error bars are one standard deviation of the PKV probability distributions. No correlation between BH mass and potential kick velocity is seen, even after disregarding the systems without dynamical mass measurements.

the majority of the systems in our sample get strong kicks, then if this distribution is characteristic of BHs it would imply that the retention fraction may be fairly low in GCs. As globular clusters (GC) are dense stellar environments, they are ideal sites for forming binaries. The escape velocities of GCs are on the order of a few tens of km s^{-1} (Gnedin et al. 2002; Belczynski et al. 2006). Thus, most of the BHs should be eventually ejected from the GC due to kicks associated with their birth or dynamical interactions (Kulkarni et al. 1993; Drukier 1996). The recent increase in the number of BHXB candidates detected in GCs challenges this theory (Strader et al. 2012; Camilo et al. 2000; Chomiuk et al. 2013; Miller-Jones et al. 2015; Giesers et al. 2018). Recent simulations have shown that if GCs retain ~ 1000 BHs, then these BHs will produce a considerable population of BHXBs in the GCs (Giesler et al., 2018). Simulations that estimate the BHs retained in GCs use various observationally unconstrained distributions ranging from random flat kick distributions up to some value (Sippel & Hurley, 2013) through to unconstrained retention fractions (Giesler et al., 2018). Our PKV distribution shows that these assumptions should be used with caution. The range of assumptions for the kick distributions also emphasise the need for a consistent, observationally constrained distribution.

According to our results the 20th percentile of the PKV distribution for BHXBs is $\sim 45 \text{ km s}^{-1}$, which is the typical v_{esc} for GCs. This suggests that BHXBs, which could have weaker recoil kicks than isolated BHs due to remaining bound, have a very high probability of getting kicked out from GCs. On the contrary, if BHXBs are Blaauw kick dominated, then isolated BHs have a higher chance of being retained in GCs. Thus, at birth, the retention fraction of BHs in GCs could be lower than the current estimates and may need to be updated. However, we note that GCs are old systems with low metallicity, and we have no observational constraints on how metallicity might affect the kick distribution.

4.7.8 Implications for BH-BH systems

When a star in the binary undergoes a SN explosion, any asymmetry in the kick could misalign the spin of the remnant BH to the orbital plane. If tidal interactions are then unable to realign the spin, this could potentially give rise to a high degree of misalignment of the spins of the BH to the orbital plane of the BH-BH binary (Gerosa et al., 2013). Recent observations of the GW merger event GW151226 suggested that natal kicks $>50 \text{ km s}^{-1}$ were needed to explain the inferred spin-orbit misalignment of the binary (O’Shaughnessy et al., 2017). The spin measurements for three other GW events GW150914, LVT151012 and GW170104 indicated that there is a possibility for these systems to either have low intrinsic spins or large spins that are misaligned with the binary orbit (Farr et al., 2017). 90% of our sources have PKVs higher than 50 km s^{-1} , thus suggesting that spin-orbit misalignment might be a common phenomenon.

Based on LIGO’s BH binary merger observations it was suggested that BHs receive high natal kicks $\sim 200 \text{ km s}^{-1}$ if the tidal processes do not realign stellar spins (Wysocki et al., 2018). If however tidal processes do realign the spins, kicks on the order of 50 km s^{-1} are still needed to explain the observations. The bimodality in our natal kick distributions, albeit based on a few sources, could potentially arise from similar tidal effects, though more work needs to be done in order to draw definitive conclusions. Theoretical estimates suggest that the majority of BH binaries that will be observed with the third LIGO run will be part of a population in which the first-born BH is slowly spinning, and support low natal kicks for BHBs (Bavera et al., 2019; Fuller & Ma, 2019). Measuring PKVs for more BHBs and future LIGO observations will be essential to reconcile these theoretical expectations of low natal kicks with our observational constraints of high PKVs.

4.7.9 BHXB spin-orbit misalignment

Studies of X-ray power density spectra of BHXBs show low frequency quasi periodic oscillations (QPOs) in the power density spectra of almost all BHXB systems (Ingram et al., 2016). Theoretical models suggest that such QPOs could be a result of Lense-Thirring precession (Stella & Vietri, 1998), which is a phenomenon where material out of the BH equatorial plane (e.g. due to misalignment of the BH spin and binary orbit) precesses due to relativistic frame dragging. Any natal kick imparted to a BH at its birth could cause a spin-orbit misalignment in the remnant BHXB. Since re-alignment timescales of BHXBs are usually longer than the ages of these systems (Martin et al., 2008), realignment of the BH spin to the orbital plane is not likely to be common (unless the donor star in the BHXB was initially an intermediate mass donor; Fragos & McClintock, 2015). We found that a majority of the BHXBs in our sample set were strongly kicked, which is consistent with the prevalence of low frequency QPOs and provides strong evidence for spin-orbit misalignment in BHXBs.

Extensive efforts to measure the spins of BHs in BHXBs have been made in the past decade. The best available methods (García et al., 2018; McClintock et al., 2014) often assume that the spin of the BH is aligned with the orbital plane of the binary. Our finding that strong natal kicks are imparted to $\sim 85\%$ of BHXBs suggests that caution may be warranted in assuming the binary orbital inclination when fitting for BH spin.

4.8 Summary

In this paper, we report on measurements of proper motions of three BHXB systems using VLBI. We collated the proper motions, systemic radial velocities and distances of 16 BHXB systems.

- We developed a methodology to determine potential kick velocity (PKV) distributions for BHXB systems. We have defined PKV as the velocity with

which a BHXB crosses the Galactic plane. Assuming the system was born in the Galactic plane, this could then be the velocity with which the system was kicked out of the Plane to be in its current Galactocentric orbit.

- We also developed a Monte Carlo simulation code to account for uncertainties in the measured proper motions, systemic radial velocities and distances when determining the potential kick velocity that the BHXB received, providing robust observational constraints on the possible kick velocities of these systems.
- We estimated PKV probability distributions for sixteen BHXBs and found that $\sim 75\%$ of our sample has a median potential kick velocity of $> 70 \text{ km s}^{-1}$, which we interpreted as a majority of BHXBs acquiring strong kicks when they are born.
- We combined the PKV probability distributions for these 16 BHXBs to obtain an aggregate PKV distribution. We found that a unimodal Gaussian distribution with a mean of $107 \pm 16 \text{ km s}^{-1}$ fit the data better than a bimodal distribution, which is broadly consistent with LIGO's BH-BH merger observations and natal kick estimations. However, the fit suffers from low number of systems in the data sample and hence we could not rule out a bimodal distribution.
- We found no significant correlation between PKVs and BH mass. We did not find any strict mass cut off for BHs to form with a SN or by direct collapse.
- We conducted Spearman and Pearson rank correlation tests to determine the correlation between the current height above the Galactic plane of a BHXB and the potential kick velocity it received. We found that even though there is a potential correlation between the two (coefficient of ~ 0.5 for both tests), we should avoid using $|z|$ as a natal kick proxy.

- We compared our aggregated PKV distribution with the pulsar peculiar velocity distribution (Verbunt et al., 2017) and found that BHs may get weaker velocity kicks than NSs by a factor of 3–4.
- Our finding that BHBX kick velocities are greater than typical escape velocities of globular clusters favours a large fraction of BHs being kicked out of the globular cluster on formation.
- The prevalence of strong kicks in our BHBX sample is in agreement with the ubiquity of low frequency QPOs and hence spin-orbit misalignment in almost all BHBXs.

Chapter 5

A search for quiescent Galactic black hole systems

In Chapter 4 we determined an observationally-constrained potential kick velocity distribution for BHXBs, and found that 75% of them receive significant kicks at birth. This implies that a search for radio sources with high proper motions could be a way to identify new BHXB candidates. In this chapter, we observe 33 radio variable targets using a filler Very Long Baseline Array program for 2–3 epochs. We have written a ParselTongue pipeline, which is a python wrapper for *AIPS*, to reduce this data. We use proper motion measurements (and in some cases the parallax) to distinguish between Galactic and extragalactic sources in this sample, as extragalactic sources are stationary with respect to the International Celestial Reference Frame. We cross-match the sources for which we could measure proper motions with the currently available optical, infrared and radio surveys. Finally, we suggest the possible follow-up observations that will be needed to ascertain the true nature of the sources for which we have measured proper motions.

5.1 Introduction

Efforts to detect and observe black holes (BHs) have been ongoing since they were theorised. As described in Chapter 1, one way to study black holes is in the form of black hole X-ray binaries (BHXBs). Most BHXBs were first discovered when they were in an outburst. During this stage, the rate of accretion onto the BH increases, resulting in brightening across the electromagnetic spectrum. This method of detecting BHXBs creates a bias in the sample of studied systems against the systems that are accreting at a low rate and exist only in a quiescent state, ($L_X < 10^{33.5}$ ergs s⁻¹; McClintock & Remillard, 2006) or ultra compact sources and short orbit sources (Arur & Maccarone, 2018) that have peak outburst luminosities lower than the triggering threshold for current all sky monitors. Since most BHXBs spend the majority of their lifetime in a quiescent state, dependence on outburst activity for their discovery also limits the rate at which they are being detected (Tetarenko et al., 2016b). Relying on X-ray outburst activity also biases us against the population of non-interacting BHs in binary systems.

The stark difference between the number of BHXBs expected in our Galaxy (10^8 ; Tetarenko et al., 2016a) and the number of known BHXB candidates (~ 60 ; Tetarenko et al., 2016b), with an even smaller fraction (~ 19 ; Tetarenko et al., 2016b) of dynamically confirmed systems (system with a known mass of the BH), suggests that a large population of BHXBs are hidden from conventional discovery techniques. In the past few years, new techniques and wide field surveys in various parts of the electromagnetic spectrum have been adopted to search for non-interacting black holes and/or quiescent BHXBs in our Galaxy to help put together a complete sample of BHs that exist in our Galaxy.

The Swift Bulge survey, an X-ray survey of the Galactic bulge (Shaw et al., 2020), was designed to detect Very Faint X-ray transients (VFXTs; Wijnands et al., 2006). This is a class of X-ray transients with very short lived outbursts that are not brighter than 10^{36} ergs s⁻¹. The low luminosities of these systems even

in an outburst is attributed to their low rate of accretion, which can be either due to a short-orbit and small accretion discs, or discs that are truncated by the magnetosphere of the neutron star (van den Eijnden et al., 2017). The survey focused on getting a detection of the faint X-ray outbursts of VFXTs and then following them up in a multiwavelength campaign.

There have been multiple efforts in the field of optical spectroscopy, measuring the radial velocity of the optically bright component in a binary. The radial velocity curve can then be used to determine the orbital parameters and then ultimately lead to the derivation of the mass function of the binary. The mass function is used to estimate the constraints on the masses of the components of the binary. Such studies have led to the discovery of possible triple systems, with a BH candidate as one of its members (Thompson et al., 2019; van den Heuvel & Tauris, 2020; Thompson et al., 2020; Liu et al., 2019; Eldridge et al., 2019; Rivinius et al., 2020). Although the nature of these systems is currently under debate (Bodensteiner et al., 2020), these discoveries have opened up the possibility of using spectroscopy as a novel way to detect non-accreting BHs in a binary (Hayashi et al., 2020). This is a promising technique to bridge the gap between expected and observed BHs in a binaries in our Galaxy. A similar photometric and spectroscopic survey of 25 globular clusters with the Multi Unit Spectroscopic Explorer (MUSE) on the European Southern Observatory’s Very Large Telescope (VLT) resulted in the detection of three detached stellar mass BH binary candidates in one of the globular clusters included in the survey, NGC 3201 (Giesers et al., 2018, 2019).

Another method was proposed a couple of years ago to look for quiescent BHXBs in our Galaxy using photometry and studying the H_α emission line with a combination of narrow and broad filters (Casares & Torres, 2018). They showed that if the width of the H_α emission line, which is a tell-tale sign of the accretion disc, could be determined with high enough accuracy and combined with the orbital period of the binary, it would help in determining the mass of the accreting

object. They have suggested that a Galactic plane survey based on the above technique could yield at least 50 quiescent black holes (Casares, 2018), almost doubling the number of black hole X-ray binaries that we know of today (Corral-Santana et al., 2016).

Other than optical/IR and X-rays, quiescent BHXBs can also be searched for at radio wavelengths. It has been argued that in the quiescent phase, the majority of the energy from the BHXB is radiated from jets in the form of radio emission rather than X-rays from accretion (Fender et al., 2003; Maccarone, 2005). Searches for quiescent BHXBs in our Galaxy at radio wavelengths could then be a highly effective method to observe this otherwise elusive population. The Milky-way ATCA and VLA Exploration of Radio-sources in Clusters (MAVERIC; eg., Shishkovsky et al., 2018; Bahramian et al., 2018) survey is one such survey, although it aims at finding X-ray binaries in globular clusters. This work is a systematic attempt to identify quiescent BHXBs in our Galaxy in the radio band.

Kirsten et al. (2014) made a serendipitous discovery of a foreground radio source whilst studying the proper motions of few compact radio sources towards the globular cluster M15. They found that one of the sources in their field of view was in fact a foreground Galactic object, which they could confirm because of a successful parallax and proper motion measurement to the source. This parallax measurement put the source at a distance of 2.2 ± 0.5 kpc, enabling the distinction from an object in the M15 globular cluster, which is known to be at a distance of 10.3 ± 0.4 kpc (van den Bosch et al., 2006). Follow-up of this source by Tetarenko et al. (2016b) confirmed the presence of a red stellar counterpart in the mass range of $0.1\text{--}0.2 M_{\odot}$. They suggested that the binary companion of this red stellar object is possibly a BHXB discovered in quiescence, which given the area of the sky surveyed to make the original detection by Kirsten et al. (2014), implies that there should be around $10^4\text{--}10^8$ such systems in our Galaxy. This was an increase in the number of expected BHXBs in our Galaxy from what was suggested by population synthesis models and surveys ($10^2\text{--}10^4$; Romani, 1998; Pfahl et al.,

2003; Corral-Santana et al., 2016). Thus the serendipitous discovery of a radio foreground source followed up by the suggestion that it could be a quiescent BHXB showed the possibility that such objects exist and could be detected in the Galactic field. This has motivated our search for more such quiescent BHXBs lurking around in our Galaxy, via an astrometric survey program.

A search for variable radio sources in the Galactic plane was conducted by Becker et al. (2010), B10 hereon, by comparing 6cm radio fluxes of sources from three surveys using the VLA. The first epoch (data set) was taken from a survey done between 1989–1991 (Becker et al., 1994), and the second and third epochs were data observed under the Co-Ordinated Radio 'N' Infrared Survey for High-mass star formation (CORNISH) survey in years 2005 and 2006 (Purcell et al., 2008). This allowed them to study the radio variability of sources in the same area of the sky and with a time baseline of 15 years. Limiting their study to regions that were covered in at least two out of the three data sets and defining their variability criterion as targets that showed difference in their peak flux densities greater than five times the rms of uncertainties of the flux at the two epochs, they found 39 sources that met their variability criterion. Comparing their variability to an extragalactic radio variability study (de Vries et al., 2004) between a 1995 and 2002 epoch of the Faint Images of the Radio Sky at Twenty Centimeters survey (FIRST; Becker et al., 1995), they were able to suggest that 6 out of the 39 sources that had the lowest variability could be background radio sources. The remaining 33 sources could be highly variable Galactic radio sources. Although the exact nature of these 33 sources could not be ascertained with the amount of information present at the time, a few scenarios could be ruled out that could not explain the high radio variability of these possibly Galactic sources. The sources are not radio flare stars due to the absence of a detectable (V magnitude =15) optical counterpart. As pulsars have a very steep spectrum and based on the flux densities of these sources at 1.4 GHz, even the weakest out of these sources would have likely been detected in pulsar surveys at 400 MHz. Becker et al. (2010) also

rule out gamma ray bursts and supernovae due to the quick rise time of their radio flux density (a few days), which would be very short as compared to the 15-year variability timescale observed for these sources.

One possibility they discussed was a few of these sources being X-ray binaries, possibly BHXBs. Since none of these sources have been detected as outbursting X-ray or optical sources, this suggests that these could be quiescent BHXBs. In this chapter, we detail the feasibility of using high precision radio interferometry to distinguish between Galactic and extragalactic radio sources from the sample of highly variable radio sources in the Becker et al. (2010) study, and potentially finding new quiescent BHXBs in the sample of Galactic sources. Our technique is inspired by a simple idea that most Galactic objects will appear to have a non-zero proper motion, whereas an extragalactic background source should be stationary with respect to the International Celestial Reference Frame, at least to the capability of current telescopes. Most NS and BHXBs receive natal kicks when the compact object in the binary is formed, giving them a higher velocity than the local standard of rest (see Chapters 1 and 4). This kick might manifest itself in the form of proper motions larger than the motion due to only the Galactic rotation, making high proper motion Galactic radio sources more likely to be X-ray binaries. Very Long Baseline Interferometry (VLBI) allows us to measure the proper motion, and in some cases the parallax, of compact radio sources if their position is measured for two or more epochs separated by several months. A smaller time baseline will allow us to estimate the proper motion, although the error bars on the measurement might be large. In this chapter, we report our findings from a proper motion measurement campaign using the Very Long Baseline Array (VLBA) to target the sample of the highly variable Becker et al. (2010) sources.

5.2 Observations

B10 suggested that 33 out of the 39 targets that had a fractional variability ($f = \text{Ratio of highest observed peak flux density to the lowest observed peak flux density}$) of >2 could be Galactic. We chose to observe 33 targets for our VLBA campaign and discarded the six targets with $f \leq 1.5$ as potential extragalactic radio sources. These observations were part of a VLBA filler program, BH208, that proposed to observe the 33 targets for three epochs, wherein the first and last epoch were separated by at least a year. As this was a filler program, depending upon the availability of the telescope, some sources were only observed for two epochs. Two epochs are still enough to obtain a proper motion constraint, though it is difficult to estimate the level of contribution in this motion due to the unknown parallax of the source. Nonetheless, any significant motion, whether due to parallax or proper motion, would imply a Galactic nature. Some targets only had a couple of months' separation between the two epochs.

The observations were planned such that two sources could be observed in a one hour observing block, with 10-15 minutes of on source time and split in two blocks to maximise uv-coverage, and 15 minutes on the phase reference calibrator. A standard phase referencing scheme was followed to obtain sub-milliarcsecond level precision on the positions of the targets. All observations were carried out in the X-band with a central frequency of 8.4 GHz, to maximise sensitivity and astrometric precision, while being relatively unaffected by scattering in the Galactic plane. We used a bandwidth of 256 MHz and a data recording rate of 2 Gbps for all observations. The observation IDs start from BH208A and run through to BH208O (see Table 5.1). All the antennas that form a part of the VLBA were used in almost all the observations, unless some antennas had to be dropped off due to weather or other technical problems. All the data were correlated using the DiFX software (Deller et al., 2011).

Depending on the target-calibrator separation the observations took three different forms. All observing blocks were an hour long. Most of the observing

blocks had a phase reference calibrator that was shared between the two nearby targets. A few observation blocks had separate calibrators for each target, i.e., two calibrators and targets (Obs ID - BH208C and BH208I). Three observing blocks (Obs ID- BH208A, BH208D and BH208L) had three targets each, wherein two of the targets fell in the same VLBA primary beam. In such cases, we observed one phase calibrator for the two targets in the same VLBA beam, using the midpoint between these two targets as the pointing centre and then correlating at the positions of both the targets. The third target had its own phase reference calibrator.

5.3 Data reduction

The data were reduced using the Astronomical Image Processing System (AIPS 31DEC17; Greisen, 2003). This VLBA survey includes 72 datasets and to minimise the time needed to process the datasets, the data were reduced in the following two stages.

5.3.1 First order reduction

The first-order reduction included obtaining the images of each target using a pipeline and determining whether the target was detected in those images. A custom pipeline was written in ParselTongue¹ (Kettenis et al., 2006), to go through the data reduction steps in AIPS starting with loading the data into *AIPS*, followed by correcting for the Earth Orientation Parameters, ionospheric Faraday rotation and dispersive delays, and conducting gain and bandpass calibration. The phase calibrator was used to solve for the phases, rates and delays and extrapolate the solutions to the target. The calibrated target data were finally split from the main dataset to image. Every target field was then individually imaged. Since natural weighting is most sensitive, but has lower natural image resolution

¹a python wrapper to *AIPS*

Table 5.1: Summary of the filler VLBA observing campaign. The Obs ID column has BH208 preceding all the reported Obs IDs (e.g., BH208A). The target names are from the B10 survey and the names in parenthesis are the shortened names that will be adopted for the rest of this chapter. The name is shortened by combining the observing ID and the number of the target in the observing block. The date of observation is given as dd/mm/yyyy.

Obs ID (BH208)	Target name	Dates of observations		
		Epoch 1	Epoch 2	Epoch 3
A	G39.1105-0.0160 (Ai)	14/08/2015	26/12/2015	-
A	G37.7347-0.1126 (Aii)	14/08/2015	26/12/2015	-
A	G37.7596-0.1001 (Aiii)	14/08/2015	26/12/2015	-
B	G37.2324-0.0356 (Bi)	31/05/2015	09/11/2015	31/01/2016
B	G32.7193-0.6477 (Bii)	31/05/2015	09/11/2015	31/01/2016
C	G32.5898-0.4468 (Ci)	31/05/2015	02/01/2016	-
C	G31.1595+0.0449 (Cii)	31/05/2015	02/01/2016	-
D	G31.1494-0.1727 (Di)	15/08/2015	30/12/2015	-
D	G30.4376-0.2062 (Dii)	15/08/2015	30/12/2015	-
D	G30.4460-0.2148 (Diii)	15/08/2015	30/12/2015	-
E	G30.1038+0.3984 (Ei)	01/06/2015	06/12/2015	04/02/2016
E	G29.7161-0.3178 (Eii)	01/06/2015	06/12/2015	04/02/2016
F	G29.5779-0.2685 (Fi)	06/09/2015	09/01/2016	31/01/2016
F	G29.4959-0.3000 (Fii)	06/09/2015	09/01/2016	31/01/2016
G	G29.6051-0.8590 (Gi)	27/09/2015	11/01/2015	-
G	G29.1978-0.1268 (Gii)	27/09/2015	11/01/2015	-
H	G29.1075-0.1546 (Hi)	24/10/2015	15/01/2016	-
H	G28.6204-0.3436 (Hii)	24/10/2015	15/01/2016	-
I	G27.8821+0.1834 (Ii)	12/07/2015	04/01/2016	-
I	G26.2818+0.2312 (Iii)	12/07/2015	04/01/2016	-
J	G26.0526-0.2426 (Ji)	31/07/2015	27/12/2015	-
J	G25.7156+0.0488 (Jii)	31/07/2015	27/12/2015	-
K	G25.4920-0.3476 (Ki)	19/07/2015	24/12/2015	-
K	G25.2048+0.1251 (Kii)	19/07/2015	24/12/2015	-
L	G24.5343-0.1020 (Li)	01/11/2015	20/01/2016	-
L	G24.5405-0.1377 (Lii)	01/11/2015	20/01/2016	-
L	G24.3367-0.1574 (Liii)	01/11/2015	20/01/2016	-
M	G23.6644-0.0372 (Mi)	10/08/2015	02/01/2016	-
M	G23.4186+0.0090 (Mii)	10/08/2015	02/01/2016	-
N	G23.5585-0.3241 (Ni)	22/07/2015	24/12/2015	-
N	G22.9743-0.3920 (Nii)	22/07/2015	24/12/2015	-
O	G22.9116-0.2878 (Oi)	01/06/2015	13/12/2015	-
O	G22.7194-0.1939 (Oii)	01/06/2015	13/12/2015	-

and higher sidelobes we test different robustness from 0 (intermediate between natural and uniform weighting) to 5 (natural weighting) to try and detect the source. The targets that were detected (a bright fringe or a 5σ detection during imaging, see 5.3.3) in one or more epochs after these tasks were then selected for a more careful calibration.

5.3.2 Second order reduction

The sources that were detected above a 5σ significance in more than one epoch were chosen to go through a second-order data reduction process. A pipeline was written to stack the phase calibrator for different epochs to improve the calibrator model and to make sure the same calibrator model was used to determine the phases and delay solutions on the target in all epochs. The best possible model of this stacked calibrator was made by assuming an initial point source model and then iteratively using self-calibration and reducing the self-calibration solution intervals with each iteration, until a minimum solution interval of 30 seconds. This model was then applied to the target epoch-wise. All data below 15° elevation were flagged to reduce systematic errors due to low elevations. Usually a check source, which is a compact extragalactic radio source, is observed to gauge the effect of systematics on the quality of the phase solutions applied to the target. Since these short, 1-hour observations were part of a filler program, we did not have time to observe a check source. In such cases, a few scans of the phase calibrator can be treated as a second target source and the change in the position of the calibrator between these scans and those that were self-calibrated can be measured. We used every second phase calibrator scan to be imaged as the check source, after applying the phase and delay solutions to these scans as derived from the remaining phase calibrator scans.

Table 5.2: Detection summary of the observations. ‘-’ denote no observations were taken; ‘Invalid data’ are the observations that did not have the correct correlation position; ‘Fr’ are images where there was a strong clear fringe but owing to the poor uv-coverage, we could not ascertain exactly where in the fringe the source was located. * in front of detections suggest that the detections are less significant than our detection threshold (6σ) or that the brightest false positive (second brightest pixel in the image) is within 1σ of the true detection. These detections are less reliable than the others.

Target name	Peak intensity (rms) , uJy/Beam		
	Epoch 1	Epoch 2	Epoch 3
Ai	624 (95)	779 (126)	-
Aii	550 (122)*	Invalid data	-
Aiii	824 (170)*	Invalid data	-
Bi	(91)	(73)	(82)
Bii	563 (99)*	599 (94)	729 (100)
Ci	1122 (108)	1117 (111)	-
Cii	(71)	(63)	-
Di	766 (148)*	761 (141)*	-
Dii	(99)	Invalid data	-
Diii	544 (99)*	Invalid data	-
Ei	1130 (73)	1206 (65)	1154 (60)
Eii	3309 (208)	3952 (190)	3335 (174)
Fi	(61)	(169)	(71)
Fii	Fr (82)	Fr (147)	Fr (75)
Gi	(65)	(78)	-
Gii	(91)	471 (75)	-
Hi	912 (142)	844 (120)	-
Hii	1101 (127)	832 (109)	-
Ii	706 (88)	605 (99)	-
Iii	(191)	650 (122)*	-
Ji	Fr (186)	Fr (130)	-
Jii	(80)	(88)	-
Ki	(150)	(171)	-
Kii	(135)	(142)	-
Li	(148)	Invalid data	-
Lii	703 (131)	Invalid data	-
Liii	(145)	(143)	-
Mi	1512 (279)*	873 (110)	-
Mii	(92)	(81)	-
Ni	(60)	(81)	-
Nii	(63)	(108)	-
Oi	447 (81)*	(53)	(71)
Oii	(73)	(61)	(76)

5.3.3 Imaging

The single source data files that were split off after applying all the above calibration steps were then individually imaged. The searching process involved imaging the target using natural weighting for the best possible sensitivity. An image of size 16384×16384 pixels (pixel size of 10^{-4} arcseconds) was made to render a large enough image to cater for the large error bars ($1''$) in the positions of the targets, as detected by the FIRST survey using the VLA (Becker et al., 1995). After spotting the location of the bright fringe pattern in the image, the target was imaged again using a smaller image size (8192×8192 pixels) focused on the bright fringe in the larger image.

The detection threshold for a true source was calculated based on the number of pixels that were searched (n), and is given by $\sigma(\sqrt{2 \ln n} \pm 0.77/\sqrt{\ln n})$ (Thompson et al., 2017). Based on this relation we apply a threshold of $6 \pm 0.2\sigma$ to confidently classify the target as a true detection. Targets such as Ci, Di, Hi, Hii and Ii had strong sidelobes in the image with natural weighting making it difficult to decide where the target was. This could be due to the short time duration of these observations resulting in a sparse uv plane coverage. The sidelobes could be successfully subdued with the use of robust -1, giving more resolution to the image. The resulting drop in sensitivity was not an issue in the cases of Ci, Hi and Hii, in which the targets had peak flux densities of ~ 1 mJy. The remaining two targets (Di, Ii) were not bright enough to get significant detections with robust 0 weighting, so the targets were imaged with natural weighting (robust 5) but dropping all the long baselines (antennas at Brewster, Hancock, North Liberty, St. Croix and Mauna Kea). This helped in obtaining a low precision position of the target with a 6σ significance.

Table 5.3: Positions of the targets detected after the imaging process. The positions with an * in front of them show that the detection was below our set threshold of 6σ and could not be claimed as reliable detections based on our additional tests.

Target	MJD	Positions	
		RA h:m:s (error)	Dec d:m:s (error)
Ai	57248	19:02:47.9904029 (86)	05:29:21.37462 (21)
	57382	19:02:47.990458 (13)	05:29:21.37449 (34)
Aii	57248	19:00:36.973018 (15)*	04:13:18.50486 (36)*
Aiii	57248	19:00:37.037722 (12)*	04:14:58.87997 (31)*
Bii	57173	18:53:21.381952 (12)	-00:29:04.26976 (29)
	57335	18:53:21.381867 (15)	-00:29:04.26945 (33)
	57418	18:53:21.381907 (10)	-00:29:04.26953 (23)
Ci	57173	18:52:24.2949065 (63)	-00:30:29.56352 (14)
	57389	18:52:24.2956740 (57)	-00:30:29.56905 (35)
Di	57249	18:48:48.093142 (26)	-01:39:54.68671 (54)
	57386	18:48:48.093298 (27)	-01:39:54.68980 (74)
Diii	57249	18:47:40.048335 (26)*	-02:18:36.49116 (51)*
Ei	57174	18:44:51.4623826 (82)	-02:20:05.80968 (15)
	57362	18:44:51.4623512 (72)	-02:20:05.80958 (14)
	57422	18:44:51.4623254 (63)	-02:20:05.81012 (13)
Eii	57174	18:46:42.0492619 (80)	-03:00:24.33092 (15)
	57362	18:46:42.0492236 (66)	-03:00:24.33018 (13)
	57422	18:46:42.0492328 (66)	-03:00:24.33059 (14)
Gii	57398	18:45:04.334436 (19)	-03:22:51.99355 (32)
Hi	57319	18:45:00.3479320 (95)	-03:28:25.62092 (23)
	57402	18:45:00.3477892 (94)	-03:28:25.62246 (21)
Hii	57319	18:44:47.2874434 (75)	-03:59:36.46651 (18)
	57402	18:44:47.2873573 (86)	-03:59:36.46626 (20)
Ii	57215	18:41:33.287570 (16)	-04:24:33.07533 (22)
	57391	18:41:33.288399 (17)	-04:24:33.07045 (50)
Iii	57391	18:38:26.363930 (15)	-05:48:35.06308 (47)
Lii	57327	18 36 32.3808402 (88)	-07 31 33.57376 (30)
Mi	57244	18:34:33.047937 (16)	-08:15:27.02078 (39)
	57389	18:34:33.047509 (11)	-08:15:27.02150 (29)
Oi	57174	18:34:02.876929 (09)*	-09:02:28.58731 (31)*

5.4 Results

The results of the data reduction are summarised in Table 5.2 and Table 5.3. The sources that were not detected and that only went through the first order of data reduction have the rms noise in the image reported in this table. We did not detect (at 5σ or greater significance) 14 out of the 33 targets in any epoch that they were observed in. We could see a strong fringe in the image for two targets (Fii and Ji) but could not locate the exact position of the targets in the images.

Seven targets were detected in only one epoch, four of which (Aii, Aiii, Diii, Lii) were only successfully observed for one epoch as these targets were part of the observations in which we required the multi-phase centre correlation capability of DiFX. Due to an error, the data were correlated only at the pointing centre, and not at the target positions in these epochs. Therefore, the time and bandwidth smearing at the positions of the targets was too large to give a useful data set. Out of these seven targets, only Gii was detected with a significance above our 6σ threshold limit. We conducted two tests in order to determine whether the detections of the other six targets with a significance of lower than 6σ are true sources. We measured the flux density of the brightest false positive in the imaging area of the other six targets and found that only Lii was detected with a significance of 1σ above the brightest false positive. We also measured the brightest negative source in the image and set the positive detection level for a true source 1σ above the brightest negative source. We found that the detections of Iii and Lii were above this detection level. So, we suggest that the detection reported for Lii and Iii are possibly true sources. We are not confident about the other four detections (Aii, Aiii, Diii and Oi) and will need to re-observe to confirm the position and flux density of these sources. We refer to these sources as marginal detections in the rest of chapter. These sources are identified with an * in Table 5.2 and Table 5.3.

There were six targets that were detected with a significance of $\geq 6\sigma$ in both the epochs they were observed in, and three targets were detected in three

epochs. One target (Di) was detected with a significance of only $\geq 5\sigma$ in both the epochs it was observed in. The flux density of the false positives in both these observations is within 1σ of the true detection candidate. On the other hand, we report that the detections are reliable using a positive detection level 1σ above the brightest negative source in the images. We also note that the Di detections are separated by 4 months and are within a few pixels of each other with similar flux density. Hence, we treat the detections of Di as true detections. Bii and Mi had marginal detections in their first epoch of observation, although their consequent epoch detections are more significant than 6σ and have similar flux density to the first epoch detections making the marginal detections in the first epochs reliable. The marginal detections have been identified with a * in Table 5.2 and Table 5.3. All the targets with detections in two or more epochs gives us a sample of ten sources to measure proper motion (and constrain the parallax in some cases).

5.5 Analysis

The proper motion in Right Ascension (RA; $\mu_\alpha \cos \delta$), in Declination (Dec; μ_δ), the parallax (π) and the reference position (RA₀, Dec₀) of the targets can be derived by fitting the measured position as a function of time (e.g. Loinard et al., 2007). The time midway between the first and last observation of every target was used as the reference date. The input errors on the measured positions in RA and Dec were the statistical and systematic errors added in quadrature. The offset in the check source (the calibrator scans treated as a target) position was smaller in magnitude than the more conservative estimate from the target-phase calibrator throw (Pradel et al., 2006). So in all cases, this more conservative systematic error was used. We used a Bayesian approach to determine $\mu_\alpha \cos \delta$, μ_δ and π using the equations that describe the motion of the target in the plane of the sky (see (2.9), Chapter 2) and using the measured positions of the targets as the data.

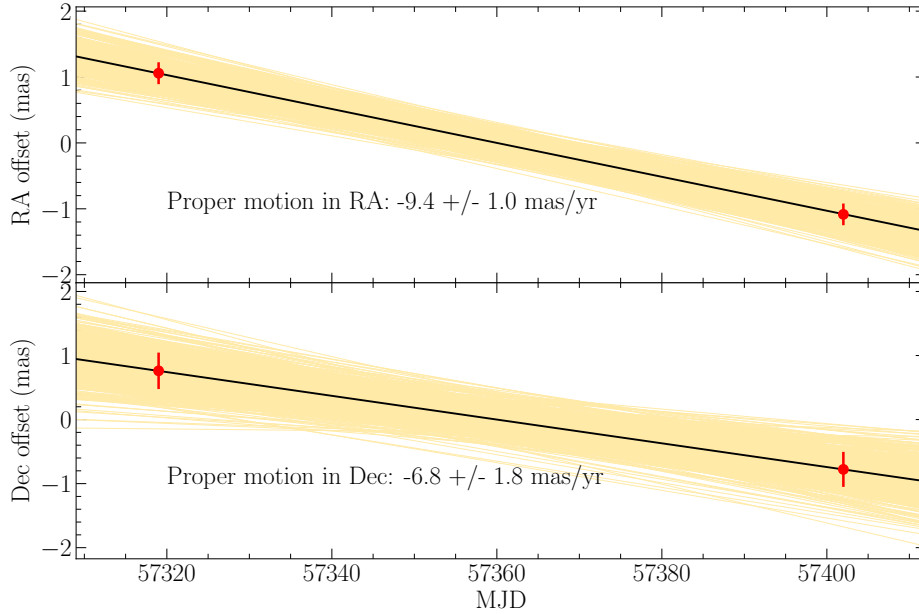
Table 5.4: Results of the MCMC fitting code to determine proper motions and parallaxes of the targets detected at two or more epochs. The targets are arranged in decreasing order of the significance of proper motion measurement, where significance is defined as the ratio of the fit value and the error on the estimated value. Mi, Di and Bii have one or more epochs that have marginal detections, but due to similar flux density and $>6\sigma$ significance of the same targets in other epoch of their observations, and these stronger detections being within a few pixels of the marginal detections, we claim that these measurements are reliable. References for plots - [1] Figure 5.1, top figure; [2] Figure 5.1, bottom figure; [3] Figure 5.2, top figure; [4] Figure 5.2, bottom figure; [5] Figure 5.3, top figure; [6] Figure 5.3, bottom figure; [7] Figure 5.4, top figure; [8] Figure 5.4, bottom figure; [9] Figure 5.5, top figure; and [10] Figure 5.5, bottom figure.

Target	π (mas)	$\mu_\alpha \cos \delta$ (mas yr ⁻¹)	μ_δ (mas yr ⁻¹)	μ_{total} (mas yr ⁻¹)	No. of epochs
Proper motion fit only					
Hi ^[1]	–	-9.4 ± 1.0	-6.8 ± 1.8	12 ± 2.0	2
Mi ^[2]	–	-16 ± 1.6	1.1 ± 2.4	16 ± 2.9	2
Di ^[3]	–	6.2 ± 1.6	-8.2 ± 2.6	10 ± 3.1	2
Ci ^[4]	–	-2.3 ± 0.4	2.8 ± 1.0	3.6 ± 1.1	2
Hii ^[5]	–	-5.4 ± 1.1	3.1 ± 1.9	6.2 ± 2.2	2
Ai ^[6]	–	2.3 ± 0.7	-0.4 ± 1.1	2.4 ± 1.2	2
Ei	–	-1.2 ± 0.3	-0.5 ± 0.5	1.2 ± 0.6	3
Eii	–	-0.7 ± 0.3	0.7 ± 0.5	1.0 ± 0.6	3
Ii ^[9]	–	-0.3 ± 1.0	3.0 ± 1.9	3.1 ± 2.1	2
Bii	–	-1.1 ± 0.4	0.4 ± 0.9	1.2 ± 0.9	3
Proper motion and parallax fit (parallax prior 0.1-5 mas)					
Hi	0.1 – 5	-22 ± 8.0	-5.4 ± 1.9	23 ± 8.0	2
Mi	0.1 – 5	-21 ± 2.9	3.8 ± 2.9	21 ± 4.1	2
Di	0.1 – 5	-2.2 ± 2.8	-4.3 ± 3.5	4.8 ± 4.4	2
Ci	0.1 – 5	0.2 ± 1.5	6.0 ± 2.1	6.0 ± 2.6	2
Hii	0.1 – 5	-19 ± 7.4	-1.7 ± 2.0	19 ± 7.7	2
Ai	0.1 – 5	-0.5 ± 1.8	5.1 ± 3.4	5.2 ± 3.8	2
Ei ^[7]	0.10 ± 0.08	-1.2 ± 0.3	-0.4 ± 0.6	1.2 ± 0.6	3
Eii ^[8]	0.26 ± 0.15	-0.7 ± 0.3	-1.0 ± 0.6	1.2 ± 0.6	3
Ii	0.1 – 5	-1.5 ± 1.2	6.3 ± 2.6	6.4 ± 2.9	2
Bii ^[10]	0.63 ± 0.2	-0.9 ± 0.4	1.0 ± 0.9	1.4 ± 1.0	3

The PYMC3 python package (Salvatier et al., 2016) was used to implement a Hamilton Markov Chain Monte Carlo (MCMC, Neal, 2012) technique with a No-U-Turn Sampler (NUTS; Hoffman & Gelman, 2011). The code was first run for all targets with a flat parallax prior between 0.1–5 mas, and a flat proper motion prior for RA and Dec between -100–100 mas yr⁻¹. The choice of the parallax prior is to cover a wide range of distance from 200 pc to 10 kpc and the proper motion prior is chosen such that it significantly exceeds the range of known BHXB proper motions (Atri et al., 2019; Gaia Collaboration et al., 2018a). The results of the fitting are presented in Table 5.4. We could not constrain the parallax and disentangle it from the proper motion for the sources with two epochs of observations, and the MCMC code simply returned the input prior of the parallax as the output trace and inflated the errors on the proper motion fits by trying to incorporate all possible parallaxes (e.g., Figure 5.8). Thus to verify whether these objects are moving or not, we run the MCMC code using a simple model to fit a straight line to estimate the proper motion, assuming a zero parallax. In Table 5.4 we report the proper motion fit results for both the MCMC runs with and without a parallax fit included in the model, and use the results of a straight line proper motion fit in our further analysis.

Even though we had three targets with three epochs where they were successfully detected, we could obtain a constraining parallax measurement with a 3σ significance for only one target, Bii (see Figure 5.6) caveat the $\sim 5\sigma$ detection of the first epoch. The parallax solution (0.26 ± 0.15) of one of the other targets, Eii, was not significant ($< 2\sigma$) but was still recognised as the maximum likelihood value by the MCMC fitting code. On the other hand, the parallax of Ei could not be constrained at all and the trace solutions showed that a value close to zero is possibly preferred (see Figure 5.7). Amongst the other sources, we could measure the proper motions of four targets, i.e., Hi, Mi, Di and Ci, with a $> 3\sigma$ significance.

G29.1075-0.1546 (Hi)



G23.6644-0.0372 (Mi)

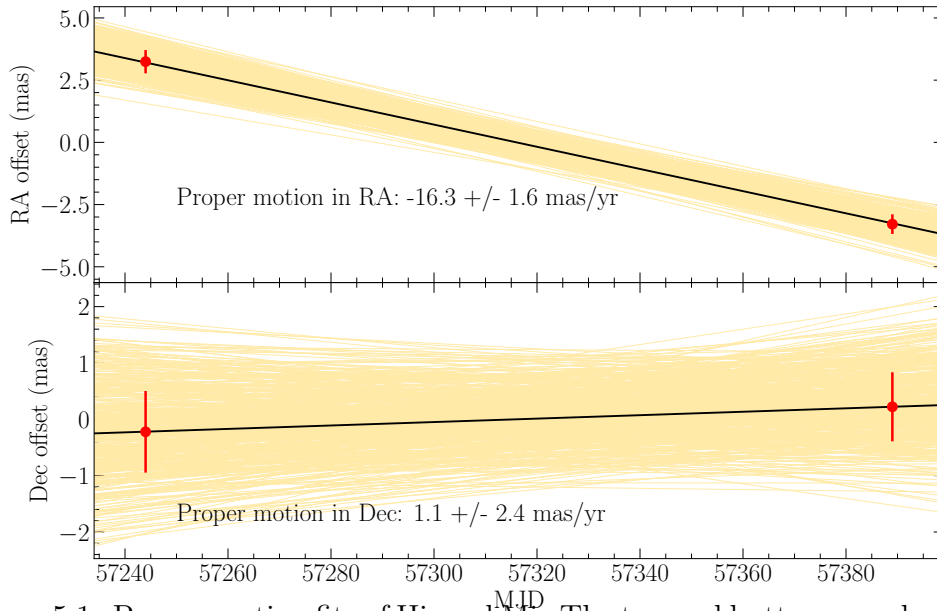
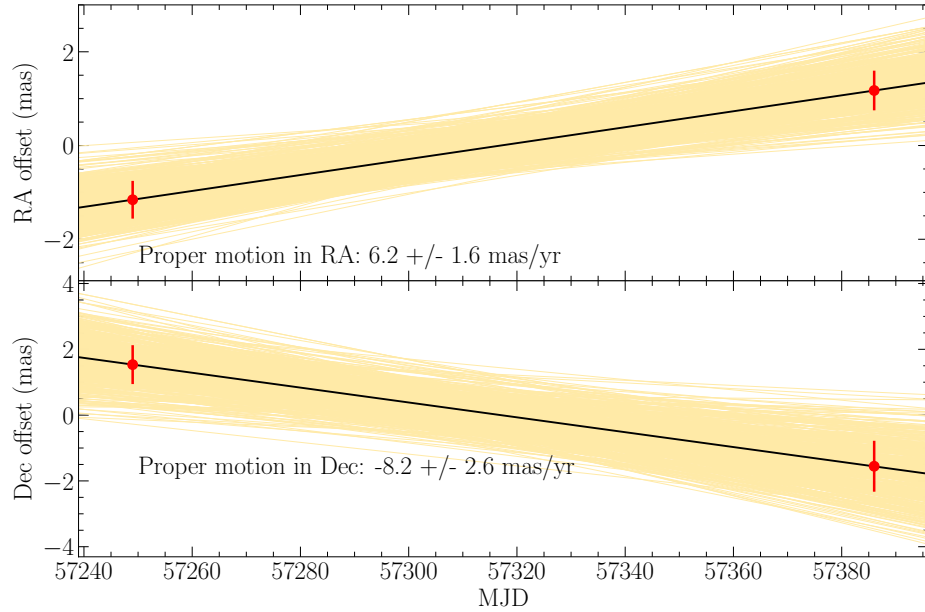


Figure 5.1: Proper motion fits of Hi and Mi. The top and bottom panels represent the motion in the plane of the sky relative to the fitted reference position in RA and Dec, respectively. The offset of the target positions relative to the reference position is denoted by the red markers and is overlaid with the trajectory given by the best fitting proper motion (black solid line). The yellow lines indicate the motion for a 1000 randomly-selected draws from the posterior distribution.

G31.1494-0.1727 (Di)



G32.5898-0.4468 (Ci)

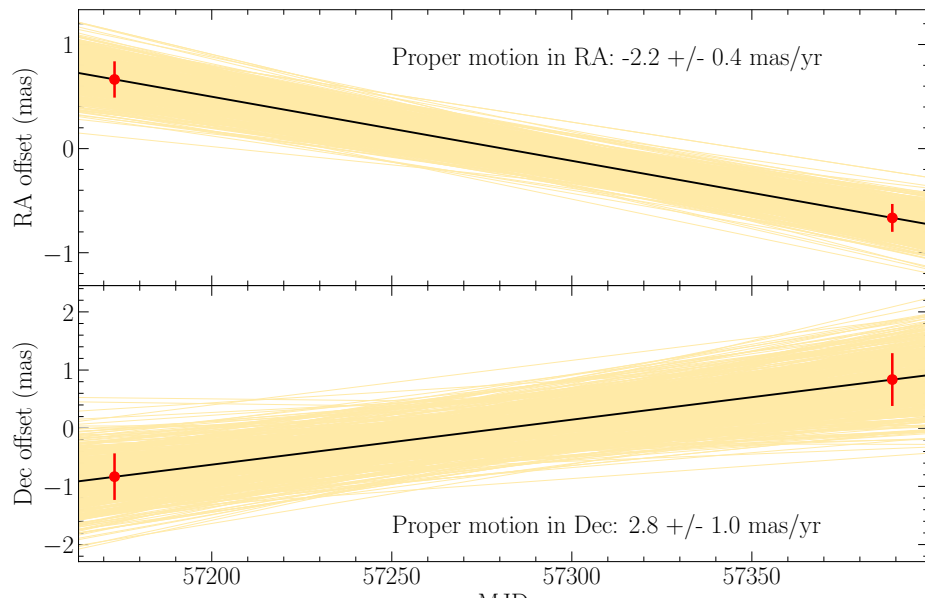
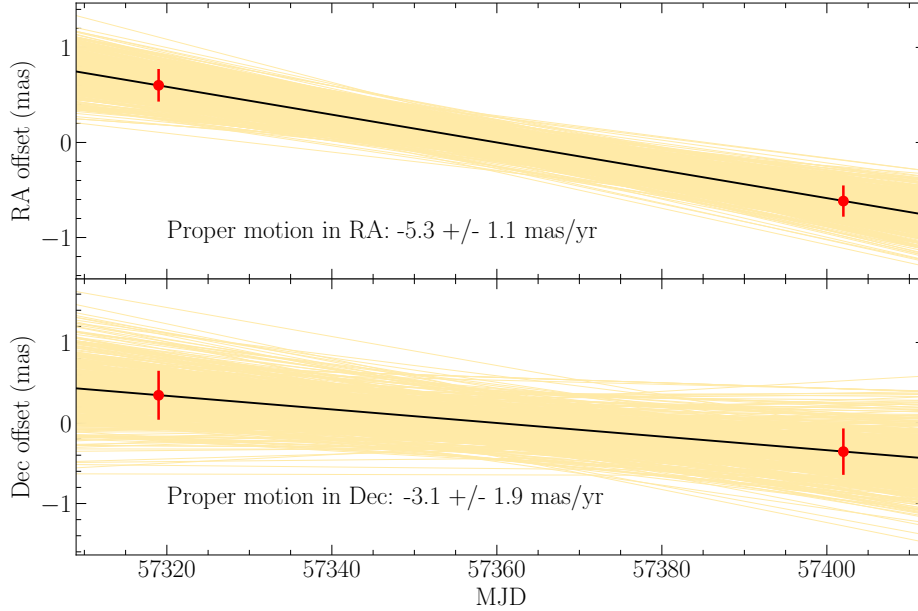


Figure 5.2: Proper motion fits of Di and Ci. The top and bottom panels represent the motion in the plane of the sky relative to the fitted reference position in RA and Dec, respectively. The offset of the target position relative to the reference position is denoted by the red markers and is overlaid with the trajectory given by the best fitting proper motion (black solid line). The yellow lines indicate the motion for a 1000 randomly-selected draws from the posterior distribution.

G28.6204-0.3436 (Hii)



G39.1105-0.0160 (Ai)

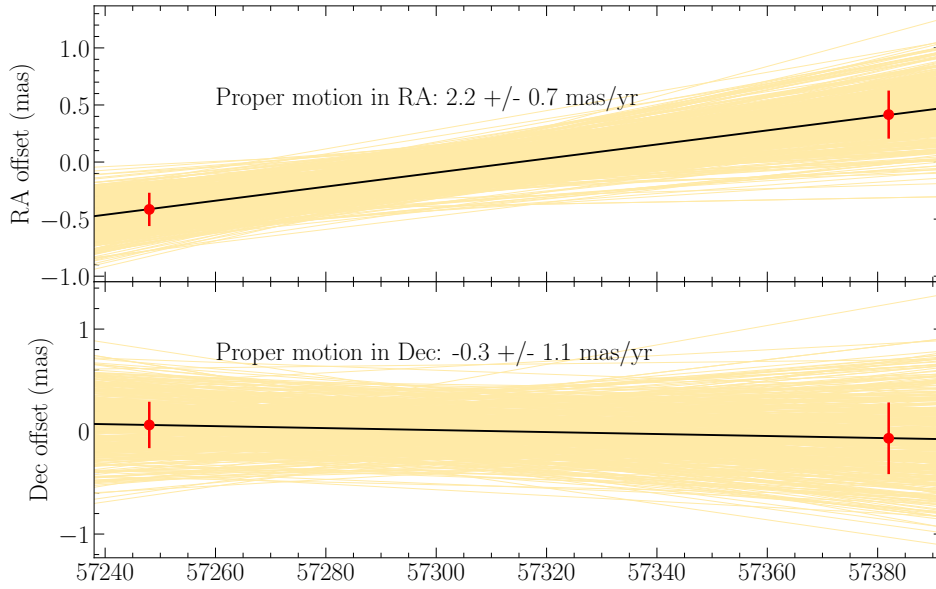
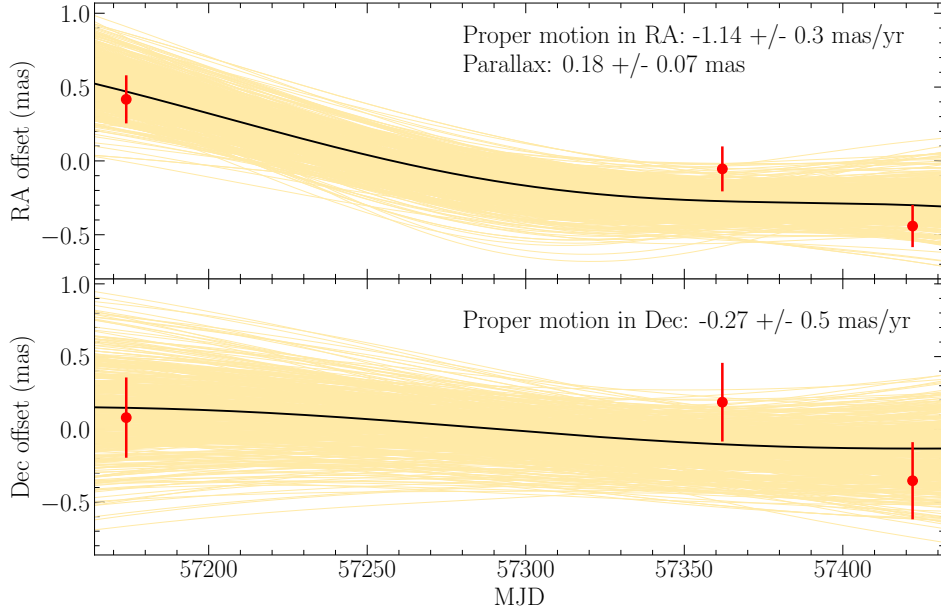


Figure 5.3: Proper motion fits of Hii and Ai. The top and bottom panels represent the motion in the plane of the sky relative to the fitted reference position in RA and Dec, respectively. The offset of the target positions relative to the reference position is denoted by the red markers and is overlaid with the trajectory given by the best fitting proper motion (black solid line). The yellow lines indicate the motion for a 1000 randomly-selected draws from the posterior distribution.

G30.1038+0.3984 (Ei)



G29.7161-0.3178 (Eii)

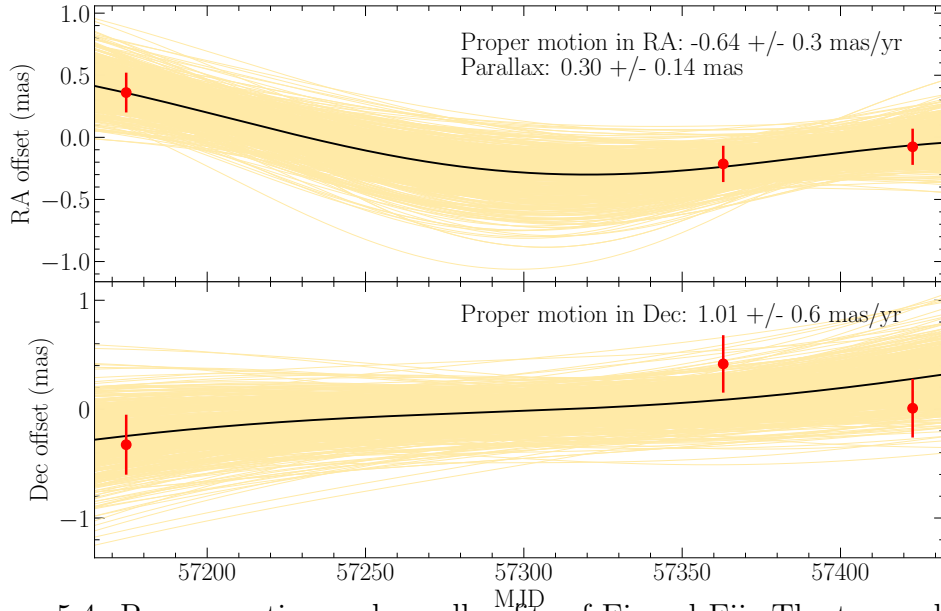
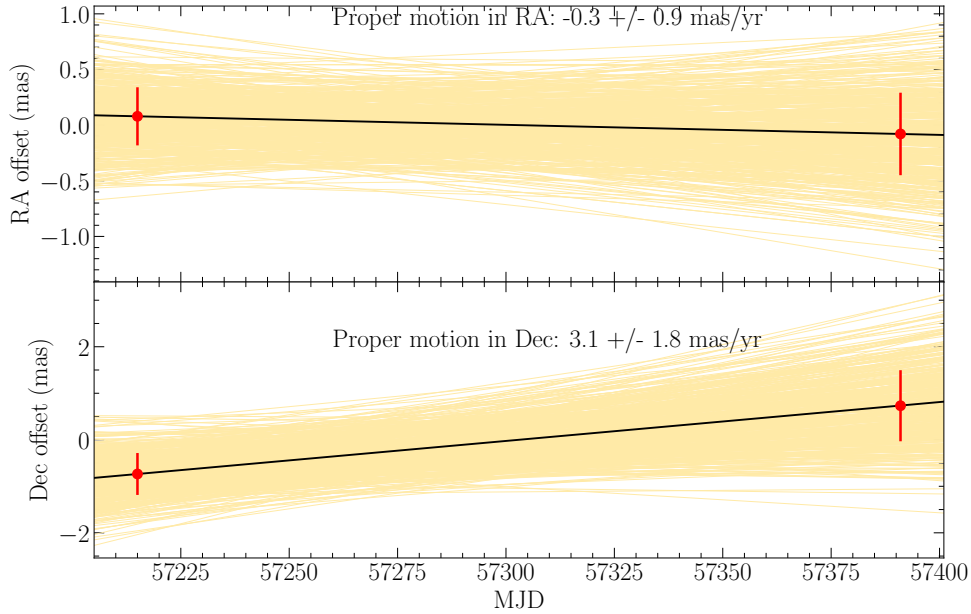


Figure 5.4: Proper motion and parallax fits of Ei and Eii. The top and bottom panels represent the motion in the plane of the sky relative to the fitted reference position in RA and Dec, respectively. The offsets of the target position from the reference position is denoted by the red markers and is overlaid with the trajectory given by the best fitting proper motion (black solid line). The yellow lines indicate the motion for a 1000 randomly-selected draws from the posterior distribution.

G27.8821+0.1834 (Ii)



G37.2324-0.0356 (Bi)

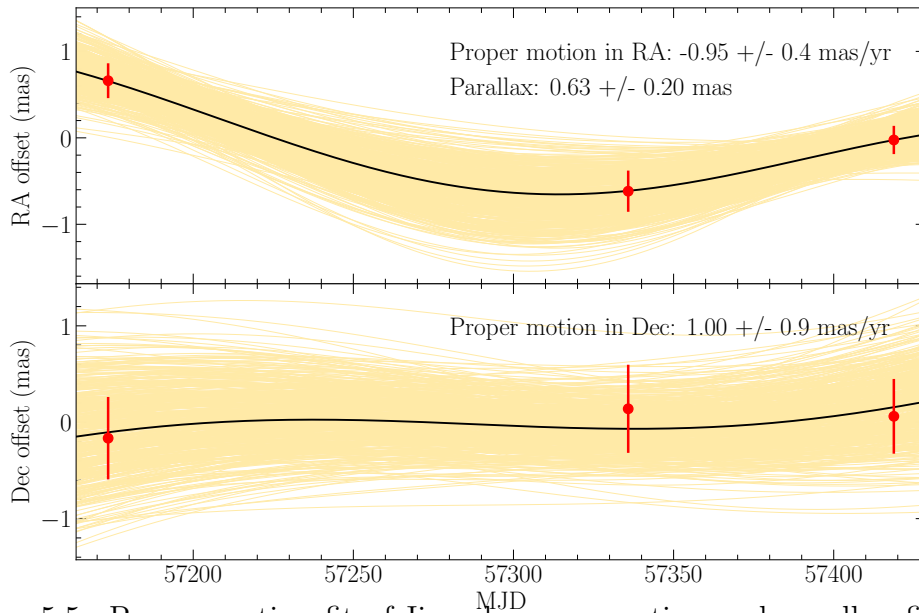


Figure 5.5: Proper motion fit of Ii and proper motion and parallax fit of Bi. The top and bottom panels represent the motion in the plane of the sky relative to the fitted reference position in RA and Dec, respectively. The offsets of the target position from the reference position is denoted by the red markers and is overlaid with the trajectory given by the best fitting proper motion (black solid line). The yellow lines indicate the motion for a 1000 randomly-selected draws from the posterior distribution.

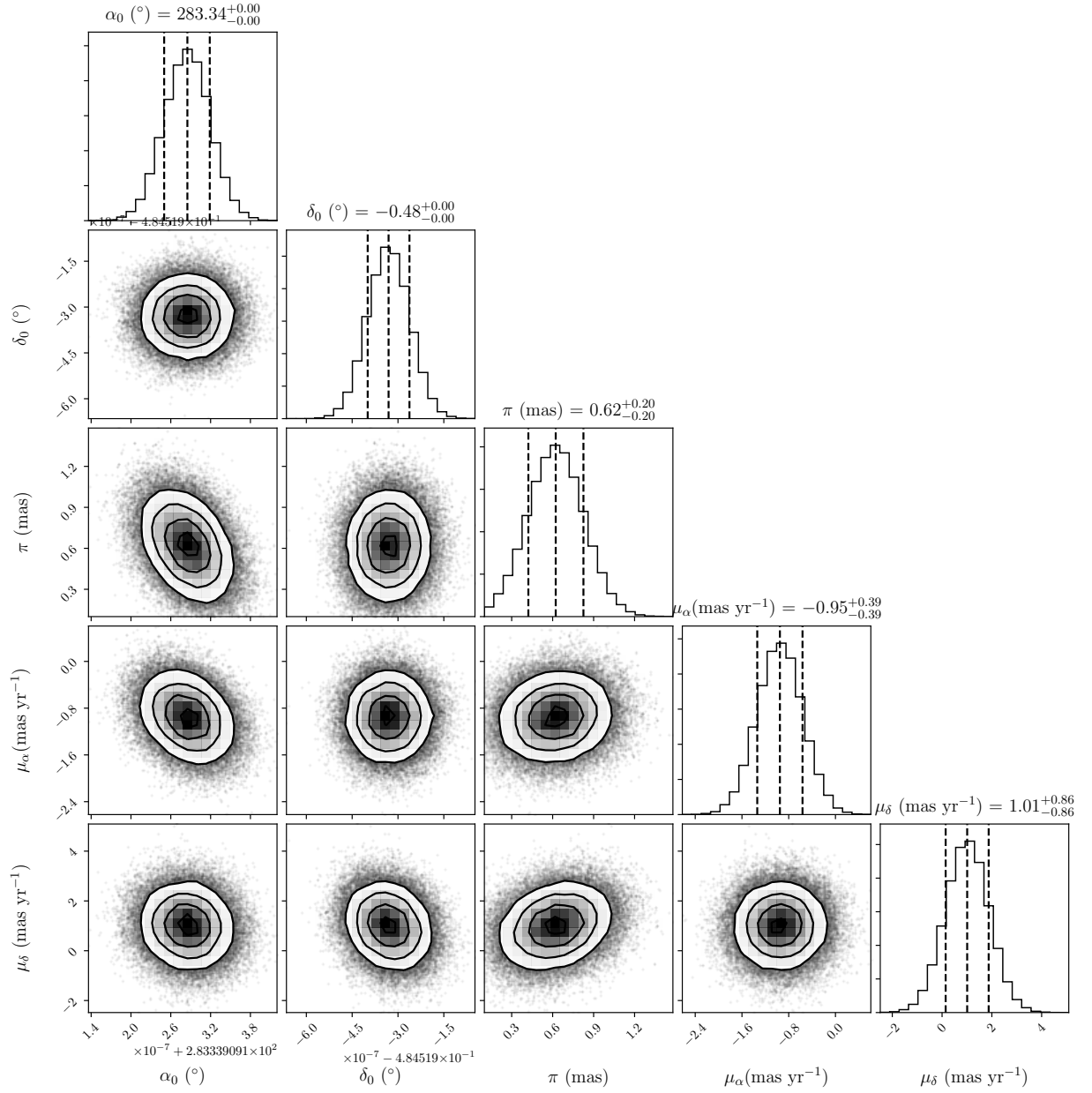


Figure 5.6: A corner plot depicting the posterior distributions for the model parameters of Bii. The contour levels and the dashed lines represent the 16th, 50th and 84th percentiles. Slight correlations are seen between π and μ_α , π and μ_δ , π and α_0 and, π and δ_0 .

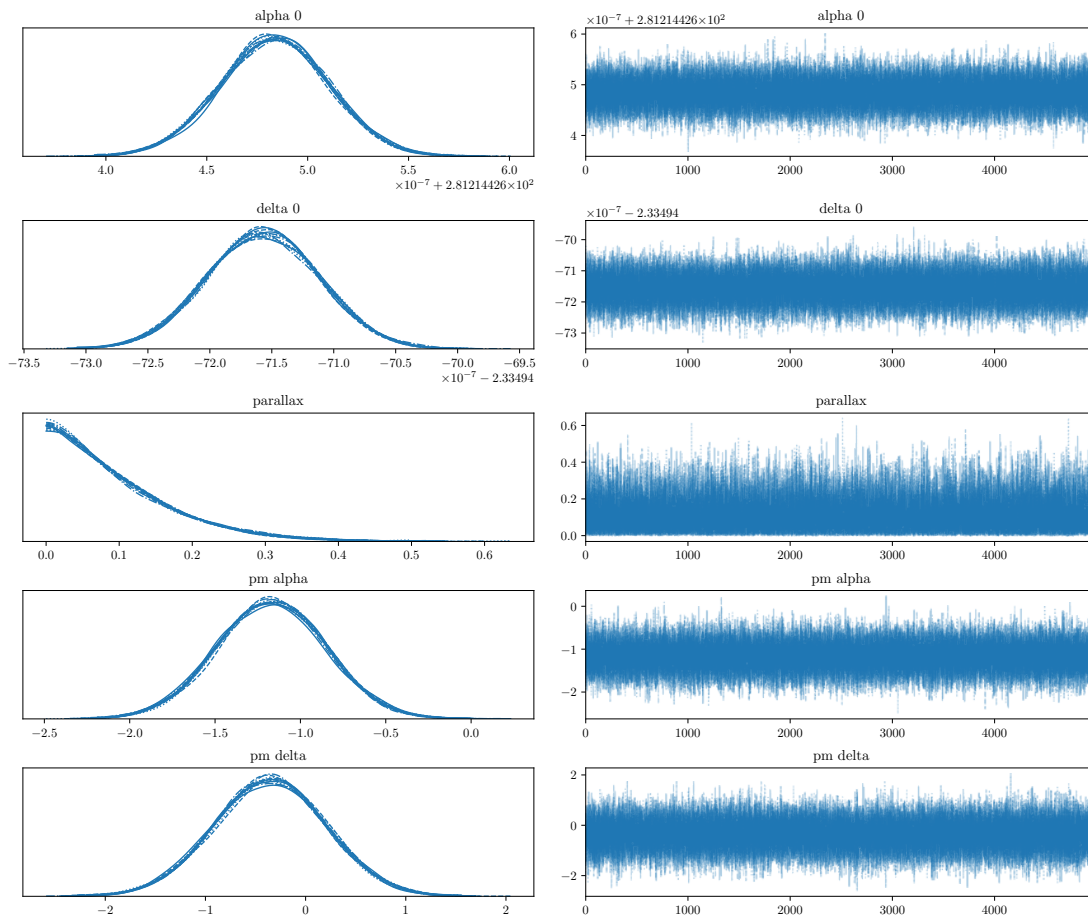


Figure 5.7: Trace solutions of the MCMC code for Ei. The left panel shows the posterior distribution of the samples of the traces. The right panel reports the solution of each iteration and clearly shows that the sampler has converged effectively and has sampled the parameter space efficiently. The parallax posterior distribution shows that the maximum likelihood value could not be obtained but the likelihood increased towards smaller values of parallax, suggesting that values closer to zero are preferred.

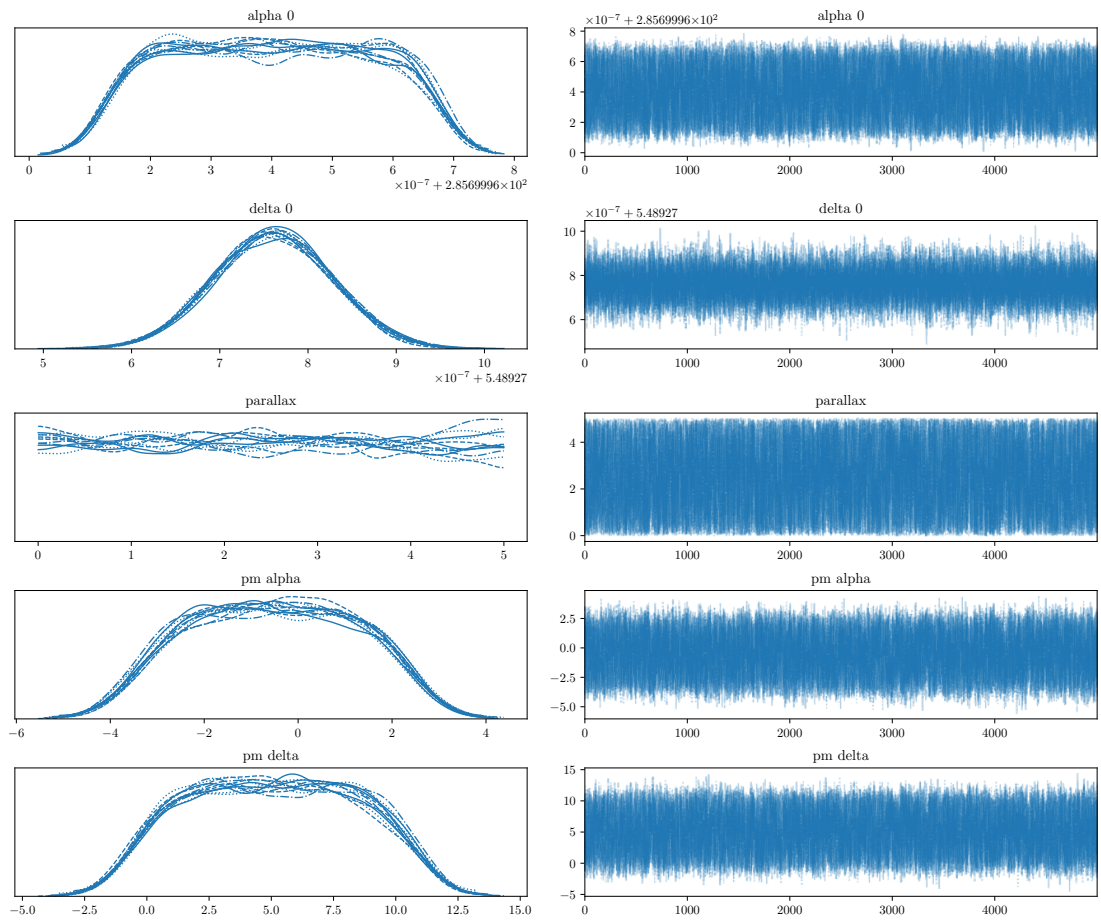


Figure 5.8: Trace solutions of the MCMC code for A_i . The left panel shows the posterior distribution of the samples of the traces. The right panel reports the solution of each iteration and clearly shows that the sampler has converged effectively and has sampled the parameter space efficiently. The posterior distribution of the parallax shows that no value of parallax is preferred and the solution represents the prior itself. All targets with two position epochs had a similar shape of the parallax posterior distribution.

5.6 Discussion

5.6.1 Source classification

We detected 11 out of the 33 targets with $\geq 6\sigma$ significance in at least one epoch. Two of targets could not be localised and were only detected as a bright fringe in the image. We also detected six targets but with a significance of $5 - 6\sigma$ and thus will need more observations to confidently report the nature and position of the targets. The 14 non-detections could be because the radio emission on the targets was resolved out on VLBA baselines. Also, the targets chosen in this study had a fractional variability of 150% and so it is also possible that the sources varied enough in flux to push the targets to a level too faint to detect with our VLBA filler program. The VLBA survey is at 8.5 GHz whereas the Becker et al. (2010) study was at 5 GHz. This could alternatively suggest that the sources that are not detected with the VLBA have a steep spectrum. Gii, Iii and Oi are detected in only one out of the two epochs they were observed in. In the case of Gii and Iii, the thermal noise level in the image of the targets was higher in the epochs with non-detections than the epochs with the detection (see Table 5.2). Even if both these targets were at the same radio flux in both the epochs, then the increased thermal noise level could have pushed the target below the 5σ threshold in the image, thus leading to a non-detection.

We were able to successfully measure proper motions for 10 out of the 33 targets we observed. All these targets were detected in all epochs they were observed in, suggesting that they did not vary below the detection threshold. The measured flux densities of these targets at different epochs agreed with each other within a 1σ limit, suggesting that they did not experience drastic variability between the epochs when they were observed. Based on just the motion of these targets, six out of the 10 targets appear to be Galactic with the total proper motion of five targets being inconsistent with zero at a $>3\sigma$ level and the $>3\sigma$ parallax measurement of one target placing it within the Galaxy (see discussion

below for Bii). The remaining four targets could not be conclusively classified as either Galactic or extragalactic as their total proper motion was consistent with zero within 2σ level. So higher accuracy on the total proper motion measurement of these targets will help conclude if they are moving significantly enough to warrant a Galactic nature. We have summarised the classification based on proper motions of these ten targets in Table 5.5.

Becker et al. (2010) compared the fractional variability of their Galactic plane population with the extragalactic population of de Vries et al. (2004) and arrived at the conclusion that six out of 39 targets with $f < 1.5$ are background sources. They also suggested that within the remaining 33 targets with high fractional variability, $f > 1.5$, are likely to be background sources. We find that 40% of the targets whose proper motions we could measure could be extragalactic (if they are not slowly moving Galactic sources), as compared to the 15% of the 33 targets as suggested by Becker et al. (2010). Hence, if fractional variability is a good test for classifying sources as extragalactic there should be a couple more Galactic sources amongst the four that we could not conclusively classify.

Multiwavelength studies of the objects in our study can help identify the nature of these sources. We performed a basic query on VizieR², which is an online library of all published astronomical catalogues, to look for possible multiwavelength counterparts of the targets in our study. Below, we report any possible counterparts in optical wavelengths from the Panoramic Survey Telescope and Rapid Response System (PANSTARRS; Chambers et al., 2016) catalogue and the *Gaia*-DR2 survey (Gaia Collaboration et al., 2018a), and infrared counterparts from the UKIRT Infrared Deep Sky Survey (UKIDSS; Lucas et al., 2008). We also compare our classification of the targets to the source type suggested in the The Co-ordinated Radio and Infrared Survey for High Mass Star Formation (CORNISH) survey (Purcell et al., 2008, 2013), a radio survey at 5 GHz using the VLA. The CORNISH survey included cross-matches with UKIDSS and the

²<https://vizier.u-strasbg.fr/viz-bin/VizieR>

Galactic Legacy Infrared Mid-Plane Survey Extraordinaire (GLIMPSE), which helped in studying the spectral energy distribution of the targets and suggesting possible source types for the targets, which are available as an online catalogue³.

5.6.1.1 Galactic sources

G32.7193-0.6477 (Bii) was detected in all three epochs in which it was observed and the MCMC proper motion and parallax code determined a 3σ parallax signature (see Figure 5.5, Figure 5.6 and Table 5.4). The proper motion of the source is consistent with zero motion within 2σ , but the parallax fit suggests that the target is possibly a slow moving Galactic radio source. Using an exponentially decreasing volume density prior (see Chapter 3) and a parallax of 0.62 ± 0.20 mas, the distance posterior distribution of the source has a median of $2.7^{+5.2}_{-1.4}$ kpc, where the upper and lower limits are the 5th and 95th percentile of the distance distribution. The target was not detected in various optical, X-ray and infrared catalogues in 2010 as searched by Becker et al. (2010). We also could not find any multiwavelength counterpart of Bii. The CORNISH catalogue suggests that this target is a radio galaxy, which contradicts our suggestion of the source being a Galactic radio source (see Table 5.5). We also note that the target was detected with a 5.7σ significance. Future VLBA observations of this target will help measuring the parallax and proper motion with greater precision and would help confirm the Galactic nature of this source.

G32.5898-0.4468 (Ci) We detected this target in two epochs and could fit a straight line to measure the motion of the source in RA and Dec (see Figure 5.2 and Table 5.4). The proper motion of the source is measured at a significance of $\geq 3\sigma$, suggesting that the source is a Galactic radio source. The source was not detected in any of the catalogues searched by Becker et al. (2010). We found an optical and IR source in the PANSTARRS catalogue and the UKIDSS catalogue, respectively, within 0.96 arcsec from the VLBA position of Ci. The positional

³<https://cornish.leeds.ac.uk/public/catalogue.php>

accuracy of 0.01 arcsec of this source with PANSTARRS and 0.1 arcsec with UKIDSS makes it an unlikely optical/IR counterpart of Ci. There is also a *Gaia* source 0.88 arcsec away and this *Gaia* source has a measured proper motion and parallax of

$$\begin{aligned}\mu_{\alpha} \cos \delta &= -4.39 \pm 3.12 \text{ mas yr}^{-1} \\ \mu_{\delta} &= -3.49 \pm 2.59 \text{ mas yr}^{-1} \\ \pi &= 0.85 \pm 2.78 \text{ mas.}\end{aligned}\tag{5.1}$$

The radio proper motion estimated in this work is

$$\begin{aligned}\mu_{\alpha} \cos \delta &= -2.3 \pm 0.4 \text{ mas yr}^{-1} \\ \mu_{\delta} &= 2.8 \pm 1.0 \text{ mas yr}^{-1}.\end{aligned}\tag{5.2}$$

The *Gaia* proper motion in RA agrees with the radio proper motion within 1σ but the Declination proper motion agrees only at the 3σ level. The high precision position measurement of *Gaia* (1.5 mas) makes this source an unlikely optical counterpart of Ci.

G31.1494-0.1727 (Di) This target was observed and successfully detected in two epochs albeit with a significance of $5\text{--}6\sigma$, enabling a proper motion measurement. The total proper motion of this source is significant at a 3σ level (see Figure 5.2 and Table 5.4), giving support to the Galactic nature of the source. We did not find any multiwavelength counterpart of Di within 1 arcsec and the Becker et al. (2010) study also could not find emission in any other wavelength from this target. The CORNISH catalogue classified this source as IR-Quiet, which are high redshift radio galaxies (Collier et al., 2014), whereas our proper motion measurement suggests that this source is Galactic.

G29.1075-0.1546 (Hi) was observed and detected in two epochs. The high total proper motion of the target (12 ± 2) is significant at a 6σ level (see Figure 5.1 and Table 5.4), which is very strong evidence that the target is Galactic. A UKIDSS target is found 0.75 arcsec away from the radio position, but is unlikely an infrared counterpart to Hi given that the nominal UKIDSS positional accuracy

is 0.1 arcsec. The CORNISH classification of this source is IR-Quiet whereas we suggest that the target is Galactic.

G28.6204-0.3436 (Hii) was detected in two epochs and a proper motion with a 3σ significance was measured (see Figure 5.3 and Table 5.4). We suggest that the source is likely Galactic, which is not consistent with the IR-Quiet classification of the CORNISH catalogue. The nearest infrared UKIDSS target is 0.73 arcsec away from the radio position, but the 0.1 arcsec positional accuracy makes it an likely counterpart of Hii.

G23.6644-0.0372 (Mi) was detected in two epochs and has a well constrained proper motion (see Figure 5.1 and Table 5.4), which is significant at a 6σ level. The high proper motion of the source suggests that Mi is Galactic. The CORNISH catalogue reports Mi as an IR-Quiet source, which suggests it is a radio-galaxy. There is a UKIDSS target 0.9 arcsec away from the radio position of Mi, but is an unlikely counterpart to Mi. Mi was not reported in any other catalogue in the Becker et al. (2010) study.

5.6.1.2 Extragalactic/Inconclusive

G39.1105-0.0160 (Ai) was detected in two epochs in our survey and the measured total proper motion is only measured at a 2σ significance level (See Figure 5.3 and Table 5.4). Becker et al. (2010) did not detect this target in the infrared, optical and X-ray catalogues available at the time, and a Vizier search in the current available catalogues also did not show any results for the source at any other wavelength. The CORNISH classification claims that this source is IR-Quiet. Based on just the proper motion, A1 could be an extragalactic radio source, or a slow moving Galactic radio source.

G30.1038+0.3984 (Ei) This target was observed in 3 epochs spread over a year, and was detected in all three epochs. Fitting a parallax and proper motion model to the source reveals a proper motion that is consistent with zero within 2σ . The MCMC code could not find a parallax solution though the traces suggest

that a zero parallax is preferred. This suggests that the target is consistent with an extragalactic radio source, which is consistent with the IR-Quiet classification in the CORNISH catalogue. There is a PANSTARSS source 0.76 arcsec away from the VLBA position of Ei, but since the positional accuracy of PANSTARSS is 0.01 arcsec it is not a likely optical counterpart of Ei.

G29.7161-0.3178 (Eii) This target was detected in 3 epochs enabling a proper motion and parallax measurement that are consistent with zero within 2σ . This suggests that the target is consistent with being an extragalactic radio source, which agrees with the CORNISH classification of this source. Eii was not detected in any other wavelength in the original Becker et al. (2010) study. In the current UKIDSS, we find an infrared source 0.75 arcsec from the radio position of Eii. The source localisation is adversely affected by the extended/blended nature in the image. This infrared source has a K band (15.96) that is 2 magnitudes brighter than the H band (13.73). This is at times the signature of an accretion disc as it is associated with the Brackett gamma emission line whose presence in the K band can make it brighter. Along with the zero proper motion, the presence of an accretion disc suggests that this source could be an AGN.

G27.8821+0.1834 (Ii) This source has a measured proper motion that suggests that the source is probably stationary with respect to the ICRF, as its proper motion is consistent with zero within 2σ . The nearest UKIDSS source is 0.9 arcsec away from the VLBA position of Ii. Our suggestion of this source being extragalactic is also consistent with the CORNISH classification of this source as IR-Quiet.

5.6.2 Extinction limitations

The search for optical and infrared counterparts in all sky surveys for the ten sources that we have measured proper motions for, did not yield any good matches. The sample studied in this work was a selection from a Galactic plane survey and covered a region of $22^\circ < l < 40^\circ$ and $b \leq 0.7^\circ$, where l and b are Galac-

Table 5.5: Distance limits, CORNISH catalogue classification and classification from this work. The distance limit (d_{lim}) is the distance at which the extinction in the target’s direction changes the apparent magnitude of the target by a magnitude of 3. CORNISH source is the source type suggested in the CORNISH catalogue by investigating the SEDs of the targets. The last column denotes the suggested nature of the source based on its proper motion measurement, i.e., Galactic or Inconclusive/Extragalactic (IC).

Target	d_{lim} (kpc)	CORNISH source	This work
Ai	0.97	IR-Quiet	IC
Bii	0.58	Radio-galaxy	Galactic
Ci	0.50	–	Galactic
Di	0.76	IR-Quiet	Galactic
Ei	5.1	IR-Quiet	IC
Eii	0.96	Radio star	IC
Hi	0.99	IR-Quiet	Galactic
Hii	2.26	IR-Quiet	Galactic
Ii	2.19	IR-Quiet	IC
Mi	5.5	IR-Quiet	Galactic

tic longitude and latitude, respectively. As a result, any possible optical and infrared emission from the targets is susceptible to high levels of extinction due to absorption and reddening from the interstellar dust. The non-detection of any optical counterparts in all of the current surveys suggest that either the target does not emit in optical wavelengths, or that the optical light from the target has suffered enough reddening to push the apparent magnitude of the target to beyond the detection capabilities of our optical telescopes. The extent of reddening ($E(g-r)$) is direction dependent and is estimated as a function of l , b and the distance to the source. The extinction effect on the magnitude of the target is related to reddening by $3.2E(g-r)$, i.e., a reddening by a factor of one will affect the optical/infrared magnitude by dimming the brightness by three magnitudes.

Since the distance to almost all of our targets is unknown, other than the loose constraints on the distance of Bii, it is not possible to derive the exact level of extinction that the optical/IR will suffer. A combination of a few all sky surveys like the Two Micron All Sky Survey (2MASS), PANSTARRS and *Gaia* has been

used to make a 3D map of the interstellar dust reddening as a function of l , b and the distance towards the target. Since we cannot estimate the exact amount of reddening, we decided to map how far the source can be for the extinction in the target’s direction to change the apparent magnitude of the target by 3 magnitudes (see d_{lim} in Table 5.5). This gives an idea of the extreme adverse effect of extinction on the detection possibility of some of the targets (Ai, Bii, Ci, Di, Eii and Hi) even if they are very close, within 1 kpc. The other targets (Ei, Hii, Ii and Mi) show the same amount of extinction although for a much larger distance, suggesting that there is a higher possibility of detecting optical counterparts to these targets.

5.6.3 Population comparison

The highly variable radio population in this work has at least six out of ten targets moving with respect to the ICRF, suggesting a Galactic origin. A search for radio stars by comparing the FIRST and the Sloan Digital Sky Survey (SDSS) revealed that the possibility of a radio star also being an optical star is as little as 1.2 in a million (Kimball et al., 2009). We can conduct population statistical tests to see if the sources in our sample could be a subset of the sources detected by the *Gaia* and of the BHB population on the basis of their measured proper motions. We plot the cumulative distribution of the total proper motions of a sample of 500,000 sources picked randomly from the *Gaia*-DR2 survey (black solid line), the total proper motions of the sources in this work (blue solid line) and the total proper motions of known BHBs (red solid line) in Figure 5.9, top panel.

We also plot up the proper motions of these targets and compared them to the proper motions of the known BHB population reported in Chapter 4 and over-plot a histogram of total proper motions of the *Gaia* subset (blue histogram, see Figure 5.9, lower panel). Proper motions of both these samples lie in the same range, with no source having a total proper motion of more than 20 mas yr^{-1} . We conducted the Anderson-Darling test (Stephens, 1974) to test the hypothesis that

the two samples being tested come from the same population. Using this test, we could not reject the hypothesis that the known BHXB sample and the radio sources in this work belong to the same population with a 25% confidence level. Anderson-Darling test is capped at 25% confidence level in the scipy module and so this test is inconclusive about the relation of these two populations. The ability of the Anderson-Darling test to be able to test whether two samples are from the same population worsens when the sample size is small, and thus in order to obtain conclusive results the sample size will have to be increased. We could also not reject the hypothesis that the radio sources in this work and the Gaia sources belong to the same population with a 12% confidence level.

5.7 Future Work

We have detected at least six sources in our survey that are moving with a proper motion that is detected at $\geq 3\sigma$ significance. Obtaining more information on the nature of these sources requires detection of multiwavelength counterparts to the targets. The Galactic radio source discovered by Kirsten et al. (2014) could be classified as a possible BHXB candidate, VLA J2130+12, due to its flat to slightly inverted radio spectrum, an upper limit on the X-ray luminosity of the source and detection of a possible low mass optical counterpart ($0.1\text{--}0.2 M_{\odot}$) using images from the Hubble Space Telescope and the distance to the source. None of the objects identified in our survey as possibly Galactic had an optical counterpart. The reason such an extensive study was possible for VLA J2130+12 was because the source was in the foreground of a very well studied globular cluster, M15. Also, VLA J2130+12 is at a height of ~ 1 kpc above the Galactic plane and thus it suffers from less extinction as compared to the sources in our study that are closer to the Galactic plane. This made the detection of the optical/IR counterpart of VLA J2130+12 possible. Our survey covers sources in the Galactic plane, which makes it difficult to find optical counterparts. The targets, even if they are bright in the optical, will suffer large extinctions as they are in the Galactic

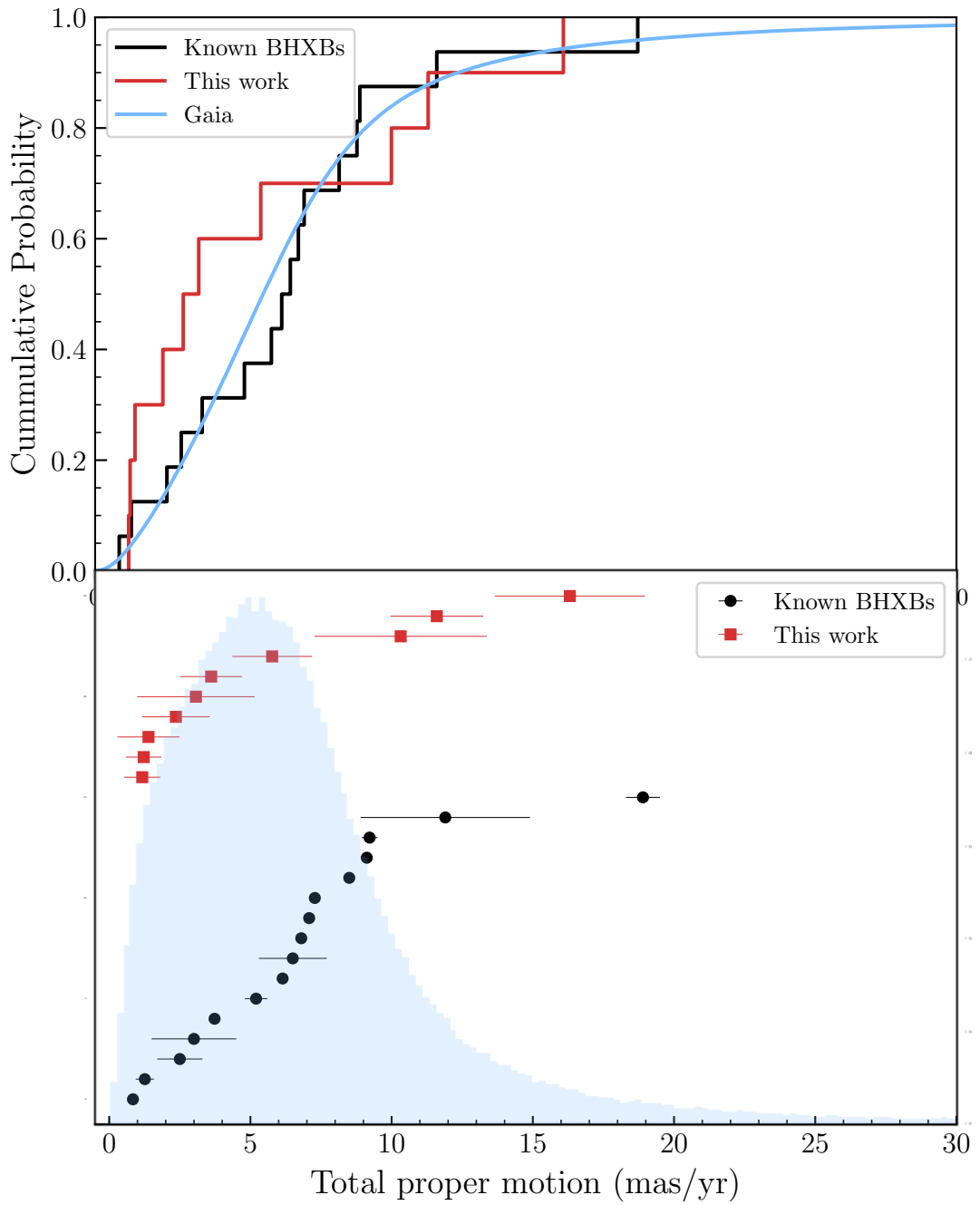


Figure 5.9: Top panel - A cumulative distribution of the total proper motions of a sample of Gaia sources (blue solid line), the radio sources in this work (red solid line) and the BHXBs known in our Galaxy (black solid line). Bottom panel - A forest plot of the total proper motion of the known BHXBs (black points), the sources for which proper motions was measured in this work (red points) and the Gaia proper motions depicted with the blue histogram.

plane, making it difficult for all sky survey telescopes like *Gaia* to detect such sources. Similarly, it is more challenging to find faint X-ray counterparts towards the Galactic plane with survey modes of satellites like Chandra and Swift due to dust scattering and extinction.

The fact that none of our Galactic candidates had any X-ray counterpart suggest that these could be BHXBs with the quiescent X-ray emission that is either highly extinguished or present at a level below the threshold of the X-ray satellites that have observed that patch of the sky. VLA J2130+12 is a quiescent BHXB candidate in our Galaxy with no X-ray counterpart (Tetarenko et al., 2016a), so if the Galactic candidates in this work are quiescent BHXBs it would not be surprising that no X-ray counterpart could be found. Upper limits on the X-rays from these targets can be obtained by using services like the ‘High Energy Lightcurve generator’⁴. Searching for X-ray emission from these targets with targeted observations using the X-ray satellite Swift would help determine whether these are Galactic radio sources but with/without X-ray emission. The correlation between radio and X-ray luminosities during the quiescent phase of BHXBs is based on the study of four systems and so the scatter of X-ray and radio correlation at low luminosity is not well characterised. So being able to study more such sources will help understand the radio X-ray correlation better. Further, telescopes like eROSITA (Merloni et al., 2012) could take deeper observations to place very stringent upper limits on the X-ray emission from these targets, caveat the confusion limits towards the Galactic plane.

Another piece of the puzzle will be explored by using optical and infrared observations. Our targets do not have convincing optical and infrared counterparts in the current available catalogues. Ideally, looking at these targets with any sensitive optical telescope should be able to tell us about the optical counterpart of the target. If the target is a binary, the optical counterpart will tell us about the parameters of the stellar component of the binary and thus help to constrain

⁴<http://xmmuls.esac.esa.int/upperlimitsserver/>

the nature of the binary. Photometry and spectroscopy of the targets that are detected with an optical counterpart in the initial focused study can help deduce the orbital parameters and mass function of the binary. Obtaining the mass function can give a dynamical measurement of the masses of the components in the binary along with a possible line-of-sight velocity measurement. Some of our targets might suffer from high extinction due to their location in the Galactic plane. In such cases, we will need infrared photometry and spectroscopy to determine the orbital parameters of the binary. The launch of James Webb Space Telescope might help push the limits to which we can detect these faint highly extinguished infrared counterparts of our Galactic candidates.

For exploring the radio wavelength spectrum of these sources will also need some more follow up programs. A collation of the flux densities of these sources from radio surveys over time e.g., the CORNISH survey (Purcell et al., 2013), the FIRST survey (Becker et al., 1994), the Becker et al. (2010) study and the Very Large Array Sky Survey (VLASS) would provide a broad band radio spectrum, enabling a spectral index fit. Sources with steep spectra could be identified from such a study, with the caveat of the high variability of the sources, and this will give the possibility of detecting highly-accelerated pulsars or redback pulsars that have been missed by pulsar studies so far. The sources that were not detected with the VLBA survey in any epochs were either resolved out or were below the sensitivity level of the VLBA. Observing these targets with mid-range resolution with the eMERLIN could prove to be useful to obtain the upper limit at which these sources are getting resolved and obtain a size-scale of these sources. The sources that have been detected in our study in three epochs still have large uncertainties on their proper motions and parallaxes. Obtaining another epoch of observation on all these targets will give a five year time baseline to fit the proper motion and reduce the uncertainties drastically. The targets that have been detected in two epochs with the VLBA in our study will need two more epochs to reduce the uncertainties on proper motion fits and get an estimate of

the parallax. Constraints on the parallax of the moving targets in our study will then help convert radio (and in some cases X-ray) fluxes to luminosities, providing a way to compare the two kinds of emission and thus understand the nature of the source.

5.8 Summary

We observed 33 highly variable radio sources with the VLBA that were identified in a previous VLA survey of the Galactic plane.

- We detected 19 out of the 33 targets with the VLBA, on one or more epochs. 8 out of these targets had a $5\text{--}6\sigma$ significance detection at one or more epochs. We classify these detections as marginal detections and discuss their reliability on a case-by-case basis.
- The non-detection of the 14 targets that were originally seen with the VLA could be due to the radio emission being resolved out or varying to below the detection threshold.
- The exact position of two out of these 19 targets could not be identified, which could be addressed by observing the target for a longer time to obtain a better uv-coverage.
- Seven out of the remaining 17 targets were detected only in one epoch, out of which four did not have valid data for the second and third epochs.
- The three targets that were detected in only one epoch even with valid data for other epochs could be due to high variability of the source or high noise in images, as is the case for Gii and Iii.
- We measured proper motions for 10 sources, out of which five are moving with a $>3\sigma$ significance and one has a parallax measurement (0.63 ± 0.20 mas) that places it within the Galaxy.

- We suggest conducting follow-up of all the targets that were not detected in this work with eMERLIN and taking another epoch of observation of all the sources that were detected in one or more epochs using the VLBA.
- Deeper optical, infrared and X-ray follow-up of the ten sources for which we measured proper motions will be key to determining the nature of these targets.
- We could successfully show that measuring the proper motion of variable radio sources is a viable technique to select a sample of Galactic targets and potentially search for quiescent BHXBs.

Discussion, Future Prospects and Conclusions

6.1 Discussion

This thesis has explored the various ways in which radio astrometry can improve our understanding of the black hole population in our Galaxy. We have used radio astrometry to measure proper motions and parallaxes, estimate natal kick velocities, and search for new Galactic BHXB candidates. We have demonstrated how astrometry of black hole X-ray binaries (BHXBs) can be used to understand the birth, evolution and distribution of these sources in our Galaxy.

6.1.1 A new technique: Improvements on previous studies

Black hole natal kicks have been studied for decades now by correlating natal kicks with the positions and distribution of BHXBs in our Galaxy. Comparison between the dispersion in the distance above/below the Galactic plane, z , for BHXBs and neutron star X-ray binaries (NSXBs) was initially used to suggest that BHs obtain weaker kicks as compared to NSs (White & van Paradijs, 1996), which with updated distances for BHXBs gave a contradictory result i.e., that BHXBs and NSXBs could get similar kicks (Jonker & Nelemans, 2004; Repetto et al., 2012).

Repetto et al. (2017) simulates a synthetic BHXB population by considering their evolution and kinematics in the Galaxy, and by assuming models of various natal kick distributions that were motivated by NSXB velocity distributions. The Galactic distribution of this synthetic population was compared to the z -distribution of the existing BHXB population in our Galaxy and it was shown that high velocity kicks are required to explain the distribution for BHXBs (Repetto & Nelemans, 2015; Repetto et al., 2017). These studies used 3D information (position in the Galaxy and distance) to estimate the need for BH natal kicks to obtain the current distribution of BHXBs, which was not enough to determine natal kick distributions of the BHXB population. Also, as low mass BHXBs in our Galaxy could be very old, the correlation between z and natal kick is not a true indicator of the strength of the kick the system received as the system could just be on a path towards the Galactic plane, as was the case for GRO J1655–40 (Mirabel et al., 2002; Gandhi et al., 2019; Atri et al., 2019). However, BHXBs will spend more time at $z=z_{\max}$ than going through the Plane and hence with a very large sample of BHXBs some statistical test might be possible to relate z_{\max} to the natal kick the BHXB received.

Six-Dimensional information (peculiar velocity) for a small sample of BHXBs (five) was used by various authors to determine if the individual systems had received a substantial kick at birth (Mirabel et al., 2001, 2002; Mirabel & Rodrigues, 2003; Mirabel, 2017; Dhawan et al., 2007). The peculiar velocity information combined with stellar evolution codes was used to estimate the natal kick of three systems (Fragos et al., 2009; Willems et al., 2005; Wong et al., 2012), but that was only possible because the three systems in question are rare cases of very well studied BHXBs that have many of their parameters measured. Although using peculiar velocity as proxy for natal kicks enabled the first attempts to test the correlation between the velocity and the birth mechanism of a BH, it had its limitations. Many of the BHXBs are found away from the Galactic plane (see Figure 1.19, Chapter 1; Repetto et al., 2012) where the local standard of rest is

not as well defined.

In this thesis, we have refined these methods of kick determination, to determine a robust natal kick velocity distribution for the BHXB population. Taking the 3D distribution of BHXBs (RA, Dec and distance), adding the information of the motion of the source in our Galaxy (proper motion in RA and Dec, and the line-of-sight velocity) and integrating the Galactocentric orbits to the possible locations of the birth of the system in the Galactic plane has provided better constraints on the potential kick velocities (PKV) of individual BHXBs. We were able to analyse the PKV distributions of 16 BHXBs, giving us a constraint on the kick velocity distribution of the overall population of BHXBs. Using a six dimensional phase space and integrating the Galactocentric orbit of a system through the Galactic potential relies heavily on the observed parameters (RA, Dec, distance, proper motion in RA and Dec, and line-of-sight velocity) and models of the Galactic potential. Combining the newly-released stellar optical astrometry survey, *Gaia*-DR2 (Gaia Collaboration et al., 2018a), our continued VLBI BHXB astrometry campaigns and ongoing optical/IR spectroscopy campaigns by collaborators (e.g., Torres et al., 2020) has significantly increased the sample of systems (from five to 16) with classified birth mechanisms.

6.1.2 Natal kicks and beyond: implications

Theoretical studies have suggested that stellar-mass black holes are formed when a massive star dies either due to the fallback of matter onto a proto-neutron star in a supernova explosion or when the star directly collapses onto itself without a supernova. The underlying reasons for the preference of one birth pathway over the other was found to be much more complicated than just a progenitor mass dependence from theoretical modelling and simulations (e.g., Sukhbold et al., 2016). Mirabel (2017) suggested that there was some evidence for anti-correlation between peculiar velocity and the mass of the BH in the system, albeit with the caveat that there were only five systems under consideration. This anti-

correlation implied that there was a higher chance of a BH with a larger mass to be born via a direct collapse. In our work we used a larger sample of 16 BHXBs to test this correlation and did not find any clear evidence supporting its existence, suggesting that a lower mass BH did not always imply that the BH was born with a successful SN explosion.

This thesis also reports the first observationally constrained PKV distribution for the BHXB population. Fitting our derived distribution with both a unimodal and a bimodal model, we found that a unimodal fit was more preferred for the kick distribution with the current sample, which supports the idea that there might not be a velocity cut-off between the direct collapse and supernova birth pathways of BHXBs. A bimodal fit could not be ruled out and further investigation is needed to explore this possibility (see §6.2). A bimodal fit to the kick distribution with the two peaks having a median of $38 \pm 12 \text{ km s}^{-1}$ and $135 \pm 13 \text{ km s}^{-1}$ might indicate a possible cut-off kick velocity for a system to have been formed by the two birth mechanisms, with the lower median supporting BH birth via direct collapse and the higher median suggesting birth via supernova explosion.

Natal kick distributions are a key input parameter for N-body simulations of globular clusters, and hence for estimating the number of black holes and BHXBs that could be retained in a globular cluster. The ongoing debate of the prevalence of BHs in GCs and attempts to reconcile the theoretical estimates of having ~ 1000 BHXBs in a typical GCs (Giesler et al., 2018) with the lack of such a large number of systems being observed will need better constraints on the kick velocity with which BHs are born. Whereas the current simulations assume simple flat priors or priors inspired by the velocity distribution of NSs, the observationally constrained BHXB PKV distribution reported in this thesis can serve as a starting point to observationally constrain these simulations. One important bias to be aware of is that this work assumes that most BHXBs are born in the Galactic plane, whereas there is a possibility that some fraction of these systems could have been halo systems, formed in and subsequently ejected from a globular

cluster. Measuring the metallicity of the systems and comparing them with solar metallicity is one way of testing the Galactic disc or halo origin of these sources, as was done for XTE J1118+480 where the higher than solar element abundance could be explained by contamination in a supernova explosion and birth in the Galactic disc (Frontera et al., 2001; González Hernández et al., 2006, 2008b). In the current situation where the ages of most systems are unknown, assuming that the systems are born in the Galactic plane is a necessary assumption for estimating their kicks.

Over the decades, the velocity distribution of NSs has been fitted (Arzoumanian et al., 2002; Chatterjee et al., 2004; Hobbs et al., 2005) using samples of objects that have been increasing in number, with the latest having 28 systems (Verbunt et al., 2017). It is theorised that, amongst other ways, fallback onto a proto-neutron star can form a BH (e.g., Gourgoulhon, 1991), inspiring studies that used neutron star velocity distributions to understand black hole birth and population synthesis. Prior to this work the only possible comparison between the natal kicks of black holes and neutron stars has been on the basis of theoretical models or the root mean square of the height of NS and BHXBs above the Galactic plane (White & van Paradijs, 1996; Jonker & Nelemans, 2004; Repetto et al., 2012; Repetto & Nelemans, 2015; Repetto et al., 2017; Mandel, 2016). We found that the BHXB kick distribution is 3–4 times lower than the NS kick velocity distribution (see Figure , Chapter 4), which could simply be indicative of a momentum conservation effect or different kick mechanisms in the two populations. This comparison will become more conclusive with an improvement (more precise velocity measurements) in the constraints on the kick distributions of the BHXB and NS populations. These comparative studies are essential to understand the mass and energy release differences between the supernova explosions accompanying the birth of BHs and NSs in binaries.

6.1.3 BHXB treasure unlocked with astrometry

Apart from natal kick estimations, high precision astrometry is crucial to understand the underlying physics of BHXBs. As discussed earlier, trigonometric parallax is a model independent way of obtaining the distance to a source, and a high significance parallax measurement makes the parallax to distance conversion prior independent. The inclination angle of the radio jets to the line-of-sight can be determined with well constrained proper motions of the ejected jets and the distance to the source. This well constrained inclination angle can then be used to find the speeds of the transient jets and also to obtain tighter constraints on the BH mass (see Chapter 3 for the relations between inclination angle, jet velocity, mass function and distance).

6.1.3.1 Increase in proper motion sample size

Optical and radio astrometry have been used to measure the transverse velocities and parallaxes of BHXBs. Prior to this work, high precision radio astrometry had been shown to successfully measure the proper motion of a few dynamically confirmed BHXBs as in the cases of XTE J1118+480 (Mirabel et al., 2001), Cyg X-1 (Mirabel & Rodrigues, 2003), V404 Cyg (Miller-Jones et al., 2009b), GRS 1915+105 (Dhawan et al., 2007) and MAXI J1836-194 (Russell et al., 2015), and parallaxes for V404 Cyg (Miller-Jones et al., 2009b), Cyg X-1 (Reid et al., 2011) and GRS 1915+105 (Reid et al., 2014). This thesis has been instrumental in measuring the proper motions of four new BHXBs and the parallax of one. Using our VLBI campaigns with the EVN, VLBA and LBA, we measured the proper motions of Swift J1753.5-0127, GX 339-4, GRS 1716-249 and MAXI J1820+070. With an intensive astrometry campaign using the VLBA and the EVN, we also measured a highly significant parallax for MAXI J1820+070.

The above required targeted radio observations of the sources while they were in a hard state during their outburst. *Gaia* on the other hand is helping increase the numbers of BHXBs with measured proper motions and parallaxes by conduct-

ing astrometry in the optical band (Gaia Collaboration et al., 2018a). Although *Gaia* has its limitations, the second data release of *Gaia* reported the proper motions of 18 BHXBs and parallax measurements for six BHXBs that did not have measurements before (Gandhi et al., 2019; Atri et al., 2019). Most of the parallax measurements were not significant but display a case for obtaining loose constraints without the effort of targeted campaigns. In the era of *Gaia*, using Bayesian inference has been recommended to obtain distances from parallaxes (Bailer-Jones, 2015; Astraatmadja & Bailer-Jones, 2016; Luri et al., 2018) and large error bars on the parallax translates to loosely constrained distance posterior distributions. The global offset that affects all *Gaia* parallax measurements is a point of debate with offsets in the range of 0.03–0.07 mas being suggested (Chan & Bovy, 2020; Xu et al., 2019; Luri et al., 2018). This limits the precision with which *Gaia* can measure parallaxes, on top the fact that BHXBs are usually at the limiting magnitude of *Gaia*.

6.1.3.2 Refined system parameters: MAXI J1820+070

We measured the parallax of MAXI J1820+070 using our VLBI astrometry campaign (0.348 ± 0.033 mas), for which *Gaia*-DR2 also measured a parallax (0.31 ± 0.11 mas). In addition to the distance estimates derived using the two parallax measurements, we report upper (3.9 kpc) and lower (1.7 kpc) limits of the distance by constraining the proper motions of the receding and approaching jets and the relation of spectral state transition fluxes to Eddington luminosity (see Chapter 4). This distance constraint (1.7–3.9 kpc) was tighter than the distance posterior distribution ($4.4^{+5.1}_{-2.0}$ kpc) estimated using the *Gaia* parallax, suggesting that *Gaia* parallax to estimate distances is not always the most constraining. We also found this to be the case for 1A 0620–00, XTE J1118+480, GS 1124–684, GRO J1655–40, SAX J1819.3–2525 and Swift J1753.5–0127 (Atri et al., 2019). The parallax of MAXI J1820+070 was underestimated by *Gaia*-DR2, although with the large error bars on the measurement the parallax agrees with the radio parallax within

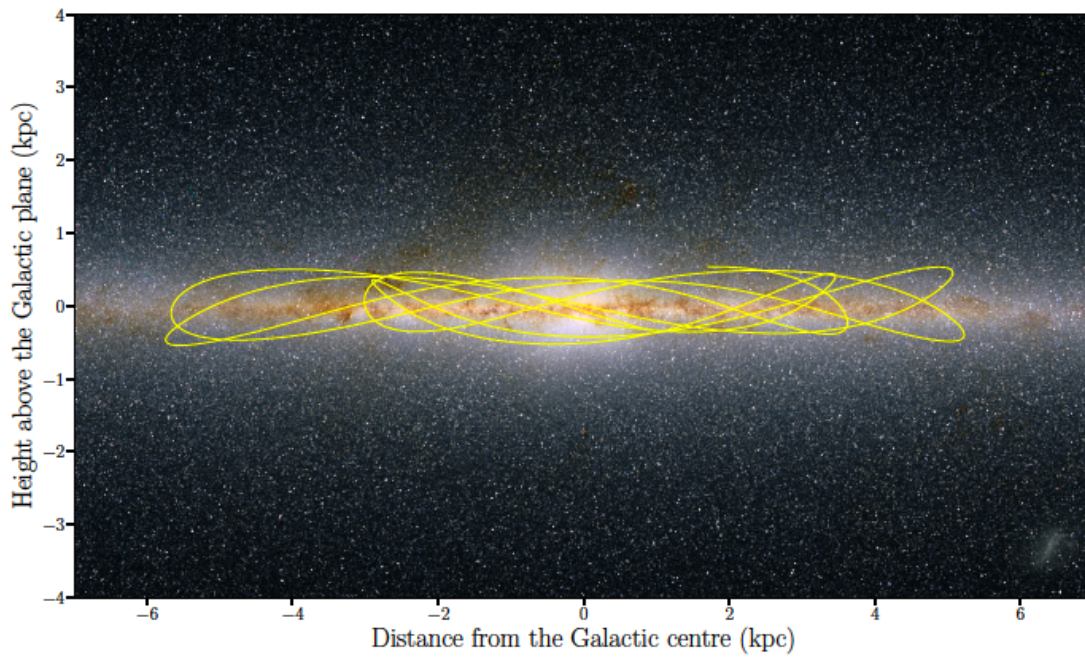


Figure 6.1: Galactocentric orbit of MAXI J1820+070 overlaid on an optical map of the Milky Way Galaxy. (0,0) is the centre of the Galaxy. The starting conditions of the orbit are the current proper motion, distance and systemic radial velocity of the system, which are then integrated back in time for 500 Myr. MAXI J1820+070 is suggested to have been born with an asymmetric natal kick accompanied by a supernova explosion.

1σ . Using the radio parallax of the source we could strongly constrain a few physical parameters of the system including the speed of jets launched in the transient state, the inclination angle of the radio jets to the line-of-sight, an updated mass function, and the X-ray and radio luminosity of various stages of the outburst.

The improved velocity constraints help in tracing the Galactocentric orbit of the source, and one such possible orbit is represented in Figure 6.1. The stronger constraints on parallax and proper motion, as compared to the *Gaia* measurements, also improve the width of the PKV distribution of the system. The PKV distribution has a separation of 80 km s^{-1} between its 5th and 95th percentile when estimated using the *Gaia* measurements as compared to the range of 50 km s^{-1} when estimated using the stronger constraints from the radio parallax and proper motion. The distance is now also being used in various other X-ray (Espinasse et al., 2020; Xu et al., 2020; Homan et al., 2020; Wang et al., 2020), infrared and optical studies of the system, improving our understanding of various aspects of the outburst and system parameters of MAXI J1820+070 (Torres et al., 2020; Markoff et al., 2020).

6.1.3.3 Astrometry to search for BHXBs

Up to now, the dominant method of discovering BHXBs has been to detect them as X-ray and/or optical transients. This thesis has investigated a method that does not depend on BHXBs going into an outburst, but rather catching them in their quiescent state at radio wavelengths. Our filler VLBA program of observing relatively bright targets ($\sim 1 \text{ mJy}$) of unknown nature was to test the possibility of the targets being Galactic and we spent just ~ 15 minutes per epoch and observed 2-3 epochs (see Chapter 5). This thesis has shown that such short observing time surveys are inexpensive ways to get initial estimates on the motions of the targets, which can then be followed up with longer observing campaigns on targets identified as Galactic.

Based on the work in Chapter 4 we now know that BHXBs that are born

with a successful supernova explosion can be observed as high velocity systems in our Galaxy. Hence, Galactic radio objects that are found to be moving at velocities larger than those expected from a typical stellar object could be objects that have received a natal kick when the system was born. One possibility for the nature of such systems is a binary with a compact object as one of the components, and more interestingly a BHXB in a quiescent phase. The radio sources detected in this study could also be accreting neutron star low-mass XRBs, cataclysmic variables, magnetars, planetary nebulae, millisecond pulsars or ultracool dwarfs. All of these can be ruled out by using a combination of the X-ray to radio luminosity ratio of these sources, radio spectral indices (Tetarenko et al., 2016b) and good distance constraints.

6.1.4 The VLBI campaigns

In this thesis, we used the EVN, the VLBA and the LBA to observe BHXBs that went into an outburst. The three arrays provide complementary Northern and Southern hemisphere coverage of the sky, with the LBA as the only VLBI array in the Southern hemisphere and the VLBA and EVN in the Northern hemisphere. The VLBA allows us to also observe geodetic blocks as the dishes are all small and the same size with quick and similar slew times, making quick switching between multiple targets possible. The EVN can observe geodetic blocks but due to longer slew times incurs substantially more observational overhead. The EVN has better sensitivity than the VLBA because of dishes that are larger in size and more in number. The VLBA and the EVN (with the Africa baseline) both have comparable resolutions of 1.4 mas and 1.6 mas, respectively, at 6 cm. Measuring the proper motion and parallax using both radio and optical astrometry, for a few sources that it is possible for, is crucial to explore any possible offsets between the two measurements for BHXBs. Such comparisons, though currently possible with our VLBI facilities, will be pushed to new frontiers by the surveying capabilities of the Square Kilometer Array (SKA; discussed in §6.1.6).

MAXI J1820+070 was an ideal case of a BHXB that stayed in outburst long enough to be able to observe it for multiple epochs within a year and fit the parallax ellipse. A few bright BHXB outbursts have been known to stay in a bright hard state for a few months and then go into multiple reflares (eg., Ulowetz et al., 2019; Zampieri et al., 2019; Shidatsu et al., 2019). Observing such sources with VLBI arrays allows high significance parallax measurements and hence a highly precise and prior-independent distance (i.e., distance posterior distribution that does not change with different priors) for BHXBs. These observations were planned such that the time on source was at least a few hours, which gave good uv-coverage, high signal to noise detections and sub-mas level astrometric accuracy.

The limiting factor for radio observations is the angular broadening for the sources in the Galactic plane, which can be reduced by observing in higher frequencies. Another limitation of such observations is typically the calibrator-target throw, since the systematic errors in the astrometry of the target are linearly dependent on this separation. With the current VLBI facilities, we are then limited by the number of compact calibrators present around the targets. In these observations we observed check sources, extragalactic compact radio sources, to check the effect and quality of the phase solutions on the astrometry of the target by applying the same solutions to the check sources as well. This allowed us to obtain an estimate of the systematic errors in the position measurement of the targets, which would include but not be limited to the errors introduced due to calibrator-target throw. For our VLBA filler campaign (Chapter 5) in which we did not have enough time to observe a separate target as a check source, we treated a few scans of the phase calibrator as the check source.

The limitation introduced in the astrometric precision due to calibrator-target throw can be circumvented by using the technique of ‘multi-view’ calibration (Rioja et al., 2009), in which we observe multiple calibrators in the same patch of the sky to solve for troposphere and ionospheric delays and reduce systematics on the position measurement of the source. A low density of targets that can

be used as calibrators makes it difficult to use this in every case. This technique also requires longer observing times as the number of calibrators that need to be observed increases, thus making it a relatively expensive technique. This technique is also dependent on having the target surrounded by the calibrators in all directions, which might not be the case for all BHXBs that are being observed.

Our work has used a VLBA filler-program to observe 33 targets, wherein each target was observed for ~ 15 minutes and almost the same amount of time on phase calibrators (see Chapter 5). The above work is limited by the thermal noise level that a short VLBI observation can achieve, and so it possible to miss the targets as non-detections just because they are fainter than the 5σ threshold level we have used for our test. So even though we have a one year time baseline in some of the targets for our VLBA survey, the short observation time adversely affects the astrometric accuracy of the position measurements. Future observations with longer observing time will increase the detection significance and thus increase the astrometric accuracy.

6.1.5 PKV limitations and improvements

The PKV distribution reported in this thesis suffers from observational and population bias. The constraints on the PKV distribution can be made tighter by obtaining more precise measurements of the radial and transverse velocity components, and the distance to the source. This problem then demands complementary campaigns in optical or radio astrometry for proper motion and parallax estimates and optical/infrared spectroscopic campaigns for radial velocity measurements. Once these parameters are obtained with at least a 10σ significance, the only source of remaining uncertainty is the model of the Galactic potential being used to integrate the orbits of the systems.

To get a more complete and well informed kick distribution the sample will need to be increased to cover a variety of sources including different masses, and present in the bulge, the disk and the halo of the Galaxy. Our sample mostly

includes sources that were detected due to an outburst except for VLA J2130+12. Chapter 5 reports some possible BHXB candidates, which could help balance our current sample of 16 BHXBs with quiescent BHXB sources. These sources though are all relatively bright (1 mJy) and could be a specific sub-selection of radio bright quiescent systems.

Since our work is also limited by sensitivity, we are mostly biased towards having good measurements for only nearby sources. We are also biased towards BHXBs that did not receive strong enough kicks to unbind them, as we are not able to observe isolated BHs with this work. The BHXBs that received high kicks have a chance of moving further away from us, and thus their detection is luminosity limited, making our sample more biased towards systems with smaller kicks. There is a possibility of upcoming telescope like the SKA and the Next Generation VLA (ngVLA; discussed in §6.1.6) to be able to detect isolated BHs in our Galaxy that might be accreting from their environment and emitting at radio wavelengths (Fender et al., 2013), and understanding their motion through the Galaxy could help in adding another subset of sources with measured PKV distributions. These sources would also be interesting because there is a possibility that these BHs are isolated as they got strong natal kicks at birth and were unbound from their binary. Observing such sources will help remove another observational bias from our sample.

We were able to use our more precise proper motion, parallax and systemic radial velocity for MAXI J1820+070 to update the PKV distribution in Chapter 4 as compared to the estimates derived from Gaia-DR2 in our published work Atri et al. (2019). The unimodal PKV distribution was still a more favourable model even with the more constrained PKV of MAXI J1820+070. The bimodal distribution is slightly more preferred with the more constrained PKV distribution of MAXI J1820+070 in Chapter 4 (Unimodal AICc -16.6, Bimodal AICc -4.4) as compared to the bimodal distribution model using the loosely constrained PKV distribution of MAXI J1820+070 (Unimodal AICc -16.3, Bimodal AICc -2.2) used

in Atri et al. (2019). This suggests that other than adding more systems with measured PKVs, improving the currently available PKV constraints can also help in reaching a consensus about the PKV distribution of the BHB population.

Our current sample of 16 BHBs will need to be increased with more systems that are found in the bulge, the halo and the disc of the Galaxy. This will be used to eliminate any bias in our PKV study due to different locations of the BHB in our Galaxy and thus the subject of different Galactic potentials. As was discussed in Chapter 4 we could not find a correlation between kick velocities and black hole masses, with black hole masses being a source of uncertainty. We would need to increase the number of sources with estimated PKVs and measured masses to test the correlation for a conclusive result. Other than the BHBs in our Galaxy, one possible way to study BHs with a wide range of masses is by including the BHs being detected by LIGO.

LIGO is detecting the mergers of stellar mass BHs and their mass range is higher than the mass of BHs in the BHBs in our Galaxy (see Chapter 1). Simulations have suggested that there is a strong correlation between the natal kick strength and BH-BH merger rates (Wong & Gerosa, 2019) making studies of natal kicks important for the community studying the LIGO sources. It is expected that we might have a better idea of natal kicks for BHs heavier than the BHs in the Galactic BHBs after the detections from the third observing run of LIGO are analysed. Laser Interferometer Space Antenna (LISA), which is expected to begin functioning in 2030, will be able to detect ultracompact binaries in our own Galaxy by detecting gravitational waves. These compact binaries can include black holes, neutron stars and white dwarfs. The possibility of being able to detect BH binary systems and measure their properties, along with their kick velocity will also help in reaching a population that is otherwise unreachable by telescopes depending on electromagnetic emissions from targets.

6.1.6 Upcoming instruments

SKA-VLBI, a combination of short baseline sensitivity with long baseline resolution, will provide opportunities to do unparalleled science. We will be able to reach an order of magnitude fainter than current capabilities within the same observing time using SKA-VLBI (Paragi et al., 2014; Paragi et al., 2019). The era of SKA-VLBI will give better opportunities to conduct in-beam multi-view calibration as the number of calibrators that can be used in a patch of sky will increase as more fainter sources will be accessible (Rioja et al., 2009). It has been shown that this technique combined with the added resolution will be able to provide an order of magnitude better astrometric accuracy (Jimenez-Monferrer et al., 2010) and has the potential to measure very small parallaxes, as small as $3\mu\text{as}$. This suggests that SKA-VLBI might be able to reach a large population of the faint BHXBs in our Galaxy not accessible to current VLBI facilities, be able to conduct microarcsecond precision astrometry for these sources and also be able to observe sources that are further away.

The ngVLA, the planned next-generation radio facility in the northern hemisphere, is expected to provide the long VLBA-like baselines providing milliarcsecond resolution with ten-times VLA-like sensitivity. Due to higher sensitivity provided by this array, techniques like multi-view calibration and in-beam calibration will also be possible by ngVLA. ngVLA is also expected to reach a range of faint BHXBs with its sensitivity and will help measure the proper motions and parallaxes of these sources due to the high resolution provided by the VLBA-like baselines. The accuracy of these measurements will be improved as compared to those possible with the current VLBA due to a possible reduction in the systematic errors.

6.2 Future Work

The PKV distribution for BHXBs that we have obtained suffers from observational biases and also focuses only on outbursting BHXBs. We expect that continued radio VLBI campaigns on outbursting BHXBs will add more sources with a range of masses to our sample set, helping in testing the mass versus kick relation without the statistical tests being affected by low numbers of systems in the sample set. We will also be able to sample more systems from the halo, the disc and the bulge of the Galaxy to study and compare the kick distributions of systems in the disc versus the halo. The model estimates of the PKV distributions of the BHXB population also suffers from the low number of events, with only four systems contributing to the lower peak of the bimodal distribution (see Chapter 4). Hence, we are planning on continuing this work with the VLBA, LBA and the EVN to double the number of BHXBs with estimated PKV distributions and reach at least a similar number of systems to that used to determine the velocity distribution for NSs (28; Verbunt et al., 2017). The third data release of *Gaia* (release date still to be decided) will report more accurate astrometry due to a longer time baseline than *Gaia*-DR2, include orbital corrections for some massive systems and might even detect some new sources. These will be used to update the existing proper motion and parallax estimates of BHXBs that either only have *Gaia* astrometry for measurements, or have improved measurements than the existing radio astrometry measurements.

We also have additional VLBI data for six sources, which over time and with observing a few of those targets for one or more epochs will help constrain their proper motions and even parallaxes in some cases. These sources had been detected during their outburst and typically go into outburst every few years. We are awaiting more outbursts from these sources to re-observe these targets for one or two more epochs to constrain their proper motions and/or parallaxes. GX339-4 is one of these six targets and we have already measured the proper motion of this target (see Chapter 4). We started an observing campaign to mea-

sure the parallax of GX 339–4 with the LBA and to observe GX 339–4 as it went into a short lived outburst in 2019. The observing scheme for this campaign was slightly different than the observations that we have done in the work reported in this thesis. We observed four calibrators around GX 339–4 to test the multi-view calibration technique and reduce the systematics affecting the position measurement. This would help obtain a parallax measurement of GX 339–4 by building the observing sample over the next few years when GX339–4 goes into repeated outbursts. This technique is also a good test bed to gear up for the SKA and ngVLA, when multi-view will be more frequently possible.

We have identified possible BHXB candidates in Chapter 5 that will need more follow-up to confirm their nature. We will be following up the sources showing significant proper motion with the VLBA to get tighter constraints on their proper motions and in some cases parallaxes. The systems that were not detected in the VLBA survey will be followed up by VLA and/or eMERLIN to identify flux variability of those sources over a longer time scale. We were able to show the success of a technique to follow up highly variable radio sources identified with the VLA in the Becker et al. (2010) study with the VLBA to find possible Galactic radio sources. The detection rate of any such future campaign can be improved by first doing a VLA survey to update the positions of the targets, and then following up with the VLBA. Our study demonstrates the feasibility of a future campaign to follow up similar variable sources reported in Very Large Array Sky Survey (VLASS) in a VLBA filler program similar to the one done in Chapter 5. If any of these sources are found to be BHXBs, this would help remove some of the observational bias from our current PKV distribution of the BHXB population.

A couple of BHXBs, namely XTE J1118+480 (Fragos et al., 2009) and GRO J1655-40 (Willems et al., 2005), have a wealth of information on them like orbital periods, masses of the binary components, velocities, distances, donor luminosity and donor effective temperature. In the last few years systems like V404 Cyg

and MAXI J1820+070 have given us an opportunity to study them as well as XTE J1118+480 and GRO J1655–40 due to their extended outburst and reflare period. Recreating a detailed evolutionary history of V404 Cyg and MAXI J1820+070 similar to the work done by Fragos et al. (2009) and Willems et al. (2005) is thus possible. This analysis will allow the estimation of the natal kicks of these systems, and comparing the PKVs of these systems with their natal kicks will be a good test of the use of PKV as a proxy for the real natal kick of BHXBs.

Our PKV distribution determination code also has application in the neutron star and pulsar velocities. Our code has the provision of using broad constraints of any of the measured parameters to estimate the PKV distribution. This is a welcome capability for objects like neutron stars and pulsars as radial velocity measurements of these sources are highly challenging and there are very few of them (mostly NS-XRBs) with any radial velocity measurements. On the other hand, their proper motions and parallaxes are being improved with VLBI facilities and there are now 57 pulsars with well constrained proper motion and parallaxes (Deller et al., 2019). Currently, the velocity distributions of pulsars are based only on the proper motion and distance. Using our code with some possible radial velocity assumptions, we will be able to obtain a PKV distribution of pulsars using the complete three dimensional motion of the objects.

6.3 Conclusions

This research has established the first observationally constrained potential kick velocity distribution of the BHXB population, which has implications in understanding black hole birth and supernova mechanisms, and is an integral input in various population synthesis codes and in black hole merger rates estimation. Using a sample of 16 BHXBs, we found that a unimodal distribution with a median of $107 \pm 16 \text{ km s}^{-1}$ and an uncertainty of $56 \pm 14 \text{ km s}^{-1}$ was more favourable than a bimodal distribution. This work was instrumental in suggesting that asymmetric black hole natal kicks and hence spin-orbit misalignment and ejection from

globular clusters might be common among BHXBs. We were able to conduct this study by combining proper motion and parallax measurements from radio and optical astrometry.

High precision radio astrometry was used to measure the third most significant parallax (0.348 ± 0.033 mas) of a BHXB, MAXI J1820+070. This parallax measurement was used to improve the precision of estimates of various parameters of the source and is also being used to understand the underlying mechanisms of the activity of this BHXB during its outburst and reflare period. The wealth of physical information from this measurement has motivated us to continue our high-precision radio VLBI astrometry campaigns for BHXBs. In the cases where the target is bright enough such that the accuracy of the astrometry is not sensitivity limited, we should move towards testing calibration techniques that present the promise of reducing systematic errors like multi-view calibration.

We also explored a technique motivated by the serendipitous detection of a quiescent BHXB candidate in the field to search for more such systems hiding in the Galaxy. A VLBA survey to measure the motions of highly variable radio sources with flat or inverted spectra identified by comparing various VLA surveys has been demonstrated as an effective technique to identify a sample of sources that could be Galactic. We found six likely Galactic candidates, and follow-up of these targets in optical/near-IR, X-rays and radio will help in understanding the nature of these targets. This technique might be useful to ascertain the nature of the variable radio sources with flat and inverted spectra from other surveys like VLASS. This could open up a method to study and detect either a new population of variable Galactic radio sources or quiescent BHXBs that have not yet been identified in any other survey.

Continued efforts to build a sample of BHXBs with measured proper motions, systemic radial velocities and distances will help obtain stricter constraints on the kick distribution and test the correlation between mass of the black hole and the kick velocity. These efforts will be continued using VLBI astrometry and optical

astrometry from *Gaia*-DR3. It is also expected that instruments like the SKA and the ngVLA will reach an order of magnitude greater sensitivity and thus will allow us to reach objects that are inaccessible to current VLBI arrays.

Appendices

Publications

The work in this thesis has contributed to the following publications.

- **P. Atri**, J. C. A. Miller-Jones, A. Bahramian, R. M. Plotkin, P. G. Jonker, G. Nelemans, T. J. Maccarone, G. R. Sivakoff, A. T. Deller, S. Chaty, M. A. P. Torres, S. Horiuchi, J. McCallum, T. Natusch, C. J. Phillips, J. Stevens, S. Weston (2019), ‘Potential Kick Velocity distribution of black hole X-ray binaries and implications for natal kicks’, *Monthly Notices of the Royal Astronomical Society*, Volume 489, Issue 3, p.3116-3134.

This work is reproduced in Chapter [3](#).

- **P. Atri**, J. C. A. Miller-Jones, A. Bahramian, R. M. Plotkin, A. T. Deller, P. G. Jonker, T. J. Maccaron, G. R. Sivakoff, R. Soria, D. Altamirano, T. Belloni, R. Fender, E. Koerding, D. Maitra, S. Markoff, S. Migliari, D. Russell, T. Russell, C. L. Sarazin, A. J. Tetarenko, and V. Tudose (2020), ‘A radio parallax to the black hole X-ray binary MAXI J1820+070’, *Monthly Notices of the Royal Astronomical Society*, Letters, Volume 493, Issue 1, p.L81-L86.

This work is reproduced in Chapter [4](#).

- T. Bassi, M. Del Santo, A. D’Ai, S. E. Motta, J. Malzac, A. Segreto, J. C. A. Miller-Jones, **P. Atri**, R. M. Plotkin, T. M. Belloni, T. Mineo and

A. K. Tzioumis (2019), ‘The long outburst of the black hole transient GRS 1716-249 observed in the X-ray and radio band’, *Monthly Notices of the Royal Astronomical Society*, Volume 482, Issue 2, p.1587-1601.

This work followed the changes in X-ray and radio emission of a BHXB, GRS 1716-249, during its 2016–2017 outburst. I provided the radio flux density of the system at three epochs using the LBA data that was acquired to measure the proper motion of the source.

- T. J. Maccarone, A. Osler, J. C. A Miller-Jones, **P. Atri**, D. M. Russell, D. L. Meier, I. M. McHardy, P. A. Longa-Peña (2020), ‘The stringent upper limit on jet power in the persistent soft state source 4U 1957+11’, *accepted for publication to Monthly Notices of the Royal Astronomical Society Letters*, arXiv:2007.00834.

This work presents a deep upper limit on the radio emission from a BHXB candidate, 4U 1957+11, in a soft state and discusses the location and velocity of the source. I provided the distance probability distribution and the potential kick velocity probability distribution estimates for this work, which led to the conclusion that this source probably obtained an asymmetric natal kick at birth.

Appendix **B**

Co-author permissions

To Whom It May Concern,

I, Pikky Atri, have outlined my contributions and the contributions of the Co-Authors to the chapters in this thesis that have been adapted from published papers (Chapter 3, Parallax of MAXI J1820+070 : a case study and Chapter 4, 'Black hole natal kicks and birth constraints') and to Chapter 5, 'A search for quiescent Galactic black hole systems'.

(Signature of candidate)

I, as a Co-Author, endorse that the level of contribution indicated by the candidate at in 'Statement of contribution by others' at the beginning of this thesis is appropriate.

Alexandra Tetarenko

(Full name of Co-Author)

(Signature of Co-Author)

To Whom It May Concern,

I, Pikky Atri, have outlined my contributions and the contributions of the Co-Authors to the chapters in this thesis that have been adapted from published papers (Chapter 3, Parallax of MAXIJ1820+070 : a case study and Chapter 4, 'Black hole natal kicks and birth constraints') and to Chapter 5, 'A search for quiescent Galactic black hole systems'.

(Signature of candidate)

I, as a Co-Author, endorse that the level of contribution indicated by the candidate at in 'Statement of contribution by others' at the beginning of this thesis is appropriate.

Arash Bahramian

(Full name of Co-Author)

(Signature of Co-Author)

To Whom It May Concern,

I, Pikky Atri, have outlined my contributions and the contributions of the Co-Authors to the chapters in this thesis that have been adapted from published papers (Chapter 3, Parallax of MAXI J1820+070 : a case study and Chapter 4, 'Black hole natal kicks and birth constraints') and to Chapter 5, 'A search for quiescent Galactic black hole systems'.

(Signature of candidate)

I, as a Co-Author, endorse that the level of contribution indicated by the candidate at in 'Statement of contribution by others' at the beginning of this thesis is appropriate.

(Full name of Co-Author)

(Signature of Co-Author)

Prof. Sylvain Chaty

To Whom It May Concern,

I, Pikky Atri, have outlined my contributions and the contributions of the Co-Authors to the chapters in this thesis that have been adapted from published papers (Chapter 3, Parallax of MAXI J1820+070 : a case study and Chapter 4, 'Black hole natal kicks and birth constraints') and to Chapter 5, 'A search for quiescent Galactic black hole systems'.

(Signature of candidate)

I, as a Co-Author, endorse that the level of contribution indicated by the candidate at in 'Statement of contribution by others' at the beginning of this thesis is appropriate.

Christopher John Phillips

(Full name of Co-Author)

(Signature of Co-Author)

To Whom It May Concern,

I, Pikky Atri, have outlined my contributions and the contributions of the Co-Authors to the chapters in this thesis that have been adapted from published papers (Chapter 3, Parallax of MAXI J1820+070 : a case study and Chapter 4, 'Black hole natal kicks and birth constraints') and to Chapter 5, 'A search for quiescent Galactic black hole systems'.

(Signature of candidate)

I, as a Co-Author, endorse that the level of contribution indicated by the candidate at in 'Statement of contribution by others' at the beginning of this thesis is appropriate.

Craig L. Sarazin

(Full name of Co-Author)

(Signature of Co-Author) 

To Whom It May Concern,

I, Pikky Atri, have outlined my contributions and the contributions of the Co-Authors to the chapters in this thesis that have been adapted from published papers (Chapter 3, Parallax of MAXI J1820+070 : a case study and Chapter 4, 'Black hole natal kicks and birth constraints') and to Chapter 5, 'A search for quiescent Galactic black hole systems'.

(Signature of candidate)

I, as a Co-Author, endorse that the level of contribution indicated by the candidate at in 'Statement of contribution by others' at the beginning of this thesis is appropriate.

Craig Owen Heinke

(Full name of Co-Author)

(Signature of Co-Author)

To Whom It May Concern,

I, Pikky Atri, have outlined my contributions and the contributions of the Co-Authors to the chapters in this thesis that have been adapted from published papers (Chapter 3, Parallax of MAXI J1820+070 : a case study and Chapter 4, 'Black hole natal kicks and birth constraints') and to Chapter 5, 'A search for quiescent Galactic black hole systems'.

(Signature of candidate)

I, as a Co-Author, endorse that the level of contribution indicated by the candidate at in 'Statement of contribution by others' at the beginning of this thesis is appropriate.

Adam T. Deller

(Full name of Co-Author)

(Signature of Co-Author)

To Whom It May Concern,

I, Pikky Atri, have outlined my contributions and the contributions of the Co-Authors to the chapters in this thesis that have been adapted from published papers (Chapter 3, 'Parallax of MAXI J1820+070 : a case study' and Chapter 4, 'Black hole natal kicks and birth constraints') and to Chapter 5, 'A search for quiescent Galactic black hole systems'.

(Signature of candidate)

I, as a Co-Author, endorse that the level of contribution indicated by the candidate at in 'Statement of contribution by others' at the beginning of this thesis is appropriate.

Diego Altamirano

(Full name of Co-Author)

(Signature of Co-Author)

To Whom It May Concern,

I, Pikky Atri, have outlined my contributions and the contributions of the Co-Authors to the chapters in this thesis that have been adapted from published papers (Chapter 3, Parallax of MAXI J1820+070 : a case study and Chapter 4, 'Black hole natal kicks and birth constraints') and to Chapter 5, 'A search for quiescent Galactic black hole systems'.

(Signature of candidate)

I, as a Co-Author, endorse that the level of contribution indicated by the candidate at in 'Statement of contribution by others' at the beginning of this thesis is appropriate.

Dipankar Maitra

(Full name of Co-Author)

(Signature of Co-Author)

To Whom It May Concern,

I, Pikky Atri, have outlined my contributions and the contributions of the Co-Authors to the chapters in this thesis that have been adapted from published papers (Chapter 3, Parallax of MAXI J1820+070 : a case study and Chapter 4, 'Black hole natal kicks and birth constraints') and to Chapter 5, 'A search for quiescent Galactic black hole systems'.

(Signature of candidate)

I, as a Co-Author, endorse that the level of contribution indicated by the candidate at in 'Statement of contribution by others' at the beginning of this thesis is appropriate.

Elmar Koering

(Full name of Co-Author)

(Signature of Co-Author)

To Whom It May Concern,

I, Pikky Atri, have outlined my contributions and the contributions of the Co-Authors to the chapters in this thesis that have been adapted from published papers (Chapter 3, Parallax of MAXI J1820+070 : a case study and Chapter 4, 'Black hole natal kicks and birth constraints') and to Chapter 5, 'A search for quiescent Galactic black hole systems'.

(Signature of candidate)

I, as a Co-Author, endorse that the level of contribution indicated by the candidate at in 'Statement of contribution by others' at the beginning of this thesis is appropriate.

A handwritten signature in black ink that reads "Gijs Nelouwers". The signature is written in a cursive style with a large initial 'G'.

(Full name of Co-Author)

(Signature of Co-Author)

To Whom It May Concern,

I, Pikky Atri, have outlined my contributions and the contributions of the Co-Authors to the chapters in this thesis that have been adapted from published papers (Chapter 3, Parallax of MAXI J1820+070 : a case study and Chapter 4, 'Black hole natal kicks and birth constraints') and to Chapter 5, 'A search for quiescent Galactic black hole systems'.

(Signature of candidate)

I, as a Co-Author, endorse that the level of contribution indicated by the candidate at in 'Statement of contribution by others' at the beginning of this thesis is appropriate.

Gregory Robert Sivakoff

(Full name of Co-Author)

(Signature of Co-Author)

To Whom It May Concern,

I, Pikky Atri, have outlined my contributions and the contributions of the Co-Authors to the chapters in this thesis that have been adapted from published papers (Chapter 3, Parallax of MAXI J1820+070 : a case study and Chapter 4, 'Black hole natal kicks and birth constraints') and to Chapter 5, 'A search for quiescent Galactic black hole systems'.

(Signature of candidate)

I, as a Co-Author, endorse that the level of contribution indicated by the candidate at in 'Statement of contribution by others' at the beginning of this thesis is appropriate.

James C.A. Miller-Jones

(Full name of Co-Author)

(Signature of Co-Author)

To Whom It May Concern,

I, Pikky Atri, have outlined my contributions and the contributions of the Co-Authors to the chapters in this thesis that have been adapted from published papers (Chapter 3, Parallax of MAXI J1820+070 : a case study and Chapter 4, 'Black hole natal kicks and birth constraints') and to Chapter 5, 'A search for quiescent Galactic black hole systems'.

(Signature of candidate)

I, as a Co-Author, endorse that the level of contribution indicated by the candidate at in 'Statement of contribution by others' at the beginning of this thesis is appropriate.

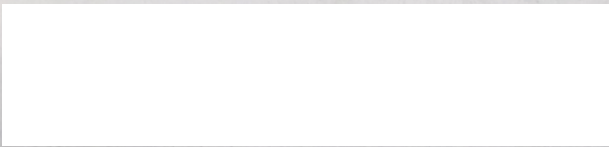
Manuel Ángel Pérez Torres

(Full name of Co-Author)

(Signature of Co-Author)

To Whom It May Concern,

I, Pikky Atri, have outlined my contributions and the contributions of the Co-Authors to the chapters in this thesis that have been adapted from published papers (Chapter 3, Parallax of MAXIJ1820+070 : a case study and Chapter 4, 'Black hole natal kicks and birth constraints') and to Chapter 5, 'A search for quiescent Galactic black hole systems'.

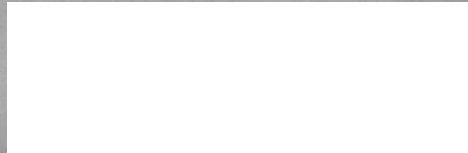


(Signature of candidate)

I, as a Co-Author, endorse that the level of contribution indicated by the candidate at in 'Statement of contribution by others' at the beginning of this thesis is appropriate.

Prof. dr. P. G. Jonker

(Full name of Co-Author)



(Signature of Co-Author)

To Whom It May Concern,

I, Pikky Atri, have outlined my contributions and the contributions of the Co-Authors to the chapters in this thesis that have been adapted from published papers (Chapter 3, Parallax of MAXI J1820+070 : a case study and Chapter 4, 'Black hole natal kicks and birth constraints') and to Chapter 5, 'A search for quiescent Galactic black hole systems'.

(Signature of candidate)

I, as a Co-Author, endorse that the level of contribution indicated by the candidate at in 'Statement of contribution by others' at the beginning of this thesis is appropriate.

Handwritten signature of Richard Plotkin in black ink.

(Full name of Co-Author)

(Signature of Co-Author)

To Whom It May Concern,

I, Pikky Atri, have outlined my contributions and the contributions of the Co-Authors to the chapters in this thesis that have been adapted from published papers (Chapter 3, 'Parallax of MAXI J1820+070 : a case study' and Chapter 4, 'Black hole natal kicks and birth constraints') and to Chapter 5, 'A search for quiescent Galactic black hole systems'.

(Signature of candidate)

I, as a Co-Author, endorse that the level of contribution indicated by the candidate at in 'Statement of contribution by others' at the beginning of this thesis is appropriate.


(Full name of Co-Author)

(Signature of Co-Author)

Prof. Rob Fender

To Whom It May Concern,

I, Pikky Atri, have outlined my contributions and the contributions of the Co-Authors to the chapters in this thesis that have been adapted from published papers (Chapter 3, Parallax of MAXI J1820+070 : a case study and Chapter 4, 'Black hole natal kicks and birth constraints') and to Chapter 5, 'A search for quiescent Galactic black hole systems'.

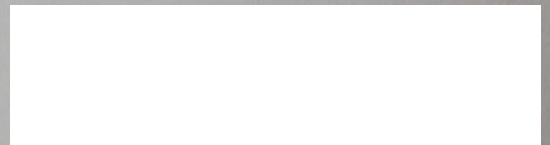


(Signature of candidate)

I, as a Co-Author, endorse that the level of contribution indicated by the candidate at in 'Statement of contribution by others' at the beginning of this thesis is appropriate.

ROBERTO SORIA

(Full name of Co-Author)



(Signature of Co-Author)

To Whom It May Concern,

I, Pikky Atri, have outlined my contributions and the contributions of the Co-Authors to the chapters in this thesis that have been adapted from published papers (Chapter 3, Parallax of MAXI J1820+070 : a case study and Chapter 4, 'Black hole natal kicks and birth constraints') and to Chapter 5, 'A search for quiescent Galactic black hole systems'.

(Signature of candidate)

I, as a Co-Author, endorse that the level of contribution indicated by the candidate at in 'Statement of contribution by others' at the beginning of this thesis is appropriate.

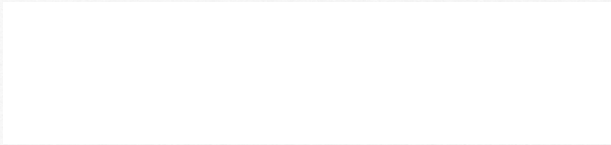
Prof. Sera B. Markoff

(Full name of Co-Author)

(Signature of Co-Author)

To Whom It May Concern,

I, Pikky Atri, have outlined my contributions and the contributions of the Co-Authors to the chapters in this thesis that have been adapted from published papers (Chapter 3, Parallax of MAXIJ1820+070 : a case study and Chapter 4, 'Black hole natal kicks and birth constraints') and to Chapter 5, 'A search for quiescent Galactic black hole systems'.



(Signature of candidate)

I, as a Co-Author, endorse that the level of contribution indicated by the candidate at in 'Statement of contribution by others' at the beginning of this thesis is appropriate.

SHINJI HORIUCHI

(Full name of Co-Author)



(Signature of Co-Author)

To Whom It May Concern,

I, Pikky Atri, have outlined my contributions and the contributions of the Co-Authors to the chapters in this thesis that have been adapted from published papers (Chapter 3, Parallax of MAXI J1820+070 : a case study and Chapter 4, 'Black hole natal kicks and birth constraints') and to Chapter 5, 'A search for quiescent Galactic black hole systems'.

(Signature of candidate)

I, as a Co-Author, endorse that the level of contribution indicated by the candidate at in 'Statement of contribution by others' at the beginning of this thesis is appropriate.

Simone Migliari

(Full name of Co-Author)

(Signature of Co-Author)

To Whom It May Concern,

I, Pikky Atri, have outlined my contributions and the contributions of the Co-Authors to the chapters in this thesis that have been adapted from published papers (Chapter 3, Parallax of MAXIJ1820+070 : a case study and Chapter 4, 'Black hole natal kicks and birth constraints') and to Chapter 5, 'A search for quiescent Galactic black hole systems'.

(Signature of candidate)

I, as a Co-Author, endorse that the level of contribution indicated by the candidate at in 'Statement of contribution by others' at the beginning of this thesis is appropriate.

Jamie Stevens

(Full name of Co-Author)

(Signature of Co-Author)

To Whom It May Concern,

I, Pikky Atri, have outlined my contributions and the contributions of the Co-Authors to the chapters in this thesis that have been adapted from published papers (Chapter 3, Parallax of MAXIJ1820+070 : a case study and Chapter 4, 'Black hole natal kicks and birth constraints') and to Chapter 5, 'A search for quiescent Galactic black hole systems'.

(Signature of candidate)

I, as a Co-Author, endorse that the level of contribution indicated by the candidate at in 'Statement of contribution by others' at the beginning of this thesis is appropriate.

Stuart Duncan Weston

(Full name of Co-Author)

(Signature of Co-Author)

To Whom It May Concern,

I, Pikky Atri, have outlined my contributions and the contributions of the Co-Authors to the chapters in this thesis that have been adapted from published papers (Chapter 3, Parallax of MAXI J1820+070 : a case study and Chapter 4, 'Black hole natal kicks and birth constraints') and to Chapter 5, 'A search for quiescent Galactic black hole systems'.

(Signature of candidate)

I, as a Co-Author, endorse that the level of contribution indicated by the candidate at in 'Statement of contribution by others' at the beginning of this thesis is appropriate.

Thomas D. Russell

(Full name of Co-Author)

(Signature of Co-Author)

To Whom It May Concern,

I, Pikky Atri, have outlined my contributions and the contributions of the Co-Authors to the chapters in this thesis that have been adapted from published papers (Chapter 3, Parallax of MAXI J1820+070 : a case study and Chapter 4, 'Black hole natal kicks and birth constraints') and to Chapter 5, 'A search for quiescent Galactic black hole systems'.

(Signature of candidate)

I, as a Co-Author, endorse that the level of contribution indicated by the candidate at in 'Statement of contribution by others' at the beginning of this thesis is appropriate.

Tim Natusch

(Full name of Co-Author)

(Signature of Co-Author)

To Whom It May Concern,

I, Pikky Atri, have outlined my contributions and the contributions of the Co-Authors to the chapters in this thesis that have been adapted from published papers (Chapter 3, Parallax of MAXI J1820+070 : a case study and Chapter 4, 'Black hole natal kicks and birth constraints') and to Chapter 5, 'A search for quiescent Galactic black hole systems'.

(Signature of candidate)

I, as a Co-Author, endorse that the level of contribution indicated by the candidate at in 'Statement of contribution by others' at the beginning of this thesis is appropriate.

Thomas J Maccarone

(Full name of Co-Author)

(Signature of Co-Author)

To Whom It May Concern,

I, Pikky Atri, have outlined my contributions and the contributions of the Co-Authors to the chapters in this thesis that have been adapted from published papers (Chapter 3, Parallax of MAXI J1820+070 : a case study and Chapter 4, 'Black hole natal kicks and birth constraints') and to Chapter 5, 'A search for quiescent Galactic black hole systems'.

(Signature of candidate)

I, as a Co-Author, endorse that the level of contribution indicated by the candidate at in 'Statement of contribution by others' at the beginning of this thesis is appropriate.

Tomaso Belloni

(Full name of Co-Author)

(Signature of Co-Author)

To Whom It May Concern,

I, Pikky Atri, have outlined my contributions and the contributions of the Co-Authors to the chapters in this thesis that have been adapted from published papers (Chapter 3, Parallax of MAXIJ1820+070 : a case study and Chapter 4, 'Black hole natal kicks and birth constraints') and to Chapter 5, 'A search for quiescent Galactic black hole systems'.

(Signature of candidate)

I, as a Co-Author, endorse that the level of contribution indicated by the candidate at in 'Statement of contribution by others' at the beginning of this thesis is appropriate.

Valeriu Tudose

(Full name of Co-Author)

(Signature of Co-Author)

Bibliography

- B. P. Abbott, et al. (2016a). ‘Astrophysical Implications of the Binary Black-hole Merger GW150914’. *The Astrophysical Journal Letters* **818**:L22.
- B. P. Abbott, et al. (2016b). ‘Binary Black Hole Mergers in the First Advanced LIGO Observing Run’. *Physical Review X* **6**(4):041015.
- S. M. Adams, et al. (2017a). ‘The search for failed supernovae with the Large Binocular Telescope: constraints from 7 yr of data’. *Monthly Notices of the Royal Astronomical Society* **469**:1445–1455.
- S. M. Adams, et al. (2017b). ‘The search for failed supernovae with the Large Binocular Telescope: confirmation of a disappearing star’. *Monthly Notices of the Royal Astronomical Society* **468**(4):4968–4981.
- M. Aglietta, et al. (1987). ‘Comments on the two events observed in neutrino detectors during the supernova 1987A outburst.’. *EPL (Europhysics Letters)* **3**:1321–1324.
- E. Agol & M. Kamionkowski (2002). ‘X-rays from isolated black holes in the Milky Way’. *Monthly Notices of the Royal Astronomical Society* **334**(3):553–562.
- H. Akaike (1974). ‘A New Look at the Statistical Model Identification’. *IEEE Transactions on Automatic Control* **19**:716–723.

- F. Antonini, et al. (2019). ‘Black hole growth through hierarchical black hole mergers in dense star clusters: implications for gravitational wave detections’. *Monthly Notices of the Royal Astronomical Society* **486**(4):5008–5021.
- K. Arur & T. J. Maccarone (2018). ‘Selection effects on the orbital period distribution of low-mass black hole X-ray binaries’. *Monthly Notices of the Royal Astronomical Society* **474**(1):69–76.
- Z. Arzoumanian, et al. (2002). ‘The Velocity Distribution of Isolated Radio Pulsars’. *The Astrophysical Journal* **568**:289–301.
- T. L. Astraatmadja & C. A. L. Bailer-Jones (2016). ‘Estimating Distances from Parallaxes. II. Performance of Bayesian Distance Estimators on a Gaia-like Catalogue’. *The Astrophysical Journal* **832**:137.
- P. Atri, et al. (2020). ‘A radio parallax to the black hole X-ray binary MAXI J1820+070’. *Monthly Notices of the Royal Astronomical Society* **493**(1):L81–L86.
- P. Atri, et al. (2019). ‘Potential kick velocity distribution of black hole X-ray binaries and implications for natal kicks’. *Monthly Notices of the Royal Astronomical Society* **489**(3):3116–3134.
- E. Bañados, et al. (2018). ‘An 800-million-solar-mass black hole in a significantly neutral Universe at a redshift of 7.5’. *Nature* **553**(7689):473–476.
- A. Bahramian, et al. (2014). ‘Discovery of the Third Transient X-Ray Binary in the Galactic Globular Cluster Terzan 5’. *The Astrophysical Journal* **780**:127.
- A. Bahramian, et al. (2018). ‘The MAVERIC Survey: A Transitional Millisecond Pulsar Candidate in Terzan 5’. *The Astrophysical Journal* **864**(1):28.
- C. A. L. Bailer-Jones (2015). ‘Estimating Distances from Parallaxes’. **127**:994.
- J. Ballet, et al. (1993). ‘GRS 1716-249 = GRO J1719-24’. *International Astronomical Union Circulars* **5874**.

- J. M. Bardeen, et al. (1972). ‘Rotating Black Holes: Locally Nonrotating Frames, Energy Extraction, and Scalar Synchrotron Radiation’. *The Astrophysical Journal* **178**:347–370.
- T. Bassi, et al. (2019). ‘The long outburst of the black hole transient GRS 1716-249 observed in the X-ray and radio band’. *Monthly Notices of the Royal Astronomical Society* **482**:1587–1601.
- S. S. Bavera, et al. (2019). ‘The origin of spin in binary black holes: Predicting the distributions of the main observables of Advanced LIGO’. *arXiv e-prints* p. arXiv:1906.12257.
- M. Bayes & M. Price (1763). ‘An Essay towards Solving a Problem in the Doctrine of Chances. By the Late Rev. Mr. Bayes, F. R. S. Communicated by Mr. Price, in a Letter to John Canton, A. M. F. R. S.’. *Philosophical Transactions of the Royal Society of London Series I* **53**:370–418.
- R. H. Becker, et al. (2010). ‘Variable Radio Sources in the Galactic Plane’. *The Astronomical Journal* **140**(1):157–166.
- R. H. Becker, et al. (1995). ‘The FIRST Survey: Faint Images of the Radio Sky at Twenty Centimeters’. *The Astrophysical Journal* **450**:559.
- R. H. Becker, et al. (1994). ‘A 5 GHz VLA Survey of the Galactic Plane’. *The Astrophysical Journal Supplemental* **91**:347.
- K. Belczynski, et al. (2002). ‘Merger Sites of Double Neutron Stars and Their Host Galaxies’. *The Astrophysical Journal Letters* **571**:L147–L150.
- K. Belczynski, et al. (2006). ‘Initial Populations of Black Holes in Star Clusters’. *The Astrophysical Journal* **650**:303–325.
- T. M. Belloni & S. E. Motta (2016). ‘Transient Black Hole Binaries’. In C. Bambi (ed.), *Astrophysics of Black Holes: From Fundamental Aspects to Latest Developments*, vol. 440 of *Astrophysics and Space Science Library*, p. 61.

- M. J. Benacquista & J. M. B. Downing (2013). ‘Relativistic Binaries in Globular Clusters’. *Living Reviews in Relativity* **16**:4.
- D. P. Bennett, et al. (2002). ‘Gravitational Microlensing Events Due to Stellar-Mass Black Holes’. *The Astrophysical Journal* **579**(2):639–659.
- F. Bernardini, et al. (2015). ‘GX 339-4 is still in the soft state’. *The Astronomer’s Telegram* **7434**.
- M. Betancourt (2019). ‘The Convergence of Markov Chain Monte Carlo Methods: From the Metropolis Method to Hamiltonian Monte Carlo’. *Annalen der Physik* **531**(3):1700214.
- L. Bildsten & R. E. Rutledge (2000). ‘Coronal X-Ray Emission from the Stellar Companions to Transiently Accreting Black Holes’. *The Astrophysical Journal* **541**(2):908–917.
- A. Blaauw (1956a). ‘Luminosities, Ages, Kinematics, and Duplicity of the Early-Type Stars’. **68**(405):495–498.
- A. Blaauw (1956b). ‘On the Luminosities, Motions, and Space Distribution of the Nearer Northern O-B5 Stars.’. *The Astrophysical Journal* **123**:408.
- A. Blaauw (1961). ‘On the origin of the O- and B-type stars with high velocities (the “run-away” stars), and some related problems’. **15**:265.
- R. D. Blandford & A. Königl (1979). ‘Relativistic jets as compact radio sources.’. *The Astrophysical Journal* **232**:34–48.
- R. D. Blandford & M. J. Rees (1978). ‘Extended and compact extragalactic radio sources: interpretation and theory.’. **17**:265–274.
- J. Bodensteiner, et al. (2020). ‘Is HR 6819 a triple system containing a black hole? – An alternative explanation’. *arXiv e-prints* p. arXiv:2006.10770.

- A. Boehle, et al. (2016). ‘An Improved Distance and Mass Estimate for Sgr A* from a Multistar Orbit Analysis’. *The Astrophysical Journal* **830**(1):17.
- J. Boersma (1961). ‘Mathematical theory of the two-body problem with one of the masses decreasing with time’. **15**:291–301.
- C. T. Bolton (1972). ‘Identification of Cygnus X-1 with HDE 226868’. *Nature* **235**(5336):271–273.
- C. T. Bolton (1975). ‘Orbital elements and an analysis of models for HDE 226868 = Cygnus X-1.’. *The Astrophysical Journal* **200**:269–277.
- J. Bovy (2015). ‘galpy: A python Library for Galactic Dynamics’. *The Astrophysical Journal Supplemental* **216**(2):29.
- W. N. Brandt, et al. (1995). ‘On the high space velocity of X-ray Nova SCO 1994: implications for the formation of its black hole’. *Monthly Notices of the Royal Astronomical Society* **277**:L35–L40.
- J. S. Bright, et al. (2020). ‘An extremely powerful long-lived superluminal ejection from the black hole MAXI J1820+070’. *Nature Astronomy* .
- K. P. Burnham & D. R. Anderson (2002). ‘Model Selection and Multimodel Inference’. In *Model Selection and Multimodel Inference*, vol. 26 of *Springer-Verlag New York*.
- M. Buxton, et al. (2013). ‘New outburst of the black-hole X-ray binary GX 339-4’. *The Astronomer’s Telegram* **5244**.
- M. Cadolle Bel, et al. (2007). ‘Simultaneous Multiwavelength Observations of the Low/Hard State of the X-Ray Transient Source SWIFT J1753.5-0127’. *The Astrophysical Journal* **659**:549–560.
- F. Camilo, et al. (2000). ‘Observations of 20 Millisecond Pulsars in 47 Tucanae at 20 Centimeters’. *The Astrophysical Journal* **535**:975–990.

- A. G. Cantrell, et al. (2010). ‘The Inclination of the Soft X-Ray Transient A0620-00 and the Mass of its Black Hole’. *The Astrophysical Journal* **710**:1127–1141.
- J. Casares (2007). ‘Observational evidence for stellar-mass black holes’. In V. Karas & G. Matt (eds.), *Black Holes from Stars to Galaxies – Across the Range of Masses*, vol. 238 of *IAU Symposium*, pp. 3–12.
- J. Casares (2018). ‘Hibernating black holes revealed by photometric mass functions’. *Monthly Notices of the Royal Astronomical Society* **473**(4):5195–5209.
- J. Casares & P. A. Charles (1994). ‘Optical studies of V404 Cyg, the X-ray transient GS 2023+338. IV. The rotation speed of the companion star.’. *Monthly Notices of the Royal Astronomical Society* **271**:L5–L9.
- J. Casares, et al. (2009). ‘Refined Orbital Solution and Quiescent Variability in the Black Hole Transient GS 1354-64 (= BW Cir)’. *The Astrophysical Journal Supplemental* **181**:238–243.
- J. Casares & M. A. P. Torres (2018). ‘A feasibility study on the photometric detection of quiescent black hole X-ray binaries’. *Monthly Notices of the Royal Astronomical Society* **481**(4):4372–4380.
- J. Casares, et al. (2004). ‘Evidence of a Black Hole in the X-Ray Transient GS 1354-64 (=BW Circini)’. *The Astrophysical Journal Letters* **613**:L133–L136.
- J. E. Cavanaugh (1997). ‘Unifying the derivations for the Akaike and corrected Akaike information criteria’. *Statistics & Probability Letters* **33**:201–208.
- K. C. Chambers, et al. (2016). ‘The Pan-STARRS1 Surveys’. *arXiv e-prints* p. arXiv:1612.05560.
- V. C. Chan & J. Bovy (2020). ‘The Gaia DR2 parallax zero-point: hierarchical modelling of red clump stars’. *Monthly Notices of the Royal Astronomical Society* **493**(3):4367–4381.

- S. Chandrasekhar (1931). ‘The Maximum Mass of Ideal White Dwarfs’. *The Astrophysical Journal* **74**:81.
- S. Chatterjee, et al. (2004). ‘Pulsar Parallaxes at 5 GHz with the Very Long Baseline Array’. *The Astrophysical Journal* **604**(1):339–345.
- S. Chaty, et al. (2002). ‘Near-infrared observations of Galactic black hole candidates’. *Monthly Notices of the Royal Astronomical Society* **331**:1065–1071.
- J. Chauhan, et al. (2019). ‘An H I absorption distance to the black hole candidate X-ray binary MAXI J1535-571’. *Monthly Notices of the Royal Astronomical Society* **488**(1):L129–L133.
- L. Chomiuk, et al. (2013). ‘A Radio-selected Black Hole X-Ray Binary Candidate in the Milky Way Globular Cluster M62’. *The Astrophysical Journal* **777**(1):69.
- N. N. Chugai (1984). ‘Pulsar Space Velocities and Neutrino Chirality’. *Soviet Astronomy Letters* **10**:87.
- G. W. Clark (1975). ‘X-ray binaries in globular clusters’. *The Astrophysical Journal Letters* **199**:L143–L145.
- S. A. Colgate (1971). ‘Neutron-Star Formation, Thermonuclear Supernovae, and Heavy-Element Reimplosion’. *The Astrophysical Journal* **163**:221.
- J. D. Collier, et al. (2014). ‘Infrared-faint radio sources: a new population of high-redshift radio galaxies’. *Monthly Notices of the Royal Astronomical Society* **439**(1):545–565.
- J. J. Condon, et al. (1998). ‘The NRAO VLA Sky Survey’. *The Astronomical Journal* **115**(5):1693–1716.
- M. Coriat, et al. (2012). ‘Revisiting a fundamental test of the disc instability model for X-ray binaries’. *Monthly Notices of the Royal Astronomical Society* **424**(3):1991–2001.

- J. M. Corral-Santana, et al. (2016). ‘BlackCAT: A catalogue of stellar-mass black holes in X-ray transients’. *Astronomy and Astrophysics* **587**:A61.
- H. T. Cromartie, et al. (2020). ‘Relativistic Shapiro delay measurements of an extremely massive millisecond pulsar’. *Nature Astronomy* **4**:72–76.
- W. H. de Vries, et al. (2004). ‘Optical Properties of faint FIRST Variable Radio Sources’. *The Astronomical Journal* **127**(5):2565–2578.
- W. Dehnen & J. Binney (1998). ‘Mass models of the Milky Way’. *Monthly Notices of the Royal Astronomical Society* **294**:429.
- M. della Valle, et al. (1994). ‘The optical and radio counterpart of the X-ray Nova Ophiuchi 1993’. *Astronomy and Astrophysics* **290**:803–806.
- A. T. Deller, et al. (2011). ‘DiFX-2: A More Flexible, Efficient, Robust, and Powerful Software Correlator’. **123**:275.
- A. T. Deller, et al. (2019). ‘Microarcsecond VLBI Pulsar Astrometry with PSR π II. Parallax Distances for 57 Pulsars’. *The Astrophysical Journal* **875**(2):100.
- A. T. Deller, et al. (2007). ‘DiFX: A Software Correlator for Very Long Baseline Interferometry Using Multiprocessor Computing Environments’. **119**:318–336.
- V. Dhawan, et al. (2007). ‘Kinematics of Black Hole X-Ray Binary GRS 1915+105’. *The Astrophysical Journal* **668**:430–434.
- G. A. Drukier (1996). ‘Retention fractions for globular cluster neutron stars’. *Monthly Notices of the Royal Astronomical Society* **280**:498–514.
- H. Edelmann, et al. (2005). ‘HE 0437-5439: An Unbound Hypervelocity Main-Sequence B-Type Star’. *The Astrophysical Journal Letters* **634**(2):L181–L184.
- A. Einstein (1916). ‘Die Grundlage der allgemeinen Relativitätstheorie’. *Annalen der Physik* **354**(7):769–822.

- J. J. Eldridge, et al. (2019). ‘Weighing in on black hole binaries with BPASS: LB-1 does not contain a $70M_{\odot}$ black hole’. *arXiv e-prints* p. arXiv:1912.03599.
- M. Elvis, et al. (1975). ‘Discovery of powerful transient X-ray source A0620-00 with Ariel V Sky Survey Experiment’. *Nature* **257**(5528):656–657.
- M. Elvis, et al. (1994). ‘Atlas of Quasar Energy Distributions’. *The Astrophysical Journal Supplemental* **95**:1.
- D. Erkal, et al. (2019). ‘A hypervelocity star with a Magellanic origin’. *Monthly Notices of the Royal Astronomical Society* **483**(2):2007–2013.
- M. Espinasse, et al. (2020). ‘Relativistic X-Ray Jets from the Black Hole X-Ray Binary MAXI J1820+070’. *The Astrophysical Journal Letters* **895**(2):L31.
- Event Horizon Telescope Collaboration, et al. (2019a). ‘First M87 Event Horizon Telescope Results. I. The Shadow of the Supermassive Black Hole’. *The Astrophysical Journal Letters* **875**(1):L1.
- Event Horizon Telescope Collaboration, et al. (2019b). ‘First M87 Event Horizon Telescope Results. IV. Imaging the Central Supermassive Black Hole’. *The Astrophysical Journal Letters* **875**(1):L4.
- Event Horizon Telescope Collaboration, et al. (2019c). ‘First M87 Event Horizon Telescope Results. II. Array and Instrumentation’. *The Astrophysical Journal Letters* **875**(1):L2.
- Event Horizon Telescope Collaboration, et al. (2019d). ‘First M87 Event Horizon Telescope Results. III. Data Processing and Calibration’. *The Astrophysical Journal Letters* **875**(1):L3.
- Event Horizon Telescope Collaboration, et al. (2019e). ‘First M87 Event Horizon Telescope Results. V. Physical Origin of the Asymmetric Ring’. *The Astrophysical Journal Letters* **875**(1):L5.

- Event Horizon Telescope Collaboration, et al. (2019f). ‘First M87 Event Horizon Telescope Results. VI. The Shadow and Mass of the Central Black Hole’. *The Astrophysical Journal Letters* **875**(1):L6.
- A. C. Fabian (2012). ‘Observational Evidence of Active Galactic Nuclei Feedback’. *Annual Review of Astronomy and Astrophysics* **50**:455–489.
- A. C. Fabian, et al. (1975). ‘Tidal capture formation of binary systems and X-ray sources in globular clusters’. *Monthly Notices of the Royal Astronomical Society* **172**:15p–18p.
- W. M. Farr, et al. (2017). ‘Distinguishing spin-aligned and isotropic black hole populations with gravitational waves’. *Nature* **548**:426–429.
- S. A. Farrell, et al. (2009). ‘An intermediate-mass black hole of over 500 solar masses in the galaxy ESO243-49’. *Nature* **460**(7251):73–75.
- R. Fender & T. Muñoz-Darias (2016). *The Balance of Power: Accretion and Feedback in Stellar Mass Black Holes*, vol. 905, p. 65.
- R. P. Fender, et al. (2004). ‘Towards a unified model for black hole X-ray binary jets’. *Monthly Notices of the Royal Astronomical Society* **355**(4):1105–1118.
- R. P. Fender, et al. (2003). ‘Jet-dominated states: an alternative to advection across black hole event horizons in ‘quiescent’ X-ray binaries’. *Monthly Notices of the Royal Astronomical Society* **343**(4):L99–L103.
- R. P. Fender, et al. (1999). ‘MERLIN observations of relativistic ejections from GRS 1915+105’. *Monthly Notices of the Royal Astronomical Society* **304**(4):865–876.
- R. P. Fender, et al. (2009). ‘Jets from black hole X-ray binaries: testing, refining and extending empirical models for the coupling to X-rays’. *Monthly Notices of the Royal Astronomical Society* **396**:1370–1382.

- R. P. Fender, et al. (2013). ‘The closest black holes’. *Monthly Notices of the Royal Astronomical Society* **430**(3):1538–1547.
- B. P. Flannery & E. P. J. van den Heuvel (1975). ‘On the origin of the binary pulsar PSR 1913+16.’. *Astronomy and Astrophysics* **39**:61–67.
- T. Fragos & J. E. McClintock (2015). ‘The Origin of Black Hole Spin in Galactic Low-mass X-Ray Binaries’. *The Astrophysical Journal* **800**(1):17.
- T. Fragos, et al. (2009). ‘Understanding Compact Object Formation and Natal Kicks. II. The Case of XTE J1118 + 480’. *The Astrophysical Journal* **697**:1057–1070.
- F. Frontera, et al. (2001). ‘A Measurement of the Broadband Spectrum of XTE J1118+480 with BeppoSAX and Its Astrophysical Implications’. *The Astrophysical Journal* **561**(2):1006–1015.
- C. Fryer, et al. (1998). ‘Population Syntheses for Neutron Star Systems with Intrinsic Kicks’. *The Astrophysical Journal* **496**:333–351.
- C. L. Fryer & V. Kalogera (2001). ‘Theoretical Black Hole Mass Distributions’. *The Astrophysical Journal* **554**:548–560.
- J. Fuller & L. Ma (2019). ‘Most Black Holes are Born Very Slowly Rotating’. *arXiv e-prints* p. arXiv:1907.03714.
- Gaia Collaboration, et al. (2018a). ‘Gaia Data Release 2. Summary of the contents and survey properties’. *Astronomy and Astrophysics* **616**:A1.
- Gaia Collaboration, et al. (2018b). ‘Gaia Data Release 2. Summary of the contents and survey properties’. *Astronomy and Astrophysics* **616**:A1.
- Gaia Collaboration, et al. (2016). ‘The Gaia mission’. *Astronomy and Astrophysics* **595**:A1.

- E. Gallo, et al. (2018). ‘Hard state neutron star and black hole X-ray binaries in the radio:X-ray luminosity plane’. *Monthly Notices of the Royal Astronomical Society* **478**(1):L132–L136.
- E. Gallo, et al. (2003). ‘A universal radio-X-ray correlation in low/hard state black hole binaries’. *Monthly Notices of the Royal Astronomical Society* **344**(1):60–72.
- P. Gandhi, et al. (2019). ‘Gaia Data Release 2 distances and peculiar velocities for Galactic black hole transients’. *Monthly Notices of the Royal Astronomical Society* **485**(2):2642–2655.
- J. A. García, et al. (2018). ‘Reflection Spectroscopy of the Black Hole Binary XTE J1752223 in Its Long-stable Hard State’. *The Astrophysical Journal* **864**:25.
- D. M. Gelino, et al. (2006). ‘The Inclination Angle and Mass of the Black Hole in XTE J1118+480’. *The Astrophysical Journal* **642**:438–442.
- A. Gelman & D. B. Rubin (1992). ‘Inference from Iterative Simulation Using Multiple Sequences’. *Statistical Science* **7**:457–472.
- J. R. Gerke, et al. (2015). ‘The search for failed supernovae with the Large Binocular Telescope: first candidates’. *Monthly Notices of the Royal Astronomical Society* **450**(3):3289–3305.
- D. Gerosa, et al. (2013). ‘Resonant-plane locking and spin alignment in stellar-mass black-hole binaries: A diagnostic of compact-binary formation’. **87**(10):104028.
- A. Gessner & H.-T. Janka (2018). ‘Hydrodynamical Neutron-star Kicks in Electron-capture Supernovae and Implications for the CRAB Supernova’. *The Astrophysical Journal* **865**:61.

- A. M. Ghez, et al. (2003). ‘Full Three Dimensional Orbits For Multiple Stars on Close Approaches to the Central Supermassive Black Hole’. *Astronomische Nachrichten Supplement* **324**(1):527–533.
- A. M. Ghez, et al. (1998). ‘High Proper-Motion Stars in the Vicinity of Sagittarius A*: Evidence for a Supermassive Black Hole at the Center of Our Galaxy’. *The Astrophysical Journal* **509**(2):678–686.
- A. M. Ghez, et al. (2000). ‘The accelerations of stars orbiting the Milky Way’s central black hole’. *Nature* **407**(6802):349–351.
- D. R. Gies, et al. (2008). ‘Stellar Wind Variations during the X-Ray High and Low States of Cygnus X-1’. *The Astrophysical Journal* **678**:1237–1247.
- B. Giesers, et al. (2018). ‘A detached stellar-mass black hole candidate in the globular cluster NGC 3201’. *Monthly Notices of the Royal Astronomical Society* **475**:L15–L19.
- B. Giesers, et al. (2019). ‘A stellar census in globular clusters with MUSE: Binaries in NGC 3201’. *Astronomy and Astrophysics* **632**:A3.
- M. Giesler, et al. (2018). ‘Low-mass X-ray binaries from black hole retaining globular clusters’. *Monthly Notices of the Royal Astronomical Society* **477**:1853–1879.
- G. Gilmore & N. Reid (1983). ‘New light on faint stars. III - Galactic structure towards the South Pole and the Galactic thick disc’. *Monthly Notices of the Royal Astronomical Society* **202**:1025–1047.
- O. Y. Gnedin, et al. (2002). ‘The Unique History of the Globular Cluster ω Centauri’. *The Astrophysical Journal Letters* **568**:L23–L26.
- J. I. González Hernández & J. Casares (2010). ‘Doppler tomography of the black hole binary A0620-00 and the origin of chromospheric emission in quiescent X-ray binaries’. *Astronomy and Astrophysics* **516**:A58.

- J. I. González Hernández, et al. (2008a). ‘Chemical Abundances of the Secondary Star in the Black Hole X-Ray Binary XTE J1118+480’. *The Astrophysical Journal* **679**:732–745.
- J. I. González Hernández, et al. (2008b). ‘Chemical Abundances of the Secondary Star in the Black Hole X-Ray Binary XTE J1118+480’. *The Astrophysical Journal* **679**(1):732–745.
- J. I. González Hernández, et al. (2006). ‘XTE J1118+480: A Metal-rich Black Hole Binary in the Galactic Halo’. *The Astrophysical Journal Letters* **644**:L49–L52.
- J. Goodman & P. Hut (1993). ‘Binary-single-star scattering. V - Steady state binary distribution in a homogeneous static background of single stars’. *The Astrophysical Journal* **403**:271–277.
- E. Gourgoulhon (1991). ‘Simple equations for general relativistic hydrodynamics in spherical symmetry applied to neutron star collapse’. *Astronomy and Astrophysics* **252**:651–663.
- E. Gourgoulhon & P. Haensel (1993). ‘Upper bounds on the neutrino burst from collapse of a neutron star into a black hole’. *Astronomy and Astrophysics* **271**:187.
- J. E. Greene & L. C. Ho (2007). ‘A New Sample of Low-Mass Black Holes in Active Galaxies’. *The Astrophysical Journal* **670**(1):92–104.
- J. E. Greene, et al. (2019). ‘Intermediate-Mass Black Holes’. *arXiv e-prints* p. arXiv:1911.09678.
- E. W. Greisen (2003). ‘AIPS, the VLA, and the VLBA’. In A. Heck (ed.), *Information Handling in Astronomy - Historical Vistas*, vol. 285 of *Astrophysics and Space Science Library*, p. 109.

- H.-J. Grimm, et al. (2002). ‘The Milky Way in X-rays for an outside observer. Log(N)-Log(S) and luminosity function of X-ray binaries from RXTE/ASM data’. *Astronomy and Astrophysics* **391**:923–944.
- J. Grindlay, et al. (2012). ‘Opening the 100-Year Window for Time-Domain Astronomy’. In E. Griffin, R. Hanisch, & R. Seaman (eds.), *New Horizons in Time Domain Astronomy*, vol. 285 of *IAU Symposium*, pp. 29–34.
- A. Gualandris, et al. (2005). ‘Has the Black Hole in XTE J1118+480 Experienced an Asymmetric Natal Kick?’. *The Astrophysical Journal* **618**:845–851.
- K. Hada (2019). ‘Relativistic Jets from AGN Viewed at Highest Angular Resolution’. *Galaxies* **8**(1):1.
- J. L. Halbwachs, et al. (2005). ‘Statistical properties of exoplanets. IV. The period-eccentricity relations of exoplanets and of binary stars’. *Astronomy and Astrophysics* **431**(3):1129–1137.
- W. E. Harris (2010). ‘A New Catalog of Globular Clusters in the Milky Way’. *arXiv e-prints* p. arXiv:1012.3224.
- T. Hayashi, et al. (2020). ‘A Strategy to Search for an Inner Binary Black Hole from the Motion of the Tertiary Star’. *The Astrophysical Journal* **890**(2):112.
- M. Heida, et al. (2017). ‘The Mass Function of GX 339-4 from Spectroscopic Observations of Its Donor Star’. *The Astrophysical Journal* **846**:132.
- J. Heise (1999). ‘A wide field view of the galactic center region’. *Nuclear Physics B Proceedings Supplements* **69**:186–195.
- J. M. Hill & P. Salinari (2000). ‘Large Binocular Telescope project’. In T. A. Sebring & T. Andersen (eds.), *Telescope Structures, Enclosures, Controls, Assembly/Integration/Validation, and Commissioning*, vol. 4004, pp. 36 – 46. International Society for Optics and Photonics, SPIE.

- R. M. Hjellming & K. J. Johnston (1981). ‘An analysis of the proper motions of SS 433 radio jets.’. *The Astrophysical Journal Letters* **246**:L141–L145.
- R. M. Hjellming & M. P. Rupen (1995). ‘Episodic ejection of relativistic jets by the X-ray transient GRO J1655 - 40’. *Nature* **375**:464–468.
- R. M. Hjellming & C. M. Wade (1971). ‘Radio Spectrum of Cygnus X-1’. *Nature* **234**(5325):138.
- G. Hobbs, et al. (2005). ‘A statistical study of 233 pulsar proper motions’. *Monthly Notices of the Royal Astronomical Society* **360**:974–992.
- M. D. Hoffman & A. Gelman (2011). ‘The No-U-Turn Sampler: Adaptively Setting Path Lengths in Hamiltonian Monte Carlo’. *arXiv e-prints* .
- D. W. Hogg, et al. (2010). ‘Data analysis recipes: Fitting a model to data’. *arXiv e-prints* .
- T. Holland-Ashford, et al. (2017). ‘Comparing Neutron Star Kicks to Supernova Remnant Asymmetries’. *The Astrophysical Journal* **844**(1):84.
- J. Homan & T. Belloni (2005). ‘The Evolution of Black Hole States’. *Astrophysics and Space Science* **300**:107–117.
- J. Homan, et al. (2020). ‘A Rapid Change in X-Ray Variability and a Jet Ejection in the Black Hole Transient MAXI J1820+070’. *The Astrophysical Journal Letters* **891**(2):L29.
- J. R. Hurley, et al. (2002). ‘Evolution of binary stars and the effect of tides on binary populations’. *Monthly Notices of the Royal Astronomical Society* **329**(4):897–928.
- R. I. Hynes (2005). ‘The Optical and Ultraviolet Spectral Energy Distributions of Short-Period Black Hole X-Ray Transients in Outburst’. *The Astrophysical Journal* **623**:1026–1043.

- D. Ilić & L. Č. Popović (2014). ‘Supermassive black holes and spectral emission lines’. In *Journal of Physics Conference Series*, vol. 548 of *Journal of Physics Conference Series*, p. 012002.
- A. Ingram, et al. (2016). ‘A quasi-periodic modulation of the iron line centroid energy in the black hole binary H1743-322’. *Monthly Notices of the Royal Astronomical Society* **461**:1967–1980.
- K. Iwamoto, et al. (1998). ‘A hypernova model for the supernova associated with the γ -ray burst of 25 April 1998’. *Nature* **395**(6703):672–674.
- I. Jang, et al. (2018). ‘Measuring the black hole mass in ultraluminous X-ray sources with the X-ray scaling method’. *Monthly Notices of the Royal Astronomical Society* **473**(1):136–147.
- H.-T. Janka (2013). ‘Natal kicks of stellar mass black holes by asymmetric mass ejection in fallback supernovae’. *Monthly Notices of the Royal Astronomical Society* **434**:1355–1361.
- H.-T. Janka (2017). ‘Neutron Star Kicks by the Gravitational Tug-boat Mechanism in Asymmetric Supernova Explosions: Progenitor and Explosion Dependence’. *The Astrophysical Journal* **837**:84.
- S. Jimenez-Monferrer, et al. (2010). ‘Multi-beam capabilities for high precision astrometry at low frequencies using VLBI’. In *10th European VLBI Network Symposium and EVN Users Meeting: VLBI and the New Generation of Radio Arrays*, vol. 10, p. 84.
- D. R. H. Johnson & D. R. Soderblom (1987). ‘Calculating galactic space velocities and their uncertainties, with an application to the Ursa Major group’. *The Astronomical Journal* **93**:864–867.
- K. J. Johnston, et al. (1995). ‘A Radio Reference Frame’. *The Astronomical Journal* **110**:880.

- P. G. Jonker & G. Nelemans (2004). ‘The distances to Galactic low-mass X-ray binaries: consequences for black hole luminosities and kicks’. *Monthly Notices of the Royal Astronomical Society* **354**:355–366.
- E. Kalemci, et al. (2013). ‘Complete Multiwavelength Evolution of Galactic Black Hole Transients during Outburst Decay. I. Conditions for “Compact” Jet Formation’. *The Astrophysical Journal* **779**:95.
- V. Kalogera (1998). ‘Formation of Low-Mass X-Ray Binaries. III. A New Formation Mechanism: Direct Supernova’. *The Astrophysical Journal* **493**(1):368–374.
- I. D. Karachentsev & D. I. Makarov (1996). ‘Orbital velocity of the Sun and the apex of the Galactic center’. *Astronomy Letters* **22**(4):455–458.
- E. A. Karitskaya & V. P. Goranskij (1995). ‘Optical Pre-Nova Identification for the X-Ray Nova GRO J0422+32 (Nova Persei, 1992)’. *Space Science Reviews* **74**:489–492.
- T. Kawamuro, et al. (2018). ‘MAXI/GSC detection of a probable new X-ray transient MAXI J1820+070’. *The Astronomer’s Telegram* **11399**.
- A. Keimpema, et al. (2015). ‘The SFXC software correlator for very long baseline interferometry: algorithms and implementation’. *Experimental Astronomy* **39**(2):259–279.
- K. I. Kellermann, et al. (1989). ‘VLA Observations of Objects in the Palomar Bright Quasar Survey’. *The Astronomical Journal* **98**:1195.
- L. Z. Kelley, et al. (2010). ‘The Distribution of Coalescing Compact Binaries in the Local Universe: Prospects for Gravitational-wave Observations’. *The Astrophysical Journal Letters* **725**:L91–L96.
- J. Kepler, et al. (1619). *Harmonices mundi libri v. quorum primus geometricus, de figurarum regularium, quae proportionibus harmonicis constituunt, ortu &*

demonstrationibus, secundus architectonicus, SEU EX geometria figurata, de figurarum regularium congruentia in plano vel solido: tertius proprie harmonicus, de proportionum harmonicarum ortu EX figuris.

- F. J. Kerr & D. Lynden-Bell (1986). ‘Review of galactic constants.’. *Monthly Notices of the Royal Astronomical Society* **221**:1023–1038.
- M. Kettenis, et al. (2006). ‘ParselTongue: AIPS Talking Python’. In C. Gabriel, C. Arviset, D. Ponz, & S. Enrique (eds.), *Astronomical Data Analysis Software and Systems XV*, vol. 351 of *Astronomical Society of the Pacific Conference Series*, p. 497.
- J. Khargharia, et al. (2010). ‘Near-infrared Spectroscopy of Low-mass X-ray Binaries: Accretion Disk Contamination and Compact Object Mass Determination in V404 Cyg and Cen X-4’. *The Astrophysical Journal* **716**:1105–1117.
- J. Khargharia, et al. (2013). ‘The Mass of the Black Hole in XTE J1118+480’. *The Astronomical Journal* **145**:21.
- A. E. Kimball, et al. (2009). ‘A Sample of Candidate Radio Stars in First and SDSS’. *The Astrophysical Journal* **701**(1):535–546.
- A. R. King, et al. (1996). ‘Black Hole Binaries and X-Ray Transients’. *The Astrophysical Journal Letters* **464**:L127.
- F. Kirsten, et al. (2014). ‘Precision astrometry of pulsars and other compact radio sources in the globular cluster M15’. *Astronomy and Astrophysics* **565**:A43.
- C. S. Kochanek, et al. (2008). ‘A Survey About Nothing: Monitoring a Million Supergiants for Failed Supernovae’. *The Astrophysical Journal* **684**(2):1336–1342.
- N. Kojiguchi, et al. (2019). ‘The 1898 and 1934 outbursts of ASASSN-18ey (= MAXI J1820+070)’. *The Astronomer’s Telegram* **13066**:1.

- J. Kormendy & L. C. Ho (2013). ‘Coevolution (Or Not) of Supermassive Black Holes and Host Galaxies’. *Annual Review of Astronomy and Astrophysics* **51**(1):511–653.
- L. Kreidberg, et al. (2012). ‘Mass Measurements of Black Holes in X-Ray Transients: Is There a Mass Gap?’. *The Astrophysical Journal* **757**:36.
- A. Kubota, et al. (1998). ‘Evidence for a Black Hole in the X-Ray Transient GRS 1009-45’. **50**:667–673.
- S. R. Kulkarni, et al. (1993). ‘Stellar black holes in globular clusters’. *Nature* **364**:421–423.
- L. D. Landau (1932). ‘To the Stars theory’. *Phys. Zs. Sowjet* **1**:285.
- J. P. Lasota (2000). ‘X-rays from quiescent low-mass X-ray binary transients’. *Astronomy and Astrophysics* **360**:575–582.
- J. P. Lasota, et al. (1996). ‘Mechanisms for the outbursts of soft X-ray transients.’. *Astronomy and Astrophysics* **314**:813–820.
- J. F. Lestrade, et al. (1990). ‘Phase-Reference VLBI Observations of Weak Radio Sources. Milliarcsecond Position of Algol’. *The Astronomical Journal* **99**:1663.
- L. Lindegren, et al. (2016). ‘Gaia Data Release 1. Astrometry: one billion positions, two million proper motions and parallaxes’. *Astronomy and Astrophysics* **595**:A4.
- J. Liu, et al. (2019). ‘A wide star-black-hole binary system from radial-velocity measurements’. *Nature* **575**(7784):618–621.
- L. Loinard, et al. (2007). ‘VLBA Determination of the Distance to Nearby Star-forming Regions. I. The Distance to T Tauri with 0.4% Accuracy’. *The Astrophysical Journal* **671**(1):546–554.

- P. W. Lucas, et al. (2008). ‘The UKIDSS Galactic Plane Survey’. *Monthly Notices of the Royal Astronomical Society* **391**(1):136–163.
- X. Luri, et al. (2018). ‘Gaia Data Release 2. Using Gaia parallaxes’. *Astronomy and Astrophysics* **616**:A9.
- T. E. Lutz & D. H. Kelker (1973). ‘On the Use of Trigonometric Parallaxes for the Calibration of Luminosity Systems: Theory’. **85**:573.
- D. Lynden-Bell & M. J. Rees (1971). ‘On quasars, dust and the galactic centre’. *Monthly Notices of the Royal Astronomical Society* **152**:461.
- A. G. Lyne & D. R. Lorimer (1994). ‘High birth velocities of radio pulsars’. *Nature* **369**:127–129.
- T. J. Maccarone (2003). ‘Do X-ray binary spectral state transition luminosities vary?’. *Astronomy and Astrophysics* **409**:697–706.
- T. J. Maccarone (2005). ‘Using radio emission to detect isolated and quiescent accreting black holes’. *Monthly Notices of the Royal Astronomical Society* **360**(1):L30–L34.
- T. J. Maccarone, et al. (2007). ‘A black hole in a globular cluster’. *Nature* **445**(7124):183–185.
- R. K. D. MacDonald, et al. (2014). ‘The Black Hole Binary V4641 Sagittarii: Activity in Quiescence and Improved Mass Determinations’. *The Astrophysical Journal* **784**:2.
- A. D. Mackey, et al. (2008). ‘Black holes and core expansion in massive star clusters’. *Monthly Notices of the Royal Astronomical Society* **386**(1):65–95.
- I. Mandel (2010). ‘Parameter estimation on gravitational waves from multiple coalescing binaries’. **81**(8):084029.

- I. Mandel (2016). ‘Estimates of black hole natal kick velocities from observations of low-mass X-ray binaries’. *Monthly Notices of the Royal Astronomical Society* **456**:578–581.
- T. H. Markert, et al. (1973). ‘Observations of the Highly Variable X-Ray Source GX 339-4’. *The Astrophysical Journal Letters* **184**:L67.
- S. Markoff, et al. (2020). ‘Infrared interferometry to spatially and spectrally resolve jets in X-ray binaries’. *Monthly Notices of the Royal Astronomical Society* **495**(1):525–535.
- R. G. Martin, et al. (2008). ‘Misalignment of the microquasar V4641 Sgr (SAX J1819.3-2525)’. *Monthly Notices of the Royal Astronomical Society* **391**:L15–L18.
- N. Masetti, et al. (1996). ‘The superhump phenomenon in GRS 1716-249 (=X-Ray Nova Ophiuchi 1993)’. *Astronomy and Astrophysics* **314**:123–130.
- M. Massi (2011). ‘Steady jets and transient jets: observational characteristics and models’. **82**:24.
- J. E. McClintock, et al. (2014). ‘Black Hole Spin via Continuum Fitting and the Role of Spin in Powering Transient Jets’. *Space Science Reviews* **183**(1-4):295–322.
- J. E. McClintock & R. A. Remillard (2006). *Black hole binaries*, vol. 39, pp. 157–213.
- J. C. McKinney, et al. (2012). ‘General relativistic magnetohydrodynamic simulations of magnetically choked accretion flows around black holes’. *Monthly Notices of the Royal Astronomical Society* **423**(4):3083–3117.
- A. Merloni, et al. (2012). ‘eROSITA Science Book: Mapping the Structure of the Energetic Universe’. *arXiv e-prints* p. arXiv:1209.3114.

- J. Michell (1784). ‘On the Means of Discovering the Distance, Magnitude, &c. of the Fixed Stars, in Consequence of the Diminution of the Velocity of Their Light, in Case Such a Diminution Should be Found to Take Place in any of Them, and Such Other Data Should be Procured from Observations, as Would be Farther Necessary for That Purpose. By the Rev. John Michell, B. D. F. R. S. In a Letter to Henry Cavendish, Esq. F. R. S. and A. S.’. *Philosophical Transactions of the Royal Society of London Series I* **74**:35–57.
- F. Mignard (2000). ‘Local galactic kinematics from Hipparcos proper motions’. *Astronomy and Astrophysics* **354**:522–536.
- J. C. A. Miller-Jones, et al. (2018). ‘The geometric distance and binary orbit of PSR B1259-63’. *Monthly Notices of the Royal Astronomical Society* **479**:4849–4860.
- J. C. A. Miller-Jones, et al. (2009a). ‘The First Accurate Parallax Distance to a Black Hole’. *The Astrophysical Journal Letters* **706**:L230–L234.
- J. C. A. Miller-Jones, et al. (2009b). ‘The formation of the black hole in the X-ray binary system V404 Cyg’. *Monthly Notices of the Royal Astronomical Society* **394**:1440–1448.
- J. C. A. Miller-Jones, et al. (2012). ‘Disc-jet coupling in the 2009 outburst of the black hole candidate H1743-322’. *Monthly Notices of the Royal Astronomical Society* **421**(1):468–485.
- J. C. A. Miller-Jones, et al. (2015). ‘Deep radio imaging of 47 Tuc identifies the peculiar X-ray source X9 as a new black hole candidate’. *Monthly Notices of the Royal Astronomical Society* **453**:3918–3931.
- J. C. A. Miller-Jones, et al. (2019). ‘A rapidly changing jet orientation in the stellar-mass black-hole system V404 Cygni’. *Nature* **569**(7756):374–377.
- F. Mirabel (2017). ‘The formation of stellar black holes’. **78**:1–15.

- I. F. Mirabel, et al. (2001). ‘A high-velocity black hole on a Galactic-halo orbit in the solar neighbourhood’. *Nature* **413**:139–141.
- I. F. Mirabel, et al. (2002). ‘The runaway black hole GRO J1655-40’. *Astronomy and Astrophysics* **395**:595–599.
- I. F. Mirabel & I. Rodrigues (2003). ‘Formation of a Black Hole in the Dark’. *Science* **300**:1119–1121.
- I. F. Mirabel & L. F. Rodríguez (1994). ‘A superluminal source in the Galaxy’. *Nature* **371**(6492):46–48.
- I. F. Mirabel, et al. (1993). ‘VLA observations of the hard X-ray sources 1E1740.7-2942 and GRS1758-258’. *Astronomy and Astrophysics Supplement Series* **97**:193–197.
- A. Moin, et al. (2016). ‘e-VLBI observations of GRB 080409 afterglow with an Australasian radio telescope network’. *Research in Astronomy and Astrophysics* **16**(11):164.
- M. Morscher, et al. (2013). ‘Retention of Stellar-mass Black Holes in Globular Clusters’. *The Astrophysical Journal Letters* **763**(1):L15.
- T. Muñoz-Darias, et al. (2013). ‘Inclination and relativistic effects in the outburst evolution of black hole transients’. *Monthly Notices of the Royal Astronomical Society* **432**(2):1330–1337.
- E. M. Murchikova, et al. (2019). ‘A cool accretion disk around the Galactic Centre black hole’. *Nature* **570**(7759):83–86.
- T. Murphy, et al. (2010). ‘The Australia Telescope 20 GHz Survey: the source catalogue’. *Monthly Notices of the Royal Astronomical Society* **402**(4):2403–2423.
- R. M. Neal (2012). ‘MCMC using Hamiltonian dynamics’. *arXiv e-prints* p. arXiv:1206.1901.

- H. Negoro, et al. (2016). ‘MAXI/GSC detection of a new outburst from GRS 1716-249/GRO J1719-24 or a new X-ray transient MAXI J1719-254’. *The Astronomer’s Telegram* **9876**.
- G. Nelemans, et al. (1999). ‘Constraints on mass ejection in black hole formation derived from black hole X-ray binaries’. *Astronomy and Astrophysics* **352**:L87–L90.
- A. Olejak, et al. (2019). ‘Synthetic catalog of black holes in the Milky Way’. *arXiv e-prints* p. arXiv:1908.08775.
- J. A. Orosz, et al. (1996). ‘Improved Parameters for the Black Hole Binary System X-Ray Nova MUSCAE 1991’. *The Astrophysical Journal* **468**:380.
- J. A. Orosz, et al. (1998). ‘Orbital Parameters for the Soft X-Ray Transient 4U 1543-47: Evidence for a Black Hole’. *The Astrophysical Journal* **499**:375–384.
- J. A. Orosz, et al. (2001). ‘A Black Hole in the Superluminal Source SAX J1819.3-2525 (V4641 Sgr)’. *The Astrophysical Journal* **555**:489–503.
- J. A. Orosz, et al. (2011). ‘The Mass of the Black Hole in Cygnus X-1’. *The Astrophysical Journal* **742**:84.
- R. O’Shaughnessy, et al. (2017). ‘Inferences about Supernova Physics from Gravitational-Wave Measurements: GW151226 Spin Misalignment as an Indicator of Strong Black-Hole Natal Kicks’. *Physical Review Letters* **119**(1):011101.
- S. P. O’Sullivan & D. C. Gabuzda (2009). ‘Magnetic field strength and spectral distribution of six parsec-scale active galactic nuclei jets’. *Monthly Notices of the Royal Astronomical Society* **400**(1):26–42.
- D. M. Palmer, et al. (2005). ‘BAT detection of a new gamma ray source SWIFT J1753.5-0127’. *The Astronomer’s Telegram* **546**.

- Z. Paragi, et al. (2019). ‘SKA-VLBI Key Science Programmes’. *arXiv e-prints* p. arXiv:1901.10361.
- Z. Paragi, et al. (2014). ‘Very Long Baseline Interferometry with the SKA’.
- D. R. Pasham, et al. (2015). ‘Evidence for High-frequency QPOs with a 3:2 Frequency Ratio from a 5000 Solar Mass Black Hole’. *The Astrophysical Journal Letters* **811**(1):L11.
- E. Pfahl, et al. (2003). ‘The Galactic Population of Low- and Intermediate-Mass X-Ray Binaries’. *The Astrophysical Journal* **597**(2):1036–1048.
- C. J. Phillips, et al. (2007). ‘Detection of compact radio emission from Circinus X-1 with the first Southern hemisphere e-VLBI experiment’. *Monthly Notices of the Royal Astronomical Society* **380**(1):L11–L14.
- R. M. Plotkin, et al. (2013). ‘The X-Ray Spectral Evolution of Galactic Black Hole X-Ray Binaries toward Quiescence’. *The Astrophysical Journal* **773**(1):59.
- P. Podsiadlowski, et al. (2004). ‘The Effects of Binary Evolution on the Dynamics of Core Collapse and Neutron Star Kicks’. *The Astrophysical Journal* **612**:1044–1051.
- K. A. Postnov & L. R. Yungelson (2014). ‘The Evolution of Compact Binary Star Systems’. *Living Reviews in Relativity* **17**:3.
- N. Pradel, et al. (2006). ‘Astrometric accuracy of phase-referenced observations with the VLBA and EVN’. *Astronomy and Astrophysics* **452**:1099–1106.
- C. R. Purcell, et al. (2013). ‘The Coordinated Radio and Infrared Survey for High-mass Star Formation. II. Source Catalog’. *The Astrophysical Journal Supplemental* **205**(1):1.
- C. R. Purcell, et al. (2008). ‘The CORNISH Survey of the Galactic Plane’. In H. Beuther, H. Linz, & T. Henning (eds.), *Massive Star Formation: Ob-*

- servations Confront Theory*, vol. 387 of *Astronomical Society of the Pacific Conference Series*, p. 389.
- M. J. Reid, et al. (2017). ‘Techniques for Accurate Parallax Measurements for 6.7 GHz Methanol Masers’. *The Astronomical Journal* **154**(2):63.
- M. J. Reid & M. Honma (2014). ‘Microarcsecond Radio Astrometry’. *Annual Review of Astronomy and Astrophysics* **52**:339–372.
- M. J. Reid, et al. (2011). ‘The Trigonometric Parallax of Cygnus X-1’. *The Astrophysical Journal* **742**:83.
- M. J. Reid, et al. (2014). ‘A Parallax Distance to the Microquasar GRS 1915+105 and a Revised Estimate of its Black Hole Mass’. *The Astrophysical Journal* **796**:2.
- M. J. Reid, et al. (2009). ‘Trigonometric Parallaxes of Massive Star-Forming Regions. I. S 252 & G232.6+1.0’. *The Astrophysical Journal* **693**(1):397–405.
- A. E. Reines, et al. (2013). ‘Dwarf Galaxies with Optical Signatures of Active Massive Black Holes’. *The Astrophysical Journal* **775**(2):116.
- S. Repetto, et al. (2012). ‘Investigating stellar-mass black hole kicks’. *Monthly Notices of the Royal Astronomical Society* **425**:2799–2809.
- S. Repetto, et al. (2017). ‘The Galactic distribution of X-ray binaries and its implications for compact object formation and natal kicks’. *Monthly Notices of the Royal Astronomical Society* **467**:298–310.
- S. Repetto & G. Nelemans (2015). ‘Constraining the formation of black holes in short-period black hole low-mass X-ray binaries’. *Monthly Notices of the Royal Astronomical Society* **453**:3341–3355.

- S. P. Reynolds (1982). ‘Theoretical studies of compact radio sources. I - Synchrotron radiation from relativistic flows.’. *The Astrophysical Journal* **256**:13–37.
- T. M. Reynolds, et al. (2015). ‘Gone without a bang: an archival HST survey for disappearing massive stars’. *Monthly Notices of the Royal Astronomical Society* **453**:2885–2900.
- G. T. Richards, et al. (2006). ‘Spectral Energy Distributions and Multiwavelength Selection of Type 1 Quasars’. *The Astrophysical Journal Supplemental* **166**(2):470–497.
- M. Rioja, et al. (2009). ‘Revisited “Cluster-Cluster” VLBI with future multi-beam low frequency radio interferometers’. In *8th International e-VLBI Workshop*, p. 14.
- T. Rivinius, et al. (2020). ‘A naked-eye triple system with a nonaccreting black hole in the inner binary’. *Astronomy and Astrophysics* **637**:L3.
- C. L. Rodriguez, et al. (2016). ‘Dynamical Formation of the GW150914 Binary Black Hole’. *The Astrophysical Journal Letters* **824**:L8.
- R. W. Romani (1998). ‘A census of low mass black hole binaries’. *Astronomy and Astrophysics* **333**:583–590.
- D. M. Russell, et al. (2019). ‘MAXI J1820+070 is close to quiescence’. *The Astronomer’s Telegram* **12534**.
- T. D. Russell, et al. (2015). ‘Radio monitoring of the hard state jets in the 2011 outburst of MAXI J1836-194’. *Monthly Notices of the Royal Astronomical Society* **450**:1745–1759.
- T. D. Russell, et al. (2014). ‘The face-on disc of MAXI J1836-194’. *Monthly Notices of the Royal Astronomical Society* **439**:1381–1389.

- I. Sagert & J. Schaffner-Bielich (2008). ‘Pulsar kicks by anisotropic neutrino emission from quark matter in strong magnetic fields’. *Astronomy and Astrophysics* **489**:281–289.
- J. Salvatier, et al. (2016). ‘PyMC3: Python probabilistic programming framework’. Astrophysics Source Code Library.
- K. Schwarzschild (1916). ‘On the Gravitational Field of a Mass Point According to Einstein’s Theory’. *Abh. Konigl. Preuss. Akad. Wissenschaften Jahre 1906,92, Berlin,1907* **1916**:189–196.
- T. Shahbaz (2003). ‘Determining the spectroscopic mass ratio in interacting binaries: application to X-Ray Nova Sco 1994’. *Monthly Notices of the Royal Astronomical Society* **339**:1031–1040.
- T. Shahbaz, et al. (2001). ‘VLT optical observations of V821 Ara(=GX339-4) in an extended “off” state’. *Astronomy and Astrophysics* **376**:L17–L21.
- T. Shahbaz, et al. (1999). ‘The mass of X-ray Nova Scorpii1994 (=GRO J1655-40)’. *Monthly Notices of the Royal Astronomical Society* **306**:89–94.
- N. I. Shakura & R. A. Sunyaev (1973). ‘Reprint of 1973A&A....24..337S. Black holes in binary systems. Observational appearance.’. *Astronomy and Astrophysics* **500**:33–51.
- I. I. Shapiro, et al. (1979). ‘Submilliarcsecond astrometry via VLBI. I - Relative position of the radio sources 3C 345 and NRAO 512’. *The Astronomical Journal* **84**:1459–1469.
- A. W. Shaw, et al. (2016). ‘No evidence for a low-mass black hole in Swift J1753.5-0127’. *Monthly Notices of the Royal Astronomical Society* **463**:1314–1322.
- A. W. Shaw, et al. (2020). ‘The Swift Bulge Survey: optical and near-IR follow-up featuring a likely symbiotic X-ray binary and a focused wind CV’. *Monthly Notices of the Royal Astronomical Society* **492**(3):4344–4360.

- M. Shidatsu, et al. (2019). ‘X-Ray and Optical Monitoring of State Transitions in MAXI J1820+070’. *The Astrophysical Journal* **874**(2):183.
- M. Shidatsu, et al. (2018). ‘X-Ray, Optical, and Near-infrared Monitoring of the New X-Ray Transient MAXI J1820+070 in the Low/Hard State’. *The Astrophysical Journal* **868**(1):54.
- L. Shishkovsky, et al. (2018). ‘The MAVERIC Survey: A Red Straggler Binary with an Invisible Companion in the Galactic Globular Cluster M10’. *The Astrophysical Journal* **855**(1):55.
- S. Sigurdsson & L. Hernquist (1993). ‘Primordial black holes in globular clusters’. *Nature* **364**:423–425.
- S. Sigurdsson & E. S. Phinney (1993). ‘Binary–Single Star Interactions in Globular Clusters’. *The Astrophysical Journal* **415**:631.
- A. C. Sippel & J. R. Hurley (2013). ‘Multiple stellar-mass black holes in globular clusters: theoretical confirmation’. *Monthly Notices of the Royal Astronomical Society* **430**:L30–L34.
- H. Sreehari, et al. (2018). ‘Constraining the mass of the black hole GX 339-4 using spectro-temporal analysis of multiple outbursts’. *ArXiv e-prints* .
- D. Steeghs, et al. (2013). ‘The Not-so-massive Black Hole in the Microquasar GRS1915+105’. *The Astrophysical Journal* **768**:185.
- L. Stella & M. Vietri (1998). ‘Lense-Thirring Precession and Quasi-periodic Oscillations in Low-Mass X-Ray Binaries’. *The Astrophysical Journal Letters* **492**:L59–L62.
- M. A. Stephens (1974). ‘EDF Statistics for Goodness of Fit and Some Comparisons’. *Journal of the American Statistical Association* **69**(347):730–737.
- H. Stiele & A. K. H. Kong (2016). ‘The 2015 hard-state only outburst of GS 1354-64’. *Monthly Notices of the Royal Astronomical Society* **459**(4):4038–4045.

- A. M. Stirling, et al. (2001). ‘A relativistic jet from Cygnus X-1 in the low/hard X-ray state’. *Monthly Notices of the Royal Astronomical Society* **327**(4):1273–1278.
- J. Strader, et al. (2012). ‘Two stellar-mass black holes in the globular cluster M22’. *Nature* **490**:71–73.
- T. Sukhbold, et al. (2016). ‘Core-collapse Supernovae from 9 to 120 Solar Masses Based on Neutrino-powered Explosions’. *The Astrophysical Journal* **821**:38.
- T. M. Tauris, et al. (2015). ‘Ultra-stripped supernovae: progenitors and fate’. *Monthly Notices of the Royal Astronomical Society* **451**:2123–2144.
- G. Taylor, et al. (1999). *Synthesis Imaging in Radio Astronomy II: A Collection of Lectures from the Sixth NRAO/NMIMT Synthesis Imaging Summer School Held at Socorro, New Mexico, USA, 17-23 June, 1998*. Astronomical Society of the Pacific conference series. Astronomical Society of the Pacific.
- B. E. Tetarenko, et al. (2016a). ‘The First Low-mass Black Hole X-Ray Binary Identified in Quiescence Outside of a Globular Cluster’. *The Astrophysical Journal* **825**:10.
- B. E. Tetarenko, et al. (2016b). ‘WATCHDOG: A Comprehensive All-sky Database of Galactic Black Hole X-ray Binaries’. *The Astrophysical Journal Supplemental* **222**:15.
- The LIGO Scientific Collaboration & The Virgo Collaboration (2018). ‘Binary Black Hole Population Properties Inferred from the First and Second Observing Runs of Advanced LIGO and Advanced Virgo’. *arXiv e-prints* .
- A. R. Thompson, et al. (2017). *Interferometry and Synthesis in Radio Astronomy, 3rd Edition*.

- T. A. Thompson, et al. (2020). ‘Response to Comment on “A Non-Interacting Low-Mass Black Hole – Giant Star Binary System”’. *arXiv e-prints* p. arXiv:2005.07653.
- T. A. Thompson, et al. (2019). ‘A noninteracting low-mass black hole giant star binary system’. *Science* **366**(6465):637–640.
- J. A. Tomsick, et al. (2012). ‘Is IGR J11014-6103 a Pulsar with the Highest Known Kick Velocity?’. *The Astrophysical Journal Letters* **750**(2):L39.
- M. A. P. Torres, et al. (2020). ‘The Binary Mass Ratio in the Black Hole Transient MAXI J1820+070’. *The Astrophysical Journal Letters* **893**(2):L37.
- M. A. P. Torres, et al. (2019). ‘Dynamical Confirmation of a Black Hole in MAXI J1820+070’. *The Astrophysical Journal Letters* **882**(2):L21.
- M. A. Tucker, et al. (2018). ‘ASASSN-18ey: The Rise of a New Black Hole X-Ray Binary’. *The Astrophysical Journal Letters* **867**(1):L9.
- J. Ulowetz, et al. (2019). ‘Rebrightening of ASASSN-18ey = MAXI J1820+070’. *The Astronomer’s Telegram* **12567**.
- C. M. Urry & P. Padovani (1995). ‘Unified Schemes for Radio-Loud Active Galactic Nuclei’. **107**:803.
- A. Vahdat Motlagh, et al. (2019). ‘Investigating state transition luminosities of Galactic black hole transients in the outburst decay’. *Monthly Notices of the Royal Astronomical Society* **485**(2):2744–2758.
- R. van den Bosch, et al. (2006). ‘The Dynamical Mass-to-Light Ratio Profile and Distance of the Globular Cluster M15’. *The Astrophysical Journal* **641**(2):852–861.
- J. van den Eijnden, et al. (2017). ‘The very-faint X-ray binary IGR J17062-6143: a truncated disk, no pulsations and a possible outflow’. *arXiv e-prints* p. arXiv:1712.03949.

- E. P. J. van den Heuvel & T. M. Tauris (2020). ‘Comment on “A non-interacting low-mass black hole – giant star binary system”’. *arXiv e-prints* p. arXiv:2005.04896.
- T. F. J. van Grunsven, et al. (2017). ‘The mass of the black hole in 1A 0620-00, revisiting the ellipsoidal light curve modelling’. *Monthly Notices of the Royal Astronomical Society* **472**:1907–1914.
- J. van Paradijs (1996). ‘On the Accretion Instability in Soft X-Ray Transients’. *The Astrophysical Journal Letters* **464**:L139.
- J. van Paradijs & N. White (1995). ‘The Galactic Distribution of Low-Mass X-Ray Binaries’. *The Astrophysical Journal Letters* **447**:L33.
- T. Venumadhav, et al. (2019). ‘New search pipeline for compact binary mergers: Results for binary black holes in the first observing run of Advanced LIGO’. **100**(2):023011.
- F. Verbunt, et al. (2017). ‘The observed velocity distribution of young pulsars’. *Astronomy and Astrophysics* **608**:A57.
- Y. Wang, et al. (2020). ‘The Evolution of the Broadband Temporal Features Observed in the Black-hole Transient MAXI J1820+070 with Insight-HXMT’. *The Astrophysical Journal* **896**(1):33.
- N. E. White & J. van Paradijs (1996). ‘The Galactic Distribution of Black Hole Candidates in Low Mass X-ray Binary Systems’. *The Astrophysical Journal Letters* **473**:L25.
- R. Wijnands, et al. (2006). ‘The XMM-Newton/Chandra monitoring campaign of the Galactic center region. Description of the program and preliminary results’. *Astronomy and Astrophysics* **449**:1117–1127.

- B. Willems, et al. (2005). ‘Understanding Compact Object Formation and Natal Kicks. I. Calculation Methods and the Case of GRO J1655-40’. *The Astrophysical Journal* **625**:324–346.
- M. G. Witte & G. J. Savonije (2002). ‘Orbital evolution by dynamical tides in solar type stars. Application to binary stars and planetary orbits’. *Astronomy and Astrophysics* **386**:222–236.
- A. M. Wolfe & G. R. Burbidge (1970). ‘Black Holes in Elliptical Galaxies’. *The Astrophysical Journal* **161**:419.
- K. W. K. Wong & D. Gerosa (2019). ‘Machine-learning interpolation of population-synthesis simulations to interpret gravitational-wave observations: A case study’. **100**(8):083015.
- T.-W. Wong, et al. (2012). ‘Understanding Compact Object Formation and Natal Kicks. III. The Case of Cygnus X-1’. *The Astrophysical Journal* **747**:111.
- A. Wongwathanarat, et al. (2013). ‘Three-dimensional neutrino-driven supernovae: Neutron star kicks, spins, and asymmetric ejection of nucleosynthesis products’. *Astronomy and Astrophysics* **552**:A126.
- L. Woodburn, et al. (2015). ‘Conversion of a New Zealand 30-Metre Telecommunications Antenna into a Radio Telescope’. *Publications of the Astronomical Society of Australia* **32**:e017.
- S. E. Woosley & T. A. Weaver (1995). ‘The Evolution and Explosion of Massive Stars. II. Explosive Hydrodynamics and Nucleosynthesis’. *The Astrophysical Journal Supplemental* **101**:181.
- D. Wysocki, et al. (2018). ‘Explaining LIGO’s observations via isolated binary evolution with natal kicks’. **97**(4):043014.

- J. Xiang, et al. (2011). ‘Using the X-Ray Dust Scattering Halo of Cygnus X-1 to Determine Distance and Dust Distributions’. *The Astrophysical Journal* **738**(1):78.
- S. Xu, et al. (2019). ‘Comparison of Gaia DR2 Parallaxes of Stars with VLBI Astrometry’. *The Astrophysical Journal* **875**:114.
- Y. Xu, et al. (2020). ‘Evidence for Disk Truncation at Low Accretion States of the Black Hole Binary MAXI J1820+070 Observed by NuSTAR and XMM-Newton’. *The Astrophysical Journal* **893**(1):42.
- Z. Yan, et al. (2014). ‘Swift/BAT detects of a new X-ray outburst of GX 339-4’. *The Astronomer’s Telegram* **6649**.
- L. Zampieri, et al. (2019). ‘Dimming of MAXI J1820+070 (ASASSN-18ey) in the optical band’. *The Astronomer’s Telegram* **12747**.
- A. A. Zdziarski, et al. (2004). ‘GX 339-4: the distance, state transitions, hysteresis and spectral correlations’. *Monthly Notices of the Royal Astronomical Society* **351**:791–807.
- A. A. Zdziarski, et al. (1998). ‘Broad-band X-ray/gamma-ray spectra and binary parameters of GX 339-4 and their astrophysical implications’. *Monthly Notices of the Royal Astronomical Society* **301**(2):435–450.
- J. Ziółkowski (2008). ‘Masses of Black Holes in the Universe’. *Chinese Journal of Astronomy and Astrophysics Supplement* **8**:273–280.
- C. Zurita, et al. (2008). ‘Swift J1753.5-0127: The Black Hole Candidate with the Shortest Orbital Period’. *The Astrophysical Journal* **681**:1458–1463.
- F. Zwicky (1957). *Morphological astronomy*.

Every reasonable effort has been made to acknowledge the owners of copyright material. I would be pleased to hear from any copyright owner who has been omitted or incorrectly acknowledged.